

# **Phenomenology of the Higgs and Flavour Physics In the Standard Model and Beyond**

DISSERTATION

zur Erlangung des akademischen Grades

doctor rerum naturalium  
(Dr. rer. nat.)  
im Fach Physik

eingereicht an der  
Mathematisch-Wissenschaftlichen Fakultät  
Humboldt-Universität zu Berlin

von  
**M.Sc. Lina Alasfar**  
geboren am 27. 09. 1994 in Riad

Präsidentin der Humboldt-Universität zu Berlin:  
Prof. Dr.-Ing. Dr. Sabine Kunst

Dekan der Mathematisch-Wissenschaftlichen Fakultät:  
Prof. Dr. Elmar Kulke

Gutachter:

1. Prof. Dr. R. Gröber, Humboldt-Universität zu Berlin
2. Prof. Dr. Dr. M. Musterman, Potsdam-Institut für Klimafolgenforschung
3. Prof. Dr. M. Mustermann, Heidelberg

**Tag der mündlichen Prüfung:** 06. November 2013



# Contents

<b>I Higgs Physics</b>	<b>3</b>
<b>1 The Standard Model Higgs boson</b>	<b>5</b>
1.1 Spontaneous symmetry breaking . . . . .	5
1.1.1 Nambu-Goldstone theorem . . . . .	8
1.2 The Higgs mechanism . . . . .	9
1.3 Yukawa interaction . . . . .	12
1.4 The Higgs and EW precision observables . . . . .	14
1.4.1 Custodial symmetry . . . . .	15
1.5 Theoretical constraints on the Higgs . . . . .	19
1.5.1 Electroweak precision data fits . . . . .	19
1.5.2 Partial-wave unitarity . . . . .	20
1.5.3 Other bounds . . . . .	23
<b>2 Experimental measurements of the Higgs boson</b>	<b>25</b>
2.1 Overview of the Large Hadron Collider . . . . .	25
2.2 Higgs properties . . . . .	27
2.2.1 Higgs boson mass measurements . . . . .	27
2.2.2 Higgs full width . . . . .	28
2.2.3 Higgs spin and parity . . . . .	30
2.3 Measurements of Higgs rates and couplings . . . . .	30
2.3.1 Higgs cross-sections . . . . .	30
2.3.2 Constraints on Higgs couplings . . . . .	33
2.4 Challenges and outlook . . . . .	34
<b>3 Higgs and effective field theories</b>	<b>37</b>
3.1 Standard Model EFT . . . . .	38
3.1.1 Single Higgs processes in SMEFT . . . . .	41
3.1.2 Higgs pair production and SMEFT . . . . .	43
3.2 The chiral Lagrangian . . . . .	45
3.2.1 Translation between SMEFT and HEFT . . . . .	46
3.2.2 EFT and $\kappa$ -formalism . . . . .	47
3.3 Conclusions . . . . .	48

<b>II Single Higgs Processes at the LHC</b>	<b>51</b>
<b>4 Overview of Higgs production at colliders</b>	<b>53</b>
4.1 Current status of the Higgs production channels . . . . .	54
4.1.1 Gluon fusion . . . . .	54
4.1.2 Vector boson fusion . . . . .	55
4.1.3 Associated production with EW bosons . . . . .	56
4.1.4 Associated production with top quarks . . . . .	57
4.2 Concluding remarks . . . . .	57
<b>5 Four top operator in Higgs production and decay</b>	<b>59</b>
5.1 Four-fermion operators in SMEFT . . . . .	60
5.2 Contribution of four-fermion operators to Higgs rates at NLO . . . . .	61
5.2.1 Analytic calculations . . . . .	61
5.2.2 NLO corrections to $t\bar{t}h$ . . . . .	67
5.2.3 Results . . . . .	69
5.3 Fit to Higgs observables . . . . .	70
5.3.1 Fit results . . . . .	74
5.3.2 Prospects for HL-LHC . . . . .	80
5.4 Summary and discussion . . . . .	81
<b>6 Virtual two-loop calculation of <math>Zh</math> production via gluon fusion</b>	<b>85</b>
6.1 General notation . . . . .	86
6.1.1 The transverse momentum expansion . . . . .	87
6.2 Born cross-section in the $p_T$ -expansion . . . . .	89
6.3 NLO calculation . . . . .	92
6.3.1 Renormalisation . . . . .	92
6.3.2 Calculation of the exact virtual corrections . . . . .	94
6.3.3 Calculation of the $p_T$ -expanded virtual corrections . . . . .	96
6.4 Results and conclusions . . . . .	96
<b>III Higgs Pair at Hadron Colliders</b>	<b>101</b>
<b>7 Overview of Higgs pair production at colliders</b>	<b>103</b>
7.1 Overview of Light Yukawa searches . . . . .	105
<b>8 Higgs pair as a probe for light Yukawas</b>	<b>109</b>
8.1 Introduction . . . . .	109
8.2 Effective Field Theory of light Yukawa couplings . . . . .	111
8.3 Higgs pair production and Higgs decays with modified light Yukawa couplings . . . . .	114
8.3.1 Higgs pair production via gluon fusion . . . . .	114
8.3.2 Higgs pair production via quark anti-quark annihilation . . . . .	117

---

8.3.3 Higgs decays . . . . .	121
8.4 Phenomenological analysis . . . . .	123
8.4.1 Event generation . . . . .	125
8.4.2 Analysis strategy . . . . .	125
8.4.3 Statistical analysis . . . . .	128
8.4.4 Results for the $b\bar{b}\gamma\gamma$ final state . . . . .	128
8.4.5 Charm-tagging and second generation bounds . . . . .	131
8.5 Conclusion . . . . .	133
<b>9 Optimised search for Higgs pair via Interpretable machine learning</b>	<b>135</b>
9.1 Introduction . . . . .	135
9.1.1 Considerations of experimental constraints . . . . .	136
9.2 Events simulation for HL-LHC and FCC-hh . . . . .	138
9.3 Exploring higher dimensional kinematic distributions . . . . .	140
9.3.1 Interpretable machine learning . . . . .	141
9.4 The $hh$ channel at future hadron colliders . . . . .	142
9.4.1 Constraints on $C_\phi$ at the HL-LHC and FCC-hh . . . . .	144
9.4.2 Two and three parameter constraints on $C_\phi$ , $C_{u\phi}$ and $C_{d\phi}$ . . . . .	146
9.4.3 Interpretation of Shapley values . . . . .	150
9.5 Summary . . . . .	154
9.6 Discussion of theoretical and systematic uncertainties . . . . .	156
9.7 Light-quark Yukawa and Self Coupling at Future Lepton Colliders . . . . .	157
<b>IV Flavour physics</b>	<b>159</b>
<b>10 Higgs and flavour</b>	<b>161</b>
10.1 Effective Field Theory for Higgs pair production . . . . .	161
10.2 Models of flavour alignment and large light-quark Yukawa couplings . . . . .	164
10.2.1 Model realizations . . . . .	164
<b>11 Flavour anomalies and Electroweak precision tests</b>	<b>169</b>
11.1 Introduction . . . . .	169
11.2 Theoretical preamble . . . . .	171
11.3 Analysis strategy . . . . .	175
11.4 Results from the SMEFT . . . . .	177
11.4.1 Analysis of EW and $b \rightarrow s\ell\ell$ data . . . . .	177
11.4.2 A minimal EFT picture . . . . .	183
11.5 Directions for UV models . . . . .	184
11.5.1 $Z'$ with vector-like partners . . . . .	184
11.5.2 Leptoquark scenarios . . . . .	188
11.6 Summary . . . . .	190
11.7 Discussions on EW fits . . . . .	191



# List of publications

1. **L. Alasfar**, J. de Blas and R. Gröber  
*“Higgs probes of top quark contact interactions and their interplay with the Higgs self-coupling,”*  
arXiv:2202.02333 [hep-ph].
2. **L. Alasfar**, G. Degrassi, P. P. Giardino, R. Gröber and M. Vitti  
*Virtual corrections to  $gg \rightarrow ZH$  via a transverse momentum expansion*  
JHEP **05** (2021), 168  
arXiv:2103.06225 [hep-ph].
3. **L. Alasfar**, A. Azatov, J. de Blas, A. Paul and M. Valli  
*B anomalies under the lens of electroweak precision*  
JHEP **12** (2020), 016  
arXiv:2007.04400 [hep-ph].
4. **L. Alasfar**, R. Corral Lopez and R. Gröber  
*Probing Higgs couplings to light quarks via Higgs pair production*  
JHEP **11** (2019), 088  
arXiv:1909.05279 [hep-ph].



# Part I

## Higgs Physics



# 1 The Standard Model Higgs boson

It's very nice to be right sometimes...  
it has certainly been a long wait.

---

Peter Higgs

Write intro here

## 1.1 Spontaneous symmetry breaking

Before talking about symmetry breaking, we need to discuss the concept of symmetry in physics. Symmetry has an essential role in studying physical systems. It manifests not only as a geometric feature of physical objects but also in the dynamics of physical systems. For example, one can find symmetries in the equation of motion, Lagrangians/Hamiltonians and actions. The magnetisation of materials is a good example of the role that symmetry plays in describing physical behaviour. For instance, **paramagnetic** materials have a positive magnetic susceptibility  $\chi_B$  due to the random arrangement of their electrons' spins. The paramagnetic material spins arrangement will therefore possess rotational symmetry. The material has no *preferred direction* in space [1]. On the contrary, **ferromagnetic** materials with the electrons' spins aligned in a certain direction, will not have such symmetry as there will be a preferred direction, see Figure 1.1.

In particle physics and quantum field theory, symmetry plays an essential role in the taxonomy and dynamics of elementary particles and their bound states, i.e. hadrons, cf. [2, 3]. There are two types of symmetries considered when studying elementary particles and their quantum fields: external and internal symmetries. The first is the symmetry of the spacetime background. Typically, this is a four-dimensional Poincaré symmetry. However, in some models, higher spacetime dimensions or non-flat geometries are considered. Though there is no current evidence of higher dimensions or indications of non-flat spacetime from colliders and cosmological observations [4]. The second class of symmetries is internal symmetries stemming from the quantum nature of these particles/fields. Because their state is described by a **ray** in complex Hilbert/Fock spaces, internal symmetries are simply symmetries of rotations in these spaces that keep the action variation unchanged. Internal symmetries are usually described in terms of simple or product of simple **Lie groups**, e.g.  $SU(N)$ <sup>1</sup>, and particles/fields will be arranged

---

<sup>1</sup>Gauge theories based on finite groups have been investigated in the literature, but their phenomenological significance is yet to be further investigated [5, 6]

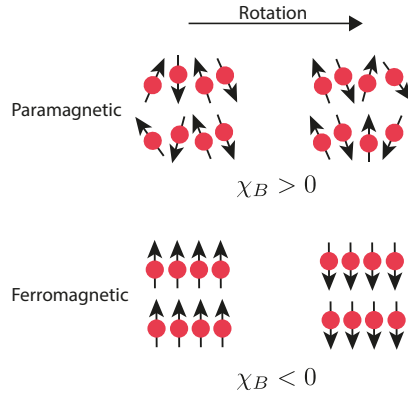


**Figure 1.1.** In paramagnetic materials, the spins are randomly distributed such that a rotation performed on the system will keep the spin distribution invariant. However, for ferromagnetic materials, where the spins are aligned in a single direction, the symmetry is broken, and the system has a preferred direction.

as multiplets in some representation of the groups. The rotations of the states could be parametrised by constants. In this case, the symmetry is called **global**, or fields of spacetime, where the symmetry is then called **local** or **gauged**.

Gauge symmetries describe rotations in the state space that depend on spacetime, the generator of the gauge transformations could propagate between two spacetime points. This is the way particle/field interactions are described in quantum field theory. The generators of these gauge transformations are called gauge bosons, and they mediate the interactions between the particles/fields and transform under the adjoint representation of the gauge group. Hence, we observe that gauge symmetries are the basis of describing the fundamental interactions of nature, which we call **gauge theories**.

An example of a gauge theory that is realised in nature is the **Standard Model** (SM). Which is a gauge theory based on the group  $G_{\text{SM}} := SU(3)_C \otimes SU(2)_L \otimes U(1)_Y$ . The first simple group is for the *strong* interaction described by quantum chromodynamics (QCD). The product of the two remaining groups  $SU(2)_L \otimes U(1)_Y$  forms the Weinberg-Salam *electroweak* (EW) model [7–9], where  $SU(2)_L$  describes the weak interaction which only couples to *left handed* fermions and  $U(1)_Y$  is the weak hypercharge  $Y$  gauge group, defined by the formula

$$Y = 2(Q - T_3). \quad (1.1)$$

Where  $Q$  is the electric charge and  $T_3$  is the third component of the weak isospin. A description of the matter content of the SM and their multiplicities with respect to  $G_{\text{SM}}$  is shown in [Table 1.1](#)

The SM has been very successful at describing particle interactions even when challenged by numerous precision tests at LEP and SLD [11–14] and later at DØ [15] and the LHC [16, 17]. Nevertheless, it fails to describe the ground state if only the fermion and gauge sectors are considered. The reason for this shortcoming is that the  $W^\pm$  and  $Z$  bosons have a mass, this violates the EW gauge symmetry. This can be easily seen

Particle/Field	$G_{\text{SM}}$ multiplicity	mass [GeV]
<b>Quarks</b>		
$Q = \begin{pmatrix} u_L \\ d_L \end{pmatrix}, \begin{pmatrix} c_L \\ s_L \end{pmatrix}, \begin{pmatrix} t_L \\ b_L \end{pmatrix}$	$(\mathbf{3}, \mathbf{2}, 1/6)$	$m_u = 2.16 \cdot 10^{-3}, m_d = 2.67 \cdot 10^{-3}$
$U = u_R, c_R, t_R$	$(\mathbf{3}, \mathbf{1}, 2/3)$	$m_c = 0.93 \cdot 10^{-2}, m_s = 1.27$
$D = d_R, s_R, b_R$	$(\mathbf{3}, \mathbf{1}, -1/3)$	$m_t = 172.4, m_b = 4.18$
<b>Leptons</b>		
$L = \begin{pmatrix} \nu_{e,L} \\ e_L \end{pmatrix}, \begin{pmatrix} \nu_{\mu,L} \\ \mu_L \end{pmatrix}, \begin{pmatrix} \nu_{\tau,L} \\ \tau_L \end{pmatrix}$	$(\mathbf{1}, \mathbf{2}, -1/2)$	$m_e = 0.511 \cdot 10^{-3}, m_\mu = 1.05 \cdot 10^{-2}$
$E = e_R, \mu_R, \tau_R$	$(\mathbf{1}, \mathbf{1}, -1)$	$m_\tau = 1.77, m_\nu = ??$
<b>Gauge bosons</b>		
$g/G_\mu^A, A = 1 \dots 8$	$(\mathbf{8}, \mathbf{1}, 0)$	0.0
$\gamma/A_\mu$	$(\mathbf{1}, \mathbf{1}, 0)$	0.0
$W_\mu^\pm$	$(\mathbf{1}, \mathbf{3}, 0)$	80.379
$Z_\mu$	$(\mathbf{1}, \mathbf{3}, 0)$	91.1876
<b>The Higgs boson</b>		
$h$	$(\mathbf{1}, \mathbf{2}, 1/2)$	125.10

**Table 1.1.** The SM constituents, their multiplicities with respect to the SM gauge group  $G_{\text{SM}} := SU(3)_C \otimes SU(2)_L \otimes U(1)_Y$  and masses. The mass of the neutrinos  $\nu$  is zero according to the SM prediction, but observations suggest that they are massive, and only the difference between the three masses is known [10]. The values of the masses are taken from the Particle Data Group (PDG) [4], and used throughout this thesis.

by looking at the mass term of a spin 1 field  $B_\mu^A$

$$\mathcal{L} = m_B B^{A,\mu} B_\mu^A, \quad (1.2)$$

and performing an  $SU(N)$  gauge transformation

$$B_\mu^A \rightarrow B_\mu^A + \partial_\mu \Lambda^A + g \varepsilon_{BC}^A B_\mu^B \Lambda^C. \quad (1.3)$$

We see that the mass term is invariant under these transformations. Secondly, because the SM is a chiral theory, as only left-handed fermions would be doublets under  $SU(2)_L$ , the Dirac mass term

$$\mathcal{L}_D = m_D \bar{\psi}_L \psi_R + \text{h.c.}, \quad (1.4)$$

cannot be a singlet under  $SU(2)_L$ , hence also violating the EW symmetry. Despite quark and lepton masses being forbidden by the EW symmetry, we indeed observe that they do have a mass, and since they also carry charges this mass has to be a Dirac mass.

In order for the EW model to be consistent at the ground state like it is in the interaction states. A mechanism for spontaneous symmetry breaking going from an interaction state to the vacuum ought to be introduced.

### 1.1.1 Nambu-Goldstone theorem

Coming back to the example of the paramagnetic-ferromagnetic materials, when heated above a certain temperature, known as the **Curie Temperature**  $T_C$  will undergo a phase transition and become paramagnetic (losing their permanent magnet property), in the mean-field theory approximation the magnetic susceptibility is related to the temperature of the metal via the relation

$$\chi_B \sim (T - T_C)^{-\gamma}, \quad (1.5)$$

where  $\gamma$  is a critical exponent. We see that if the metal temperature  $T > T_C$  the metal is in an *disordered phase* and when  $T < T_C$  it is in the *ordered phase*, i.e.  $\chi_B$  is the **order parameter** of this system. At the Curie temperature, the system will be at the *critical point* where the susceptibility is divergent. The exponent  $\gamma$  is not used to describe the system at the critical point. There is a “pictorial” description of the metal at the critical point which is helpful in picturing the Goldstone theorem. Starting at  $T > T_C$ , the metal would be in a paramagnetic phase, where the spins are randomly arranged. As the temperature becomes lower and lower, thermal fluctuations start to lessen. One or more regions of the metal, some of the spins will start to get aligned. With continued cooling, nearing  $T_C$ , these turned spins will affect their neighbours turning them into their directions. At the critical point  $T = T_C$ , the system behaves in a peculiar manner, when one would see regions of spins in “up” and others in “down” directions. The system will resemble a fractal of these regions, becoming scale-invariant. Additionally, waves of oscillating local magnetisation will propagate. These waves, or spinless quasiparticles (called **Magnons**) are Goldstone bosons emerging from spontaneous symmetry breaking.

Which will manifest at  $T < T_C$  as the spins will be arranged in a certain single direction and the metal becomes ferromagnetic.

**Theorem 1** (Nambu-Goldstone). When a continuous symmetry has a conserved currents but broken in the ground state (vacuum) is called to be spontaneously broken. There is a scalar boson associated with each broken generator of this spontaneously broken symmetry. The modes of these bosons are fluctuations of the order parameter.

This theorem first emerged from condensed matter physics, particularly superconductors [18, 19]. However, it soon got applied to relativistic quantum field theories [20].

## 1.2 The Higgs mechanism

In order to solve the aforementioned shortcomings of the Weinberg-Salam model, Nambu-Goldstone theorem has been first proposed by P. W. Anderson [21]. However, the way that Anderson formulated his theory was unfamiliar to particle physicists and used a non-relativistic picture to illustrate how photons could gain mass in an electron plasma with a plasma frequency  $\omega_p$

$$m_\gamma^{\text{plasma}} = \frac{\hbar\omega_p}{c^2} \quad (1.6)$$

Later on, a theory that explains the mass generation of the EW gauge bosons has been published in an almost simultaneous manner by R. Braut and F. Englert [22], P. Higgs [23] and G. Guralnik, C. R. Hagen, and T. Kibble [24, 25]<sup>2</sup>. The Higgs mechanism starts by considering the spontaneous symmetry breaking (SSB) of the EW sector of the SM via the pattern

$$SU(2)_L \otimes U(1)_Y \longrightarrow U(1)_Q \quad (1.7)$$

This is achieved by the vacuum expectation value (vev) of a complex scalar field  $\phi \sim (\mathbf{1}, \mathbf{2}, +1/2)$ , with the Lagrangian

$$\mathcal{L} = D_\mu \phi^* D^\mu \phi - V, \quad V := \mu^2 \phi^* \phi + \lambda(\phi^* \phi)^2, \quad (1.8)$$

with  $V$  denoting the Higgs potential, illustrated in Figure 1.2, which gives non-vanishing vacuum for  $\mu^2 < 0$ . The field  $\phi$  is given explicitly by

$$\phi = \begin{pmatrix} \phi^1 + i\phi^2 \\ \frac{1}{\sqrt{2}}(h + v) - i\phi^3 \end{pmatrix} \quad (1.9)$$

The covariant derivative

$$D_\mu = \partial_\mu - ig_2 \frac{\sigma_a}{2} W_\mu^a - ig_1 \frac{1}{2} B_\mu, \quad (1.10)$$

---

<sup>2</sup>All of these authors have contributed to the theory of SM spontaneous symmetry breaking (SSB). By calling it the “Higgs” mechanism or boson. I, by no means, have intended to ignore the role played by the rest, rather, I wanted to stick the most widely-used terminology in the field.

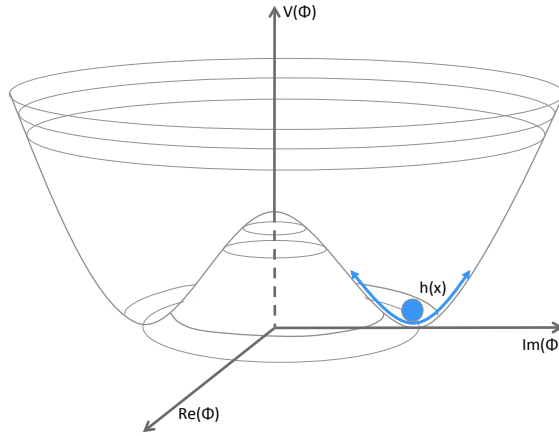


**Figure 1.2.** The characteristic shape of the Higgs potential showing a non-zero vacuum. While the physical Higgs boson is an oscillation within the energy well illustrated in the diagram with blue arrows., this illustration is taken from [26].

dictates the coupling between the Higgs field and the EW gauge bosons and  $g_3$ ,  $g_2$  and  $g_1$  are, respectively, the coupling constants of  $SU(3)_C$ ,  $SU(2)_L$  and  $U(1)_Y$ . The minimum of the scalar potential is then obtained by

$$\frac{\partial V}{\partial \phi} |_{\phi \rightarrow v} = 0, \quad (1.11)$$

which for a tachyonic mass  $\mu^2 < 0$  will have a real non-vanishing values  $v$  corresponding to the vev of this field  $\langle \phi \rangle = (\frac{0}{\sqrt{2}})$ .

According to Nambu-Goldstone theorem, the three broken generators of  $SU(2)_L \otimes U(1)_Y$  will become massive, and they are the  $W^\pm$  and  $Z$  bosons, while the photon will remain massless. We will have three massless Goldstone bosons  $G^\pm = \frac{1}{2}(\phi^1 \pm i\phi^2)$  and  $G^0 = \phi^3$  that are “eaten” by the aforementioned massive photons. Where they become the longitudinal polarisations of  $W^\pm$  and  $Z$  boson. In order to see this more concretely, we start by looking at the terms of the EW Lagrangian where the field  $\phi$  couples to the gauge bosons, in the unbroken phase

$$D_\mu \phi^* D^\mu \phi = \frac{1}{2} |\partial_\mu \phi|^2 + \frac{1}{8} g_2^2 |\phi|^2 |W_\mu^1 + iW_\mu^2|^2 + \frac{1}{8} |\phi|^2 |g_2 W_\mu^3 - g_1 B_\mu|^2 \quad (1.12)$$

After SSB, we write the gauge bosons in the mass basis

$$\begin{aligned} W_\mu^\pm &= \frac{1}{\sqrt{2}}(W_\mu^1 \pm iW_\mu^2), \\ Z_\mu &= \frac{1}{\sqrt{g_1^2 + g_2^2}} (g_2 W_\mu^3 - g_1 B_\mu), \\ A_\mu &= \frac{1}{\sqrt{g_1^2 + g_2^2}} (g_2 W_\mu^3 + g_1 B_\mu). \end{aligned} \quad (1.13)$$

From this, the electric charge is identified as the coupling constant to the photon  $A_\mu$

$$e = \frac{g_1}{\sqrt{g_1^2 + g_2^2}}. \quad (1.14)$$

It is useful to define **Weinberg angle**  $\theta_W$ , an important EW parameter relating the electric charge to the weak coupling  $g_2$

$$\sin \theta_W = \frac{e}{g_2} \approx 0.231214, \quad (1.15)$$

typically the sin and cos of the Weinberg angle are denoted by  $s_W$  and  $c_W$ , respectively. We use the unitary gauge, to absorb the Goldstone bosons into the  $W^\pm$  and  $Z$  longitudinal polarisations. In this gauge the Higgs doublet can be written as

$$\phi \rightarrow \begin{pmatrix} 0 \\ \frac{1}{\sqrt{2}}(h + v) \end{pmatrix}, \quad v = 246 \text{ GeV}. \quad (1.16)$$

With these substitutions, one can read off the masses of the gauge bosons their bilinear terms in (1.12)

$$m_W = \frac{v g_2}{2} \quad m_Z = \frac{v}{2} \sqrt{g_1^2 + g_2^2} \quad m_A = 0. \quad (1.17)$$

Since  $\phi$  is a complex doublet. We have seen that it has four components, and three of them correspond to the Goldstone bosons, thus one remains physical  $h$  which is what we now identify with the “Higgs boson” discovered in the Summer of 2012 [27, 28]. The couplings between the Higgs and the electroweak bosons is related to their mass via the vev

$$g_{hVV} = \frac{2m_V^2}{v}, \quad g_{hhVV} = \frac{2m_h^2}{v^2}. \quad (1.18)$$

By substituting (1.16), into the Higgs potential (1.8) one can write the mass of the physical Higgs boson in terms of the vev

$$m_h = \sqrt{2\lambda}v. \quad (1.19)$$

The physical Higgs mass is related to the  $\mu$  parameter via the relation

$$m_h^2 = -2\mu^2, \quad (1.20)$$

One can see that the mass term after SSB changes its sign, characterising the order-parameter for this system, analogous to the magnetic susceptibility for the magnetisation of materials example. One could also identify the self-couplings of  $h$ , the trilinear and quartic couplings

$$g_{hhh} = 3\lambda v = 3\frac{m_h^2}{v}, \quad g_{hhhh} = 3\lambda = 3\frac{m_h^2}{v^2}. \quad (1.21)$$

### 1.3 Yukawa interaction

It is possible to also use the Higgs vev to give fermions their masses by introducing a Yukawa-interaction terms, first introduced by S. Weinberg [9]

$$\mathcal{L}_{\text{Yuk}} = -y_e \bar{L} \phi E - y_d \bar{Q} \phi D - y_u \bar{Q} \tilde{\phi} U + \text{h.c.}, \quad (1.22)$$

with  $\tilde{\phi} = i\sigma_2\phi$  and  $y_e, y_d, y_u$  are  $3 \times 3$  matrices. These matrices are free parameters in the SM. As the Higgs boson acquires a the vev, the fermions will acquire a mass  $m_f = vy'_f$  and the Higgs boson coupling to the fermions is given by

$$g_{h\bar{f}f} = \frac{m_f}{v}, \quad (1.23)$$

and the Yukawa matrices will be fixed in the mass basis  $y'_f$  by measurements of the fermion masses.

Leptonic Yukawa matrix is diagonal, with a degeneracy between the flavour and masses basis, this manifests as lepton family number conservation (the lepton family operator commutes with the Hamiltonian.). However, for the quarks, the situation is more complicated. One can rotate these matrices to the mass basis via a bi-unitary transformation via the unitary matrices  $\mathcal{V}_Q, \mathcal{U}_Q$  for  $q = u, d$

$$y_q \longrightarrow y'_f = \mathcal{V}_q^\dagger y_q \mathcal{U}_q = \text{diag}(m_{q_1}, m_{q_2}, m_{q_3}). \quad (1.24)$$

However, there is no degeneracy here as the Hamiltonian does not commute with the quark flavour operator. This is because the transformation matrices for the up and down-type quarks are not the same. The charged EW quark currents contains flavour mixing described by the Cabibbo-Kobayashi-Maskawa (CKM) matrix [29, 30]. More details on the flavour sector of the SM is discussed in [chapter 10](#)

[Figure 1.3](#) shows all the SM couplings' strengths, with the thickness of the chord is proportional to the strength of the coupling, one can see the Higgs couplings in orange. In this figure, we cannot easily see Higgs coupling to the fermions, except for its couplings to the third generation. Strictly speaking, if we further examined the Yukawa coupling using a logarithmic scale and focused on the quark sector as [Figure 1.4](#) illustrates. We

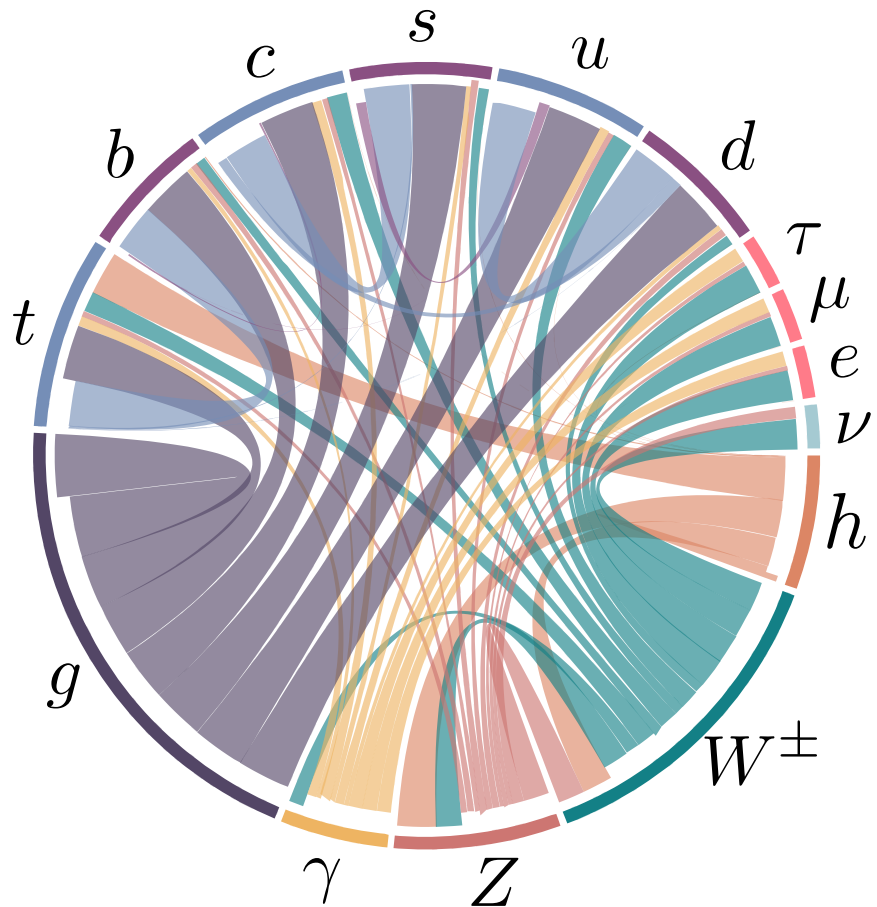


**Figure 1.3.** The SM Yukawa couplings are proportional to the quark masses, because of the the Higgs Yukawa couplings span about 6 orders of magnitude, as seen in the case of quarks here. This large hierarchy cannot be explained by the SM.

observe that these Yukawa couplings span about 6 orders of magnitudes with marked hierarchy amongst generations. As these couplings are in fact free parameters in the SM, and only determined by the experimental measurements of the quark (or equally applies lepton) masses. This hierarchy of quark masses therefore cannot be explained by the SM Higgs mechanism, and sometimes known as the old flavour puzzle.

In later chapters, we will examine the experimental effort to better measure these couplings and how Higgs pair production can be used to probe them in [chapter 8](#). Even the potential of using techniques from *interpretable machine learning* to further improve Higgs pair sensitivity to probing light Yukawas [chapter 9](#). Then in [chapter 10](#) we'll examine the EFT and UV models to modify them.

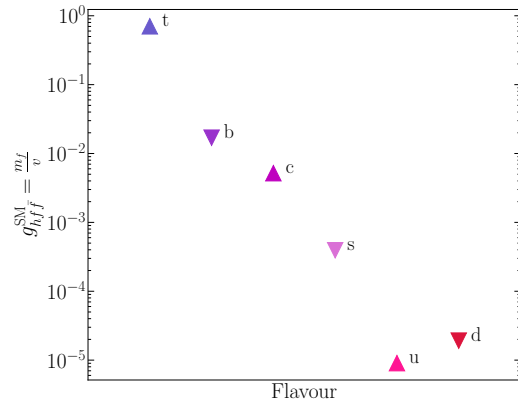


**Figure 1.4.** A chord diagram showing the SM couplings, with the coupling strength illustrated by the chord thickness. Higgs couplings are coloured in orange.

## 1.4 The Higgs and EW precision observables

Higgs physics is intertwined with the EW sector for example, the Higgs vev is determined from Fermi's constant  $v = (\sqrt{2}G_F)^{-1/2}$ , and is fixed by muon lifetime measurements, and comparing it with the theoretical predictions [31–34]

$$\tau_\mu^{-1} = \frac{G_F^2 m_\mu^5}{192\pi^3} \left(1 - \frac{8m_e^2}{m_\mu}\right) \left[1 - 1.810 \frac{\alpha}{\pi} + (6.701 \pm 0.002) \left(\frac{\alpha}{\pi}\right)^2\right], \quad (1.25)$$

which leads to the numerical value of  $G_F$  [4]

$$G_F = 1.1663787(6) \cdot 10^{-5} \text{ GeV}^{-2}, \quad (1.26)$$

given the value of the fine structure constant  $\alpha^{-1} = 137.03599976(50)$ .

Another important EW precision observable (EWPO) is the ratio between the  $W$  and

$Z$  masses

$$\rho = \frac{m_W^2}{c_W^2 m_Z^2}. \quad (1.27)$$

At leading order, this parameter is equal to unity in the SM. The  $\rho$  parameter depends on the representation of the scalar sector of the EW model having  $\phi_i$  scalars with  $T_i$  weak isospin and  $T_{3,i}$  being its third component, and a vev  $v_i$ , via the relation [35, 36]

$$\rho = \frac{\sum_i [T_i(T_i + 1) - T_{3,i}^2] v_i^2}{2 \sum_i T_{3,i}^2 v_i^2}. \quad (1.28)$$

From (1.28) one can see that a real triplet scalar, for instance, would not fit the experimental EW measurement of  $\rho$ . Hence, a complex doublet is the simplest scalar possible for the EW symmetry breaking, and the Higgs boson was expected to be seen almost four decades before its discovery. However, radiative corrections to the EW gauge bosons mass from vacuum polarisation diagrams could potentially cause  $\rho$  to deviate significantly from unity. This is not the case, as the experimentally measured value of  $\rho$  [4]

$$\rho_{\text{exp}} = 1.00038 \pm 0.00020 \quad (1.29)$$

Additionally, it is possible to think of an extended Higgs sector, where there are multiple scalars with different  $SU(2)_L$  multiplicities. Or, a composite Higgs sector, where the Higgs boson is a pseudo Nambu-Goldstone boson, cf. [37, 38]. How can such models be built assuring the  $\rho$  parameter is protected from change? The answer to this question lies in a symmetry of the Higgs Lagrangian known as custodial symmetry.

### 1.4.1 Custodial symmetry

After SSB, a residual global symmetry known as the custodial symmetry protects the  $\rho$  parameter from obtaining large radiative corrections at higher orders in perturbation theory. This symmetry must be kept in extended or composite Higgs models. This symmetry can be seen by rewriting the Higgs potential as

$$V = \frac{\lambda}{4} (\phi_1^2 + \phi_2^2 + \phi_3^2 + \phi_4^2 - 2\mu^2)^2. \quad (1.30)$$

This potential is invariant under  $SO(4) \simeq SU(2)_L \otimes SU(2)_R$  rotations. However, when the Higgs field squires a non-vanishing vev,  $\phi_4 \rightarrow h + v$ , the potential becomes

$$V = \frac{\lambda}{4} (\phi_1^2 + \phi_2^2 + \phi_3^2 + h^2 + 2vh + v^2 - 2\mu^2)^2, \quad (1.31)$$

which is only invariant under  $SO(3) \simeq SU(2)_V$  transformations, the diagonal part of the original group. This global SSB pattern comes alongside the EW SSB of the gauge group  $SU(2)_L \otimes U(1)_Y$  as global  $SU(2)_L$  is itself the gauged  $SU(2)_L$  group. Additionally the  $T^3$  component of the  $SU(2)_R$  global group is the gauged  $U(1)_Y$  and the  $T^3$  component of the custodial group  $SU(2)_V$  is gauged as well and identified to be the electric charge

operator, i.e. the generator of  $U(1)_Q$ .

$$\underbrace{SU(2)_R}_{\supset U(1)_Y} \otimes \overbrace{SU(2)_L}^{\text{gauged}} \longrightarrow \underbrace{SU(2)_V}_{\supset U(1)_Q}. \quad (1.32)$$

This pattern indicates that the symmetry is already broken by the gauging of the diagonal part of  $SU(2)_R$  (the hypercharge). The custodial symmetry is only *approximate* in the limit of  $g_1 \rightarrow 0$ , and  $\rho = 1$  is a consequence of  $g_1 \neq 0$ . The symmetry breaking pattern  $\mathbf{2} \otimes \mathbf{2} = \mathbf{3} \oplus \mathbf{1}$  also allows us to identify the Goldstone bosons as the custodial triplet and the physical Higgs  $h$  as the custodial singlet, explaining the electric charge pattern they have.

We could use the isomorphism between the special orthogonal and special unitary groups to parametrise the Higgs doublet as an  $SU(2)_L \otimes SU(2)_R$  bidoublet

$$\mathcal{H} = (\tilde{\phi} \ \phi) = \frac{1}{\sqrt{2}} \begin{pmatrix} \phi_4 - i\phi_3 & \phi_1 + i\phi_2 \\ \phi_1 - i\phi_2 & \phi_4 + i\phi_3 \end{pmatrix}, \quad (1.33)$$

with the bi-unitary transformations

$$\mathcal{H} \longrightarrow \mathcal{U}_L \mathcal{H} \mathcal{U}_R^\dagger \quad (1.34)$$

which leaves any traces of the form  $\text{Tr}(\mathcal{H}^\dagger \mathcal{H})$ , invariant. The Higgs potential could be rewritten in terms of the bidoublet

$$V = -\frac{\mu^2}{2} \text{Tr}(\mathcal{H}^\dagger \mathcal{H} + \frac{\lambda}{4} (\text{Tr}(\mathcal{H}^\dagger \mathcal{H}))^2) \quad (1.35)$$

The vev is hence written in this representation as

$$\langle \mathcal{H} \rangle = \frac{v}{\sqrt{2}} \mathbb{1}_{2 \times 2}. \quad (1.36)$$

We can also look at the Yukawa sector, and observe that in the case where  $y_u = y_d = y$ , we can also write the left-handed and right-handed quarks as  $SU(2)_L \otimes SU(2)_R$  bidoublets and  $SU(2)_R$  doublets, respectively. Hence, the quark part of the Yukawa Lagrangian in (1.22) becomes

$$\mathcal{L}_{yuk} \supset \frac{y}{\sqrt{2}} (\bar{u}_L \ \bar{d}_L) \begin{pmatrix} \phi_4 - i\phi_3 & \phi_1 + i\phi_2 \\ \phi_1 - i\phi_2 & \phi_4 + i\phi_3 \end{pmatrix} \begin{pmatrix} u_R \\ d_R \end{pmatrix}, \quad (1.37)$$

which is invariant under custodial transformations, but when  $y_u \neq y_d$ , this Lagrangian term breaks custodial symmetry. Thus, the differences between the up-type and down-type quark masses  $m_u - m_d$  are considered **spurions** of the custodial symmetry and one expects to see radiative corrections to  $\rho$  being proportional to these spurions.

In order to see this more concretely, we start by examining the radiative corrections

that could contribute to the deviation of  $\rho$  from unity, i.e.  $\Delta\rho$  these corrections are known as the **oblique correction**. These oblique corrections come from electroweak vacuum polarisations  $\Pi_{VV}(p^2)$ , as shown in Figure 1.5, for more details on these corrections and their calculation see Refs.. [39, 40]

The 1-loop correction to the  $\rho$  parameter is given in terms of the  $\Pi_{VV}$  by

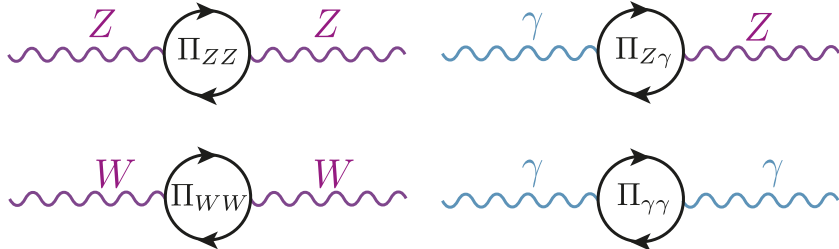


**Figure 1.5.** The oblique corrections, are radiative correction with electroweak gauge bosons propagators. Namely vacuum polarisations of the  $Z$ ,  $W^\pm$  and  $\gamma$  bosons.

$$\Delta\rho = \frac{\Pi_{WW}(0)}{m_W^2} - \frac{\Pi_{ZZ}(0)}{m_Z^2} \quad (1.38)$$

Where the dominant contributions are given by [41]

$$\Delta\rho = \frac{3G_F}{8\sqrt{2}\pi^2} \left( (m_t^2 + m_b^2) - \frac{2m_t^2 m_b^2}{m_t^2 - m_b^2} \ln \frac{m_t^2}{m_b^2} \right) + \dots \quad (1.39)$$

Since  $m_b \ll m_t$ , the correction is non-vanishing, and (1.39) shows clearly how the radiative corrections are proportional to the spurions of the custodial symmetry. However, this radiative correction is absorbed into the SM definition of  $\rho$ , i.e. the  $\overline{\text{MS}}$  definition of the  $\rho$ -parameter  $\rho^{\overline{\text{MS}}}$ .

One can study new physics (NP) effects that violates custodial symmetry, by looking at deviations from  $\rho = 1$  from it. Given the experimentally measured value of  $\rho$  (1.29) many NP models violating custodial symmetry can already be excluded. Nevertheless,  $\rho$  alone does not capture the full story of EWPO's. For instance, adding a new quark doublet would not necessarily violate the custodial symmetry though it still can be excluded by EWPO. It is hence useful to introduce new parameters known as **the oblique parameters** [40, 42–45] <sup>3</sup>

<sup>3</sup>The are also called the Peskin–Takeuchi parameters, however, W. Marciano and J. Rosner also D. Kennedy and P. Langacker published the same parametrisation proposals almost simultaneously. Therefore, I preferred not to use this eponym, instead calling them the oblique parameters, as they stem from the oblique corrections .

## The oblique parameters

$$\begin{aligned}
 S &:= \frac{4c_W^2 s_W^2}{\alpha} \left[ \frac{\Pi_{ZZ}^{\text{NP}}(m_Z^2) - \Pi_{ZZ}^{\text{NP}}(0)}{m_Z^2} - \frac{c_W^2 - s_W^2}{c_W s_W} \frac{\Pi_{Z\gamma}^{\text{NP}}(m_Z^2)}{m_Z^2} - \frac{\Pi_{\gamma\gamma}^{\text{NP}}(m_Z^2)}{m_Z^2} \right], \\
 T &:= \frac{\rho^{\overline{\text{MS}}} - 1}{\alpha} = \frac{1}{\alpha} \left[ \frac{\Pi_{WW}^{\text{NP}}(0)}{m_W^2} - \frac{\Pi_{ZZ}^{\text{NP}}(0)}{m_Z^2} \right], \\
 U &:= \frac{4s_W^2}{\alpha} \left[ \frac{\Pi_{WW}^{\text{NP}}(m_W^2) - \Pi_{WW}^{\text{NP}}(0)}{m_W^2} - \frac{c_W}{s_W} \frac{\Pi_{Z\gamma}^{\text{NP}}(m_Z^2)}{m_Z^2} - \frac{\Pi_{\gamma\gamma}^{\text{NP}}(m_Z^2)}{m_Z^2} \right] - S.
 \end{aligned} \tag{1.40}$$

The NP contributions to the EW vacuum polarisations  $\Pi_{VV}^{\text{NP}}(p^2)$  could either come from loop or tree-level effects. Typically both  $T$  and  $U$  are related to custodial symmetry violation. However,  $U$  has an extra suppression factor of  $m_{\text{NP}}^2/m_Z^2$  compared to  $T$  and  $S$ . The most recent fit result for these parameters is [4]

$$\begin{aligned}
 S &= -0.01 \pm 0.10, \\
 T &= 0.03 \pm 0.13, \\
 U &:= 0.02 \pm 0.11.
 \end{aligned} \tag{1.41}$$

But since  $T$  and  $S$  tend to give stronger constraint on NP, due to the suppression factor of  $U$ . One can perform a two-parameter fit of  $S$  and  $T$  setting  $U = 0$ , thus shown in Figure 1.6, with the numerical values [4],

$$\begin{aligned}
 S &= 0.00 \pm 0.07, \\
 T &= 0.05 \pm 0.06.
 \end{aligned} \tag{1.42}$$

The Peskin-Takeuchi parameters are important in constraining effective operators in the Higgs sector , namely

$$\begin{aligned}
 \hat{O}_S &= \phi^\dagger \sigma_i \phi W_{\mu\nu}^i B^{\mu\nu}, \\
 \hat{O}_T &= |\phi^\dagger D_\mu \phi|^2.
 \end{aligned} \tag{1.43}$$

For example,  $\hat{O}_S$  appears in Technicolour models causing large deviations of  $S$  compared to its measured value [43, 46–48]. Moreover, The constraints on  $T$  parameter is important for top mass generation ans well as modifications to  $Zb\bar{b}$  coupling in such models [49, 50]. We will revisit the  $\hat{O}_T$  when we discuss the Higgs and effective field theories in chapter 3

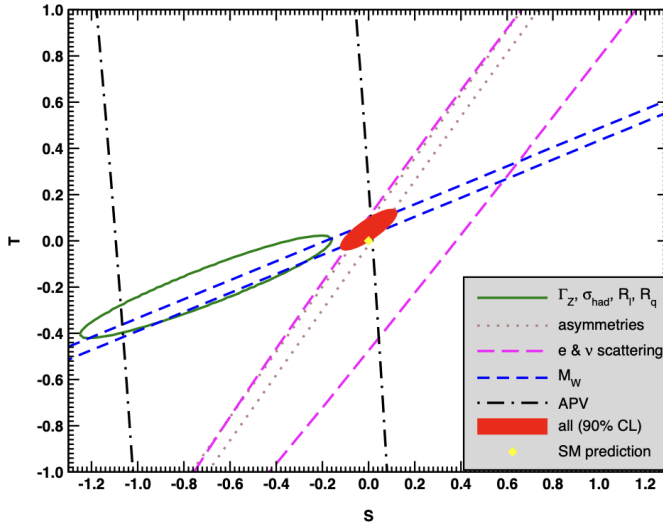


**Figure 1.6.** Fit results from various EWPO's for  $T$  and  $S$  setting  $U = .$  The contours show  $1\sigma$  contours (39.35% for closed contours and 68% for the rest). This plot is obtained from the PDG [4]

## 1.5 Theoretical constraints on the Higgs

### 1.5.1 Electroweak precision data fits

Even prior to the discovery of the Higgs boson at LHC in 2012, many theoretical aspects of the Higgs sector provided marked bounds on the Higgs properties, particularly its mass. For instance, using the EWPO measurements at LEP provided an input for a fit based of radiative effects coming from the Higgs boson to such observables [11] as in diagram (a) of Figure 1.8, the bounds improved with the improvements of EWPO measurements, these bounds were known as the “blue band” plots seen with their progression in Figure 1.7.

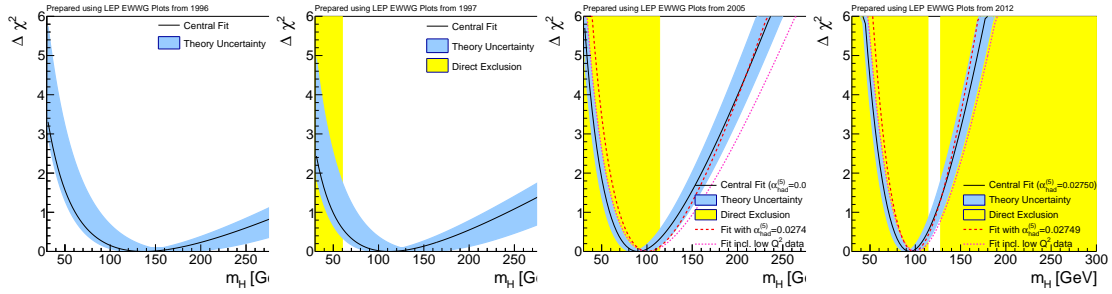


**Figure 1.7.** Progression of the “blue band” plots with LEP data from 1996 up to 2021 prior to the announcement of the Higgs boson discovery. These plots were taken from [26], based on data from LEP [11]

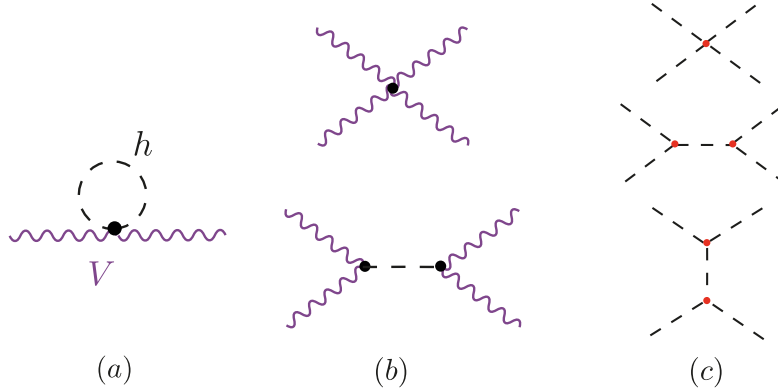


**Figure 1.8.** Diagrams contributing to theoretical bounds on the Higgs, (a) shows an example of radiative corrections to EWPO from the Higgs bosons. The diagrams in (b) show an elastic scattering of EW vector bosons leading to a bound on the Higgs mass from perturbative unitarity, similarly in (c) diagrams for  $hh \rightarrow hh$  scattering leading to constraints on Higgs self-coupling.

### 1.5.2 Partial-wave unitarity

Another bound on Higgs mass emerged from studying the amplitudes of EW vector bosons elastic scattering having longitudinal polarisations  $V_L V_L \rightarrow V_L V_L$  at high energies  $E \gg m_W$  (see diagrams (b) in Figure 1.8 ), where the Goldstone equivalence theorem holds [51]. This bound comes from applying the partial wave perturbative unitarity on the EW boson scattering amplitude. I will derive here this bound starting from the **Optical theorem**, which a direct result from the unitarity of the **S** matrix.

#### The optical theorem

Let  $\mathcal{M}_{aa}$  be a covariant matrix element for an elastic scattering process with for a particle  $a$  then the following relation applies

$$\sum_f \int d\Phi_n(p_a, p_i^f) |\mathcal{M}_{af}|^2 = 2\Im(\mathcal{M}_{aa}), \quad (1.44)$$

where the sum is over all intermediate states  $n$ -particle states  $f$  with momenta  $p_i^f$  and  $d\Phi_n(p_a, p_i^f)$  is the  $n$ -particle phase space.

If we only consider a  $2 \rightarrow 2$  process with momentum states.  $|p_1, p_2\rangle \rightarrow |k_1, k_2\rangle$ , then (1.44), after expanding the 2-particle phase space , simplifies to

$$\begin{aligned} & \int \frac{d^3 k_1}{(2\pi)^3 2E_1} \int \frac{d^3 k_2}{(2\pi)^3 2E_2} (2\pi)^4 \delta^4(p_1 + p_2 - k_1 - k_2) |\mathcal{M}(s, t)|^2, \\ &= \frac{1}{16\pi} \int_{-1}^1 d(\cos \theta) |\mathcal{M}(s, t)|^2, \end{aligned} \quad (1.45)$$

with the Mandelstam variables

$$\begin{aligned} s &= k_1 + k_2, \\ t &= k_1 - p_1, \\ u &= k_1 - p_2, \\ s + t + u &= 4m \end{aligned} \tag{1.46}$$

Recall that the relation between the Mandelstam variable  $t$ , and the scattering angle for the elastic scattering is given by

$$t = \frac{1}{2}(s - 4m^2)(\cos \theta - 1) \tag{1.47}$$

We could expand the matrix element  $\mathcal{M}(s, t)$  in terms of *partial waves*, isolating  $s$  from scattering angle dependence

$$\mathcal{M}(s, t) = 16\pi \sum_j (2j + 1) a_j P_j(\cos \theta). \tag{1.48}$$

Where  $a_j$  are called the  $j$ th partial wave amplitude, and  $P_j(\cos \theta)$  are the Legendre polynomials

$$P_j(z) = \frac{1}{j!} \frac{1}{2^j} \frac{d^j}{dz^j} (z^2 - 1)^j \tag{1.49}$$

Which satisfies the orthonormality condition

$$\int_{-1}^1 dz P_j(z) P_k(z) = \frac{1}{2j + 1} \delta_{jk} \tag{1.50a}$$

$$P_j(1) = 1 \quad \forall j. \tag{1.50b}$$

We hence get for the LHS of (1.44) scattering

$$\begin{aligned} &\int \frac{d^3 k_1}{(2\pi)^3 2E_1} \int \frac{d^3 k_2}{(2\pi)^3 2E_2} (2\pi)^4 \delta^4(p_1 + p_2 - k_1 - k_2) |\mathcal{M}(s, t)|^2, \\ &= \frac{1}{16\pi} \int_{-1}^1 d(\cos \theta) \left[ 16\pi \sum_j (2j + 1) a_j(s) P_j(\cos \theta) \right] \times \\ &\quad \left[ 16\pi \sum_k (2k + 1) a_k^*(s) P_k(\cos \theta) \right], \\ &\Rightarrow = 32\pi \sum_j (2j + 1) |a_j(s)|^2. \end{aligned} \tag{1.51}$$

And the RHS of (1.44)

$$2\Im(\mathcal{M}_{aa}) = \underbrace{2\Im(\mathcal{M}(s, 0))}_{t \text{ is integrated out.}} = 32\pi \sum_j (2j+1)\Im(a_j(s)). \quad (1.52)$$

Otherwise large cancellations needed,  $a_j(s)$ 's are hierachal. Thus, we could compare the partial wave amplitudes term-by-term

$$|a_j(s)|^2 \leq \Im(a_j(s)) \Rightarrow \Re(a_j(s))^2 + \Im(a_j(s))^2 \leq \Im(a_j(s)) \quad (1.53)$$

Rearranging terms, we get

$$\Re(a_j(s)) + \left( \Im(a_j(s)) - \frac{1}{2} \right)^2 \leq \frac{1}{4} \quad (1.54)$$

The partial wave amplitude has to lie within the unitarity circle. We use though perturbation theory if the partial wave amplitude respects the inequality

$$\Re(a_j(s)) \leq \frac{1}{2} \quad (1.55)$$

This is known as the perturbative partial wave unitarity bound.

When (1.55) is applied for  $V_L V_L \rightarrow V_L V_L$ , in the Goldstone boson equivalence theorem regime in particular for  $V = W$  boson, we get for the  $S$ -wave partial amplitude

$$a_0 \sim \frac{m_h^2}{16\pi v^2} \left( 2 + \mathcal{O}\left(m_h^2/s\right) \right). \quad (1.56)$$

Looking at the asymptotic behaviour as  $s \rightarrow \infty$ , we obtain the bound

$$\frac{m_h^2}{8\pi v^2} < \frac{1}{2} \Leftrightarrow m_h \leq 870 \text{ GeV}. \quad (1.57)$$

Indeed this bound is obsolete now after th Higgs mass measurement, however it is very important to demonstrate the power of this technique in constraining Higgs parameters. As this method can be applied to any elastic scattering with the Higgs acts as a mediator like  $ZZ \rightarrow ZZ$ ,  $WW \rightarrow ff$  and constrain the corresponding couplings  $g_{ZZh}$ ,  $g_{ffh}$  and so on. An important bound can be derived by examining the Higgs elastic scattering  $hh \rightarrow hh$  shown in (c) of Figure 1.8 in order to set bounds on Higgs self-interactions  $g_{hhh}$  and  $g_{hhhh}$ . This is what exactly has been done in ref. [52] where they have found that the  $S$ -wave partial amplitude for this process is given by

$$a_0 = -\frac{1}{2} \frac{\sqrt{s(s-4m_h^2)}}{16\pi s} \left[ g_{hhh}^2 \left( \frac{1}{s-m_h^2} - 2 \frac{\log \frac{s-3m_h^2}{m_h^2}}{s-4m_h^2} \right) + g_{hhhh} \right], \quad (1.58)$$

which leads to unitarity bounds on the trilinear  $g_{hhh}$  and the quartic  $g_{hhhh}$  couplings

$$\left| g_{hhh}/g_{hhh}^{\text{SM}} \right| \lesssim 6.5 \quad \text{and} \quad \left| g_{hhhh}/g_{hhhh}^{\text{SM}} \right| \lesssim 65. \quad (1.59)$$

A stronger constrained can be obtained by looking at the one-loop correction to the  $hh \rightarrow hh$  scattering amplitude, within the full kinematic range. The unitarity bound here is obtained by looking at the one-loop amplitude at the threshold, and is given by

$$\left| g_{hhhh}/g_{hhhh}^{\text{SM}} \right| \lesssim 6. \quad (1.60)$$

It should be noted that the unitarity bounds on  $\kappa_\lambda$  depends on the ansatz use estimating the size the New Physics contributions to the scattering amplitudes. These bounds are, hitherto, the strongest on these two couplings even when compared to the ones coming from current experimental searches.

### 1.5.3 Other bounds

Further theoretical bounds could be obtained by studying quantum effects on the Higgs potential. For example, if we looked at the solution of the renormalisation group equation (RGE) for the Higgs self-coupling  $\lambda$  with the boundary condition  $\lambda(v) = \lambda_0$  and ignoring other SM particle-contributions

$$\lambda(Q^2) = \frac{\lambda_0}{1 - \frac{3}{4\pi^2} \log \frac{Q^2}{v^2}} \quad (1.61)$$

We see that the running of  $\lambda$  will hit a pole, known as **Landau pole** when the denominator vanishes. This will happen at the scale

$$Q_c = v e^{4\pi^2/3\lambda_0} = v e^{4\pi^2 v^2 / 3m_h^2} \quad (1.62)$$

This indicates that the theory will break down at scales larger or equal to  $Q_c$ . Since the “critical scale” is a function of the Higgs mass, this allows us to set an upper limit on the Higgs mass assuming the SM will be valid up to a certain scale  $Q_c$ . This bound is known as **quantum triviality** bound [53]. This is because the low energy behaviour of (1.61) leads to a vanishing interaction, and if we want the Higgs Lagrangian to be perturbative for all scales, then  $\lambda$  has to be vanishing and the theory becomes non-interacting or *trivial*.

Another bound coming from the RGE of  $\lambda$  is the **stability bound**, which considers the stability of the Higgs potential given the running of  $\lambda$  by requiring that the Higgs potential is an operator bounded from below. This bound is obtained by approximating the solution of the RGE at small  $\lambda$

$$\lambda(Q^2) \sim \lambda_0 + \frac{1}{16\pi^2} \left[ -\frac{12m_t^4}{v^4} + \frac{3}{16} (2g_2^4 + (g_2^2 + g_1^2)^2) \right] \log \frac{Q^2}{v^2} \quad (1.63)$$

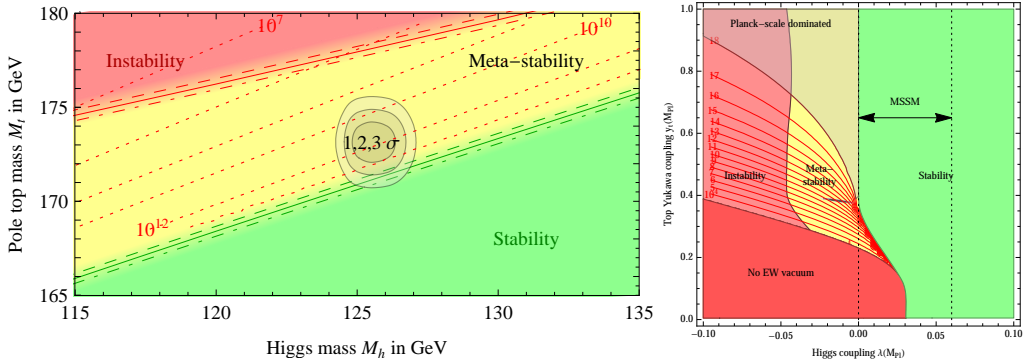


**Figure 1.9.** Phase diagrams of the Higgs vacuum in the  $m_t - m_h$  (left) and  $m_t - \lambda(M_{pl})$  (right) planes showing areas of instability, meta stability and absolute stability. In the  $m_t - \lambda(M_{pl})$  diagram, the allowed range of the Higgs self-coupling  $\lambda$  in the Minimal Supersymmetric SM (MSSM), this plot is taken from [57]

For the Higgs potential to be bounded from below  $\lambda(Q^2)$  ought to be  $\lambda(Q^2) > 0$ . With this relation for  $\lambda_0$  in terms of the mass, we get a bound on  $m_h$

$$m_h^2 > \frac{v^2}{8\pi^2} \left[ -\frac{12m_t^4}{v^4} + \frac{3}{16} (2g_2^4 + (g_2^2 + g_1^2)^2) \right] \log \frac{Q^2}{v^2} \quad (1.64)$$

Which leads to  $m_h \approx 130$  GeV if we assume that the SM is valid up to the Grand Unified Theory (GUT) scale of  $\sim 10^{16}$  GeV and  $m_h \approx 180$  GeV for  $Q$  being at the Planck scale  $\sim 10^{19}$  GeV.

More sophisticated calculations and discussion for the Higgs potential and vacuum stability has been a subject of great interest in pre and post-Higgs discovery eras cf. [53–56] and the most state-of-the-art calculation for the vacuum stability at NNLO has been performed in ref. [57] where they also included finite temperature effects to construct a phase diagram in the  $m_t - m_h$  and  $m_t - \lambda(M_{pl})$  planes as shown in Figure 1.9. Indicating that the measured Higgs mass is likely compatible with a metastable vacuum rather than absolute stability. This indicates that there is a finite probability for the Higgs vacuum (false vacuum) to decay into a lower energy state (true vacuum) via quantum tunnelling.

## 2 Experimental measurements of the Higgs boson

The observation of the Higgs boson, then the extensive measurement of its properties and couplings has been on the top of the LHC programme priorities [58]. In the time this thesis was in the writing, the particle physics community will be celebrating a decade since the Higgs boson's discovery. Looking back 10 years ago, when I have witnessed the discovery of the Higgs boson via news press-conference in summer of 2012, and decided to be a part of this enormous step that humanity has taken, I feel astonished by the progress made in understanding this newly discovered particle!

In this chapter, I will start by an overview of the extraordinary LHC and its experiments in section 2.1. Then, I will review the state-of-the-art status of experimental measurements of the Higgs properties in section 2.2, cross-sections and couplings in section 2.3, and at the end I will discuss the challenges and outlook for the future runs of the LHC section 2.4, of which the rest of this thesis is going to be aimed to address a small part of them.

### 2.1 Overview of the Large Hadron Collider

The Large Hadron Collider (LHC) is the largest particle accelerator in the CERN accelerators complex, with a circumference of about 26 km, with over 9590 superconducting magnets cooled to 1.9 K. It was built as an upgrade to the Large electron positron collider (LEP) which ended its operation in the year 2000. The LHC contains four main experiments situated at the four beam collision points and detectors, and these experiments are: ATLAS, CMS, LHCb and ALICE, there also smaller experiments such as LHCf, MilliQan, TOTEM and others. For more details about the LHC cf. [59, 60] or see the LHC technical design report [61] for more technical details.

The LHC started operation in September of 2008, with low energy proton beams, then gradually increased to an energy of 3.5 TeV per proton to reach a centre of mass energy  $\sqrt{s}$  of 7 TeV, and data-taking period started from 2011. By 2012, its energy has increased to  $\sqrt{s} = 8$  TeV and operated at this energy for about a year and half, then stopping in mid 2013 concluding what is known as **Run-I**. In 2015, the **Run-II** started with almost double the energy  $\sqrt{s} = 13$  TeV, and lasted for ca. 3 years. As this thesis being written, preparations are being made to get **Run-III** started until 2024. During these runs, heavier nuclei such as  $^{207}\text{Pb}$  and  $^{131}\text{Xe}$  have been collided either with protons or with themselves [62].

From, 2025 and beyond, the **High-Luminosity LHC** (HL-LHC) era will commence,

see Figure 2.2. Where the LHC will be shutdown for extensive upgrades [63] to potentially increase its energy to  $\sqrt{s} = 14$  TeV and higher collision rates hence the term *high luminosity*. Which leads us to an important notion in particle physics phenomenology *integrated luminosity*.

The performance of colliders depends on many factors, but for phenomenological studies, like this thesis, one mainly considers the centre of mass energy  $\sqrt{s}$  and the integrated luminosity  $\mathcal{L}$ . This is mainly due to the fact that particle colliders experiments are basically “counting experiments”, and all of the bounds on physical observables or model parameters are obtained from the number of signal versus background events, and the number of expected events  $N_{explic}$  for a given resonance  $R$  and a subsequent decay final state  $X$  at any collider experiments is given by

$$N_{explic} = \sigma(pp \rightarrow R) \mathcal{B}(R \rightarrow X) \mathcal{L} \epsilon_{SEL}. \quad (2.1)$$

Here  $\epsilon_{SEL}$  is the selection efficiency, which depends on many factors like the detector geometry and particle identification performance etc., as well as the signal one searches for, it can be improved by better detected or selection cuts. The production cross-section increases typically with quadratically with  $\sqrt{s}$ , hence comes the need for higher energies but this can only achieved by building new colliders from scratch. The integrated luminosity can be increased much more easily, by longer running time of the same collider as it is the time integral of the collider’s luminosity  $L(t)$  over its operation time  $T$

$$\mathcal{L} = \int^T L(t). \quad (2.2)$$

Therefore, we see that the integrated luminosity for the LHC experiments will increase over time, when more collisions taking place, as seen in figure Figure 2.1 showing the integrated luminosity for ATLAS and CMS experiments. As the protons travel in the LHC in **bunches**, and as these bunches cross, protons collide at a certain frequency  $f$ , when two bunches with  $N_1$  and  $N_2$  protons per bunch, respectively. Each bunch will have an effective cross-section  $4\pi\sigma_i$  corresponding to their physical sizes  $\sigma \sim 16 \mu\text{m}$ , the luminosity is therefore given -approximately- by

$$L = \frac{f N_1 N_2}{4\pi\sigma_1\sigma_2}, \quad (2.3)$$

which is for the LHC averages to about  $10^{34}$  collisions  $\text{cm}^{-2} \text{s}^{-1}$  [64, 65].

The total physics-viable  $pp$ -collisions integrated luminosity for Run-I was  $4.57/\text{fb}$  for  $7\text{TeV}$  and  $20.3/\text{fb}$  for  $8\text{TeV}$  (ATLAS [66]) and  $5.55/\text{fb}$  at  $7\text{TeV}$  and  $21.8/\text{fb}$  at  $8\text{TeV}$  (CMS [67]). As for Run-II the integrated luminosity is  $139/\text{fb}$  at  $13\text{TeV}$  (ATLAS [68]) and  $137/\text{fb}$  at  $13\text{TeV}$  (CMS [67]). The expected integrated luminosity by the end of Run-III is  $300/\text{fb}$  [69] and  $3000/\text{fb}$  by the end of the HL-LHC at energy of  $14\text{TeV}$  [63].

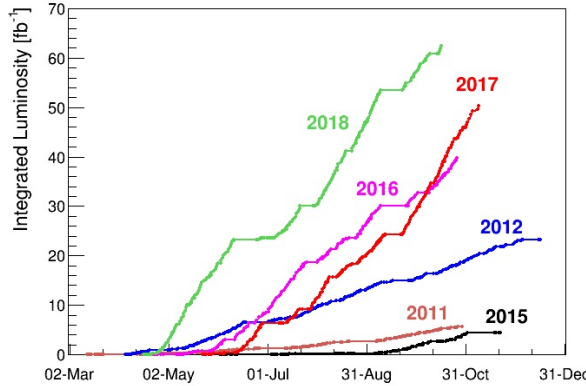


**Figure 2.1.** The integrated luminosity of the CMS and ATLAS experiments combined over the period from 2011-2018, source [64].



**Figure 2.2.** A timeline of the LHC operation showing Run-I, Run-II and future planned runs of the LHC, including the HL-LHC, source [62].

## 2.2 Higgs properties

### 2.2.1 Higgs boson mass measurements

In order to measure the mass of the Higgs boson with high precision, one needs to consider final states that can be reconstructed with high momentum and mass resolution, this is typically achieved when no hadronic constituents in the decays involved, such as

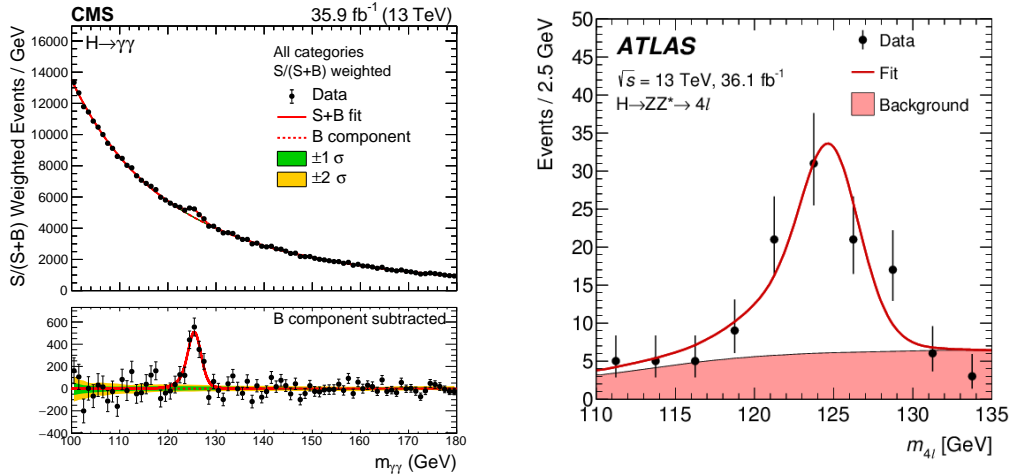


**Figure 2.3.** The invariant mass distributions of diphoton  $m_{\gamma\gamma}$  (CMS [70]) and four lepton  $m_{4\ell}$  (ATLAS [71]) final states showing a clear peak at the Higgs mass, with smooth background. These final states are ideal for Higgs mass measurements.

$h \rightarrow \gamma\gamma$  and  $h \rightarrow ZZ^* \rightarrow 4\ell$ . Reconstructing the invariant mass distributions  $m_{\gamma\gamma}$  and  $m_{4\ell}$  one observes that the Higgs peak is narrow over a relatively smooth background, see Figure 2.3, which is ideal for the measurement of the Higgs mass. It should be noted that the width of the resonance is due to the detector resolution and does not correspond to the actual Higgs width.

There have been consistent improvements of the Higgs mass measurements since its discovery. In Figure 2.4 I have performed a meta analysis on ATLAS and CMS measurements of the Higgs mass in Run-I and Run-II of the LHC for both diphoton and  $ZZ^*$  final states based on the data from the studies [70–73] using a random effects model [74]. The pooling of the studies yielded a mass measurement of  $m_h = 125.21 \pm 0.10$ , which translates to a 0.11% accuracy, the heterogeneity off the studies was found to be  $I^2 = 49\%$  ( $p = 0.05$ ). Different measurements combination techniques were used in [70] and [4] yielded different central values but all of the results agree within the uncertainties.

## 2.2.2 Higgs full width

The SM values of the Higgs boson full width is  $\Gamma_h = 4.1$  GeV and it can be accessed in the LHC by looking at the ratio of on-shell versus off-shell Higgs production and decay to the  $ZZ^{(*)}$  state, and  $ZZ^{(*)} \rightarrow 4\ell, 2\ell 2\nu$ , namely

$$\frac{\sigma(gg \rightarrow h \rightarrow ZZ^*)}{\sigma(gg \rightarrow h^* \rightarrow ZZ)} = \kappa_g^2 \kappa_Z^2 \frac{4m_Z^2}{m_h \Gamma_h}, \quad (2.4)$$

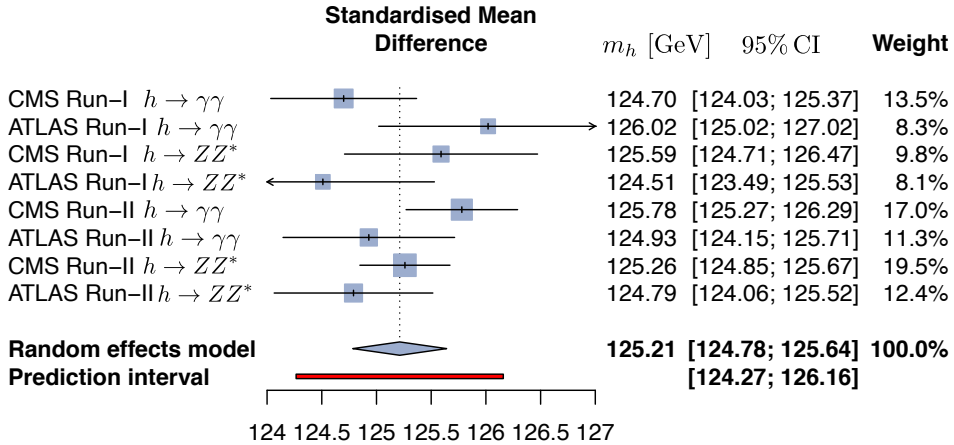


**Figure 2.4.** A meta analysis preformed to combine all the measurements of the Higgs mass from Run-I and Run-II, the combined result was obtained from pooling all of the studies using the random effects model method.

where the  $\kappa$  here denote the ratio between the measured/ or modified coupling with the Higgs and the SM prediction, i.e.

$$\kappa_X := \frac{g_{XXh}}{g_{X}^{SM}}. \quad (2.5)$$

Which is commonly used in reporting experimental constrains/ measurements of the Higgs couplings, as in the next section [section 2.3](#). We shall discuss the  $\kappa$  formalism more in [chapter 3](#).

We see from (2.4) that if one fixes the coupling between the gluons and the  $Z$  boson and the Higgs it is possible to access the full width directly. Unfortunately, it is not possible to directly measure the Higgs full width at the LHC, as this requires full reconstruction of the collision event and study the recoil mass which is only possible at lepton colliders [75, 76]. Alas, it is still possible to extract bounds on  $\Gamma_h$  using (2.4). ATLAS used this method to constrain the full width of the Higgs using Run-II data [77], while CMS has preformed the same analysis using Run-I and Run-II data combined [78], the results are

95% CL bounds of  $\Gamma_h$

$$\Gamma_h < 14.4 \text{ GeV} \quad (\text{ATLAS}) \qquad 0.08 \text{ GeV} < \Gamma_h < 9.16 \text{ GeV} \quad (\text{CMS}), \quad (2.6)$$

with the combined bound being  $\sim 3\Gamma_h^{\text{SM}}$ .

### 2.2.3 Higgs spin and parity

As we have seen in section 1.2, the Higgs boson is a scalar and  $\mathcal{CP}$  even ( $J^p = 0^+$ ) in the SM. However, the discovery of a peak in the  $m_{\gamma\gamma}$  distribution, would not automatically imply that the particle discovered is scalar, it could be a spin-2 boson, or a pseudoscalar ( $J^p = 0^-$ ). In order to study the  $J^p$  properties of the Higgs, one needs to examine the differential distributions of angular variables such as rapidity  $y$  or transverse momentum  $p_T$ . Both ATLAS and CMS collaborations studied using Run-I data the angular distributions of the Higgs decays  $h \rightarrow ZZ^*$ ,  $h \rightarrow WW^*$  and  $h \rightarrow \gamma$ , to study an anomalous  $VVh$  coupling. Then test the alternative hypothesis for  $J^p$  against the SM [79, 80]. The analysis results show that the SM  $0^+$  hypothesis is favoured at  $> 99.9\%$  CL.

## 2.3 Measurements of Higgs rates and couplings

### 2.3.1 Higgs cross-sections

The total inclusive Higgs cross-section has been measured using the final states  $h \rightarrow \gamma\gamma$  and  $h \rightarrow ZZ^* \rightarrow 4\ell$ , and their combinations. The measurements have been done at the three energies the LHC was operating at: 7 TeV, 8 TeV [81] and 13 TeV [82–84] and combined with more data and compared to the SM prediction as shown in [85]. As shown in Figure 2.5, the measured inclusive cross-section is in agreement with the SM prediction across all of the LHC operation energies.

In addition to the inclusive cross-section measurements, differential cross-sections of the Higgs have been measured for  $p_T$  and  $y$  as we have seen in subsection 2.2.3 for Higgs's  $J^p$  determination. Additionally, the differential cross-sections for other variables have been measured, and they include  $N_{\text{jets}}, p_T^{\text{jet}}, m_{jj}, \delta\phi_{jj}$  and others using the channels  $h \rightarrow ZZ^*$ ,  $h \rightarrow WW^*$  and  $h \rightarrow \gamma$ . The most recent results using the full Run-II data can be found in Refs. [83, 85–87].

In addition to the total inclusive cross-section, a collection of measurements of Higgs production and decay rates has been carried out by both ATLAS and CMS. These measurements also carried out in what is known as Standard Template Cross-Sections (STXS) framework. The STXS's are fiducial cross-sections in exclusive phase-space regions or bins separately per Higgs boson production channel. They have the advantage of standardisation of cuts and final results such that measurements could be easily combined across analyses. More details about the STXS framework can be found in the reports of LHC Higgs cross-sections working group (LHCHXSWG) cf. [88]. In Table 2.1 I summarise the state-of-art measurements of the Higgs rates separated into production and decay channels using the total LHC Run-II data from ATLAS and CMS experiments. Additionally,

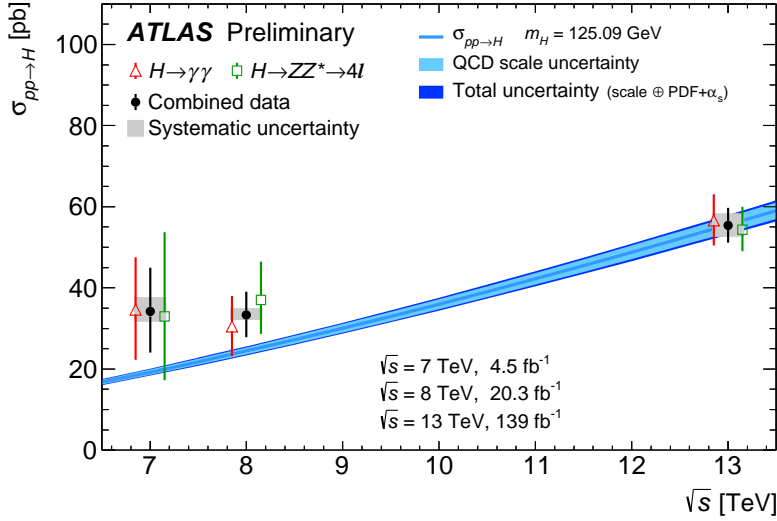


**Figure 2.5.** The total inclusive cross-section measurements by ATLAS collaboration [85] for 7, 8 and 13 TeV using  $h \rightarrow \gamma\gamma$  and  $h \rightarrow ZZ^* \rightarrow 4\ell$ . channels and their combination (black points) compared to the SM prediction with the uncertainties shown as blue line with light and dark blue bands for QCD scale uncertainties and total uncertainties, respectively.

I give the HL-LHC projections from CMS experiment as a comparison. The results in this table are written in terms of the signal strength, which is directly extracted from measuring the number of events dividing them by the standard model,

$$\mu_{\text{Exp}} := \frac{\sigma \cdot \mathcal{B}}{\sigma^{\text{SM}} \cdot \mathcal{B}^{\text{SM}}} \quad (2.7)$$

Production	Decay	$\mu_{\text{Exp}} \pm \delta\mu_{\text{Exp}}$ (symmetrised)		Ref.	
		LHC Run-II			
		CMS $137 \text{ fb}^{-1}$	ATLAS $139 \text{ fb}^{-1}$		
ggF	$h \rightarrow \gamma\gamma$	$0.99 \pm 0.12$ $1.030 \pm 0.110$		$1.000 \pm 0.042$ [89–91]	
	$h \rightarrow ZZ^*$	$0.985 \pm 0.115$ $0.945 \pm 0.105$		$1.000 \pm 0.040$	
	$h \rightarrow WW^*$	$1.285 \pm 0.195$ $1.085 \pm 0.185$		$1.000 \pm 0.037$ [89, 91, 92]	
	$h \rightarrow \tau^+\tau^-$	$0.385 \pm 0.385$ $1.045 \pm 0.575$		$1.000 \pm 0.055$	
	$h \rightarrow b\bar{b}$	$2.54 \pm 2.44$ —		$1.000 \pm 0.247$ [91, 92]	
	$h \rightarrow \mu^+\mu^-$	$0.315 \pm 1.815$ —		$1.000 \pm 0.138$ [91, 92]	
VBF	$h \rightarrow \gamma\gamma$	$1.175 \pm 0.335$ $1.325 \pm 0.245$		$1.000 \pm 0.128$ [89–91]	
	$h \rightarrow ZZ^*$	$0.62 \pm 0.41$ $1.295 \pm 0.455$		$1.000 \pm 0.134$	
	$h \rightarrow WW^*$	$0.65 \pm 0.63$ $0.61 \pm 0.35$		$1.000 \pm 0.073$ [89, 91, 92]	
	$h \rightarrow \tau^+\tau^-$	$1.055 \pm 0.295$ $1.17 \pm 0.55$		$1.000 \pm 0.044$	
	$h \rightarrow b\bar{b}$	— $3.055 \pm 1.645$		— [89]	
	$h \rightarrow \mu^+\mu^-$	$3.325 \pm 8.075$ —		$1.000 \pm 0.540$ [91]	
$t\bar{t}h$	$h \rightarrow \gamma\gamma$	$1.43 \pm 0.30$ $0.915 \pm 0.255$		$1.000 \pm 0.094$ [89–91]	
	$h \rightarrow VV^*$	$0.64 \pm 0.64 (ZZ^*)$ $0.945 \pm 0.465 (WW^*)$ $1.735 \pm 0.545$		$1.000 \pm 0.246 (ZZ^*)$ $1.000 \pm 0.097 (WW^*)$ —	
	$h \rightarrow \tau^+\tau^-$	$0.845 \pm 0.705$ $1.27 \pm 1.0$		$1.000 \pm 0.149$ [89, 91, 92]	
	$h \rightarrow b\bar{b}$	$1.145 \pm 0.315$ $0.795 \pm 0.595$		$1.000 \pm 0.116$	
$Vh$	$h \rightarrow \gamma\gamma$	$0.725 \pm 0.295$ $1.335 \pm 0.315$		$1.000 \pm 0.233 (Zh)$ $1.000 \pm 0.139 (W^\pm h)$ [89–91]	
	$h \rightarrow ZZ^*$	$1.21 \pm 0.85$ $1.635 \pm 1.025$		$1.000 \pm 0.786 (Zh)$ $1.000 \pm 0.478 (W^\pm h)$ [89, 91, 92]	
	$h \rightarrow WW^*$	$1.850 \pm 0.438$ —		$1.000 \pm 0.184 (Zh)$ $1.000 \pm 0.138 (W^\pm h)$ [91, 93]	
	$h \rightarrow b\bar{b}$	— $1.025 \pm 0.175$		$1.000 \pm 0.065 (Zh)$ $1.000 \pm 0.094 (W^\pm h)$ [89, 91]	
$Zh$ CMS	$h \rightarrow \tau^+\tau^-$	$1.645 \pm 1.485$		[92]	
	$h \rightarrow b\bar{b}$	$0.94 \pm 0.32$	—		
$W^\pm h$ CMS	$h \rightarrow \tau^+\tau^-$	$3.08 \pm 1.58$		[92]	
	$h \rightarrow b\bar{b}$	$1.28 \pm 0.41$			

**Table 2.1.** The experimental single Higgs production and decay rates measurements from the complete data of LHC Run II and projections for the HL-LHC. The uncertainties were symmetrised here.

### 2.3.2 Constraints on Higgs couplings

The measurements of the Higgs rates and their combination (also including STXS) have been used to set bounds on the Higgs couplings, the most recent bounds - as this thesis being written - have been reported by ATLAS using the Higgs inclusive rates and STXS for the full Run-II data [94], and by CMS using Higgs rates shown in Table 2.1 [92]. In Figure 2.6, I present the aggregation the ATLAS and CMS bounds on the Higgs coupling modifiers in the  $\kappa$  formalism defined in eq. (2.5). The aggregation of these bounds was preformed using the method described in [95] assuming there is no correlation between ATLAS and CMS measurements.

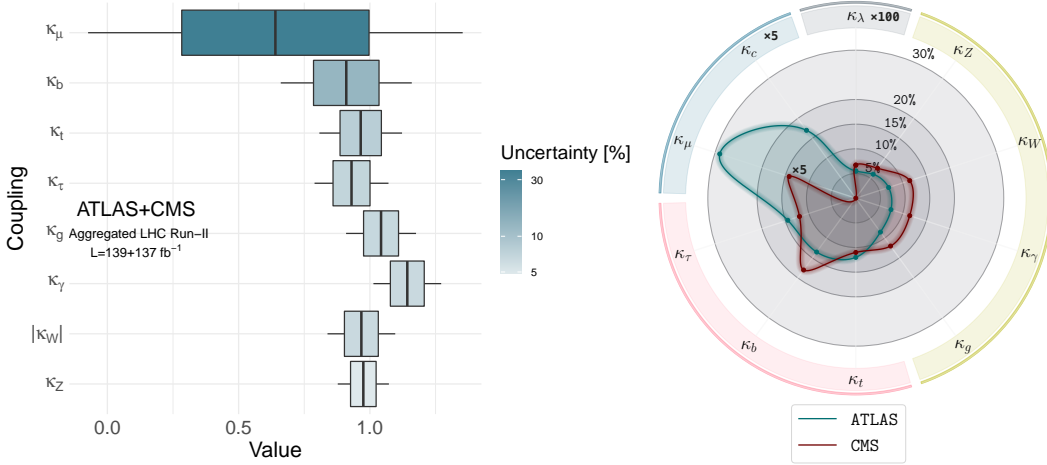


**Figure 2.6.** Meta analysis aggravating the most recent bounds from ATLAS [94] and CMS [92] on the Higgs coupling modifiers  $\kappa$ . [update the fig](#)

Examining Figure 2.6, we observe that the bounds on the Higgs boson's coupling to the gauge boson, including the effective couplings to  $\gamma$  and  $g$ , as well as the couplings to the third-generation fermions are in few percent within the SM prediction. The bounds on the coupling to the  $W$  boson seems to favour a negative value in CMS fits, due to the channel used to constraint it  $h \rightarrow WW$  which depends on  $\kappa_W^2$ , thus making the best fit value of  $\sim -1$  within the SM prediction. An independent analysis on the relative signs of  $\kappa_W$  and  $\kappa_t$  was preformed using  $th/t\bar{h}$  processes in Ref. [96], hence only the absolute value of  $\kappa_W$  is reported in my combination of the analysis results. Additionally, the observation of the decays  $h \rightarrow b\bar{b}$  [97–99] and  $h \rightarrow \tau\tau$  [100, 101] leading to direct measurements of the beauty and  $\tau$  Yukawa couplings has made their bounds comparable to the gauge bosons and top couplings with the Higgs, having less than 10% uncertainty. Au contraire, bounds on the Yukawa couplings of second and first generation fermions remain very weak.

Recently, searches for the decay  $h \rightarrow \mu\mu$  [102, 103] using the whole Run-II data by both collaborations, yielded an evidence for its observation of about  $3\sigma$ . Improving the constraints on  $\kappa_\mu$ , though as seen in Figure 2.6, the uncertainty remains high

$\sim 36\%$ . Searches for the Higgs decaying to charm pairs is significantly more challenging than the dimuon decays and only yielded an upper 95% CL bounds on  $|\kappa_c|$  of 8.5 for ATLAS [104, 105] and 70 for CMS [106]. There is no planned direct searches for the first generation Yukawa couplings (*direct*) measurements planned for the LHC as it is not possible to directly access decays of the Higgs to up or down quarks. Other methods for probing these couplings will be extensively discussed in chapter 9.

By the end of the HL-LHC, it is projected that the couplings of the Higgs, including the couplings with gauge bosons, third generation fermions as well as the muon Yukawa will be measured at few percent level, particularly the couplings with the gauge bosons will be reaching  $\sim 1\%$  level uncertainty [107]. This is highlighted by Figure 2.7, this figure shows the improvement in the  $\kappa$  measurement uncertainty expected by the HL-LHC over Run-II.

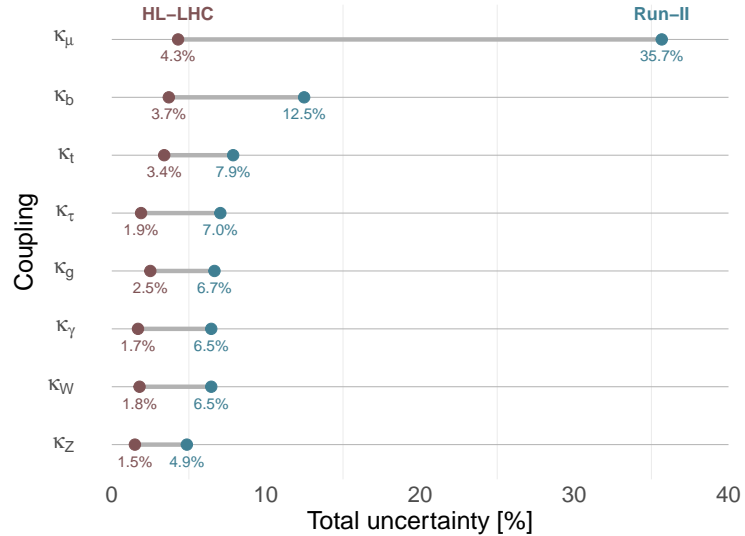


**Figure 2.7.** Dumbbell plot illustrating the improvement of the uncertainties on the Higgs coupling's measurement project for the HL-LHC compared to the current combined CMS and ATLAS measurements of Run-II.

## 2.4 Challenges and outlook

The future runs of the LHC hold a lot of potential for further understanding of the 10-year old Higgs boson ! Although, for some processes and couplings there will still be a lot of challenges. For instance, the observation of  $h \rightarrow c\bar{c}$  will require highly efficient charm-tagging, which is expected to improve at the HL-LHC by a factor of 2.5 [108]. The signal strength with rare decay  $h \rightarrow Z\gamma$  currently is constrained to 3.6 times the SM values at 95% CL [109] and it is projected to be measured at the HL-LHC with  $\sim 10\%$  uncertainty.

One of the couplings of the Higgs which we did not discuss above is the Higgs self-interaction (trilinear and quartic), as I have shown in subsection 1.5.2 that the perturbative unitarity bound derived in Ref. [52] is the strongest bound on these couplings so far. This is due to the fact that to experimentally measure the Higgs self-coupling, one needs to search for double Higgs production to access the trilinear self-coupling, and triple Higgs production for the quartic. These processes are very challenging, due to their low inclusive cross-section  $\sim 30$  fb for  $hh$  [110] and  $< 0.1$  fb for  $hhh$  at LHC maximum expected operational energy of 14 TeV and the latter is challenging even for future colliders of inclusive cross section at 100 TeV of only  $\sim 5$  fb [111]; as opposed to single Higgs production with inclusive cross-section of  $\sim 70$  pb. Certainly the difficulty is aggravated when one considers that the second Higgs would also decay, further lowering the signal strength. The triple Higgs production thus, will not be accessible at the LHC and consequently the quartic self-coupling. However, there is a lot of potential for the trilinear self-coupling, particularly at the HL-LHC.

In chapter 5 I will discuss the potential for using single Higgs processes as proposed by several studies, cf. [112–119] and the challenges accompanying it. Later in chapter 7 the Higgs pair production at the LHC will be overviewed along the current and future searches for this process and the bounds from them on the trilinear Higgs self-coupling.

Another elusive couplings that we have came across are the light Yukawas. In particular light quark Yukawa couplings of the first generation. After overviewing the proposed methods for constraining them, in chapter 8 I will discuss a novel method for directly measuring light quark Yukawa coupling using Higgs pair production. And in chapter 9 a sophisticated method based on interpretable machine learning will be showcased, by which, it is possible to simultaneously constrain the two elusive Higgs interactions: light Yukawas and the trilinear self-coupling using Higgs pair production.



## 3 Higgs and effective field theories

The study of the Higgs properties, couplings and rates aims to shed light on the structure of its potential, how and why it is responsible for the EW symmetry breaking. Explaining the vacuum expectation value and the mass of the Higgs has been the aim of many theoreticians and phenomenologists. This is because the SM provides no insights on the nature of the Higgs potential and its parameters, as in the SM these are input parameters that is needed to be provided from experimental observations. The Higgs potential shown in eq. (1.8) is the minimal one that could cause the EW symmetry breaking, but nature may not have taken this minimalist approach. In particular, that this potential suffers from severe fine-tuning as we have discussed in the hierarchy problem [add a discussion about this](#).

In order to test whether the Higgs potential and the way it generates SSB is the minimalist SM way or there are other more complex structures involved one needs to measure Higgs rates and compare them with the SM, as overviewed in the previous chapter, using the  $\kappa$  formalism. Alas, this approach does not help in understanding what would the new physics (NP) structures be more likely to case a certain deviation, if any observed. Conversely, we would be interested in knowing what the allowed NP structures given the current (or future) measurements of the Higgs rates are. Of course, by looking at concrete models, one-by-one, confronting them with Higgs data one would get an insight on the aforementioned questions but withal very tedious as there are numerous ways NP might manifest itself.

In order to make our search for NP more accessible and model-agnostic, we could revert to **effective field theories** (EFT), one of the most perspicacious concepts of quantum field theory. In the EFT framework, the interactions mediated by the NP at small scale of an arbitrary complexity can be systematically simplified by approximating these interactions via integrating the UV degrees of freedom thus leaving only numerable operators added to the SM. The premise of EFT's can be simply illustrated in [Figure 3.1](#), the LHC-for example- would not be able to resolve the UV degrees of freedom at their scale  $\Lambda$ , rather one can only observe the effective interactions they mediates. These new effective interactions are parametrised using a set of free parameters known as **Wilson coefficients**, that would be constrained from experiments. These “phenomenological Lagrangians” as called by Weinberg [120], are not necessarily renormalisable but would still allow for robust predictions that can be tested at colliders, including higher order effects . These predictions usually manifest as modifications to rates.

In this chapter I will be discussing the EFT's that modify Higgs rates, including single Higgs and Higgs pair production at leading order. In later chapters like ?? EFT operators from the top quark sector that modify Higgs rates at NLO will be shown. Lastly, in ?? more EFT operators that are responsible for lepton flavour universality

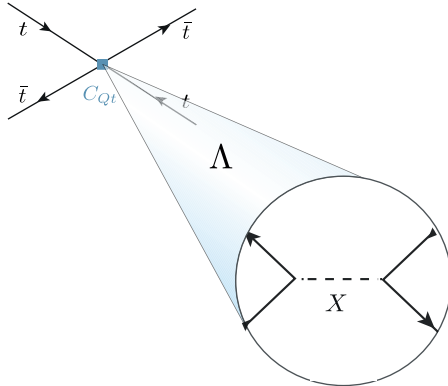


**Figure 3.1.** eft

violation also at NLO will be showcased. This chapter is organised as follows: In ?? the Higgs sector of Standard Model effective field theory (SMEFT) will be presented along with the parametrisation of single and di-Higgs rates in terms of the SMEFT Wilson coefficients. Au contraire to the SMEFT formalism, section 3.2 will present a non-linear EFT formalism known as the Chiral Lagrangian or (Higgs)EFT . Finally I will conclude this chapter with section 3.3.

### 3.1 Standard Model EFT

There is no unique way of defining an EFT for the Higgs boson  $h(x)$ . One could consider the field  $h$  as an EW singlet or as a part of the doublet  $\phi$  like the SM. The first ansatz way is more compatible with a heavier Higgs and the effective coupling based on it could be derived from the EW chiral Lagrangian (EWChL) as we shall see in section 3.2. However, after the discovery of the Higgs, having a mass close to  $m_Z$ , the second option for an EFT seemed more fitting, though more restrictive. Assuming that the NP resonances would occur at masses  $\Lambda \gg m_Z$ , one could integrate them out yielding a set of effective operators of mass dimension  $> 4$ . Hence, one can think of the SM Lagrangian of mass dim 2 and 4 as a part of a more general EFT that contain the same fields and symmetries known as the Standard Model Effective field theory (SMEFT).

From simple dimensional analysis, we know that the Higher dimensional operators need to contain an inverse mass with some power  $p = 4 - d$  in the couplings, we will have a clear power counting in the SMEFT Lagrangian, such that we could collect all operators of the same mass dimension  $d$  into a  $d$ -mass-dimensional Lagrangians taking the form

$$\mathcal{L}^{(d)} = \frac{1}{\Lambda^{d-4}} \sum_i C_i \mathcal{O}_i. \quad (3.1)$$

For any  $d > 4$  the Lagrangian in eq. (3.1) is not be renormalisable in the strict sense, yet it is still predictive via fitting the Wilson coefficients  $C_i$  order-by-order. This power-

counting property allows for predictability even when we, in principle, have infinite number of free Wilson coefficients, as all of these operators are suppressed by the NP scale (irrelevant operators w.r.t. the renormalisation group) [1]. In order to illustrate this, we let  $\Lambda = 1$ , then the effects of dimension-six operators will be in percent level, while dimension-eight operators will have effects of order  $\sim 10^{-4}$ , allowing us to ignore the dimension-eight and higher operators. Regarding dimension-five, we have only one operator called the Weinberg operator [121]

$$\mathcal{O}_{\nu\nu} = (\tilde{\phi} L_p)^T \hat{C} (\tilde{\phi}^\dagger L_q), \quad (3.2)$$

where  $\hat{C}$  is the charge conjugation operator. The Weinberg operator violates leptonic number and generates neutrino masses after EW symmetry breaking, similar effects are generated from dimension-seven operators [122]. These effects do not yield considerable collider phenomenology. Hence, I shall be discussing SMEFT with dimension-six operators only, for studies on Higher dimensional SMEFT operators cf. [122–125]. The SMEFT Lagrangian up to dimension-six operators is given by

$$\mathcal{L}_{\text{SMEFT}}^{d=6} = \mathcal{L}_{\text{SM}} + \frac{1}{\Lambda^2} \sum_i C_i \mathcal{O}_i. \quad (3.3)$$

The study of dimension-six effective operators in characterising NP effects at energies beyond colliders reach has been first proposed in [127, 128]. Nowadays, phenomenological studies of EFT's with dimension-six operators primarily focus on using a set of complete and non-redundant “basis”. This is due to the fact that different effective operators will correspond to same observables e.g. same scattering amplitudes of SM particles. This is the case if the operators can be related by using equations of motion, Fierz transformations, integration by parts or field redefinitions. This leads to non-trivial and counter-intuitive relations between operators. Thus making the construction of basis for the dimension-six SMEFT Lagrangian of eq. (3.3) a cumbersome task. Such task has been accomplished recently by [126, 129] forming what is known as **Warsaw Basis**. Another set of basis is the strongly-interacting light Higgs basis (SILH), originally proposed by [130], before the Warsaw basis, and completed in [131, 132]. A more recent set of basis has been published in [133] using a subset of couplings characterising the interactions of mass eigenstates in the effective Lagrangian.

The complete  $d = 6$  SMEFT is described by 2499 independent parameters [129]. However, if one suppresses the flavour indices, then the dimension-six operators themselves are much less, in the Warsaw basis for example, assuming Baryon number conservation and dropping the flavour indices one has only 59 operators, listed in Table 3.1. It should be noted that all of the basis of SMEFT will produce the same phenomenology, the choice of basis is sometimes helpful in simplifying the analysis. In this thesis, I will mainly focus on Warsaw basis.

The SMEFT operators can either modify SM parameters (couplings, masses) or introduce new vertices that do not exist in the SM, like four-fermion operators, or both like  $\mathcal{O}_{\phi e}$ . An example of operators modifying SM parameters is  $\mathcal{O}_{\phi D}$ , which leads to

$X^3$		Pure Higgs		$\psi^2 \phi^3 + \text{h.c.}$	
$\mathcal{O}_G$	$f^{ABC} G_\mu^{A\nu} G_\nu^{B\rho} G_\rho^{C\mu}$	$\mathcal{O}_{\phi\square}$	$(\phi^\dagger \phi) \square (\phi^\dagger \phi)$	$\mathcal{O}_{e\phi}$	$(\phi^\dagger \phi) (\bar{l}_p e_r \phi)$
$\mathcal{O}_{\widetilde{G}}$	$f^{ABC} \widetilde{G}_\mu^{A\nu} G_\nu^{B\rho} G_\rho^{C\mu}$	$\mathcal{O}_{\phi D}$	$(\phi^\dagger D_\mu \phi)^* (\phi^\dagger D_\mu \phi)$	$\mathcal{O}_{u\phi}$	$(\phi^\dagger \phi) (\bar{q}_p u_r \widetilde{\phi})$
$\mathcal{O}_W$	$\epsilon^{IJK} W_\mu^{I\nu} W_\nu^{J\rho} W_\rho^{K\mu}$	$\mathcal{O}_\phi$	$(\phi^\dagger \phi)^3$	$\mathcal{O}_{d\phi}$	$(\phi^\dagger \phi) (\bar{q}_p d_r \phi)$
$\mathcal{O}_{\widetilde{W}}$	$\epsilon^{IJK} \widetilde{W}_\mu^{I\nu} W_\nu^{J\rho} W_\rho^{K\mu}$				
$X^2 \phi^2$		$\psi^2 X \phi + \text{h.c.}$		$\psi^2 \phi^2 D$	
$\mathcal{O}_{\phi G}$	$\phi^\dagger \phi G_{\mu\nu}^A G^{A\mu\nu}$	$\mathcal{O}_{eW}$	$(\bar{l}_p \sigma^{\mu\nu} e_r) \tau^I \phi W_{\mu\nu}^I$	$\mathcal{O}_{\phi l}^{(1)}$	$(\phi^\dagger i \overleftrightarrow{D}_\mu \phi) (\bar{l}_p \gamma^\mu l_r)$
$\mathcal{O}_{\phi \widetilde{G}}$	$\phi^\dagger \phi \widetilde{G}_{\mu\nu}^A G^{A\mu\nu}$	$\mathcal{O}_{eB}$	$(\bar{l}_p \sigma^{\mu\nu} e_r) \phi B_{\mu\nu}$	$\mathcal{O}_{\phi l}^{(3)}$	$(\phi^\dagger i \overleftrightarrow{D}_\mu^I \phi) (\bar{l}_p \tau^I \gamma^\mu l_r)$
$\mathcal{O}_{\phi W}$	$\phi^\dagger \phi W_{\mu\nu}^I W^{I\mu\nu}$	$\mathcal{O}_{uG}$	$(\bar{q}_p \sigma^{\mu\nu} T^A u_r) \widetilde{\phi} G_{\mu\nu}^A$	$\mathcal{O}_{\phi e}$	$(\phi^\dagger i \overleftrightarrow{D}_\mu \phi) (\bar{e}_p \gamma^\mu e_r)$
$\mathcal{O}_{\phi \widetilde{W}}$	$\phi^\dagger \phi \widetilde{W}_{\mu\nu}^I W^{I\mu\nu}$	$\mathcal{O}_{uW}$	$(\bar{q}_p \sigma^{\mu\nu} u_r) \tau^I \widetilde{\phi} W_{\mu\nu}^I$	$\mathcal{O}_{\phi q}^{(1)}$	$(\phi^\dagger i \overleftrightarrow{D}_\mu \phi) (\bar{q}_p \gamma^\mu q_r)$
$\mathcal{O}_{\phi B}$	$\phi^\dagger \phi B_{\mu\nu} B^{\mu\nu}$	$\mathcal{O}_{uB}$	$(\bar{q}_p \sigma^{\mu\nu} u_r) \widetilde{\phi} B_{\mu\nu}$	$\mathcal{O}_{\phi q}^{(3)}$	$(\phi^\dagger i \overleftrightarrow{D}_\mu^I \phi) (\bar{q}_p \tau^I \gamma^\mu q_r)$
$\mathcal{O}_{\phi \widetilde{B}}$	$\phi^\dagger \phi \widetilde{B}_{\mu\nu} B^{\mu\nu}$	$\mathcal{O}_{dG}$	$(\bar{q}_p \sigma^{\mu\nu} T^A d_r) \phi G_{\mu\nu}^A$	$\mathcal{O}_{\phi u}$	$(\phi^\dagger i \overleftrightarrow{D}_\mu \phi) (\bar{u}_p \gamma^\mu u_r)$
$\mathcal{O}_{\phi WB}$	$\phi^\dagger \tau^I \phi W_{\mu\nu}^I B^{\mu\nu}$	$\mathcal{O}_{dW}$	$(\bar{q}_p \sigma^{\mu\nu} d_r) \tau^I \phi W_{\mu\nu}^I$	$\mathcal{O}_{\phi d}$	$(\phi^\dagger i \overleftrightarrow{D}_\mu \phi) (\bar{d}_p \gamma^\mu d_r)$
$\mathcal{O}_{\phi \widetilde{WB}}$	$\phi^\dagger \tau^I \phi \widetilde{W}_{\mu\nu}^I B^{\mu\nu}$	$\mathcal{O}_{dB}$	$(\bar{q}_p \sigma^{\mu\nu} d_r) \phi B_{\mu\nu}$	$\mathcal{O}_{\phi ud} + \text{h.c.}$	$i(\widetilde{\phi}^\dagger D_\mu \phi) (\bar{u}_p \gamma^\mu d_r)$
$(\bar{L}L)(\bar{L}L)$			$(\bar{R}R)(\bar{R}R)$		
$\mathcal{O}_{ll}$	$(\bar{l}_p \gamma_\mu l_r) (\bar{l}_s \gamma^\mu l_t)$		$\mathcal{O}_{ee}$	$(\bar{e}_p \gamma_\mu e_r) (\bar{e}_s \gamma^\mu e_t)$	
$\mathcal{O}_{qq}^{(1)}$	$(\bar{q}_p \gamma_\mu q_r) (\bar{q}_s \gamma^\mu q_t)$		$\mathcal{O}_{uu}$	$(\bar{u}_p \gamma_\mu u_r) (\bar{u}_s \gamma^\mu u_t)$	
$\mathcal{O}_{qq}^{(3)}$	$(\bar{q}_p \gamma_\mu \tau^I q_r) (\bar{q}_s \gamma^\mu \tau^I q_t)$		$\mathcal{O}_{dd}$	$(\bar{d}_p \gamma_\mu d_r) (\bar{d}_s \gamma^\mu d_t)$	
$\mathcal{O}_{lq}^{(1)}$	$(\bar{l}_p \gamma_\mu l_r) (\bar{q}_s \gamma^\mu q_t)$		$\mathcal{O}_{eu}$	$(\bar{e}_p \gamma_\mu e_r) (\bar{u}_s \gamma^\mu u_t)$	
$\mathcal{O}_{lq}^{(3)}$	$(\bar{l}_p \gamma_\mu \tau^I l_r) (\bar{q}_s \gamma^\mu \tau^I q_t)$		$\mathcal{O}_{ed}$	$(\bar{e}_p \gamma_\mu e_r) (\bar{d}_s \gamma^\mu d_t)$	
			$\mathcal{O}_{ud}^{(1)}$	$(\bar{u}_p \gamma_\mu u_r) (\bar{d}_s \gamma^\mu d_t)$	
			$\mathcal{O}_{ud}^{(8)}$	$(\bar{u}_p \gamma_\mu T^A u_r) (\bar{d}_s \gamma^\mu T^A d_t)$	
$(\bar{L}L)(\bar{R}R)$			$(\bar{L}R)(\bar{L}R) + \text{h.c.}$		
$\mathcal{O}_{le}$	$(\bar{l}_p \gamma_\mu l_r) (\bar{e}_s \gamma^\mu e_t)$		$\mathcal{O}_{quqd}^{(1)}$	$(\bar{q}_p^j u_r) \epsilon_{jk} (\bar{d}_s^k d_t)$	
$\mathcal{O}_{lu}$	$(\bar{l}_p \gamma_\mu l_r) (\bar{u}_s \gamma^\mu u_t)$		$\mathcal{O}_{quqd}^{(8)}$	$(\bar{q}_p^j T^A u_r) \epsilon_{jk} (\bar{q}_s^k T^A d_t)$	
$\mathcal{O}_{ld}$	$(\bar{l}_p \gamma_\mu l_r) (\bar{d}_s \gamma^\mu d_t)$		$\mathcal{O}_{lequ}^{(1)}$	$(\bar{l}_p^j e_r) \epsilon_{jk} (\bar{q}_s^k u_t)$	
$\mathcal{O}_{qe}$	$(\bar{q}_p \gamma_\mu q_r) (\bar{e}_s \gamma^\mu e_t)$		$\mathcal{O}_{lequ}^{(3)}$	$(\bar{l}_p^j \sigma_{\mu\nu} e_r) \epsilon_{jk} (\bar{q}_s^k \sigma^{\mu\nu} u_t)$	
$\mathcal{O}_{qu}^{(1)}$	$(\bar{q}_p \gamma_\mu q_r) (\bar{u}_s \gamma^\mu u_t)$		$\mathcal{O}_{ledq}$	$(\bar{l}_p^j e_r) (\bar{d}_s q_{tj})$	
$\mathcal{O}_{qu}^{(8)}$	$(\bar{q}_p \gamma_\mu T^A q_r) (\bar{u}_s \gamma^\mu T^A u_t)$				
$\mathcal{O}_{qd}^{(1)}$	$(\bar{q}_p \gamma_\mu q_r) (\bar{d}_s \gamma^\mu d_t)$				
$\mathcal{O}_{qd}^{(8)}$	$(\bar{q}_p \gamma_\mu T^A q_r) (\bar{d}_s \gamma^\mu T^A d_t)$				

**Table 3.1.** Complete list of the dimension-six SMEFT operators in the Warsaw basis [126]. The  $\mathcal{CP}$  violating operators contains the dual fields  $\tilde{X}$ . The flavour labels of the form  $p, r, s, t$  on the  $\mathcal{O}$  operators are suppressed on the left hand side of the tables.

modification of the  $Z$  boson mass after EW symmetry breaking

$$\frac{C_{\phi D}}{\Lambda^2} |\phi^\dagger D_\mu \phi|^2 \rightarrow \frac{C_{\phi D} v^4}{16\Lambda^2} (g_2^2 + g_1^2) Z^\mu Z_\mu. \quad (3.4)$$

Additionally, from field redefinitions, we get indirect contributions to the  $W$  mass from  $C_{\phi D}$ , combining both effects as a deviation in the  $\rho$  parameter, we get

$$\delta\rho = \frac{v^2}{2\Lambda^2} C_{\phi D}. \quad (3.5)$$

Which allows us to constrain  $C_{\phi D}$  from the  $T$  parameter

$$T = \frac{-2\pi v^2}{\Lambda^2} \frac{(g_1^2 + g_2^2)}{g_1^2 g_2^2} C_{\phi D} \quad (3.6)$$

Another operator that affects the oblique parameters directly is  $\mathcal{O}_{\phi WB}$ , as it modifies the  $S$  parameter in the following way

$$S = \frac{16\pi v^2}{g_1 g_2 \Lambda^2} C_{\phi WB} \quad (3.7)$$

Other SM coupling modifications by SMEFT operators related to EWPO's are investigated in [134], and chapter 11. Additionally, the contributions of the SMEFT Wilson coefficients to SM parameters are not only from tree-level effects like in eq. (3.4) but could also come at (N)NLO, either from finite or RGE contributions.

SMEFT is suitable as a low energy limit for supersymmetric models [135] or some classes of composite Higgs models [136, 137]

### 3.1.1 Single Higgs processes in SMEFT

Single Higgs production and decay processes are modified at LO by a relatively long list of operators summarised in eqs. (3.8), (3.9) and (3.10). Explicit formulae for the Higgs rates dependence on the Wilson coefficients of these operators can be found in [138]

SMEFT operators modifying Higgs rates at LO

Higgs operators

$$C_{\phi D}, \mathcal{O}_{\phi\square}, \mathcal{O}_{\phi G}, \mathcal{O}_{\phi W}, \mathcal{O}_{\phi B}, \mathcal{O}_{\phi WB}, \mathcal{O}_{\phi l}^{(1)}, \\ \mathcal{O}_{\phi l}^{(3)}, \mathcal{O}_{\phi e}, \mathcal{O}_{\phi q}^{(1)}, \mathcal{O}_{\phi q}^{(3)}, \mathcal{O}_{\phi u}, \mathcal{O}_{\phi d}, \mathcal{O}_{\tau\phi}, \mathcal{O}_{t\phi}, \mathcal{O}_{b\phi}, \mathcal{O}_{tb\phi}. \quad (3.8)$$

Top-quark operators

$$\mathcal{O}_{tG}, \mathcal{O}_{tW}, \mathcal{O}_{tB}, \quad (3.9)$$

other

$$\mathcal{O}_G, \mathcal{O}_{ll}^{(1)}, \mathcal{O}_{Qq}^{(1),(3)}, \mathcal{O}_{tu}, \mathcal{O}_{td}^{(1),(8)}, \mathcal{O}_{Qu}^{(1),(8)}, \mathcal{O}_{Qd}^{(1),(8)}. \quad (3.10)$$

The third generation quarks are denoted by  $Q$  while the first and second generation quarks are assumed to have the same coupling and denoted by  $q, u, d$ .

Some of these operators are strongly constrained from EWPO data such as  $\mathcal{O}_{\phi D}$  and  $\mathcal{O}_{\phi WB}$ . Others are weakly constrained from Higgs data alone like the four-fermion or top sector operators, and require additional experimental data to constrain them. Global fits on SMEFT Wilson coefficients can be found in [139]. Where they have used Higgs and EW data on a subset of the SMEFT Wilson coefficients of the operators listed above. The fit also includes RGE and NLO (even NNLO for  $m_W$ ) effects. While in [140], a global fit for a larger set of operators, but only with LO effects, including EW, Higgs and top data for  $C_G$  the fits are found in [141]. More recent study [142] has utilised EWPO data to constrain the four-fermion operators appearing in Higgs rates at LO and others involving four heavy quarks, using their NLO effects to EW bosons pole masses. We shall see in chapter 5 that the four-fermions operators with all heavy quarks will contribute also to Higgs rates at NLO. A wider scope analysis including a wide range of Higgs, top, di-boson and EWPO data has been preformed in [143].

The dependence of single Higgs rates on the SMEFT Wilson coefficients gets more complicated once NLO and higher effects are taken into an account. As shown in the fit results reported from [139], the RGE of these Wilson coefficients introduces new operators that do not appear at LO, also loop corrections to masses of the EW and Higgs bosons as well as their process will depend on some SMEFT coefficients. A prominent example of an operator appearing only at NLO in single Higgs processes is  $\mathcal{O}_\phi$ , which modifies the Higgs self interactions, namely the trilinear coupling.

Typically, in order to probe the Higgs trilinear self-coupling directly, one ought to observe Higgs pair production, see Part III. However, due to the appearance of Higgs self-interaction and its modifiers-  $C_\phi$  in SMEFT context- in (N)NLO EW [144, 145] and Higgs observables [112–119], one can extract bounds on the Higgs trilinear coupling from single Higgs and EWPO data. Figure 3.2 illustrates example Feynman diagrams of single Higgs processes of which the trilinear Higgs self-coupling enters via NLO corrections. Using the results from the aforementioned references, a global fit with all operators that enter at tree-level in addition to the loop effects from the Higgs self-coupling has been

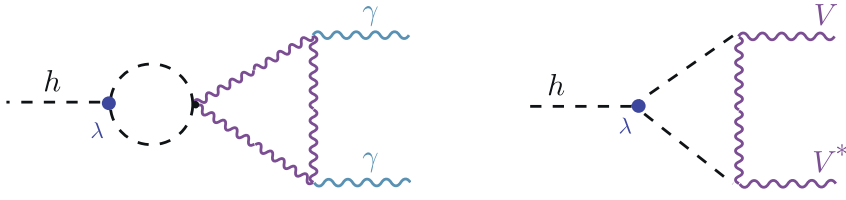


**Figure 3.2.** NLO EW corrections of single Higgs processes, were the Higgs trilinear self-coupling (the red circle) enters. Here the Higgs decay to two photons is shown as an example.

performed in ref. [146] and later as we have seen in ref. [139]. Additionally, experimental searches for Higgs trilinear self-coupling have been presented by ATLAS [147] and CMS [92].

### 3.1.2 Higgs pair production and SMEFT

Higgs pair production in Hadron colliders is sensitive to six  $\mathcal{CP}$  even SMEFT operators, under the assumption of Minimal Flavour violation (MFV)<sup>1</sup>. These operators are

$$\mathcal{O}_{\phi D}, \mathcal{O}_{\phi \square}, \mathcal{O}_\phi, \mathcal{O}_{t\phi}, \mathcal{O}_{\phi G}, \mathcal{O}_{tG}, \quad (3.11)$$

and their effects, with the corresponding colours are illustrated in Figure 3.3, except for  $\mathcal{O}_{\phi D}$  and  $\mathcal{O}_{\phi \square}$ , as they modify all SM Higgs vertices. However, MFV is not the only way to approach SMEFT, there exist more complex flavour structures that allow for significant enhancements of the first and second generation Yukawas with being excluded by flavour observables. Such formalisms will be discussed in chapter 8 and chapter 9, where I discuss the potential for Higgs pair production in probing operators modifying Light Yukawa couplings. Moreover, for Higgs pair production with  $\mathcal{CP}$  operators, see ref. [148]. The main operator to constrain from Higgs pair as mentioned before is  $\mathcal{O}_\phi$ , for two reasons; a) the other operators are already strongly constraint from single Higgs and top processes b) the effect of  $\mathcal{O}_\phi$  on Higgs pair production is significantly higher than in single Higgs or EW observables. This is illustrated in Figure 3.4, by comparing the relative change of the gluon fusion cross-sections at NLO QCD for single and di-Higgs production. This is not surprising, since  $C_\phi$  appears at LO in Higgs pair production. Another advantage for Higgs pair production searches is the sensitivity of this process to non-linear couplings, for example diagrams (b) and (d) of Figure 3.3. Although in SMEFT these diagrams correspond to the same operators in (a) and (c), respectively, in an another EFT this is not necessary the case.

<sup>1</sup>MFV assumes that new physics operators will follow the same flavour hierarchies as the SM.

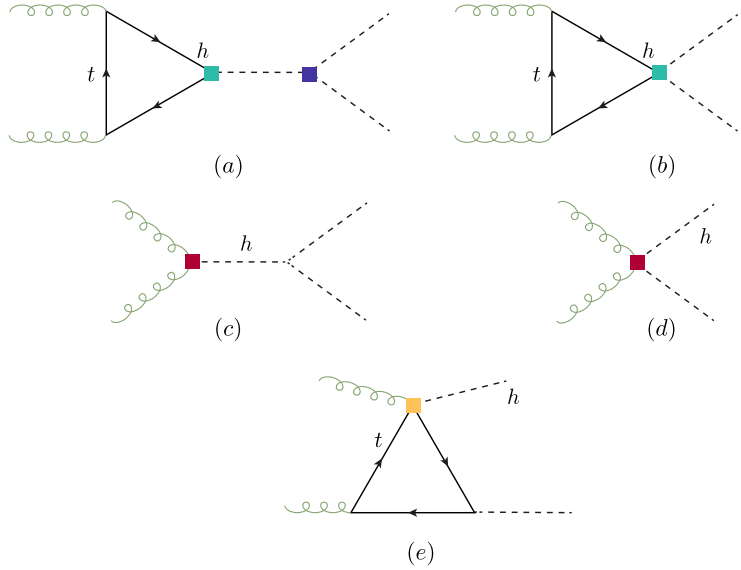


**Figure 3.3.** Example of diagrams illustrating how the dimension-six SMEFT operators enter in Higgs pair production at Hadron colliders.

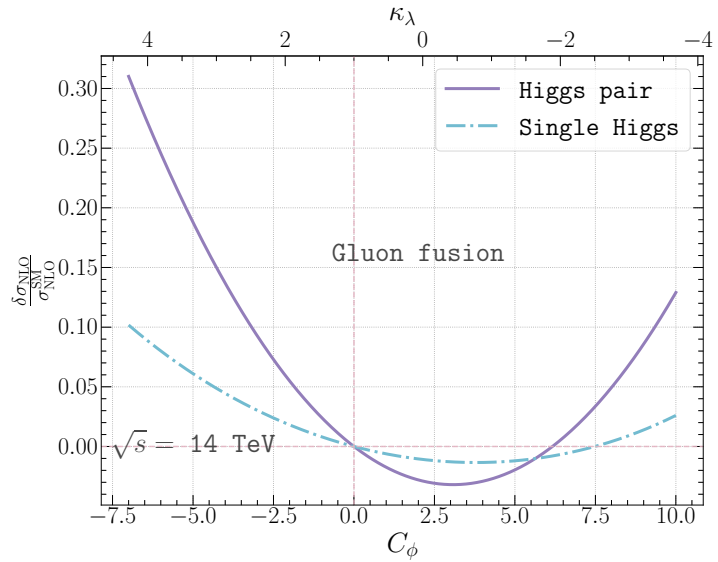


**Figure 3.4.** The relative change of the NLO QCD cross-section of gluon fusion production of single Higgs (dashed line) and Higgs pair (solid line) at a  $pp$  collider with  $\sqrt{s} = 14$  TeV as a function of  $C_\phi$  or the corresponding  $\kappa_\lambda$ .

## 3.2 The chiral Lagrangian

Given the strong bounds on the  $\rho$  parameter, it would plausible to assume that NP would maintain the custodial symmetry  $SU(2)_V$ , and treat the chiral symmetry breaking pattern  $SU(2)_L \otimes SU(2)_R \rightarrow SU(2)_V$  in the same way the QCD chiral symmetry breaking is treated in terms of considering the pions as pNG bosons in order to describe their interaction. For pions this is known as **chiral perturbation theory** [149, 150]. The same mathematical description could be applied for the case of EW symmetry breaking by constructing the EW chiral Lagrangian (EWChL). In the EWChL the Goldstone fields  $\pi^a(x)$  of the SM are part of  $SU(2)$  unitary transformation

$$\mathcal{U}(x) = e^{i\pi^a(x)\sigma_a/v}, \quad (3.12)$$

which implies that the Goldstone fields transform non-linearly under  $SU(2)_L \otimes SU(2)_R$ . As for the Higgs field  $h(x)$ , it is added as an  $SU(2)_L \otimes U(1)_Y$  singlet, and appears in the EWChL at any power in principle. As contrary to the power counting in the NP scale  $\Lambda$  like in SMEFT, in the EWChL, one counts the *chiral dimension*  $\chi$ , defined for the fields as [151, 152]

$$[\phi]_\chi = 0, \quad [X]_\chi = 0, \quad [\partial_\mu]_\chi = 1, \quad [\psi]_\chi = 2. \quad (3.13)$$

The zeroth order term of the EWChL will have  $\chi = 2$ , higher order terms could be considered as terms generated perturbatively from  $L$  loop interactions, with chiral dimensions  $\chi = 2L + 2$ , hence the first order EWChL or HEFT would have operators of  $\chi = 4$ . Hence the expansion of the EWChL is in chiral order as well as in powers of  $h(x)/v$ . This power-counting results in some SMEFT dimension-six operators being considered of higher order in HEFT a prominent example of this is  $C_{tG}$  being of chiral dimension 5 in HEFT.

The relevant terms for single and di-Higgs production of the EWChL /HEFT is typically parametrised in the Unitary gauge by [146, 153]

$$\begin{aligned} \mathcal{L}_{\text{HEFT}} = & \frac{h}{v} \left[ \left( \delta c_W m_W^2 W_\mu^+ W^{-\mu} + \delta c_Z \frac{m_Z^2}{2} Z_\mu Z^\mu \right) \right. \\ & + c_{ww} \frac{g_2^2}{2} W_{\mu\nu}^+ W^{-\mu\nu} + c_{w\square} g_2^2 \left( W_\mu^- \partial_\nu W^{+\mu\nu} + \text{h.c.} \right) + c_{\gamma\gamma} \frac{\alpha}{8\pi} A_{\mu\nu} A^{\mu\nu} \\ & + c_{zz} \frac{g_2^2 + g_1^2}{4} Z_{\mu\nu} Z^{\mu\nu} + c_{z\gamma} \frac{eg_1}{16\pi^2} Z_{\mu\nu} A^{\mu\nu} + c_{z\square} g_2^2 Z_\mu \partial_\nu Z^{\mu\nu} + c_{\gamma\square} g_2 g_1 Z_\mu \partial_\nu A^{\mu\nu} \Big] \\ & + \frac{\alpha_s}{8\pi} \left( c_{gg} \frac{h}{v} + c_{gg}^{(2)} \frac{h^2}{2v^2} \right) \text{Tr} [G_{\mu\nu} G^{\mu\nu}] - \sum_f \left[ m_f \left( c_f \frac{h}{v} + c_{ff} \frac{h^2}{2v^2} \right) \bar{f}_R f_L + \text{h.c.} \right] \\ & - c_{hh} \frac{m_h^2}{2v} h^3 + \dots, \end{aligned} \quad (3.14)$$

I have omitted here the kinetic and mass terms of the Higgs,  $\mathcal{CP}$  violating terms, as well as couplings not contributing to the LHC phenomenology and Higher chiral order operators. In addition to NP effects, this Lagrangian also includes the LO and NLO SM vertices, for example the parameter  $\delta c_V = 1$  corresponds to the tree-level coupling between the Higgs field and the EW bosons  $V = W, Z$ . While the coupling  $c_{gg} = 4/3$  corresponds to the SM effective coupling at NLO if the heavy top limit (HTL)  $m_t \rightarrow \infty$ . In contrast to eqs. (??) and (??) the couplings of one and two Higgs bosons to fermions or gluons become de-correlated. Giving this Lagrangian a richer phenomenology for Higgs pair production.

The HEFT coefficients modifying the Higgs pair production via gluon fusion are

$$c_{hh}, \textcolor{blue}{c_t} \text{ (a)}, \textcolor{teal}{c_{tt}} \text{ (b)}, \textcolor{red}{c_{gg}} \text{ (c)}, \textcolor{red}{c_{gg}^{(2)}} \text{ (d)}, \quad (3.15)$$

with the same colours highlighted in the operator insertions of Figure 3.3 and the letter next to the coefficient indicates the diagram its operator contributes to. Full parametrisation of the Higgs pair cross-section at NLO (inclusive and differential) and NNLO (inclusive) can be found in refs. [154–156] and implemented at NLO in **POWHEG-BOX** [157]. UV-complete models that yield in the EWChL are composite Higgs models [136, 137, 158], dilaton theories [159], techni-dilaton models [160], technicolour models [161] and other models with induced EW symmetry breaking [162, 163].

### 3.2.1 Translation between SMEFT and HEFT

In order to facilitate the translation between SMEFT and HEFT or to the  $\kappa$ -formalism, one needs to put the SMEFT Lagrangian into the canonical form, that is to convert the operators with covariant derivatives acting on the Higgs to canonically normalised Higgs kinetic term. This is done done by the field redefinition.

$$\phi = \begin{pmatrix} 0 \\ h(1 + c_{h,kin}) + v \end{pmatrix} \quad (3.16)$$

with

$$c_{h,kin} = \left( C_{\phi,\square} - \frac{1}{4} C_{\phi D} \right) \frac{v^2}{\Lambda^2}. \quad (3.17)$$

This field redefinition will generate derivative interactions of the form  $h(\partial_\mu h)^2$  and  $h^2(\partial_\mu h)^2$ . In order to remove these terms, and for sake of simplicity one needs to use a gauge-dependent field redefinition<sup>2</sup>

$$h \rightarrow h + c_{h,kin} \left( h + \frac{h^2}{v} + \frac{h^3}{3v^2} \right). \quad (3.18)$$

This field redefinition hence leads to a dependence on  $c_{h,kin}$  of all Higgs boson couplings. There are however some caveats to the translation between HEFT and SMEFT, for

---

<sup>2</sup>For gauge-independent formalism cf. [164].

example, HEFT is less restrictive than SMEFT and it covers loop effects. This makes some points of the HEFT parameter space unmappable to SMEFT. In addition, the power counting is different in both formalisms, as mentioned before there will be some operators present in SMEFT that are absent in HEFT and vice-versa. In [Table 3.2](#), the translation between the HEFT and SMEFT Wilson coefficients of the operators relevant to Higgs pair production at LO is shown. More general translation between

HEFT	SMEFT (Warsaw)
$c_{hh}$	$1 - 2 \frac{v^4}{m_h^2} C_\phi + 3c_{h,kin}$
$c_f$	$1 + c_{h,kin} - C_{f\phi} \frac{v^3}{\sqrt{2}m_f}$
$c_{ff}$	$-C_{f\phi} \frac{3v^3}{2\sqrt{2}m_f} + c_{h,kin}$
$c_{gg}$	$8\pi/\alpha_s v^2 C_{\phi G}$
$c_{gg}^{(2)}$	$4\pi/\alpha_s v^2 C_{\phi G}$

**Table 3.2.** Translation between the Wilson coefficients of HEFT and SMEFT for the operators relevant to Higgs pair production

SMEFT in Warsaw and SILH basis and HEFT can be done automatically using [Rosetta](#) package [\[165\]](#)

### 3.2.2 EFT and $\kappa$ -formalism

The  $\kappa$  formalism provides an experimentally accessible and well-defined in terms of QFT way to study the Higgs properties [\[166\]](#). The  $\kappa$  parameters are part of more generalised formalism called the **Higgs Pseudo-observables** (PO's), which is discussed in [chapter 4](#). If the new physics contributions do not generate new Lorentz structures there is a possible translation between the Wilson coefficients in the SMEFT Warsaw basis, and the  $\kappa$  formalism. In particular, taking the rescaling of the trilinear coupling,  $\kappa_\lambda$ , the translation is given by

$$\kappa_\lambda = 1 - \frac{v^4}{m_h^2} \frac{C_\phi}{\Lambda^2} + 3c_{h,kin}, \quad (3.19)$$

A similar relation exists for the rescaling of the quark Yukawa couplings  $\kappa_q$

$$\kappa_q = 1 + c_{h,kin} - \frac{v^3}{\sqrt{2}m_q} \frac{C_{q\phi}}{\Lambda^2}. \quad (3.20)$$

One can see the similarities between  $\kappa$ -formalism and HEFT in these two examples, but this is not always the case. Other translations could be obtained by comparing how SMEFT operators modify the Higgs couplings with the SM, and matching it with the corresponding  $\kappa$  or other Higgs PO's.

However, one should be careful while interpreting results quoted in terms of Wilson

coefficients in the SMEFT framework extracted from di-Higgs, multi-Higgs or multi-vector bosons searches, as these results include couplings that are not present in the SM. For example, the  $hhq\bar{q}$  coupling, though being linearly related to the quark Yukawa coupling  $hq\bar{q}$ , is not a rescaling of any SM Higgs coupling as has been discussed in ???. With this in mind, one can strictly remain within a linear EFT and link the rescaling of the quark Yukawa,  $\kappa_q$ , to the  $hhq\bar{q}$  coupling through

$$g_{hhq\bar{q}}^{\text{linear-EFT}} = -\frac{3}{2} \frac{1-\kappa_q}{v} g_{hq\bar{q}}^{\text{SM}}. \quad (3.21)$$

This relation will no longer hold once a non-linear EFT, like HEFT, is used. Hence, the  $\kappa$ -formalism, in a strict sense, is not applicable to multi-Higgs studies.

### 3.3 Conclusions

Effective field theories provide a systematic yet simplified approach for NP searches by simplifying its complex interaction structures. This can be thought of as a dimensionality reduction approach by collapsing all the NP interaction into their effective ones as observed at colliders with energy reaches below the NP scale  $\Lambda$ . The linear approach to EFT is called the SMEFT, which preserves the SM fields and symmetries and the Higgs boson is a part of an  $SU(2)_L$  doublet  $\phi$  like the SM case. While non-linear approaches such as the chiral EW Lagrangian (or HEFT) treats the Higgs boson as an added singlet. The latter approach is more general and introduces independent parameters involving multiple Higgs bosons. For example, the couplings  $f\bar{f}h$  and  $f\bar{f}hh$  will be both generated in SMEFT and HEFT, but in SMEFT they are related by the Wilson coefficient  $C_{\phi f}$ , while in HEFT they have independent Wilson coefficients  $c_f$  and  $c_{ff}$  respectively.

Most of the Wilson coefficients involving Higgs interactions are strongly bounds by EWPO's, Higgs and top data. In addition to theoretical bounds found in [167]. However, the Wilson coefficients modifying the Higgs self-couplings, though bounds from the first two aforementioned data and perturbative unitarity [52, 168] exist, these bounds remain weak. This can be improved by the searches for Higgs pair production at the HL-LHC, as this process is far more sensitive to these Wilson coefficients than EWPO and single-Higgs data, as they only appear at NLO in the theoretical predictions of the later two experimental observables. In ??, I show the best bounds on the Wilson coefficients relevant to Higgs production as well as heavy quark four-fermion operators, with a heatmap indicating the contribution of each operator in prominent Higgs, top and EW precision observables. Although this is a subset of the total SMEFT operators and observables used in the fits, one can see the interconnectivity of the measurements. The main objective of this thesis is to extend these connections by exploiting the potential of single-Higgs data and Higgs pair production to constrain the Higgs trilinear coupling modifiers (mainly in SMEFT) and the interplay between  $C_\phi$  and heavy quark four-fermion operators in single Higgs data. Moreover, the SMEFT picture can be further extended by unravelling interplay between Light quark couplings modifiers in

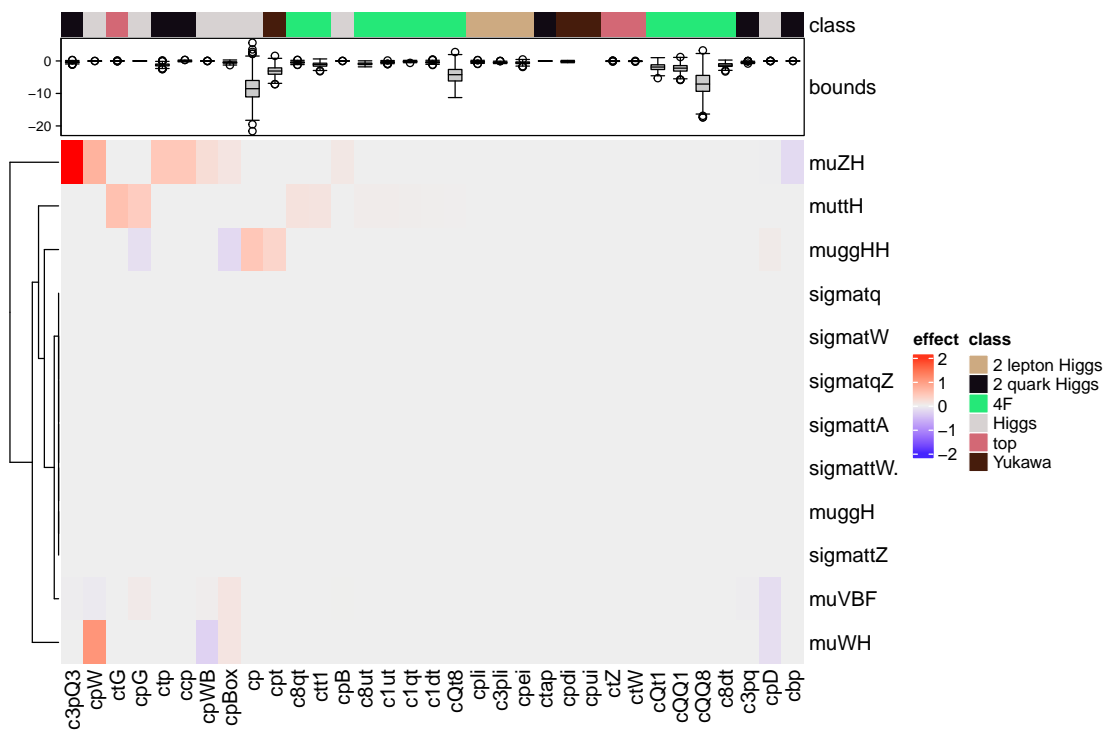


Figure 3.5

Higgs pair production. Lastly, I will show another connection between Higgs operators in SMEFT and flavour anomalies. Emphasising the complex interconnectivity between experimental observables and SMEFT operators.

## Part II

# Single Higgs Processes at the LHC



## 4 Overview of Higgs production at colliders

The production of the Higgs boson at the LHC occurs via four distinct processes: gluon fusion (ggF), vector boson fusion (VBF), associated production with electroweak boson ( $Vh$ ) and the production with top ( and anti-top) pair ( $t\bar{t}h$ ). It should be noted that sometimes the ggF category will include the quark anti-quark annihilation, but this is negligible in the SM, but becomes important for significant modifications of light Yukawa couplings. These process are illustrated in [Figure 4.1](#), and their details were summarised in [Table 4.1](#). All of these four channels have been observed at the LHC with  $> 5\sigma$  precision.

Since the experimental measurements of this Higgs were discussed previously in [section 2.3](#), the aim of this chapter is to provide an overview of the current theoretical status of these channels in [section 4.1](#). I will then conclude this overview in [section 4.2](#).

Process	Cross-section 13 TeV (pb)	Theo. accuracy	Exp. uncertainty (%)	Contribution (%)
ggF	48.51	N3LO QCD & NLO EW	6.5	88
tth & th	0.58	NLO QCD & NLO EW	20.0	1
VBF	3.78	NNLO QCD* & NLO EW	10.0	7
Vh	2.25	NNLO QCD & NLO EW	15.0	4

**Table 4.1.** Summary of the Higgs

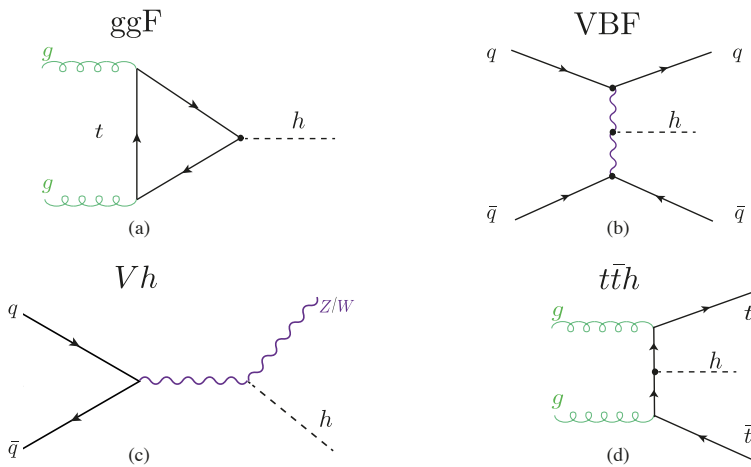


**Figure 4.1.**  $\sim 88\%$  ggF,  $\sim 7\%$  VBF,  $\sim 4\%$  Vh,  $\sim 1\%$   $t\bar{t}h$ .

## 4.1 Current status of the Higgs production channels

### 4.1.1 Gluon fusion

The ggF channel has the highest cross-section amongst the Higgs production channels, and consequently has the lowest experimental uncertainties. In order to increase the precision of the channel, Higher order corrections need to be included. The current state-of-the-art theoretical computation for the Higgs inclusive cross-section is N<sup>3</sup>LO in QCD and NLO in EW [169]. A full differential cross-section for the final state  $gg \rightarrow h \rightarrow \gamma\gamma$  has been computed recently to N<sup>3</sup>LO in QCD for the kinematic variables  $y_h$ ,  $y_{\gamma_1}$ ,  $y_{\gamma_2}$ ,  $\Delta y_{1,2}$  using the projection-to-born method [170]. The same final state fiducial differential cross-section in  $p_T$  with experimental cuts has been computed up to third re-summed and fixed order, i.e. N<sup>3</sup>LL' N<sup>3</sup>LO dependence [171], the theoretical computation of this fiducial cross-section with difference orders compared to the experimental measurement by ATLAS [86] is shown in Figure 4.2. We can see that the resummed result has significantly smaller theoretical uncertainties. The current total theoretical uncertainty with this order calculation is 5.4%, with only 2.7% of it coming from the perturbation order cut-off of the calculation, while the rest comes from the branching fraction, PDF+ $\alpha_s$ , EW corrections and mass uncertainties. When compared to Table 2.1, the projected experimental uncertainty of this final states at the HL-LHC is 4.2%, we see that the uncertainties will becomes comparable, and if the PDF uncertainties are reduced the uncertainties will remain experimentally-dominated for this channel. The predictions can be further improved by the computation of mixed QCD-EW effects.

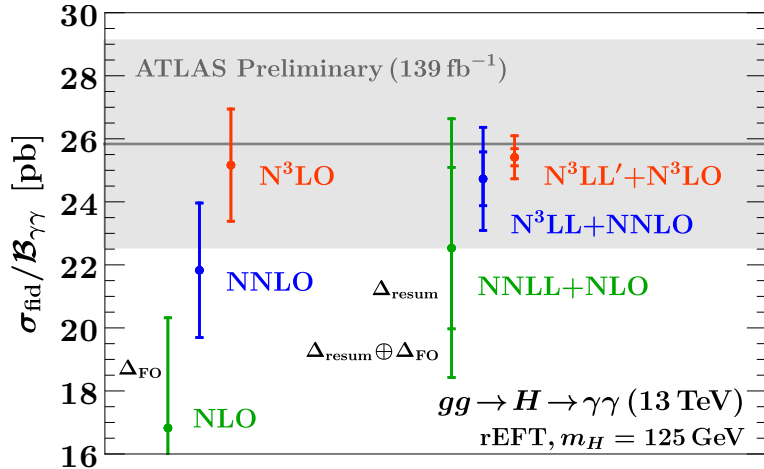


**Figure 4.2.** The total fiducial cross-section for the final state  $gg \rightarrow h \rightarrow \gamma\gamma$  at both fixed and resumed third order compared to the experimental ATLAS measurement [86] this figure is taken from [171]

Alas, these computations invokes three-loop integrals with both gluons and EW bosons, computed in [172] or two-loop ones with two particle final states appearing in the real

corrections with the process  $gg \rightarrow hg$  computed in [173] using differential equations. The computation was completed by inclusion of light quark initial states for the real corrections in [174] with exact quark mass dependence, reducing the EW uncertainty from 2% to  $\sim 0.6\%$ .

The computation of the three-loop form-factors with full top-mass dependence has been achieved in [175, 176] correction the cross-section by  $-0.26\%$ . However, there remains an intricate interplay between the mass effects of  $gg$ ,  $qg$  and  $qq$  initial states for the real matrix elements that cannot be fully controlled due to the light quark mass effects.

NLO corrections to the  $h + j$  and  $h + 2j$  processes were computed by [177] in the FT approximation, which used exact born and real correction amplitudes, and approximates the two-loop virtuals by

$$|\mathcal{A}^{2\text{-loop}}(m_t, \mu_R^2)|^2 \approx |\mathcal{A}^{1\text{-loop}}(m_t \rightarrow \infty, \mu_R^2)|^2 \frac{|\mathcal{A}^{1\text{-loop}}(m_t)|^2}{|A^{(0)}(m_t) \rightarrow \infty|^2}. \quad (4.1)$$

Although this approximation works very well even for  $p_T \gg m_t$ , the full top mass effects computations have been carried out in [178–180] using the high energy expansion technique.

### 4.1.2 Vector boson fusion

The VBF channel has a very distinctive signature, making it very suitable channel for Higgs signal extraction. The suppressed colour exchange between the quarks result in a little jet activity in the central rapidity region, and the quarks will be scattered resulting in two forward jets. The decay products of the Higgs are found in the region between these two forward jets. These features allows for excellent measurement of Higgs couplings and more difficult decays, and  $\mathcal{CP}$  properties determination. Some of these features are also shared with the  $Vh$  production channel via Higgs-strahlung. Both of these channels contain the  $VVh$  vertex which could be written generally as [153]

$$T^{\mu\nu}(p_1, p_2) = a_1 g^{\mu\nu} + a_2 \left( g^{\mu\nu} - 2 \frac{p_2^\mu p_2^\nu}{p_1 \cdot p_2} \right) + a_3 \frac{p_1^\alpha p_2^\beta}{p_1 \cdot p_2} \epsilon^{\mu\nu\alpha\beta}. \quad (4.2)$$

In the SM only  $a_1 \neq 0$ , and the other coefficients represent the anomalous coupling, for example if  $a_3 \neq 0$  then the Higgs is  $\mathcal{CP}$  odd. The study of the azimuthal angle distribution  $d\sigma_{VBF}/d\Delta\phi_{jj}$  allows for the determination of these coefficients, with very little dependence on the Higher order corrections on VBF [181].

The NLO QCD inclusive cross-section is known since the 90's [182], and later these corrections were made for the differential distributions cf. [183, 184]. Unlike the ggF channel, that has an NLO K-factor of 1.6 at 13 TeV [185], the VBF NLO corrections are small  $\sim 10\%$ . The two-loop NNLO QCD cross-section has been computed, the most recent is via the structure function approach [186] and later in STXS level 1.2 bins with EW corrections [187] implemented in an MC generator **HAWK**. Despite these corrections being small, they are non-negligible and their inclusion is important for uncertainties

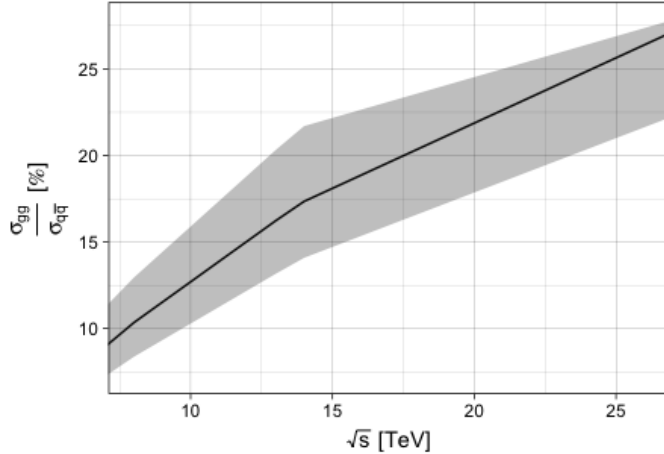


**Figure 4.3.** The ratio of the *LO* gluon fusion production cross-section  $gg \rightarrow Zh$  ( $\sigma_{gg}$ ) with respect to the *NLO* Drell-Yan process  $q\bar{q} \rightarrow Zh$  cross-section ( $\sigma_{q\bar{q}}$ ) at a  $pp$  collider with centre-of-mass energy  $\sqrt{s}$ . The error band captures the total theoretical uncertainties on both cross-sections dominated by  $\sigma_{gg}$ .

reduction.

#### 4.1.3 Associated production with EW bosons

The channels  $pp \rightarrow Wh/Zh$  are quark-initiated tree-level processes at *LO* interpreted as **Drell-Yan process** [188, 189]. These process has been computed up to *NNLO* in QCD ( $\sim \alpha_s^2$ ), and *NLO* EW ( $\sim \alpha^2$ ) [190].

Despite arising for the first time at *NNLO* in perturbation theory to the partonic cross-section, the gluon fusion channel  $gg \rightarrow Zh$  has a non-negligible contribution to the hadronic cross-section  $pp \rightarrow Zh$ , which could reach  $> 16\%$  of the total cross-section contribution at 14 TeV [191], see Figure 4.3. The contribution becomes more significant when looking at large invariant mass bins in the differential cross-section. This is due to the significant abundance of gluons at the LHC for large energy fraction  $Q$  as well as the extra enhancement coming from the top quark initiated contribution near the  $t\bar{t}$  threshold [192]. The gluon fusion channel has a higher scale uncertainties than the quark induced one, as one can see from the uncertainty band of Figure 4.3 predominantly coming from the gluon fusion part  $\sigma_{gg}$ . With that in mind, and the absence of gluon fusion channel for  $Wh$  channel, the  $Zh$  channel has higher theoretical uncertainties. This further motivates *NLO* calculation of the  $gg \rightarrow Zh$  channel to higher orders in perturbation theory, in order to reduce these uncertainties. Facilitating the precision measurement of the  $Zh$  channel at the future LHC runs, which in term provides better constraints on several observables, such as sign and magnitude of the top Yukawa coupling, dipole operators [193].

The leading order (*LO*) contribution to the  $gg \rightarrow Zh$  amplitude, given by one-loop

diagrams, was computed exactly in refs.[194, 195]. However, for the NLO, the virtual corrections contain multi-scale two-loop integrals some of which are still not known analytically (for the box diagram). The first computation of the NLO terms has been done by [196] using an asymptotic expansion in the limit  $m_t \rightarrow \infty$  and  $m_b = 0$ , and pointed to a  $K$ -factor of about  $\sim 2$ . Later, the computation has been improved via soft gluon resummation, and including NLL terms found in ref.[197], the NLL terms has been matched to the fixed NLO computation of [196]. Top quark mass effects to the  $gg \rightarrow Zh$  process were first implemented using a combination of large- $m_t$  expansion (LME) and Padé approximants [198]. A data-driven approach to extract the gluon fusion dominated non-Drell-Yan part of  $Zh$  production using the known relation between  $Wh$  and  $Zh$  associated production when only the Drell-Yan component of the two processes is considered has been investigated in ref.[199]. The differential distributions of  $gg \rightarrow Zh$  at NLO was studied in ref.[200] via LO matrix element matching.

More recent studies of the NLO virtual corrections to this process were based on the high-energy (HE) expansion improved by Padé approximants with the LME, which extended the validity range of the HE expansion [201]. However, this expansion is only valid for in the invariant mass region  $\sqrt{\hat{s}} \gtrsim 750 \text{ GeV}$  and  $\sqrt{\hat{s}} \lesssim 350 \text{ GeV}$ , which only covers  $\sim 32\%$  of the hadronic cross section. Additionally, numerical computation of the two-loop virtual corrections, though implemented exactly in [202], are rather slow for practical use in MC simulations. This highlights the importance of an analytical method that can cover the remaining region of the cross-section and can be merged with the HE expansion via Padé approximants. Fortunately, the two-loop corrections to the triangle diagrams can be computed exactly. And the loop integrals appearing in the box correction having no analytic expression can be expanded in small  $Z$  (or Higgs) transverse momentum,  $p_T$ . This method was first used for Higgs pair production in [203], to compute the NLO virtual corrections to the box diagrams in the forward kinematics. In chapter 6, I will discuss the calculation preformed by my collaborators and myself and published in [204], which includes the full top mass dependence of the virtual two-loop correction to  $gg \rightarrow Zh$  in an analytic form using the same  $p_T$  expansion technique.

#### 4.1.4 Associated production with top quarks

## 4.2 Concluding remarks

The precise determination of the Higgs boson properties is one of the main focus of the Large Hadron Collider (LHC) physics programme. In order to achieve precision-level Higgs measurements both experimental and theoretical uncertainties need to be improved. Though the first can be improved with Higher luminosities and energies, better detectors and improved analysis techniques. Theoretical uncertainties require higher-order calculations, inclusion of mixed EW and QCD terms, inclusion of mass effects and suitable parton distribution functions with Higher order in QCD. As we have seen, a lot of effort is being put into improving the theoretical predictions of Higgs production channels. Moreover, many computer tools have been made available to compute these

cross-sections, for example `iHixs2` [205] or to generate full events, like `POWHEG` [206–212] and `MadGraph5_aMC@NLO` [213], and many others can be found with greater detail in the Higgs cross-sections working group [214].

Sometimes, to improve the measurement of the process, it is not sufficient to only improve the theoretical prediction of the channel itself, but also its backgrounds, which is particularly important for  $t\bar{t}h$ . Hence, higher order calculations of processes like  $t\bar{t}W$  with parton-shower effects as well as improved analysis to distinguish  $t\bar{t}(h \rightarrow b\bar{b})$  have a significant impact on  $t\bar{t}h$  measurements. Event generator tools with SMEFT implementation in Higgs processes with patron showing interface capabilities have been implemented in a `MadGraph5_aMC@NLO` model `SMEFTatNLO` [215] which enabled loop computations with SMEFT operators and consequently fits of the SMEFT Wilson coefficients with Higgs data at NLO as we have seen in [chapter 3](#).

There is plenty of room for future improvements in the reduction of theory uncertainty budget, and providing better theoretical prediction of the Higgs processes in the SM and beyond. From inclusion of patron shower matching , merging and validation to inclusion of two-loop calculations of gluon fusion  $Zh$  and EW NLO effects of  $t\bar{t}h$ , all in preparation to the HL-LHC Higgs precision era !

## 5 Four top operator in Higgs production and decay

In the previous chapters, the SMEFT has been portrayed as a robust and practical parametrisation of NP degrees of freedom for LHC searches, keeping in mind that these degrees of freedom have masses that are higher than the LHC reach. We have seen in chapter 3 the SMEFT parametrisation for dimension-six operators involving the Higgs boson, and discussed some constraints on them. The operator  $\mathcal{O}_\phi$  stands out as one of the weakly constrained SMEFT operators involving the Higgs, this is due to the current low experimental sensitivity on the Higgs self-coupling as shown in ??.

The physics of the top quark and the Higgs are deeply intertwined, and when one starts looking at the operators entering at NLO of Higgs processes, and by restricting oneself to pure Higgs or EW operators, one would miss the full picture in a global fit. Namely, the top quark operators. Though many of the top quark operators are strongly constraint from top observables, a few set of dimension-six operators remain as weakly constraint as the trilinear Higgs self-coupling or more. These operators are four-fermion operators involving the top quark. They would be constrained directly from the production of four tops observation. However, this process has a small cross-section at the LHC of  $12 \text{ fb}$  [216], which is more or less comparable to the Higgs pair production. Experimental searches for the production of four top quarks has been first made by CMS [217] combining different LHC runs, followed by ATLAS [218], the latter reporting a  $4.3\sigma$  observation of this processes with cross-section of  $24^{+7}_{-6} \text{ fb}$ . When the whole third generation quarks is included, one sees the same story with  $t\bar{t}b\bar{b}$  contact interaction which require the observation of  $t\bar{t}b\bar{b}$  production for a direct constraint, see [219, 220] for experimental searches and [221, 222] for SMEFT fits. It should be noted that for the production of four tops, or two tops two beauty quarks in SMEFT, the contact terms do not interfere with the SM process, and only appear proportional to  $\mathcal{O}(1/\Lambda^4)$ . This makes the SMEFT global analysis of these operators depend highly on the EFT truncation scheme used, i.e. whether to keep quadratic terms or not.

These four-fermion operators enter in single Higgs processes at NLO, in a similar manner as the Higgs self-coupling. In this chapter, the exact NLO corrections to the Higgs rates, i.e. production and decay, due to these four-fermion operators have been computed, and it was found to be significantly larger or at the same scale as the corrections from  $C_\phi$ . Since the four-fermions operators are weakly constrained they should be included in fits involving Higgs data. We shall demonstrate that, there is a significant correlation amongst the Higgs self-coupling and the four-fermion operators.

As the direct bounds for  $t\bar{t}t\bar{t}$  and  $t\bar{t}b\bar{b}$  contact interactions are weak, single Higgs data provides competitive bounds of these operators alongside other alternative constraints

like top quark pair production [215] and electroweak precision data [223].

The chapter is structured as follows: in section 5.1 the SMEFT four-fermion operators of the third generation are presented. In ?? the full NLO calculation of Higgs rates due to the four-fermion operators is illustrated. Afterwards, in section 5.3, a fit from Higgs data combining the Higgs trilinear coupling and the four-fermion operators is presented, for both Run-II and HL-LHC, with more collaborate results for the latter is found in ???. The results are further discussed in section 5.4.

## 5.1 Four-fermion operators in SMEFT

Before estimating the corrections of the four-fermion operators to Higgs rates, we start by introducing these operators in SMEFT. We are interested here in four-fermion operators of the third generation, that arise at dimension-six level. Using the same convention as the Higgs SMEFT operators in chapter 3, we recall the relearnt part of the SMEFT Lagrangian [126],

$$\begin{aligned} \Delta\mathcal{L}_{\text{SMEFT}}^{d=6} = & \frac{C_{tt}}{\Lambda^2}(\bar{t}_R\gamma_\mu t_R)(\bar{t}_R\gamma^\mu t_R) + \frac{C_{Qt}^{(1)}}{\Lambda^2}(\bar{Q}_L\gamma_\mu Q_L)(\bar{t}_R\gamma^\mu t_R) + \frac{C_{Qt}^{(8)}}{\Lambda^2}(\bar{Q}_L T^A \gamma_\mu Q_L)(\bar{t}_R T^A \gamma^\mu t_R) \\ & + \frac{C_{QQ}^{(1)}}{\Lambda^2}(\bar{Q}_L\gamma_\mu Q_L)(\bar{Q}_L\gamma^\mu Q_L) + \frac{C_{QQ}^{(3)}}{\Lambda^2}(\bar{Q}_L\sigma_a\gamma_\mu Q_L)(\bar{Q}_L\sigma_a\gamma^\mu Q_L) \quad (5.1) \\ & + \left[ \frac{C_{QtQb}^{(1)}}{\Lambda^2}(\bar{Q}_L t_R)i\sigma_2(\bar{Q}_L^T b_R) + \frac{C_{QtQb}^{(8)}}{\Lambda^2}(\bar{Q}_L T^A t_R)i\sigma_2(\bar{Q}_L^T T^A b_R) + \text{h.c.} \right] \\ & + \frac{C_{bb}}{\Lambda^2}(\bar{b}_R\gamma_\mu b_R)(\bar{b}_R\gamma^\mu b_R) + \frac{C_{tb}^{(1)}}{\Lambda^2}(\bar{t}_R\gamma_\mu t_R)(\bar{b}_R\gamma^\mu b_R) + \frac{C_{tb}^{(8)}}{\Lambda^2}(\bar{t}_R T^A \gamma_\mu t_R)(\bar{b}_R T^A \gamma^\mu b_R) \\ & + \frac{C_{Qb}^{(1)}}{\Lambda^2}(\bar{Q}_L\gamma_\mu Q_L)(\bar{b}_R\gamma^\mu b_R) + \frac{C_{Qb}^{(8)}}{\Lambda^2}(\bar{Q}_L T^A \gamma_\mu Q_L)(\bar{b}_R T^A \gamma^\mu b_R), \end{aligned}$$

here the notation is slightly modified from the standard Warsaw basis one. The flavour indices were suppressed since only the the third generation is considered throughout this chapter. Adopting the same notation from previous chapters,  $Q_L$  denotes the left-handed  $SU(2)_L$  doublet quarks while  $t_R$  and  $b_R$  refer to the right-handed singlets, the rest of the objects in (5.1) follow the same conventions as in chapter 3. In studies involving SMEFT fits, such as [140] the  $SU(3)_C$  singlet and octet left-handed operators  $C_{QQ}^{(1),SU(3)}$ ,  $C_{QQ}^{(8)}$  are used instead of the singlet and triplet of  $SU(2)_L$  appearing in eq. (5.1). These two conventions are related via the relations

$$\begin{aligned} C_{QQ}^{(1),SU(3)} &= 2C_{QQ}^{(1)} - \frac{2}{3}C_{QQ}^{(3)}, \\ C_{QQ}^{(8)} &= 8C_{QQ}^{(3)}. \end{aligned} \quad (5.2)$$

Additionally, all of these Wilson coefficients are assumed to be real.

From here on, only operators that induce sizeable NLO correction to Higgs processes are taken into account. These operators turns out to be the ones that introduce loop corrections to the top or beauty Yukawa, top or beauty masses and finite corrections from top loops. Such corrections will be proportional to the top mass. On the contrary, corrections from beauty loops are highly suppressed by  $m_b$ . Also, operators that have chiral structure that does not enable them to enter in the Yukawa renormalisation group equation (RGE)'s will not be constrained from Higgs data as they would only contribute through small finite terms, as we shall see later. Hence, only four top and the  $\mathcal{O}_{QtQb}^{(1),(8)}$  operators will be considered, as they will possess corrections with top quark loops.

## 5.2 Contribution of four-fermion operators to Higgs rates at NLO

This section will demonstrate the calculation of NLO Higgs production and decay rates from the four-heavy-quarks operators discussed above. For the production of Higgs via gluon fusion or Higgs decay to gluon, photons and beauty quarks, the results were computed fully analytically and presented in this section. However, for the associated production of the Higgs with top pair  $t\bar{t}h$ , the corrections were computed numerically, due to the length of the the analytic expressions if the result.

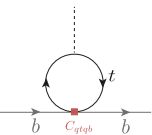
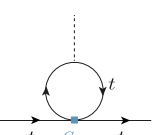
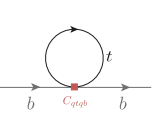
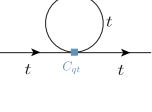
### 5.2.1 Analytic calculations

The NLO corrections to gluon fusion,  $h \rightarrow gg$ ,  $h \rightarrow \gamma\gamma$  and  $h \rightarrow b\bar{b}$  all come from the sub-diagrams listed in [Table 5.1](#), with top loops entering in the mass renormalisation or to/beauty Yukawa vertex correction. Where  $N_c = 3$  the number of colours, and  $c_F = (N_c^2 - 1)/(2N_c) = 4/3$  the  $SU(3)$  quadratic Casimir in the fundamental representation. The effect of beauty loops coming from for  $C_{QtQb}^{(1/8)}$ , can be easily read from this table by exchanging  $t \leftrightarrow b$ , which is significantly smaller than the corrections coming from top loops.

We see that these corrections correspond to the Wilson coefficients appearing in the RGE's [include them in the appendix](#), and operators with (LL)(LL) or (RR(RR)) chiral structures do not contribute to these processes.

By considering the two-loop corrections to the gluon fusion illustrated in [Figure 5.1](#) we find that such correction contain the sub-diagrams shown in [Table 5.1](#), except for diagram (e), which is found to be vanishing for on-shell gluons. Additionally, these diagrams indicated that the two-loop corrections will be reduced to a product of two one-loop functions after the integral reduction.

Following the Feynman rules derived in ref. [224] for the four-fermion operators of interest here, the  $ggtoh$  two-loop amplitude was calculated, then Dirac algebra and further algebraic manipulations were preformed in Mathematica using `PackageX` [225]. Reduction of the resulting two-loop to Master integrals has been preformed using `KIRA` [226], all of the resulting master integrals were indeed products on one-loop functions as expected. The computation has been cross-checked independently, using a different

Diagram	colour factor		mass/coupling
	singlet	octet	
	$2N_c + 1$	$c_F$	$y_t m_b m_t^2$
	1	$c_F$	$y_t m_t^3$
	$2N_c + 1$	$c_F$	$m_t^3$
	1	$c_F$	$m_t^3$

**Table 5.1.** The sub diagrams contributing to the NLO corrections of gluon fusion Higgs production higgsdecay to gluon, photon and beauty quarks.

pipeline : **FeynArts** [227], for amplitude generation then **FeynRules** [228] and **Fire** [229] for algebriac manipulation and loop-integral reduction.

The sub-diagrams appearing in the two-loop calculation, correspond to mass and vertex renormalisation, hence they contain poles that require counter-terms. A mixture of on-shell (OS) and  $\overline{\text{MS}}$  – schemes has been used for the mass and  $hq\bar{q}$  coupling renormalisation, respectively. The renormalisation of SM quantities in the OS and NP ones in the  $\overline{\text{MS}}$  scheme was proposed by [230], which provides consistency since the NP is assumed to be of a Higher scale than the SM.

The top/beauty mass renormalisation can be expressed as

$$m_{t/b}^{\text{OS}} = m_{t/b}^{(0)} - \delta m_{t/b}, \quad (5.3)$$

with the corresponding counter-terms

$$\begin{aligned} \delta m_t &= \frac{1}{16\pi^2} \frac{C_{Qt}^{(1)} + c_F C_{Qt}^{(8)}}{\Lambda^2} m_t^3 \left[ \frac{2}{\bar{\epsilon}} + 2 \log \left( \frac{\mu_R^2}{m_t^2} \right) + 1 \right] \\ &\quad + \frac{1}{16\pi^2} \frac{(2N_c + 1) C_{QtQb}^{(1)} + c_F C_{QtQb}^{(8)}}{\Lambda^2} \left[ \frac{1}{\bar{\epsilon}} + \log \left( \frac{\mu_R^2}{m_b^2} \right) + 1 \right] m_b^3, \end{aligned} \quad (5.4)$$

$$\delta m_b = \frac{1}{16\pi^2} \frac{(2N_c + 1) C_{QtQb}^{(1)} + c_F C_{QtQb}^{(8)}}{\Lambda^2} \left[ \frac{1}{\bar{\epsilon}} + \log \left( \frac{\mu_R^2}{m_t^2} \right) + 1 \right] m_t^3, \quad (5.5)$$

with  $\bar{\epsilon}^{-1} = \epsilon^{-1} - \gamma_E + \log(4\pi)$ , in dimensional regularization with  $d = 4 - 2\epsilon$ . It is possible to convert from OS to the  $\overline{\text{MS}}$  scheme for mass counter-terms via the following relations

$$\delta m_t^{\overline{\text{MS}}} = \frac{1}{8\pi^2} \frac{C_{Qt}^{(1)} + c_F C_{Qt}^{(8)}}{\Lambda^2} m_t^3 \frac{1}{\bar{\epsilon}} + \frac{1}{16\pi^2} \frac{(2N_c + 1) C_{QtQb}^{(1)} + c_F C_{QtQb}^{(8)}}{\Lambda^2} \frac{1}{\bar{\epsilon}} m_b^3, \quad (5.6)$$

$$\delta m_b^{\overline{\text{MS}}} = \frac{1}{16\pi^2} \frac{(2N_c + 1) C_{QtQb}^{(1)} + c_F C_{QtQb}^{(8)}}{\Lambda^2} \frac{1}{\bar{\epsilon}} m_t^3. \quad (5.7)$$

The effect of changing to the mass renormalision scheme is small for the top mass but rather significant, up to 100% for the beauty mass.

The top/beauty Higgs coupling in SMEFT, is written as

$$g_{ht\bar{t}/hb\bar{b}} = \frac{m_{t/b}}{v} - \frac{v^2}{\Lambda^2} \frac{C_{t\phi/b\phi}}{\sqrt{2}}. \quad (5.8)$$

Hence, a modification of the Higgs couplings to bottom and top quarks is generated by operator mixing, even if  $C_{t\phi/b\phi}$  are zero at  $\Lambda$ . From this, the  $\overline{\text{MS}}$  counter-term should

take the form

$$\delta g_{ht\bar{t}/hb\bar{b}} = \frac{m_{t/b}}{v} \delta m_{t/b} - \frac{v^2 \delta C_{t\phi/b\phi}}{\sqrt{2}}, \quad (5.9)$$

where  $\delta C_{t\phi/b\phi}$  is directly read from the anomalous dimension, see App for the explicit expression of the RGE's.

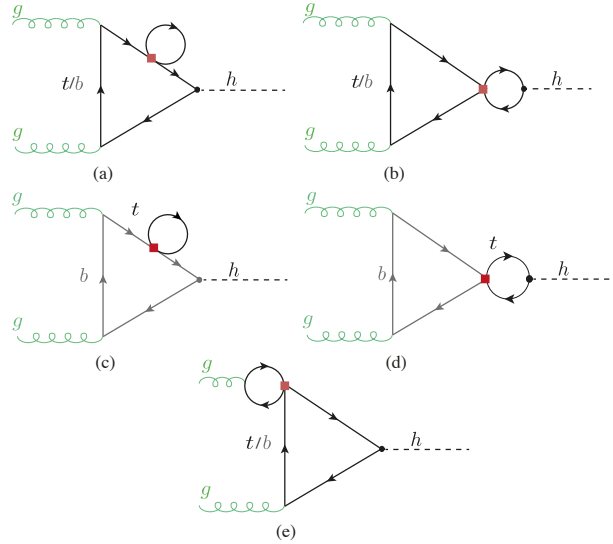


**Figure 5.1.** Example Feynman diagrams for four-fermion-operator contributions to the Higgs production via gluon fusion. The red box indicates the four-fermion operator.

#### Correction to gluon fusion and $h \rightarrow gg$

The modification of the Higgs production via gluon fusion can be written as

$$\frac{\sigma_{ggF}}{\sigma_{ggF}^{\text{SM}}} = 1 + \frac{\sum_{i=t,b} 2\text{Re}(F_{\text{LO}}^i F_{\text{NLO}}^*)}{|F_{\text{LO}}^t + F_{\text{LO}}^b|^2} \quad (5.10)$$

with

$$F_{\text{LO}}^i = -\frac{8m_i^2}{m_h^2} \left[ 1 - \frac{1}{4} \log^2(x_i) \left( 1 - \frac{4m_i^2}{m_h^2} \right) \right] \quad (5.11)$$

and

$$\begin{aligned}
 F_{\text{NLO}} = & \frac{1}{4\pi^2 \Lambda^2} (C_{Qt}^{(1)} + c_F C_{Qt}^{(8)}) F_{\text{LO}}^t \left[ 2m_t^2 + \frac{1}{4}(m_h^2 - 4m_t^2) \left( 3 + 2\sqrt{1 - \frac{4m_t^2}{m_h^2}} \log(x_t) \right) \right. \\
 & \left. + \frac{1}{2}(m_h^2 - 4m_t^2) \log\left(\frac{\mu_R^2}{m_t^2}\right) \right] \\
 & + \frac{1}{32\pi^2 \Lambda^2} ((2N_c + 1) C_{QtQb}^{(1)} + c_F C_{QtQb}^{(8)}) \left[ F_{\text{LO}}^b \frac{m_t}{m_b} \left( 4m_t^2 - 2m_h^2 \right. \right. \\
 & \left. \left. - (m_h^2 - 4m_t^2) \sqrt{1 - \frac{4m_t^2}{m_h^2}} \log(x_t) - (m_h^2 - 4m_t^2) \log\left(\frac{\mu_R^2}{m_t^2}\right) \right) + (t \leftrightarrow b) \right]. \tag{5.12}
 \end{aligned}$$

Only top quark loops contribute to the parts proportional to  $C_{Qt}^{(1),(8)}$ . The variable  $x_i$  for a loop particle with mass  $m_i$  is given by

$$x_i = \frac{-1 + \sqrt{1 - \frac{4m_i^2}{m_h^2}}}{1 + \sqrt{1 - \frac{4m_i^2}{m_h^2}}}. \tag{5.13}$$

Using the same amplitudes, the  $h \rightarrow gg$  partial width modification can be written as

$$\frac{\Gamma_{h \rightarrow gg}}{\Gamma_{h \rightarrow gg}^{\text{SM}}} = 1 + \frac{\sum_{i=t,b} 2\text{Re}(F_{\text{LO}}^i F_{\text{NLO}}^*)}{|F_{\text{LO}}^t + F_{\text{LO}}^b|^2} \tag{5.14}$$

### Correction to Higgs decays to photons

Analogously, since the decay  $h \rightarrow \gamma\gamma$  contains the same topologies as gluon fusion, we could use the result from the above calculation to calculate the correction to the partial width for this decay

$$\frac{\Gamma_{h \rightarrow \gamma\gamma}}{\Gamma_{h \rightarrow \gamma\gamma}^{\text{SM}}} = 1 + \frac{2\text{Re}(F_{\text{LO},\gamma} F_{\text{NLO},\gamma}^*)}{|F_{\text{LO},\gamma}|^2}. \tag{5.15}$$

However, one should pay attention to the change in the prefactors, and the extra EW contributions for  $h \rightarrow \gamma\gamma$

$$F_{\text{LO},\gamma} = N_C Q_t^2 F_{\text{LO}}^t + N_C Q_b^2 F_{\text{LO}}^b + F_{\text{LO}}^W + F_{\text{LO}}^G, \tag{5.16}$$

and  $F_{\text{NLO},\gamma}$  is obtained from  $F_{\text{NLO}}$  by replacing the LO form factor that appears inside of it by  $F_{\text{LO}}^i \rightarrow N_c Q_i^2 F_{\text{LO}}^i$ , with the charges  $Q_t = 2/3$  and  $Q_b = -1/3$ . The

$W$  boson contribution

$$F_{\text{LO}}^W = 2 \left( 1 + 6 \frac{m_W^2}{m_h^2} \right) - 6 \frac{m_W^2}{m_h^2} \left( 1 - 2 \frac{m_W^2}{m_h^2} \right) \log^2(x_W), \quad (5.17)$$

with  $m_W$  the  $W$  mass, and the Goldstone contribution

$$F_{\text{LO}}^G = 4 \frac{m_W^2}{m_h^2} \left( 1 + \frac{m_W^2}{m_h^2} \log^2(x_W) \right). \quad (5.18)$$

Four-fermion operators also affect the  $h \rightarrow Z\gamma$  partial width. However, as in the diphoton case, the effect is expected to be small due to the dominance of the  $W$  boson loop. Because of this, and given the smallness of the  $h \rightarrow Z\gamma$  branching ratio and the relatively low precision expected in this channel at the LHC, the effects of four-fermion interactions in this decay are neglected.

#### Correction to Higgs decays to $b\bar{b}$

The dominant four-fermion contributions to decay channel  $h \rightarrow b\bar{b}$  come from the operators with Wilson coefficients  $C_{QtQb}^{(1),(8)}$ . The corresponding diagram at NLO is shown in fig 5.2. Adopting the same renormalisation procedure as outlined in the previous subsection, we obtain the following expression for the correction to the  $h \rightarrow b\bar{b}$  decay rate in the presence of  $\mathcal{O}_{QtQb}^{(1),(8)}$ ,

$$\begin{aligned} \frac{\Gamma_{h \rightarrow b\bar{b}}}{\Gamma_{h \rightarrow b\bar{b}}^{\text{SM}}} = & 1 + \frac{1}{16\pi^2} \frac{m_t}{m_b} (m_h^2 - 4m_t^2) \frac{(2N_c + 1)C_{QtQb}^{(1)} + c_F C_{QtQb}^{(8)}}{\Lambda^2} \\ & \times \left[ 2 + \sqrt{1 - \frac{4m_t^2}{m_h^2} \log(x_t)} - \log\left(\frac{m_t^2}{\mu_R^2}\right) \right], \end{aligned} \quad (5.19)$$

which carries an enhancement factor of  $m_t/m_b$  and is hence expected to be rather large.

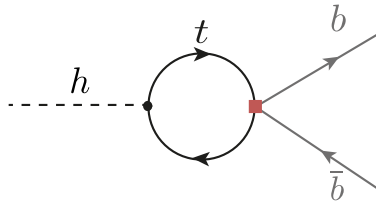


Figure 5.2. Feynman diagram contributing to the NLO  $h \rightarrow b\bar{b}$  process.

The results of the NLO effects from the four-fermion operators reported above, do not take into account the running of the Wilson coefficients. This would be based on the assumption that these coefficients are defined at the process scale. Nevertheless,

when we want to compare different process or assume that the four-fermion operators are defined at the UV scale, i.e.  $\Lambda$ , for example after matching with some UV model. One has take into account the running of these Wilson coefficients from  $\Lambda$  down to the process scale Those running effects can be included via the renormalisation group equation (RGE) for the operators with Wilson coefficient  $C_{t\phi}$  and  $C_{b\phi}$  [231, 232], that lead approximatively to

$$C_{t\phi}(\mu_R) - C_{t\phi}(\Lambda) = \frac{1}{16\pi^2 v^2} \left[ -2y_t(m_h^2 - 4m_t^2)(C_{Qt}^{(1)} + c_F C_{Qt}^{(8)}) \log\left(\frac{\mu_R^2}{\Lambda^2}\right) + \frac{y_b}{2}(m_h^2 - 4m_b^2) \left( (2N_c + 1)C_{QtQb}^{(1)} + c_F C_{QtQb}^{(8)} \right) \log\left(\frac{\mu_R^2}{\Lambda^2}\right) \right] \quad (5.20)$$

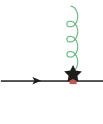
and

$$C_{b\phi}(\mu_R) - C_{b\phi}(\Lambda) = \frac{y_t}{32\pi^2 v^2} \left[ (m_h^2 - 4m_t^2) \left( (2N_c + 1)C_{QtQb}^{(1)} + c_F C_{QtQb}^{(8)} \right) \log\left(\frac{\mu_R^2}{\Lambda^2}\right) \right], \quad (5.21)$$

where  $y_{t/b} = \sqrt{2}m_{t/b}/v$ . Note that the combinations of Wilson coefficients appearing in (5.20)(5.21) are the same as in  $F_{NLO}$  in (5.12). Effectively, we can then obtain the result under the assumption that the four-fermion operators are the only non-zero ones at the high scale by replacing in (5.12)  $\mu_R \rightarrow \Lambda$ , noting that we have renormalised the top and beauty quark masses in the OS scheme. Including the leading logarithmic running of  $C_{b\phi}$  of (5.21) from the high scale  $\Lambda$  to the electroweak scale is achieved by setting in (5.19)  $\mu_R \rightarrow \Lambda$ . The expression in (5.19) agrees with results obtained from the full calculation of the NLO effects in the dimension-six SMEFT, first computed in [233].

### 5.2.2 NLO corrections to $t\bar{t}h$

Unlike the previous processes, the associated production of the Higgs with top quark pair involves new topologies not limited to Yukawa vertex or mass renormalisation. At the LHC, there are two sub-processes responsible for the  $t\bar{t}h$  production: gluon-initiated process illustrated in Figure 5.3 and quark-initiated one, see in Figure 5.4. We see the new *finite* topologies induced by the four-fermion operator corrections in (d) triangle and (e) box topologies in Figure 5.3 and (b) triangle topology in Figure 5.4. Additionally, the  $t\bar{t}g$  vertex correction in the quark-initiated process (diagram (c)) of Figure 5.4 is non-vanishing as the gluon is off-shell. This vertex correction has a UV pole that requires a counter-term for its cancellation



$$= \frac{ig_s}{12\pi^2 \Lambda^2} T_{ij}^A p_g^2 \gamma^\mu \left( C_{tt} P_R + \left( C_{QQ}^{(1)} + C_{QQ}^{(3)} \right) P_L + \frac{C_{Qt}^{(8)}}{4} \right) \left( \frac{1}{\epsilon} - 1 \right). \quad (5.22)$$

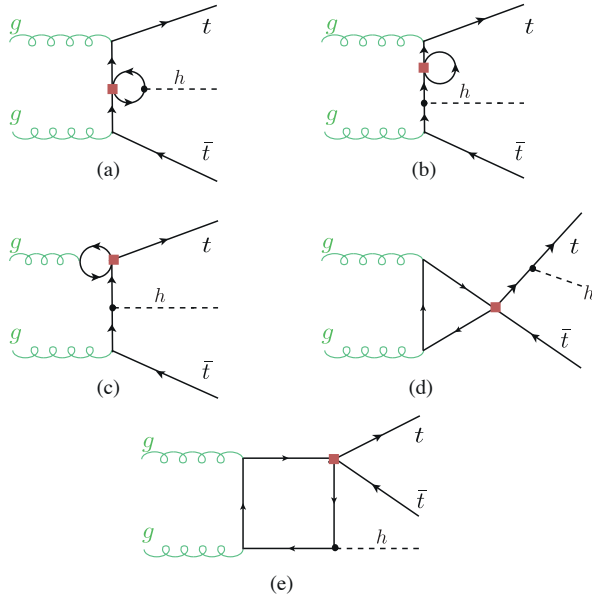


**Figure 5.3.** Feynman diagrams including the four-fermion loop contributions to the  $gg \rightarrow t\bar{t}h$  subprocess.

Another difference between  $t\bar{t}h$  and the rest of the processes considered, is that this process has multiple colour projectors, as the quark anti quark triplets or the gluon pairs do not have to recombine to only a singlet state rather to both a singlet and an octet, according to the expansion of product  $\mathbf{3} \otimes \overline{\mathbf{3}} \rightarrow \mathbf{1} + \mathbf{8}$ . This breaks the degeneracy between the singlet and octet Wilson coefficients. Lastly, due to the new topologies and  $t\bar{t}g$  vertex correction, operators with single chirality will contribute to NLO corrections, namely  $C_{ttt}$  and  $C_{QQ}^{(1,3)}$ .

All of the four-fermion operators are implemented in the loop-capable UFO model **SMEFTatNLO** model [215] and their contribution to NLO corrections of  $t\bar{t}h$  can hence be computed via **Madgraph\_aMCNLO** [213] (version 3.1.0) with some tweaking to remove the NLO QCD corrections. This is done via a use-defined loop filter function in Madgraph. The results were reproduced by an analytic computation based on the reduction of one-loop amplitudes via the method developed by G. Ossola, C.G. Papadopoulos and R. Pittau (OPP reduction) [234]. The OPP reduction was done using the **CutTools** programme [235]. This programme takes the full one-loop amplitude and then reduces it to terms with 1,2,3 and 4-point loop functions in four dimensions, keeping spurious terms from the  $\epsilon$  part of the amplitude. To correct for such terms, one needs to compute the divergent UV counter-term as well as a finite rational terms, denoted  $R_2$  as in Ref. [236].<sup>1</sup> The amplitudes were generated in the same way as for gluon fusion. The UV and  $R_2$  counter-terms, that need to be supplemented to **CutTools**, were computed manually fol-

<sup>1</sup>Another rational term  $R_1$  appears due to the mismatch between the four and  $d$  dimensional amplitudes, but this is computed automatically in **CutTools**.

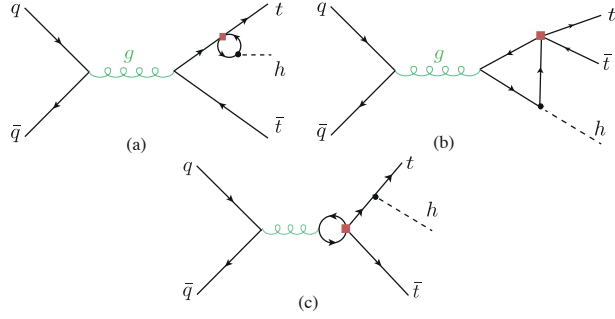


**Figure 5.4.** Feynman diagrams including the four-fermion loop contributions to the  $q\bar{q} \rightarrow t\bar{t}h$  subprocess.

lowing the method detailed in [236]. For both codes, the NNPDF23 parton distribution functions set at NLO [237] was used.

The singlet and octet operators  $\mathcal{O}_{Q_t Q_b}^{(1),(8)}$  contribute to  $t\bar{t}h$  only via beauty loops and in principle, could be directly dismissed like the other beauty quark operators mentioned above. However, it is instructive to investigate their effect albeit it is expected to be small. Since the **SMEFTatNLO** model does not have these operators, it was needed to implement them manually in that model. This is simply done by include the vertices generated by these operators as well as their UV and  $R_2$  counter-terms, only relevant for  $t\bar{t}h$  calculation. The calculation of the NLO correction by these operators was done both in Madgraph using a modified UFO model and with the code based on **CutTools**. The effects were comparable to the leading log effects computed using **SMEFTsim** package [238] of  $\sim 10^{-6}$ . Hence confirming the expectation that beauty quark loops have a negligible effect.

In order to take the effect of Wilson coefficients' running, the relevant contribution for the gluon-initiated process as the same as the stated for the gluon fusion in (5.20). While for the quark-initiated process, one needs to consider the operator mixing in the running, particularly between operators that contain second and third generation quarks mixed together. These corrections can be obtained from the RGEs in refs. [129, 231, 232].

### 5.2.3 Results

The NLO correction from the four-fermion operators of the third generation quarks on the Higgs rates i.e., partial width  $\Gamma$  or cross-section  $\sigma$ , is extracted from the above computation using the formula

$$\delta R(C_i) = R/R^{\text{SM}} - 1, \quad (5.23)$$

here effect from the operator with Wilson coefficient  $C_i$  on the Higgs rate  $R$  is denoted by  $\delta R(C_i)$ . Only contributions linear in the Wilson coefficients are considered. In order to isolate the finite terms from the ones coming from the RGE leading log approximation, the correction is further expanded to finite  $\delta R_{C_i}^{\text{fin}}$  and leading log terms  $\delta R_{C_i}^{\text{log}}$  as follows

$$\delta R(C_i) = \frac{C_i}{\Lambda^2} \left( \delta R_{C_i}^{fin} + \delta R_{C_i}^{log} \log \left( \frac{\mu_R^2}{\Lambda^2} \right) \right). \quad (5.24)$$

Using this formula, one can obtain the correction at any NP scale  $\Lambda$ , though in the remainder of this chapter this scale is set to 1 TeV. In Table 5.2, the finite and logarithmic corrections for the operators considered in this study is reported. Using this table in filling the formula (5.24) will give the correction to Higgs rates. However, since some of the rates are Higgs partial widths, the Higgs total width  $\Gamma_h$  will be affected and therefore all of Higgs rates are changed. An important observation from Table 5.2 is that the finite terms, are either larger or at the same order than the leading log ones, except for  $h \rightarrow b\bar{b}$  corrections from  $C_{QtQb}^{(1),(8)}$ . This highlights the importance of the full NLO calculation for these corrections in constraining these four-fermion operators, in particular  $\mathcal{O}_{Qt}^{(1),(8)}$ .

As mentioned earlier, there is a degeneracy amongst the singlet and octet operators, seen clearly in the analytic result for gluon fusion and Higgs decays considered. This degeneracy is though broken for  $\mathcal{O}_{Qt}^{(1),(8)}$  due to  $t\bar{t}h$ . Since, the effect of  $\mathcal{O}_{QtQb}^{(1),(8)}$  is negligible for this process, the true degree of freedom for these operators' Wilson coefficients is the linear combination

$$C_{QtQb}^+ = (2N_c + 1)C_{QtQb}^{(1)} + c_F C_{QtQb}^{(8)}. \quad (5.25)$$

### 5.3 Fit to Higgs observables

Using the results from the previous NLO calculations, and combining them with the calculations of NLO Higgs rates from the trilinear Higgs self-coupling  $\lambda_3$ , preformed in ref. [113–116, 118] we could expand on the previous fits for  $\lambda_3$  from Higgs data, to include four-fermion SMEFT Wilson coefficients as well. In order to examine the true sensitivity of single Higgs observables to  $\lambda_3$ . Although combined fits from Higgs data including  $\lambda_3$  and SMEFT operators modifying Higgs rates at LO has been preformed [146]. Such fits would not be sufficient in determine the actual sensitivity for  $\lambda_3$ , in particular when the SMEFT operators are weakly constraint and possess significant modifications to Higgs rates as we have seen in Table 5.2. This chapter does not include a global SMEFT fit, but merely motivates it by illustrating how the sensitivity for probing the Higgs-self coupling from single Higgs data gets diluted when the four-fermion operators are included, and how these two are correlated.

In the previous references, the modification to Higgs self coupling was reported in terms of the  $\kappa$ -formalism, for the consistency of this analysis, the NLO corrections from the trilinear self-coupling will be converted from this formalism to the SMEFT notation, in terms of the Wilson coefficient  $C_\phi$ . For more details on the conversion between SMEFT and  $\kappa$ -formalism see [app here or something](#). In order to keep track of power counting (in terms of  $\Lambda$ ) in SMEFT, we expand the results of [114] after converting it to SMEFT ,

Operator	Process	$\mu_R$	$\delta R_{C_i}^{fin}$ [TeV $^2$ ]	$\delta R_{C_i}^{log}$ [TeV $^2$ ]
$\mathcal{O}_{Qt}^{(1)}$	ggF	$\frac{m_h}{2}$	$9.91 \cdot 10^{-3}$	$2.76 \cdot 10^{-3}$
	$h \rightarrow gg$	$m_h$	$6.08 \cdot 10^{-3}$	$2.76 \cdot 10^{-3}$
	$h \rightarrow \gamma\gamma$		$-1.76 \cdot 10^{-3}$	$-0.80 \cdot 10^{-3}$
	$t\bar{t}h$ 13 TeV	$m_t + \frac{m_h}{2}$	$-4.20 \cdot 10^{-1}$	$-2.78 \cdot 10^{-3}$
	$t\bar{t}h$ 14 TeV		$-4.30 \cdot 10^{-1}$	$-2.78 \cdot 10^{-3}$
$\mathcal{O}_{Qt}^{(8)}$	$\Gamma_h$	$\frac{m_h}{2}$	$4.93 \cdot 10^{-4}$	$1.68 \cdot 10^{-4}$
	ggF	$\frac{m_h}{2}$	$1.32 \cdot 10^{-2}$	$3.68 \cdot 10^{-3}$
	$h \rightarrow gg$	$m_h$	$8.11 \cdot 10^{-3}$	$3.68 \cdot 10^{-3}$
	$h \rightarrow \gamma\gamma$		$-2.09 \cdot 10^{-3}$	$-1.07 \cdot 10^{-3}$
	$t\bar{t}h$ 13 TeV	$m_t + \frac{m_h}{2}$	$6.53 \cdot 10^{-2}$	$-2.40 \cdot 10^{-3}$
$\mathcal{O}_{QtQb}^{(1)}$	$t\bar{t}h$ 14 TeV		$7.29 \cdot 10^{-2}$	$2.40 \cdot 10^{-3}$
	$\Gamma_h$	$\frac{m_h}{2}$	$6.58 \cdot 10^{-4}$	$2.24 \cdot 10^{-4}$
	ggF	$\frac{m_h}{2}$	$2.84 \cdot 10^{-2}$	$9.21 \cdot 10^{-3}$
	$h \rightarrow gg$	$m_h$	$1.57 \cdot 10^{-2}$	$9.21 \cdot 10^{-3}$
	$h \rightarrow \gamma\gamma$		$-1.30 \cdot 10^{-3}$	$-0.78 \cdot 10^{-3}$
$\mathcal{O}_{QtQb}^{(8)}$	$h \rightarrow b\bar{b}$		$9.25 \cdot 10^{-2}$	$1.68 \cdot 10^{-1}$
	$\Gamma_h$	$\frac{m_h}{2}$	$5.49 \cdot 10^{-2}$	$7.37 \cdot 10^{-2}$
	ggF	$\frac{m_h}{2}$	$5.41 \cdot 10^{-3}$	$1.76 \cdot 10^{-3}$
	$h \rightarrow gg$	$m_h$	$2.98 \cdot 10^{-3}$	$1.76 \cdot 10^{-3}$
	$h \rightarrow \gamma\gamma$		$-0.25 \cdot 10^{-3}$	$-0.15 \cdot 10^{-3}$
$\mathcal{O}_{QQ}^{(1)}$	$h \rightarrow b\bar{b}$		$1.76 \cdot 10^{-2}$	$3.20 \cdot 10^{-2}$
	$\Gamma_h$	$\frac{m_h}{2}$	$1.05 \cdot 10^{-2}$	$1.41 \cdot 10^{-2}$
$\mathcal{O}_{QQ}^{(3)}$	$t\bar{t}h$ 13 TeV		$1.75 \cdot 10^{-3}$	$1.90 \cdot 10^{-3}$
	$t\bar{t}h$ 14 TeV	$m_t + \frac{m_h}{2}$	$2.35 \cdot 10^{-3}$	$1.90 \cdot 10^{-3}$
$\mathcal{O}_{tt}$	$t\bar{t}h$ 13 TeV		$1.32 \cdot 10^{-2}$	$5.50 \cdot 10^{-3}$
	$t\bar{t}h$ 14 TeV	$m_t + \frac{m_h}{2}$	$1.42 \cdot 10^{-2}$	$5.50 \cdot 10^{-3}$
$\mathcal{O}_{tt}$	$t\bar{t}h$ 13 TeV		$4.60 \cdot 10^{-3}$	$2.01 \cdot 10^{-3}$
	$t\bar{t}h$ 14 TeV	$m_t + \frac{m_h}{2}$	$5.09 \cdot 10^{-3}$	$2.01 \cdot 10^{-3}$

**Table 5.2.** The NLO corrections from the four heavy-quark SMEFT operators of this study to single Higgs rates. We have separated the contributions into the finite piece  $\delta R_{C_i}^{fin}$  and the leading log running of the Wilson coefficients  $\delta R_{C_i}^{log}$ , see (5.24).

to get

$$\delta R_{\lambda_3} \equiv \frac{R_{\text{NLO}}(\lambda_3) - R_{\text{NLO}}(\lambda_3^{\text{SM}})}{R_{\text{LO}}} = -2 \frac{C_\phi v^4}{\Lambda^2 m_h^2} C_1 + \left( -4 \frac{C_\phi v^4}{\Lambda^2 m_h^2} + 4 \frac{C_\phi^2 v^8}{m_h^4 \Lambda^4} \right) C_2. \quad (5.26)$$

In (5.26), the coefficient  $C_1$  corresponds to the contribution of the trilinear coupling to the single Higgs processes at one loop, adopting the same notation as [114]. The values of  $C_1$  for the different processes of interest for this paper are given in ???. The coefficient

$C_2$  describes universal corrections and is given by

$$C_2 = \frac{\delta Z_h}{1 - \left(1 - \frac{2C_\phi v^4}{\Lambda^2 m_h^2}\right)^2 \delta Z_h}, \quad (5.27)$$

where the constant  $\delta Z_h$  is the SM contribution from the Higgs loops to the wave function renormalisation of the Higgs boson,

$$\delta Z_h = -\frac{9}{16} \frac{G_F m_h^2}{\sqrt{2}\pi^2} \left( \frac{2\pi}{3\sqrt{3}} - 1 \right). \quad (5.28)$$

The coefficient  $C_2$  thus introduces additional  $\mathcal{O}(1/\Lambda^4)$  (and higher order) terms in  $\delta R_{\lambda_3}$ . In ref. [114] considering the  $\kappa$  formalism the full expression of (5.27) is kept, while we define two different descriptions: one in which we expand  $\delta R_{\lambda_3}$  up to linear order and an alternative scheme in which we keep also terms up to  $\mathcal{O}(1/\Lambda^4)$  in the EFT expansion. Keeping the full expression in (5.27) and including terms up to  $\mathcal{O}(1/\Lambda^4)$  in  $C_2$  lead to nearly the same results as the simple  $\mathcal{O}(1/\Lambda^4)$  fit.

Process	$C_1$	$\delta R_{C_\phi}^{fin}$
ggF/ $gg \rightarrow h$	$6.60 \cdot 10^{-3}$	$-3.10 \cdot 10^{-3}$
$t\bar{t}h$ 13 TeV	$3.51 \cdot 10^{-2}$	$-1.64 \cdot 10^{-2}$
$t\bar{t}h$ 14 TeV	$3.47 \cdot 10^{-2}$	$-1.62 \cdot 10^{-2}$
$h \rightarrow \gamma\gamma$	$4.90 \cdot 10^{-3}$	$-2.30 \cdot 10^{-3}$
$h \rightarrow b\bar{b}$	0.00	0.00
$h \rightarrow W^+W^-$	$7.30 \cdot 10^{-3}$	$-3.40 \cdot 10^{-3}$
$h \rightarrow ZZ$	$8.30 \cdot 10^{-3}$	$-3.90 \cdot 10^{-3}$
$pp \rightarrow Zh$ 13 TeV	$1.19 \cdot 10^{-2}$	$-5.60 \cdot 10^{-3}$
$pp \rightarrow Zh$ 14 TeV	$1.18 \cdot 10^{-2}$	$-5.50 \cdot 10^{-3}$
$pp \rightarrow W^\pm h$	$1.03 \cdot 10^{-2}$	$-4.80 \cdot 10^{-3}$
VBF	$6.50 \cdot 10^{-3}$	$-3.00 \cdot 10^{-3}$
$h \rightarrow 4\ell$	$8.20 \cdot 10^{-3}$	$-3.80 \cdot 10^{-3}$

**Table 5.3.** The relative correction dependence on  $C_\phi$  for single Higgs processes taken from [118]. If the  $\sqrt{s}$  is not indicated, the  $C_1$  coefficient (see eq. (5.26)) is the same for both 13 and 14 TeV.

A Bayesian fit was preformed using Markov-chain Monte Carlo (MCMC) method. Using a flat prior  $s \pi(C_i) = const.$  and a log likelihood of a Gaussian distribution

$$\log(L) = -\frac{1}{2} \left[ (\vec{\mu}_{\text{Exp}} - \vec{\mu})^T \cdot \mathbf{V}^{-1} \cdot (\vec{\mu}_{\text{Exp}} - \vec{\mu}) \right]. \quad (5.29)$$

Constructed as follows:

**Experimental input**  $\vec{\mu}_{\text{Exp}}$  The signal strength from experimental measurements of single

Higgs rates defined as

$$\mu_{\text{Exp}} \equiv \sigma_{\text{Obs}} / \sigma_{\text{SM}}. \quad (5.30)$$

These measurements as taken from LHC Run II for centre-of-mass energy of  $\sqrt{s} = 13$  TeV and integrated luminosity of  $139 \text{ fb}^{-1}$  for ATLAS and  $137 \text{ fb}^{-1}$  for CMS. In addition to HL-LHC projections by CMS for  $\sqrt{s} = 14$  TeV and integrated luminosity of  $3000 \text{ fb}^{-1}$ . Both of these input types have been already discussed in [link here](#) and summarised in [Table 2.1](#).

**Theoretical prediction  $\vec{\mu}$**  The corresponding theoretical predictions for each of the experimental measurement /projection have been built using the modification to the cross-sections and branching ratios coming from the SMEFT four-fermion operators and  $C_\phi$ . To keep with the power-counting, the signal strength is also expanded in powers of  $\Lambda$ , keeping only  $\Lambda^{-2}$  terms.

$$\mu(C_\phi, C_i) = \frac{\sigma_{\text{Prod}}(C_\phi, C_i) \times \text{BR}(C_\phi, C_i)}{\sigma_{\text{Prod,SM}} \times \text{BR}_{\text{SM}}} \approx 1 + \delta\sigma(C_\phi, C_i) + \delta\Gamma(C_\phi, C_i) - \delta\Gamma_h(C_\phi, C_i). \quad (5.31)$$

**Uncertainties and correlations  $\mathbf{V}$**  The correlation matrix  $\mathbf{V}$  is build from thee experimental uncertainties found in [Table 2.1](#). For Run-II data, only ATLAS collaboration reported the correlation amongst different channels, and only correlations  $> 10\%$  are considered. While for the HL-LHC, the whole correlation matrix found on the webpage [239]. The HL-LHC projections for the S2 scenario explained in [191] were used. These assume the improvement on the systematics that is expected to be attained by the end of the HL-LHC physics programme, and that theory uncertainties are improved by a factor of two with respect to current values. Theoretical uncertainties were not considered in this fit

The python package `pymc3` [240] was used to construct the posterior distribution. We use the `Arviz` Bayesian analysis package [241] to extract the credible intervals (CIs) from the highest density posterior intervals (HDPI) of the posterior distributions, where the intervals covering 95% (68%) of the posterior distribution are considered the 95% (68%) CIs. In the Gaussian limit, these 95% (68%) CIs should be interpreted as equivalent to the 95% (68%) Frequentist Confidence Level (CL) two-sided bounds. `HEPfit` [242] code was used to validate the fits. Given that current bounds on these operators are rather weak, one may wonder about the uncertainty in our fits associated to the truncation of the EFT. Note that, since the four-quark operators only enter into the virtual corrections at NLO, Higgs production and decay contain only linear terms in  $1/\Lambda^2$  in the corresponding Wilson coefficients, i.e. the quadratic terms coming from squaring the amplitudes are technically of next-to-NLO. Hence, the quadratic effects in the signal strengths come from not linearising the corrections to the product  $\sigma_{\text{Prod}} \times \text{BR}$ . These effects have been investigated, and found to have a negligible effect on the fit. The operators of single chirality  $\mathcal{O}_{tt}^{(1)/(3)}$  and  $\mathcal{O}_{QQ}^{(1)/(3)}$  were not included in the fit, as their effect on Higgs rates is limited to small  $\delta R$  for  $t\bar{t}h$ . Thus, they cannot be contained simultaneously with  $C_\phi$  using single Higgs data.

### 5.3.1 Fit results

In Figure 5.5 and Figure 5.6 the 68% and 95% highest posterior density contours of the two-parameter posterior distributions and their marginalisation for the two-parameter fits involving  $C_\phi$  and one of the four-heavy quark Wilson coefficients, evaluated at the scale  $\Lambda = 1$  TeV for Run-II LHC measurements . Both linearised and quadratically truncated  $\delta R_{\lambda_3}$  fits are shown, and we observe that the 95% CI bounds (shown on top of the panels) and correlations depends on the truncation.

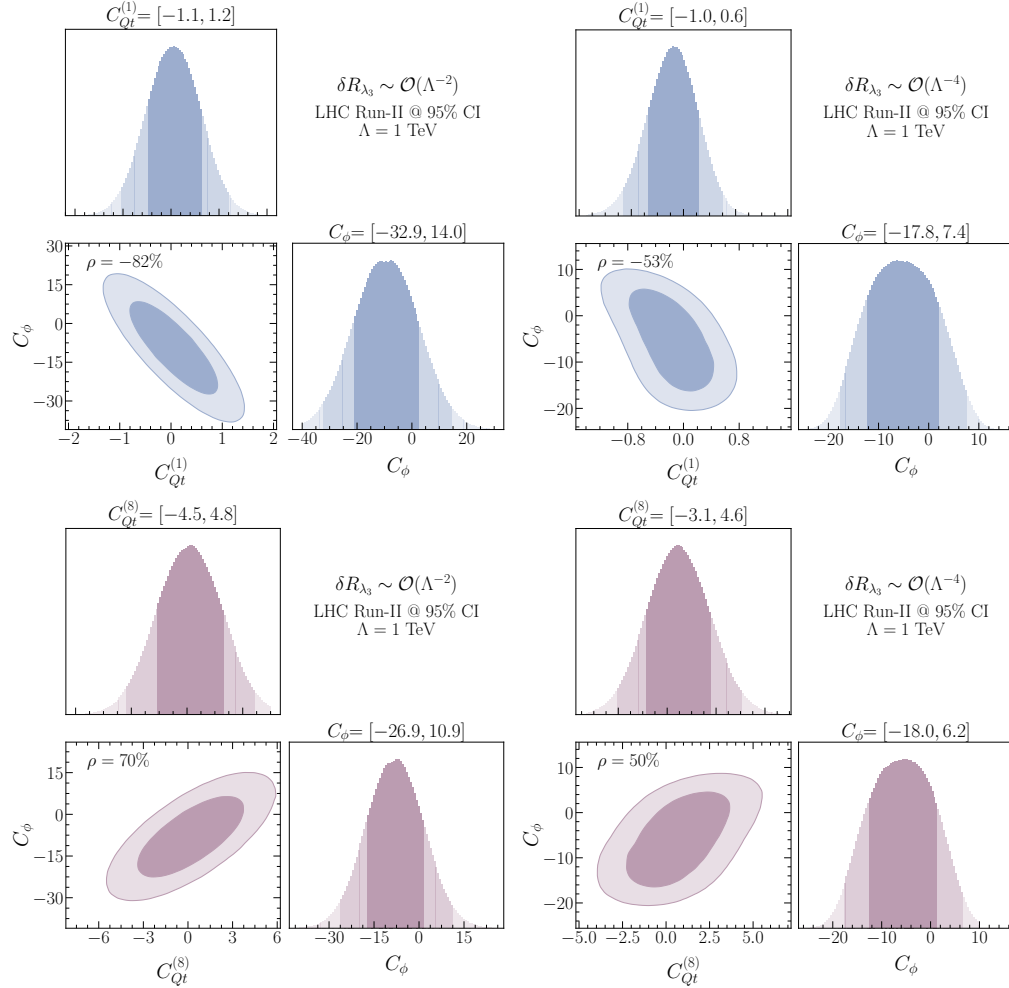


**Figure 5.5.** The 68% and 95% highest density posterior contours of the posterior distribution of  $C_\phi$  with  $C_{Qt}^{(1)}$  (up) and  $C_\phi$  with  $C_{Qt}^{(8)}$  (down) with the marginalised one-dimensional posteriors for each of the Wilson coefficients and their 68% and 95% HDPIs (shown above in numbers the 95% CI bounds). The limits correspond to values of the Wilson coefficients evaluated at the scale  $\Lambda = 1$  TeV. On the left we used the linear scheme in  $\delta R_{\lambda_3}$  while on the right we keep up to quadratic terms in  $\delta R_{\lambda_3}$ .

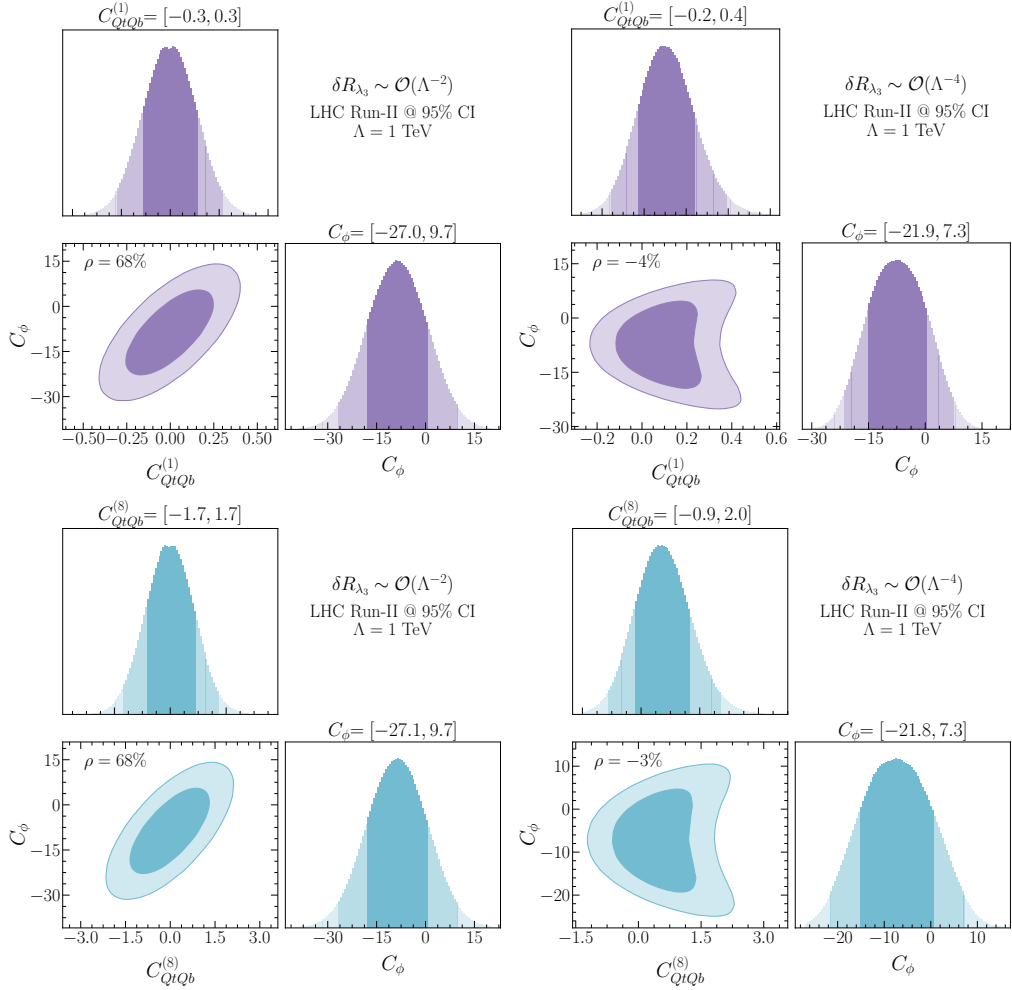


**Figure 5.6.** The 68% and 95% highest density posterior contours of the posterior distribution of  $C_\phi$  with  $C_{QtQb}^{(1)}$  (up) and  $C_\phi$  with  $C_{QtQb}^{(8)}$  (down) with the marginalised one-dimensional posteriors for each of the Wilson coefficients. and their 68% and 95% HDPIs (shown above in numbers the 95% CI bounds). The limits correspond to values of the Wilson coefficients evaluated at the scale  $\Lambda = 1$  TeV. Similar to  $C_{Qt}^{(1),(8)}$ , the left plot shows the linearised  $\delta R_{\lambda_3}$  while the right one shows the quadratic scheme in the trilinear Higgs self-coupling modification. Due to the degeneracy between these Wilson coefficients the posterior contours and their marginalised intervals look very similar for both of them (except for the range they cover).

We observe that the four-fermion operators are strongly correlated with Higgs self-coupling modifier  $\mathcal{O}_\phi$ , in the linear fit. With Pearson's correlation of  $\gtrsim 0.7$  with  $p$ -value  $< 10^{-4}$ . In the case of quadratic  $\delta R_{\lambda_3}$  fit, we observe diminished Pearson correlation, but in this scenario Pearson's correlation test is not particularly applicable, as we have non-linear relation between the variables.

The two-parameter fit results for three four-fermion Wilson coefficients are mesmerised

in the forest plots in Figure 5.7 marginalising the posteriors distributions over  $C_\phi$ . The finite effects were isolated by performing fits with  $\delta R^{fin}$  only. The finite effects are small for  $O_{QtQb}^{(1)/(8)}$  but dominant for the four-top operators  $O_{Qt}^{(1)/(8)}$  mainly coming from  $t\bar{t}h$ . The effect of EFT truncations of  $\delta R_{\lambda_3}$  can also be observed as shifts in the mean value for the Wilson coefficients, but the 95% CI's themselves are not significantly affected. In these plots, the fits results from this study are also confronted with the limits obtained from fits to top data [140, 143, 221, 222, 243, 244]. Showing that when the Wilson coefficient running is taken into an account, the 95% CI bounds obtained from Higgs data are consistently stronger than the ones from top data.

In Figure 5.8 the fit results for  $C_\phi$  after marginalising over the four-fermion Wilson coefficients in both EFT truncations schemes of  $\delta R_{\lambda_3}$ . In addition to a single parameter fit for  $C_\phi$ . Additionally the current 95 % CL bound on  $C_\phi$  extracted from Higgs pair production search using the final state  $b\bar{b}\gamma\gamma$  performed by ATLAS using Run-II data [245], translated from  $\kappa$  formalism.

The mean values and the 95%CI's change depending on the four-fermion Wilson coefficient that was paired with  $C_\phi$  in the two.-parameter fit. As expected, the single parameter fits for  $C_\phi$  yield stronger bound on  $C_\phi$  than the two-parameter fits, thus the inclusion of the four-fermion operators in single Higgs data dilutes  $C_\phi$  bounds . Additionally, the truncation order of  $\delta R_{\lambda_3}$  appears to have a significant effect on the length of the CI's, with quadratic fits giving more stringent constraint on  $C_\phi$ . Instead, for Higgs pair production it makes only a negligible effect if linear or up to quadratic terms in the EFT expansion are kept for the  $C_\phi > 0$  bound, while the bound weakens at linear order in  $1/\Lambda^2$  for  $C_\phi < 0$  [246]. For instance, the quadratic single parameter fit for  $C_\phi$  is comparable to the direct bound from Higgs pair production. However, this changes dramatically, when one includes the four-fermion operators in a combined fit, and the single Higgs data constraints on  $C_\phi$  become less significant compared to the direct  $hh$  bounds.

It should be noted that the strongest bound on the Higgs self-coupling currently comes from the perturbative unitarity bound of ref. [52], as discussed in chapter.

One of the important aspects of multivariate studies is the correlation among variables. Apart from the two-parameter fits discussed above, here we also consider a four-parameter fit to  $C_\phi$  plus the three directions in the four heavy-quark operator parameter space that the Higgs rates are mostly sensitive too, i.e. neglecting  $C_{QQ}^{(1),(3)}$  and  $C_{tt}$ , and trading  $C_{QtQb}^{(1)}$  and  $C_{QtQb}^{(8)}$  by  $C_{QtQb}^+$ . When considering two- or four-parameter fits of  $C_\phi$  and the four-heavy-quark Wilson coefficients, we observe a non-trivial correlation patterns amongst these coefficients. Figure 5.9 illustrates these correlation patterns clearly for the four-parameter fit. We observe that the Wilson coefficients  $C_{Qt}^{(1),(8)}$  are strongly correlated because, in analogy to  $C_{QtQb}^{(1),(8)}$ , they only appear in certain linear combination whenever correcting the Yukawa coupling. However, unlike  $C_{QtQb}^{(1),(8)}$  they are not completely degenerate because the main part of the NLO correction to  $t\bar{t}h$  does not contain the aforementioned linear combination. The four-parameter fit also reveals that the Wilson coefficients  $C_{Qt}^{(1),(8)}$  have a large correlation with  $C_{QtQb}^+$  because all of the

### 5.3 Fit to Higgs observables

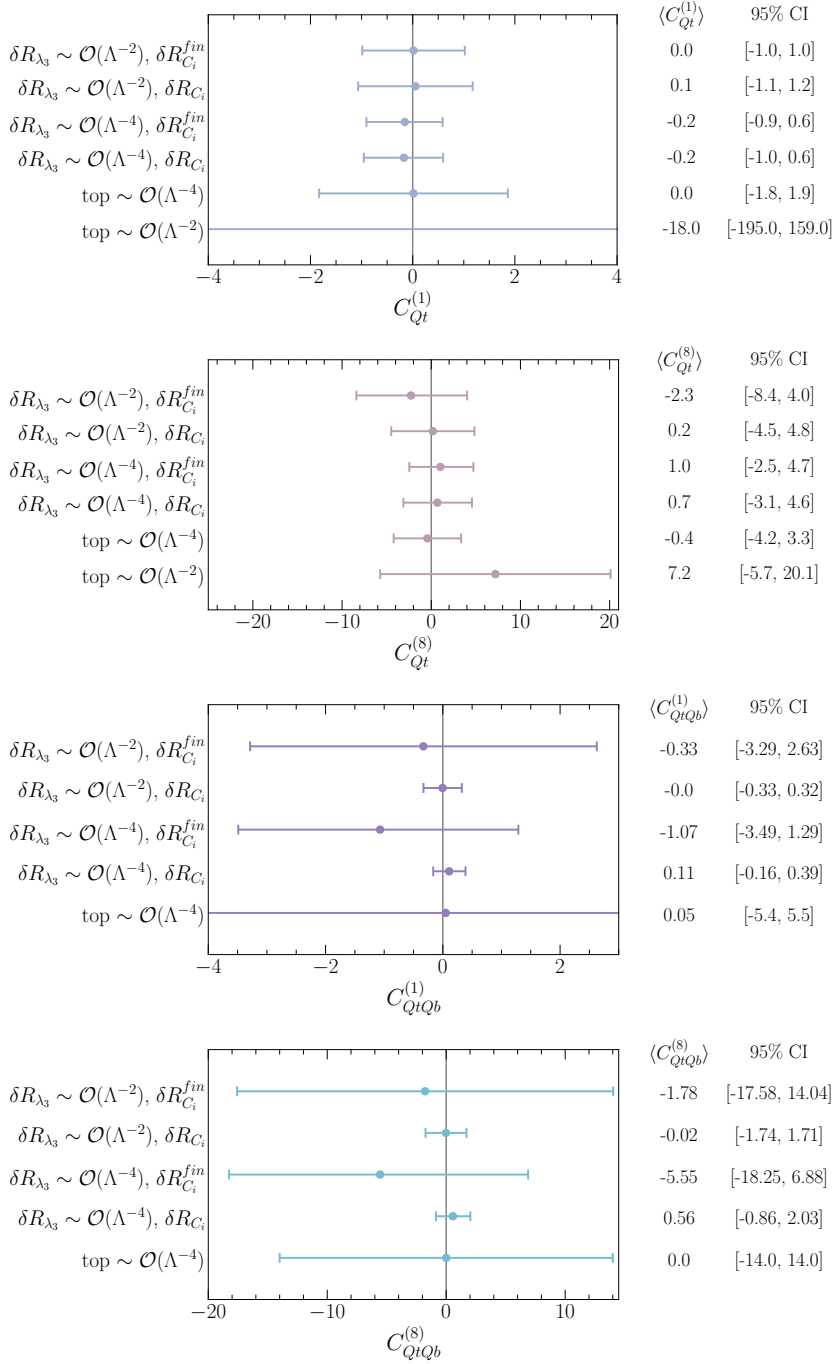


**Figure 5.7.** Forest plots illustrating the means and 95% CIs of the posteriors built from the four-fermion Wilson coefficients with  $C_\phi$  marginalised. The plots confront also the truncation of the EFT at  $\mathcal{O}(1/\Lambda^2)$  and  $\mathcal{O}(1/\Lambda^4)$  of  $\delta R_{\lambda_3}$  as defined in (5.26). The 95% CI bounds stem from Higgs data. The last two rows for each operator show instead the limits obtained by a single parameter fit to top data, linear and quadratic. The top data results are taken from [140] for  $C_{Qt}^{(1),(8)}$  and [222] for  $C_{QtQb}^{(1),(8)}$ .

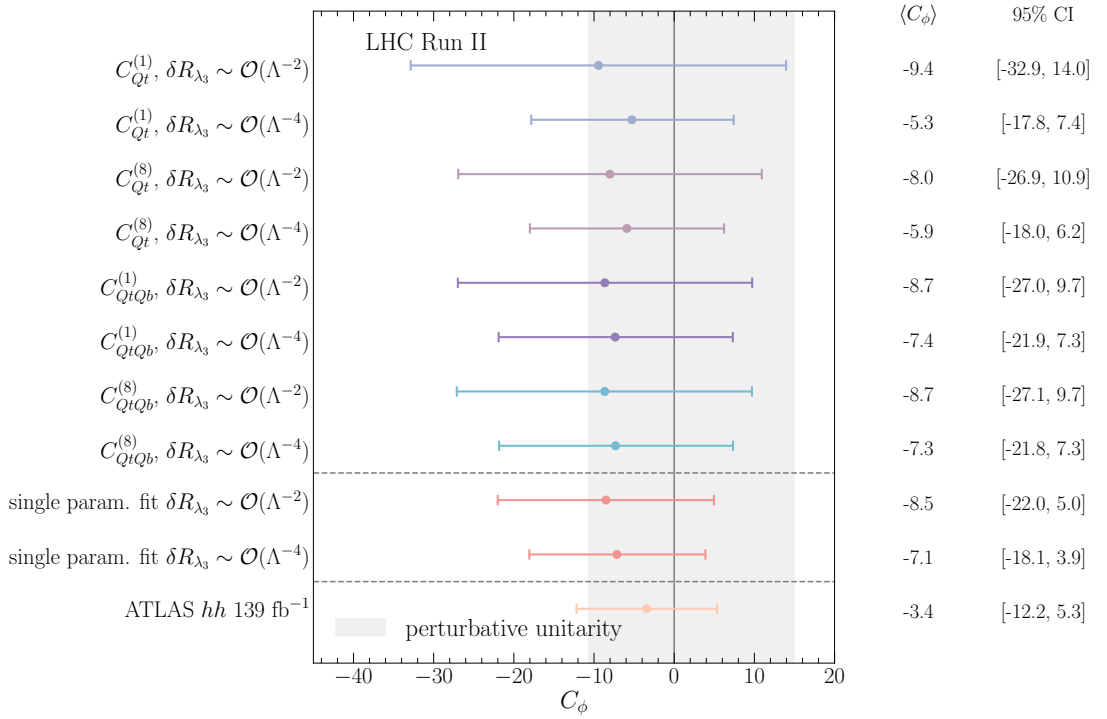


**Figure 5.8.** A forest plot illustrating the means and 95% CIs of the posteriors built from the  $C_\phi$  in a two-parameter fit with the four-fermion operators marginalised. We compare the fit results for  $C_\phi$  from full run-II Higgs data keeping terms up to  $\mathcal{O}(1/\Lambda^2)$  or  $\mathcal{O}(1/\Lambda^4)$  in  $\delta R_{\lambda_3}$ . For comparison, also the 95% CI and means for the single parameter fit for  $C_\phi$  with the same single Higgs data is shown as well as the bounds on  $C_\phi$  from the  $139 \text{ fb}^{-1}$  search for Higgs pair production [245]. The horizontal grey band illustrates the perturbative unitarity bound [52].

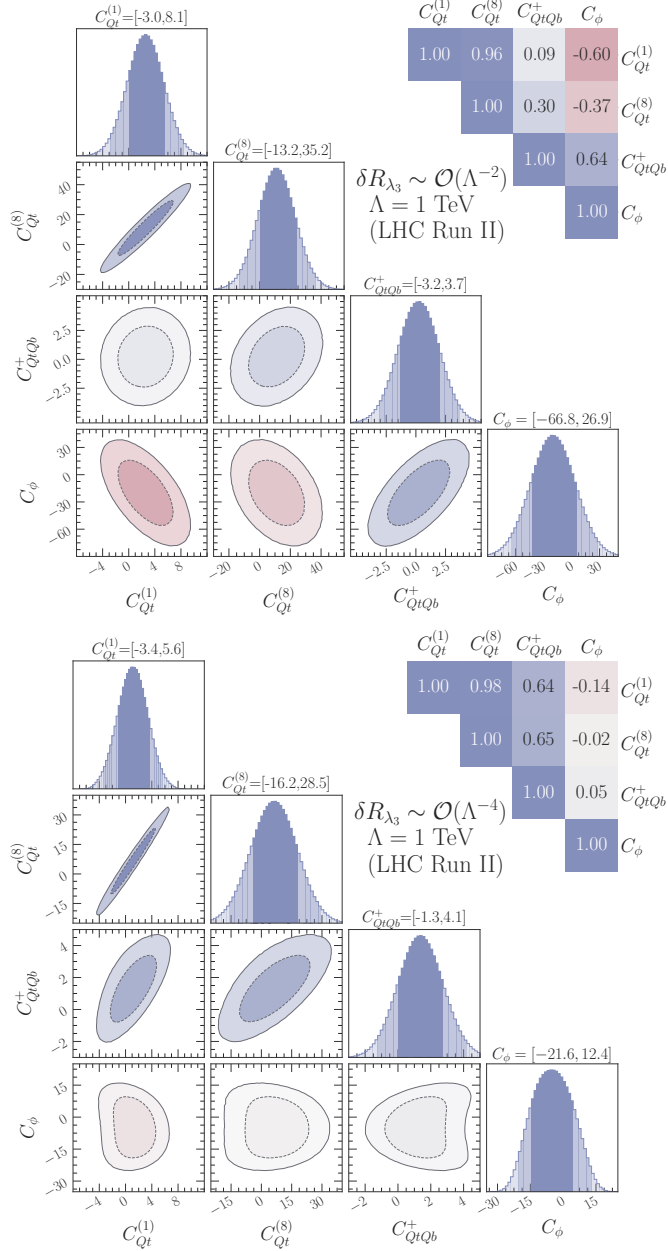


**Figure 5.9.** The marginalised 68% and 95% HDPI's for the four-parameter fits including the different four-quark Wilson coefficients and  $C_\phi$ . The numbers above the plots show the 95% CI bounds while the correlations are given on the top-right side. These limits correspond to values of the Wilson coefficients evaluated at the scale  $\Lambda = 1 \text{ TeV}$ . The upper panel shows the fit including up to  $\mathcal{O}(1/\Lambda^2)$  in  $\delta R_{\lambda_3}$  while the lower one shows the fit with including also  $\mathcal{O}(1/\Lambda^4)$ .

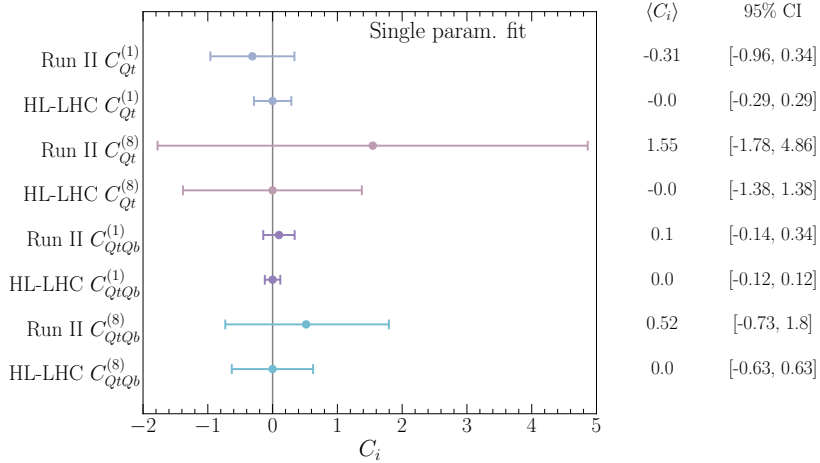


**Figure 5.10.** Results of a single parameter fit showing the improvement in constraining power of the HL-LHC over the current bounds from Run-2 data. The limits correspond to values of the Wilson coefficients evaluated at the scale  $\Lambda = 1$  TeV.

four Wilson coefficients appear in a linear combination in the NLO corrections except for  $h \rightarrow b\bar{b}$  and  $t\bar{t}h$ . However, this correlation is not as strong due to the large NLO correction of the Higgs decay  $h \rightarrow b\bar{b}$  from  $C_{QtQb}^{(1),(8)}$ . Moreover, the correlation between the four-heavy-quark Wilson coefficients and  $C_\phi$  depends on the  $\delta R_{\lambda_3}$  truncation.

### 5.3.2 Prospects for HL-LHC

We now turn to examine the potential of the HL-LHC. For this, we use the CMS projections for the single Higgs signal strengths provided in refs. [91, 239] for a centre-of-mass energy of  $\sqrt{s} = 14$  TeV and integrated luminosity of  $3\text{ ab}^{-1}$ . We use the projections for the S2 scenario explained in [191]. These assume the improvement on the systematics that is expected to be attained by the end of the HL-LHC physics programme, and that theory uncertainties are improved by a factor of two with respect to current values. These projections are assumed to have their central values in the SM prediction with the total uncertainties summarised in table 2.1 in Appendix ??.<sup>2</sup>

In Figure 5.10 we confront the results of the fits to Run-2 data with the projections for the HL-LHC for single parameter fits. For the operators  $\mathcal{O}_{Qt}^{(1),(8)}$  the constraining power of the HL-LHC is roughly a factor two better as the current bounds we could set from single Higgs data, while for the operators  $\mathcal{O}_{QtQb}^{(1),(8)}$  the improvement is a little less. In Figure 5.12 we show the limits on  $C_\phi$  in a single parameter fit for Run-2 and the projections for the HL-LHC including in  $\delta R_{\lambda_3}$  up to order  $\mathcal{O}(1/\Lambda^2)$  or  $\mathcal{O}(1/\Lambda^4)$ . While for Run-2 data the inclusion of  $\mathcal{O}(1/\Lambda^4)$  made a huge difference, this is less pronounced for the HL-LHC projections. Our results are very similar to the projections presented in

<sup>2</sup>The correlation matrix for the S2 scenario can be found on the webpage [239].

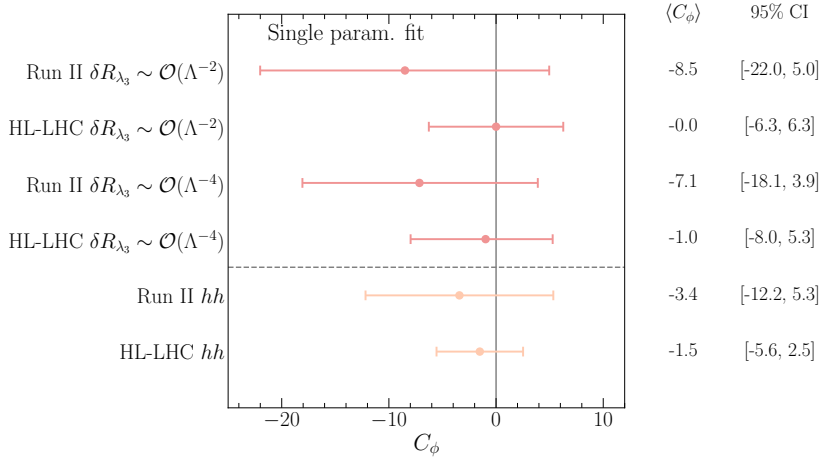


**Figure 5.11.** A forest plot illustrating the means and 95% CIs of the posteriors built from the  $C_\phi$  in a single-parameter fit, showing also the differences in including terms of  $\mathcal{O}(1/\Lambda^2)$  or up to  $\mathcal{O}(1/\Lambda^4)$  in the definition of  $\delta R_{\lambda_3}$ . For comparison, also the limits and projections from searches for Higgs pair production are shown.

a  $\kappa_\lambda$  fit in [247]. We confront this also with data from searches for Higgs pair production  $139 \text{ fb}^{-1}$  [245] and HL-LHC projections [248] on Higgs pair production, showing that Higgs pair production will still allow to set stronger limits on  $C_\phi$ .

## 5.4 Summary and discussion

In this paper, we have computed the NLO corrections induced by third generation four-quark operators in Higgs observables that are relevant for its production and decay at the LHC. Our results show that such processes are sensitive to the all possible chiral structures for the third generation four-quark operators in the dimension-six SMEFT, but in different degrees. Operators with different chiralities are, for instance, the only ones that can contribute to Higgs production via gluon fusion, and the decay of the Higgs boson to gluons, photons and bottom quarks pairs. The latter are particularly sensitive to the top-bottom operators  $\mathcal{O}_{QtQb}^{(1),(8)}$ , which then also significantly affect the total decay width. In the associate production of a Higgs boson with a top quark pair, on the other hand, all the third generation four-fermion operators enter. Sensitivity to four-quark operators where all fields have the same chirality, however, is only possible for large values of the Wilson coefficients, in a way that they can generate contributions beyond the size of current theory uncertainties. The  $t\bar{t}h$  process is also rather important in setting limits on the four-quark operators  $\mathcal{O}_{Qt}^{(1)}$  and  $\mathcal{O}_{Qt}^{(8)}$ , due to the comparatively large NLO corrections they induce in this process with respect to others. It also breaks a degeneracy among the Wilson coefficients of those two operators, which always appear in a single combination for all other processes.

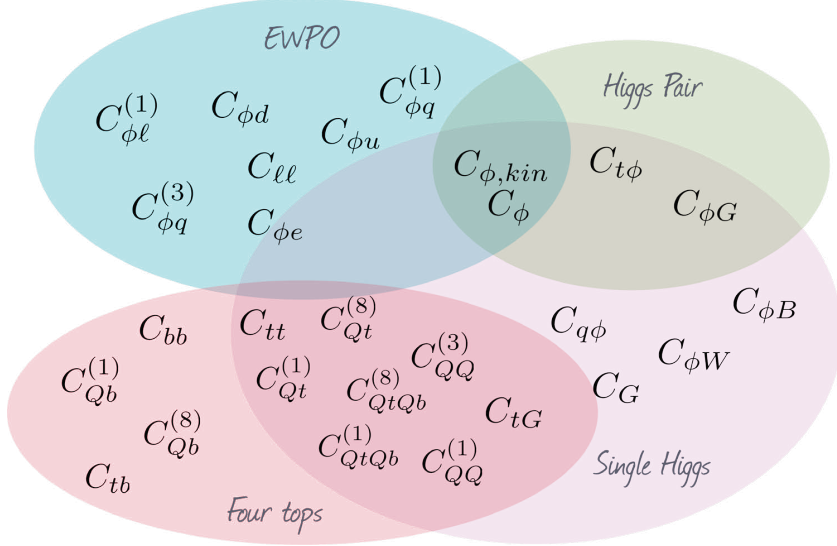


**Figure 5.12.** A forest plot illustrating the means and 95% CIs of the posteriors built from the  $C_\phi$  in a single-parameter fit, showing also the differences in including terms of  $\mathcal{O}(1/\Lambda^2)$  or up to  $\mathcal{O}(1/\Lambda^4)$  in the definition of  $\delta R_{\lambda_3}$ . For comparison, also the limits and projections from searches for Higgs pair production are shown.

To illustrate the constraining power of single Higgs processes in bounding these four-quark operators, we performed several simplified fits to these interactions and find that the resulting limits from our fits are, in some cases, comparable or better than similar results obtained from top data [140, 222].

We have also performed a combined fit including the above-mentioned four-quark operators and the operator  $(\phi^\dagger \phi)^3$ , that modifies the Higgs potential and the trilinear Higgs self-coupling. Due to the lack of powerful constraints from top data, the inclusion of the four-fermion operators diminishes the power of setting limits on the trilinear Higgs self-coupling from single Higgs observables. From our analysis we conclude that, in the absence of strong direct bounds on the third-generation four-quark operators, these should be included into a global fit on Higgs data, when attempting to obtain model-independent bounds on the trilinear Higgs self-coupling. The results of our calculations are presented such that they can be easily used by the reader in truly global fits including all other interactions entering at the LO. We leave this, as well as the inclusion of differential Higgs data, to future work.

Finally, we also illustrated the increase in constraining power expected during the high-luminosity phase of the LHC by presenting the HL-LHC projections of the above-mentioned fits.

Moving beyond hadron colliders, it must be noted that the interplay between the Higgs trilinear and four heavy-quark operators in Higgs processes is expected to be less of an issue at future leptonic Higgs factories, such as the FCC-ee [249, 250], ILC [251,

[252], CEPC [253, 254] or CLIC [255, 256]. At these machines, the effects of  $C_\phi$  are still “entangled” with those of the four-fermion operators in the Higgs rates, but only through the decay process, i.e. via the contributions to the BRs. However, Higgs production is purely electroweak, namely via Higgs-strahlung ( $Zh: e^+e^- \rightarrow Zh$ ) or  $W$  boson fusion, and receives no contributions from the four-quark operators at the same order in perturbation theory where  $C_\phi$  modifies these processes, i.e. NLO. Moreover, at any of these future  $e^+e^-$  Higgs factories there is the possibility of obtaining a sub-percent determination of the total  $Zh$  cross section at  $e^+e^-$  colliders, by looking at events recoiling against the  $Z$  decay products with a recoil mass around  $m_h$ . This observable is therefore completely insensitive to the four-quark operators, while still receiving NLO corrections from  $C_\phi$ . Although, in practice, in a global fit one needs to use data from all the various Higgs rates at two different energies to constrain all possible couplings entering at LO in the Higgs processes and also obtain a precise determination of  $C_\phi$  [168], the previous reasons should facilitate the interpretation of the single-Higgs bounds on the Higgs self-coupling at  $e^+e^-$  machines.

We conclude this paper with a few words on the relevance of the results presented here when interpreted from the point of view of specific models of new physics. In particular, one important question is *are there models where one expects large contributions to four-top operators while all other interactions entering in Higgs processes are kept small?* Indeed, large contributions to four-top operators can be expected in various BSM scenarios.<sup>3</sup> For instance, in Composite Higgs Models, in which the top quark couples to the strong dynamics by partial compositeness, one expects on dimensional grounds that some of the four-top quark operators are of order  $1/f^2$ , where  $f$  indicates the scale of strong dynamics [257]. By its own nature, however, Composite Higgs models also predict sizeable contributions to the single Higgs couplings  $\sim 1/f^2$ . While, in general, sizeable modifications of the Higgs interactions are typically expected in scenarios motivated by “naturalness”, this is not necessarily the case in other scenarios. It is indeed possible to think of simple models where modifications of the Higgs self-interactions or contributions to four-quark operators are the only corrections induced by the dimension-six interactions at tree level, see [258]. Thinking, for instance, in terms of scalar extensions of the SM, there are several types of colored scalars whose tree-level effects at low energies can be represented by four-quark operators only, e.g. for complex scalars in the  $(6, 1)_{\frac{1}{3}}$  and  $(8, 2)_{\frac{1}{2}}$  SM representations ( $\Omega_1$  and  $\Phi$  in the notation of [258]). If these colored states are the only moderately heavy new particles, our results can provide another handle to constrain such extensions. One must be careful, though, as a consistent interpretation of our results for any such models would require to include higher-order corrections in the matching to the SMEFT. At that level, as shown e.g. by the recent results in [259], multiple contributions that modify Higgs processes at LO are generated at the one-loop level, and are therefore equally important as the NLO effects of the (tree-level) generated

---

<sup>3</sup>Generically, models where four-top interactions are much larger than four-fermion operators of the first and second generation can be easily conceived from some UV dynamics coupling mostly to the third generation of quarks hence respecting the Yukawa hierarchies.

four-quark operators.<sup>4</sup> In any case, one must note that, even if similar size contributions to single Higgs processes are generated, the four-top or Higgs trilinear effects can provide extra information on the model. For instance, in some of the most common scalar extensions of the SM, with an extra Higgs doublet,  $\varphi \sim (1, 2)_{\frac{1}{2}}$ , tree-level contributions to some of the four-heavy-quark operators discussed in this paper are generated together with modifications on the Higgs trilinear self-coupling. These two effects are independent but they are both correlated with the, also tree level, modifications of the single Higgs couplings. Essentially, the LO effects on Higgs observables are proportional to  $\lambda_\varphi y_\varphi^f$ , where  $\lambda_\varphi$  is the scalar interaction strength of the  $(\varphi^\dagger \phi)(\phi^\dagger \phi)$  operator and  $y_\varphi^f$  the new scalar Yukawa interaction strength, whereas the NLO effects are proportional to the square of each separate coupling. Hence, these effects might help to resolve (even if only weakly) the flat directions in the model parameter space that would appear in a LO global fit. At the end of the day, for a proper interpretation of the SMEFT results in terms of the widest possible class of BSM models, all the above simply remind us of the importance of being global in SMEFT analyses, to which our work contributes by including effects in Higgs physics that enter at the same order in perturbation theory as modifications of the Higgs self-coupling.

---

<sup>4</sup>Furthermore, given that some SMEFT interactions induce tree-level contributions to Higgs processes that in the SM are generated at the loop level, e.g.  $\mathcal{O}_{\phi G}$  in gluon fusion, a consistent interpretation in terms of new physics models may require to include up to two-loop effects in the matching for such operators, for which there are currently no results or tools available.

## 6 Virtual two-loop calculation of $Zh$ production via gluon fusion

As we have seen in the previous sections, Higgs couplings to the weak vector bosons, i.e.  $Z$  and  $W$  is approaching the precision level. Moreover, the associated Higgs production with these bosons is the first channel used to observe the Higgs decaying into beauty quarks  $h \rightarrow b\bar{b}$  by both ATLAS and CMS [260, 261]. Hence, the  $Vh$  Higgs production channels are important channels to look for in the future runs of the LHC for better measurement of the  $VVh$  coupling as well as Higgs coupling to the beauty quark. As the statistical and systematic uncertainties coming from the experimental setup of the LHC will be eventually reduced in the future runs, due to higher integrated luminosity, upgraded detectors and improved analysis techniques. There is an exigency to reduce theoretical uncertainties emerging from the perturbative calculations of cross-sections. In order to accomplish that, one should include more terms in the perturbative expansion in the couplings, particularly the strong coupling  $\alpha_s$ . Additionally, this channel can receive contributions from new particles [262], particularly at the large invariant-mass region where the gluon fusion contribution becomes more important. Therefore, better understanding of the SM prediction of the  $Zh$  gluon fusion channel is crucial for both the SM precision measurements of Higgs production within the SM and for testing NP in this channel, e.g. new vector-like leptons.

This chapter is structured as follows : In [section 6.1](#) contains the general notation we have used for the gluon fusion  $Zh$  process calculation. Then, in [subsection 6.1.1](#) the transverse momentum expansion method is discussed. Calculation of the LO form-factors in the transverse momentum expansion is illustrated in [section 6.2](#) as a proof of concept for the  $p_T$ -expansion technique. Outline of the two-loop calculation is discussed in [section 6.3](#). Finally, in [section 6.4](#), the results of our calculation are shown with concluding remarks at the end.

This chapter is a slightly modified version of [204] published in JHEP and has been reproduced here with the permission of the copyright holder and the co-authors.

## 6.1 General notation

The amplitude  $g_a^\mu(p_1)g_b^\nu(p_2) \rightarrow Z^\rho(p_3)h(p_4)$  can be written as

$$\mathcal{A} = i\sqrt{2}\frac{m_Z G_F \frac{\alpha_s^0}{4\pi}(\mu_R)}{\pi} \delta_{ab} \epsilon_\mu^a(p_1) \epsilon_\nu^b(p_2) \epsilon_\rho(p_3) \hat{\mathcal{A}}^{\mu\nu\rho}(p_1, p_2, p_3), \quad (6.1)$$

$$\hat{\mathcal{A}}^{\mu\nu\rho}(p_1, p_2, p_3) = \sum_{i=1}^6 \mathcal{P}_i^{\mu\nu\rho}(p_1, p_2, p_3) \mathcal{A}_i(\hat{s}, \hat{t}, \hat{u}, m_t, m_h, m_Z), \quad (6.2)$$

where  $\mu_R$  is the renormalisation scale and  $\epsilon_\mu^a(p_1) \epsilon_\nu^b(p_2) \epsilon_\rho(p_3)$  are the polarization vectors of the gluons and the  $Z$  boson, respectively. It is possible to decompose the amplitude into a maximum of 6 Lorentz structures encapsulated by the tensors  $\mathcal{P}_i^{\mu\nu\rho}$ . Due to the presence of the  $\gamma_5$  these projectors are proportional to the Levi-Civita total anti-symmetric tensor  $\epsilon^{\alpha\beta\gamma\delta}$ . One can choose to an orthogonal basis explicitly shown in ??, such that

$$\mathcal{P}_i^{\mu\nu\rho} \mathcal{P}_{j\mu\nu\rho} = 0, \quad \text{for } i \neq j \quad (6.3)$$

By this choice one obtains unique form factors corresponding to each projector

$$\mathcal{A}_i(\hat{s}, \hat{t}, \hat{u}, m_t, m_h, m_Z), \quad (6.4)$$

that are multivariate complex functions of the top ( $m_t$ ), Higgs ( $m_h$ ) and  $Z$  ( $m_Z$ ) bosons masses, and of the partonic Mandelstam variables

$$\hat{s} = (p_1 + p_2)^2, \quad \hat{t} = (p_1 + p_3)^2, \quad \hat{u} = (p_2 + p_3)^2, \quad (6.5)$$

where  $\hat{s} + \hat{t} + \hat{u} = m_Z^2 + m_h^2$  and all the momenta are considered to be incoming. The form-factors  $\mathcal{A}_i$  can be perturbatively expanded in orders of  $\alpha_s$ ,

$$\mathcal{A}_i = \sum_{k=0} \left( \frac{\alpha_s}{\pi} \right)^k \mathcal{A}_i^{(k)} \quad (6.6)$$

Where  $\mathcal{A}_i^{(0)}$  and  $\mathcal{A}_i^{(1)}$  are the LO and NLO terms, respectively. Using Fermi's Golden Rule, we can write the Born partonic cross-section as

$$\hat{\sigma}^{(0)}(\hat{s}) = \frac{m_Z^2 G_F^2 \alpha_s(\mu_R)^2}{64\hat{s}^2(2\pi)^3} \int_{\hat{t}-}^{\hat{t}+} d\hat{t} \sum_i |\mathcal{A}_i^{(0)}|^2, \quad (6.7)$$

where  $\hat{t}^\pm = [-\hat{s} + m_h^2 + m_Z^2 \pm \sqrt{(\hat{s} - m_h^2 - m_Z^2)^2 - 4m_h^2 m_Z^2}] / 2$ .

The LO has two sets of diagrams, the triangle, and box diagrams shown in Figure 6.1. In (a), the triangle diagrams contain a neutral Goldstone boson  $G^0$ , instead in (b) the  $Z$  boson is mediated. The interplay between these two diagram types depends on the  $\xi$  gauge. Moreover, the  $Z$  boson is strictly off-shell, due to Furry's theorem. In the Landau gauge the  $Z$ -mediated diagrams will also vanish, this can be seen by considering the

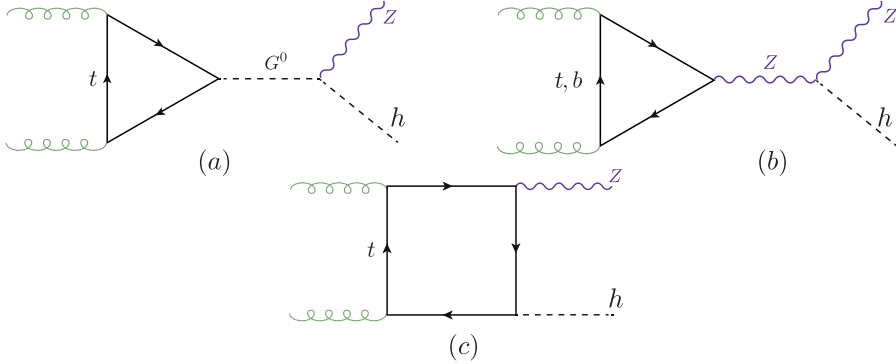


**Figure 6.1.** Feynman diagrams type for the LO  $gg \rightarrow Z h$  process. The triangle diagrams in a general  $\xi$  gauge involve  $Z$  and the neutral Goldstone  $G^0$  propagators.

subamplitude  $ggZ^*$  which in the Landau gauge can be related to the decay of a massive vector boson with mass  $\sqrt{\hat{s}}$  into two massless ones, a process that is forbidden by the Landau-Yang theorem [263, 264]. The triangle diagrams are also proportional to the mass difference between the up and down type quarks. In this calculation, the first and second generation quarks are assumed to be massless, as well as the  $b$  quark, hence light quarks loops do not contribute to this process. The same would apply to the box diagrams (c), as they are proportional to the quark Yukawa coupling, and vanish in the massless quarks case. Moreover, triangle diagrams with  $b-$  quark loops contribute to  $\sim 1\%$  of the total amplitude, computed in the limit  $m_b \rightarrow 0$ .

### 6.1.1 The transverse momentum expansion

Choosing to expand in small  $p_T$  of the  $Z$  boson, the first step is expressing  $p_T$  in terms of the Mandelstam variables and masses

$$p_T^2 = \frac{\hat{t}\hat{u} - m_Z^2 m_h^2}{\hat{s}}. \quad (6.8)$$

From eq.(6.8), together with the relation between the Mandelstam variables, one finds

$$p_T^2 + \frac{m_h^2 + m_Z^2}{2} \leq \frac{\hat{s}}{4} + \frac{\Delta_m^2}{\hat{s}}, \quad (6.9)$$

where  $\Delta_m = (m_h^2 - m_Z^2)/2$ . Eq.(6.9) implies  $p_T^2/\hat{s} < 1$  that, together with the kinematical constraints  $m_h^2/\hat{s} < 1$  and  $m_Z^2/\hat{s} < 1$ . With these relations in mind, one can expand the amplitudes in terms of small  $p_T^2/\hat{s}$ ,  $m_h^2/\hat{s}$  and  $m_Z^2/\hat{s}$ , which is technically valid throughout the whole phase space, contrary to the LME and HE limits. The caveat for this expansion is that, the amplitude does not depend on  $p_T$  explicitly. Instead, one would expand in

the reduced Mandelstam variables  $t'/s' \ll 1$  or  $u'/s' \ll 1$ , defined as

$$s' = p_1 \cdot p_2 = \frac{\hat{s}}{2}, \quad t' = p_1 \cdot p_3 = \frac{\hat{t} - m_Z^2}{2}, \quad u' = p_2 \cdot p_3 = \frac{\hat{u} - m_Z^2}{2} \quad (6.10)$$

and satisfy

$$s' + t' + u' = \Delta_m. \quad (6.11)$$

The choice of the expansion parameter  $t'$  or  $u'$  depends whether one expands in the forward or backwards kinematics. Because the process  $gg \rightarrow Zh$ , has two particles in the final states with different masses, the amplitude is not symmetric under the their exchange. One therefore cannot compute the cross-section by integrating only the forward-expanded amplitude [204], contrary what has been done for the Higgs pair [203]. In order to overcome this issue, one could further examine the projectors in ?? and observe that they can be split into symmetric and anti-symmetric parts with respect to the exchange  $t' \leftrightarrow u'$ . Then, expand the symmetric part in the forward kinematics, like the Higgs pair case. As for the anti-symmetric part, the antisymmetric factor is simply extracted by multiplying the form-factors by  $1/(\hat{t} - \hat{u})$ , written as  $1/(2s' - 4t' - 2\Delta_m)$ , then perform the expansion in the forward kinematics and finally multiply back by  $(\hat{t} - \hat{u})$ .

In order to implement the  $p_T$ -expansion at the Feynman diagrams level we start by splitting the momenta into longitudinal and transverse with respect to the beam direction, by introducing the vector [203],

$$r^\mu = p_1^\mu + p_3^\mu, \quad (6.12)$$

which satisfies

$$r^2 = \hat{t}, \quad r \cdot p_1 = \frac{\hat{t} - m_Z^2}{2}, \quad r \cdot p_2 = -\frac{\hat{t} - m_h^2}{2}, \quad (6.13)$$

and hence can be also written as

$$r^\mu = -\frac{\hat{t} - m_h^2}{\hat{s}} p_1^\mu + \frac{\hat{t} - m_Z^2}{\hat{s}} p_2^\mu + r_\perp^\mu = \frac{t'}{s'} (p_2^\mu - p_1^\mu) - \frac{\Delta_m}{s'} p_1^\mu + r_\perp^\mu, \quad (6.14)$$

where

$$r_\perp^2 = -p_T^2. \quad (6.15)$$

substituting the definition of  $p_T$  from eq.(6.8) one obtains

$$t' = -\frac{s'}{2} \left\{ 1 - \frac{\Delta_m}{s'} \pm \sqrt{\left(1 - \frac{\Delta_m}{s'}\right)^2 - 2\frac{p_T^2 + m_Z^2}{s'}} \right\} \quad (6.16)$$

implying that the expansion in small  $p_T$  (the minus sign case in eq.(6.16)) can be realized at the level of Feynman diagrams, by expanding the propagators in terms of the vector  $r^\mu$  around  $r^\mu \sim 0$  or, equivalently,  $p_3^\mu \sim -p_1^\mu$ , see eq.(6.14).

## 6.2 Born cross-section in the $p_T$ -expansion

As a baseline test for the validity and convergence behaviour of the  $p_T$  expansion we start by computing the LO amplitude, and consequently the Born partonic cross-section in the  $p_T$  expansion then compare it with the exact results found in [194, 195].

Starting by defining the one-loop functions appearing in the similar calculation of the Born cross-section for  $gg \rightarrow hh$  in the same expansion carried out in ref. [203]

$$B_0[\hat{s}, m_t^2, m_t^2] \equiv B_0^+, \quad B_0[-\hat{s}, m_t^2, m_t^2] \equiv B_0^-, \quad (6.17)$$

$$C_0[0, 0, \hat{s}, m_t^2, m_t^2, m_t^2] \equiv C_0^+, \quad C_0[0, 0, -\hat{s}, m_t^2, m_t^2, m_t^2] \equiv C_0^- \quad (6.18)$$

$$B_0[q^2, m_1^2, m_2^2] = \frac{1}{i\pi^2} \int \frac{d^n k}{\mu^{n-4}} \frac{1}{(k^2 - m_1^2)((k+q)^2 - m_2^2)}, \quad (6.19)$$

$$C_0[q_a^2, q_b^2, (q_a + q_b)^2, m_1^2, m_2^2, m_3^2] = \frac{1}{i\pi^2} \int \frac{d^d k}{\mu^{d-4}} \frac{1}{[k^2 - m_1^2][(k+q_a)^2 - m_2^2][(k-q_b)^2 - m_3^2]} \quad (6.20)$$

are the Passarino-Veltman functions [265], with  $d$  the dimension of spacetime and  $\mu$  the 't Hooft mass. There are only two non-vanishing form-factors at LO, one is symmetric  $\mathcal{A}_2$ , and the other is antisymmetric  $\mathcal{A}_6$ , in the  $p_T$ -expansion, these form-factors are give by,

up to order  $\mathcal{O}(p_T^2)$

$$\begin{aligned}
\mathcal{A}_2^{(0,\Delta)} &= -\frac{p_T}{\sqrt{2}(m_Z^2 + p_T^2)}(\hat{s} - \Delta_m)m_t^2 C_0^+, \\
\mathcal{A}_2^{(0,\square)} &= \frac{p_T}{\sqrt{2}(m_Z^2 + p_T^2)} \left\{ \right. \\
&\quad \left( m_t^2 - m_z^2 \frac{\hat{s} - 6m_t^2}{4\hat{s}} - p_T^2 \frac{12m_t^4 - 16m_t^2\hat{s} + \hat{s}^2}{12\hat{s}^2} \right) B_0^+ \\
&- \left( m_t^2 - \Delta_m \frac{m_t^2}{(4m_t^2 + \hat{s})} + m_z^2 \frac{24m_t^4 - 6m_t^2\hat{s} - \hat{s}^2}{4\hat{s}(4m_t^2 + \hat{s})} - \right. \\
&\quad \left. p_T^2 \frac{48m_t^6 - 68m_t^4\hat{s} - 4m_t^2\hat{s}^2 + \hat{s}^3}{12\hat{s}^2(4m_t^2 + \hat{s})} \right) B_0^- \\
&+ \left( 2m_t^2 - \Delta_m + m_z^2 \frac{3m_t^2 - \hat{s}}{\hat{s}} + p_T^2 \frac{3m_t^2\hat{s} - 2m_t^4}{\hat{s}^2} \right) m_t^2 C_0^- \\
&+ \left( \hat{s} - 2m_t^2 + m_z^2 \frac{\hat{s} - 3m_t^2}{\hat{s}} + p_T^2 \frac{2m_t^4 - 3m_t^2\hat{s} + \hat{s}^2}{\hat{s}^2} \right) m_t^2 C_0^+ \\
&+ \log \left( \frac{m_t^2}{\mu^2} \right) \frac{m_t^2}{(4m_t^2 + \hat{s})} \left( \Delta_m + 2m_z^2 + p_T^2 \frac{2\hat{s} - 2m_t^2}{3\hat{s}} \right) \\
&- \left. \Delta_m \frac{2m_t^2}{(4m_t^2 + \hat{s})} + m_z^2 \frac{\hat{s} - 12m_t^2}{4(4m_t^2 + \hat{s})} + p_T^2 \frac{8m_t^4 - 2m_t^2\hat{s} + \hat{s}^2}{4\hat{s}(4m_t^2 + \hat{s})} \right\}, 
\end{aligned} \tag{6.22}$$

and

$$\mathcal{A}_6^{(0,\Delta)} = 0, \tag{6.23}$$

$$\begin{aligned}
\mathcal{A}_6^{(0,\square)} &= \frac{\hat{t} - \hat{u}}{\hat{s}^2} p_T \left[ \frac{m_t^2}{2} \left( B_0^- - B_0^+ \right) - \frac{\hat{s}}{4} \right. \\
&- \left. \frac{2m_t^2 + \hat{s}}{2} m_t^2 C_0^- + \frac{2m_t^2 - \hat{s}}{2} m_t^2 C_0^+ \right], 
\end{aligned} \tag{6.24}$$

where these form-factors were divided into triangle ( $\Delta$ ) and box ( $\square$ ) contributions, and  $B_0$  functions are understood as the finite part of the integrals on the right hand side of eq.(6.19).

Using several truncations of the  $p_T$ -expansion, and comparing it to the exact LO result, one can see in Figure 6.2 the exact Born partonic LO cross section (red line) as a function of the invariant mass of the  $Zj$  system,  $M_{Zh}$ , in comparison to the  $p_T$ -expansions. For the numerical evaluation of the cross section here and in the following, we used as SM

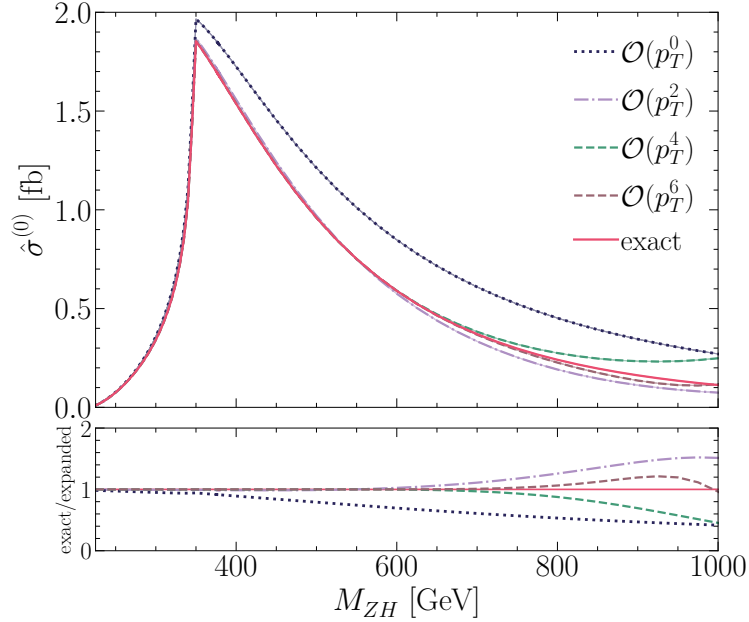


**Figure 6.2.** The Born partonic cross-section as a function of the invariant mass  $M_{Zh}$ . The exact (red line) is plotted together with results at different orders in the  $p_T$ -expansion (dashed lines). In the bottom part, the ratio of the full result over the  $p_T$ -expanded one at various orders is shown. This plot has been already published in [204]

input parameters

$$\begin{aligned} m_Z &= 91.1876 \text{ GeV}, & m_h &= 125.1 \text{ GeV}, & m_t &= 173.21 \text{ GeV}, \\ m_b &= 0 \text{ GeV}, & G_F &= 1.16637 \text{ GeV}^{-2}, & \alpha_s(m_Z) &= 0.118. \end{aligned}$$

From the ratio plotted in the lower panel of Figure 6.2, we observe that the  $\mathcal{O}(p_T^0)$  expansion is in good agreement with the exact result when  $M_{Zh} \lesssim 2m_t$ . Inclusion of higher order terms up to  $\mathcal{O}(p_T^6)$  extended the validity of the expansion to reach  $M_{Zh} \lesssim 750$  GeV. This is the similar behaviour seen in [203] for Higgs pair. Therefore, one would expect the  $p_T$ -expanded two-loop virtual correction to be an accurate approximation with the exact (numerical) result for the region of the invariant mass of  $M_{Zh} \sim 700 - 750$  GeV. Similar conclusions can be seen more explicitly in Table 6.1, where it is shown that the partonic cross-section at  $\mathcal{O}(p_T^4)$  agrees with the full result for  $M_{ZH} \lesssim 600$  GeV on the permille level and the agreement further improves when  $\mathcal{O}(p_T^6)$  terms are included.

$M_{Zh}$ [GeV]	$\mathcal{O}(p_T^0)$	$\mathcal{O}(p_T^2)$	$\mathcal{O}(p_T^4)$	$\mathcal{O}(p_T^6)$	full
300	0.3547	0.3393	0.3373	0.3371	0.3371
350	1.9385	1.8413	1.8292	1.8279	1.8278
400	1.6990	1.5347	1.5161	1.5143	1.5142
600	0.8328	0.5653	0.5804	0.5792	0.5794
750	0.5129	0.2482	0.3129	0.2841	0.2919

**Table 6.1.** The partonic cross section  $\hat{\sigma}^{(0)}$  at various orders in  $p_T$  and the full computation for several values of  $M_{Zh}$ . This table has been already published in [204].

### 6.3 NLO calculation

The virtual two-loop corrections to  $gg \rightarrow Zh$  are shown in Figure 6.3, which involve corrections to the triangle topology in (a) and (b). The corrections to the box topology in (c) and a new topology , dented by double triangle in (d). Both two-loop corrections to the triangles, and the double triangle diagrams can be computed exactly analytically. However, the two-loop box diagrams contain master-integrals (MI's) that have no analytic solutions, so far. The two-loop box diagrams will be computed in the  $p_T$ -expansion.

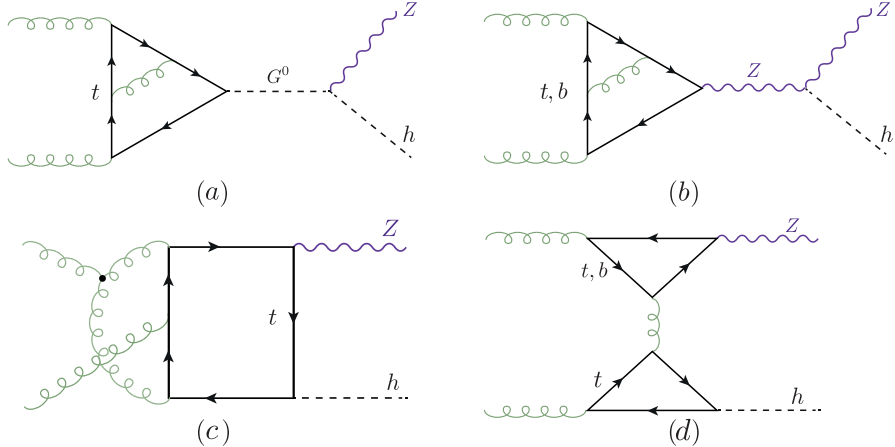


**Figure 6.3.** Feynman diagrams types for the virtual NLO corrections to the  $gg \rightarrow Zh$  process.

#### 6.3.1 Renormalisation

The two-loop corrections to the triangle and box diagrams contain both UV and IR divergences. The first emerges from UV divergent sub-diagrams, such as top mass renormalisation and QCD vertex correction. While the IR divergences come from massless

loops. In order to remove these divergences, one introduces adequate counter-terms. On the other hand, the double triangle is both UV and IR finite.

We start by the gluon wavefunction renormalisation of the incoming gluons (external legs) such that the amplitude is renormalised by  $Z_A^{1/2}$  for each gluon.

$$Z_A = 1 + \frac{\alpha_s^0}{4\pi} \frac{2}{3\epsilon} \left( \frac{\mu_R^2}{m_t^2} \right)^\epsilon. \quad (6.25)$$

The on-shell scheme for the top mass renormalisation has been used, in which the bare mass is replaced by the renormalised one  $m_0 = Z_m m$  in the propagators this gives the  $\overline{\text{MS}}$  renormalised mass.

$$Z_m = 1 + C_F \frac{3}{\epsilon}. \quad (6.26)$$

In order to convert the mass definition to the on-shell scheme we add the finite renormalisation term

$$Z_m^{OS} = 1 - 2C_F, \quad (6.27)$$

here  $C_F = (N_c^2 - 1)/2N_c$  is one of the two Casimir invariants of QCD along with  $C_A = N_c$ . The  $q\bar{q}g$  vertex correction involves a renormalisation of the strong couplings constant  $\alpha_s$  which is done via replacing the bare constant  $\alpha_s^0$  with the renormalised one, hence it becomes  $\alpha_s^0 = \frac{\mu_R^{2\epsilon}}{S_\epsilon} Z_{\alpha_s} \alpha_s$ , where

$$Z_{\alpha_s} = 1 - \frac{\alpha_s}{4\pi} \frac{1}{\epsilon} \left( \beta_0 - \frac{2}{3} \right) \left( \frac{\mu_R^2}{m_t^2} \right)^\epsilon, \quad (6.28)$$

and the constant  $\beta_0 = \frac{11}{3}C_A - \frac{2}{3}N_f$ , where  $N_f$  is the number of “active” flavours. The 5-flavour scheme  $N_f = 5$  is adopted here.

The loop integrals were evaluated via dimensional regularisation in  $d = 4 - 2\epsilon$  dimensions. Which requires some caution when  $\gamma_5$  is present in the amplitude. We let  $\gamma_5$  naively anti-commute with all  $d$ -dimensional  $\gamma_\mu$ 's and then correct that with the finite renormalisation constant known as **Larin counter-term** [266]

$$Z_5 = 1 - 2C_F. \quad (6.29)$$

The renormalised amplitude is written as

$$\mathcal{M}(\alpha_s, m, \mu_R) = Z_A \mathcal{M}(\alpha_s^0, m^0). \quad (6.30)$$

Putting all the above substitutions together, we get the renormalised two-loop form-

factor:

$$(\mathcal{A}^{(1)})^R = \mathcal{A}^{(1)} - \mathcal{A}_{UV}^{(0)} - \mathcal{A}_{UV,m}^{(0)} + \mathcal{A}_{\text{Larin}}^{(0)} \quad (6.31)$$

$$\mathcal{A}_{UV}^{(0)} = \frac{\alpha_s}{4\pi} \frac{\beta_0}{\epsilon} \left( \frac{\mu_R^2}{\hat{s}} \right)^{-\epsilon} \mathcal{A}^{(0)}.$$

$$\mathcal{A}_{UV,m}^{(0)} = \frac{\alpha_s}{4\pi} \left( \frac{3}{\epsilon} - 2 \right) C_F \left( \frac{\mu_R^2}{\hat{s}} \right)^{-\epsilon} m^0 \partial_m \mathcal{A}^{(0)}. \quad (6.32)$$

$$\mathcal{A}_{\text{Larin}}^{(0)} = -\frac{\alpha_s}{4\pi} C_F \mathcal{A}^{(0)}.$$

The following IR-counter-term is used in order to cancel the IR divergences.

$$\mathcal{A}_{IR}^{(0)} = \frac{e^{\gamma_E \epsilon}}{\Gamma(1-\epsilon)} \frac{\alpha_s}{4\pi} \left( \frac{\beta_0}{\epsilon} + \frac{C_A}{\epsilon^2} \right) \left( \frac{\mu_R^2}{\hat{s}} \right)^{2\epsilon} \mathcal{A}^{(0)} \quad (6.33)$$

The one-loop form-factors, need to be expanded up to order  $\mathcal{O}(\epsilon^2)$ , for the UV and IR counter-terms.

### 6.3.2 Calculation of the exact virtual corrections

The two-loop calculations of the triangle diagrams involves the diagrams of with virtual  $Z^*$  and  $G^0$ , depending on the gauge of choice. Observations found in ref.[196] shows that due to Landau-Yang theorem in the Landau gauge the diagrams with the  $Z^*$  exchange vanishes. Therefore, the part of the top triangle diagrams can be obtained from the decay amplitude of a pseudoscalar boson into two gluons which is known in the literature in the full mass dependence up to NLO terms [267, 268]. On the contrary, in the unitary gauge, the NLO calculation needs to be done with the  $Z^*$  exchange diagrams only. The calculations result in apparently different Lorentz structures, that are linked via the Schouten identity

$$q^\alpha \epsilon^{\beta\gamma\delta\phi} + q^\beta \epsilon^{\gamma\delta\phi\alpha} + q^\gamma \epsilon^{\delta\phi\alpha\beta} + q^\gamma \epsilon^{\delta\phi\alpha\beta} + q^\delta \epsilon^{\phi\alpha\beta\gamma} + q^\phi \epsilon^{\alpha\beta\gamma\delta} = 0 \quad (6.34)$$

A cross-check has been preformed in order to ensure that the NLO calculation introduces no new Lorentz structures, and gives the same result in a general  $R_\xi$  gauge as the results in [267, 268]. The two-loop calculation has been carried out in  $R_\xi$  gauge. The amplitudes have been automatically generated by **FeynArts** [227] and contracted with the projectors as defined in ?? using **FeynCalc** [269, 270] and **Package X** [271] and in-house Mathematica routines. The two-loop integrals were reduced to a set of master integrals MI, illustrated graphically in Figure 6.4 using **Kira** [272]. These MI's are either products of one-loop functions (a)-(c), (e),(f),(h) and (l) or can be found in the literature [268, 273]. Their implementation in our calculation has been validated numerically using **SecDec** [274, 275]. The virtual correction for the triangle diagrams

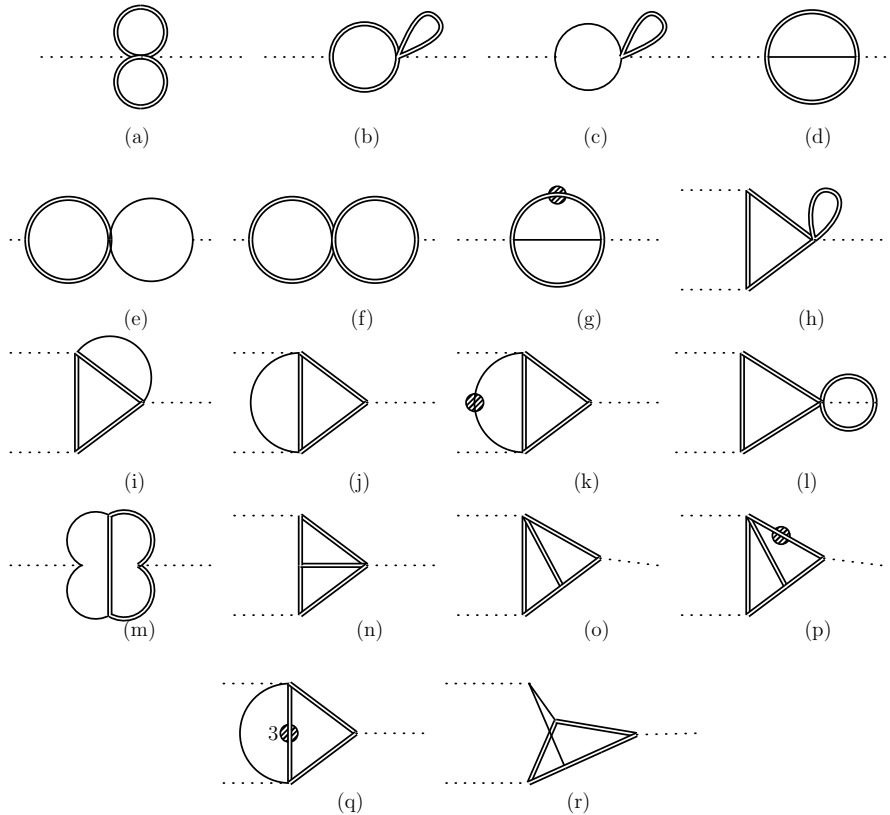


**Figure 6.4.** The list of two-loop master integrals (MI's) resulting from the reduction of the two-loop triangle corrections, and the product of one-loop MI's appearing in this list also appear in the calculation of the double-triangle diagrams. A single line denotes a massless propagator, while a double line denotes a massive one. The dot denotes a squared propagator, unless the number of the exponent is indicated, here only 3 appears in diagram (q).

can be separated according to their colour factors into

$$\mathcal{A}^{(1)} = C_F \mathcal{A}_{CF}^{(1)} + C_A \mathcal{A}_{CA}^{(1)}, \quad (6.35)$$

The  $C_A$  part contains a double pole  $\mathcal{O}(1/\epsilon^2)$  and a single pole  $\mathcal{O}(1/\epsilon)$ , both coming from the IR divergence. Whilst the  $C_F$  part contains a UV divergent pole that needs to be cured via mass renormalisation. The poles do not have a dependence on the renormalisation scale  $\mu_R$ . However, there is a dependence on that scale in the finite part, as well. No new Lorentz structures appeared, and the final result in  $R_\xi$  matched the one found in [267, 268] for the Landau gauge. The explicit results are shown in ??

The calculation of the double triangle diagrams (d) of Figure 6.3 is fairly straightforward, all of the integrals can be rewritten in terms of products of one-loop functions. All of the Lorentz structures appear in the double triangle except for  $\mathcal{P}_6$ , analogous to the triangle case. The explicit forms of form-factors corresponding to these structures are presented in ???. Although we write the amplitude using a different tensorial structure with respect to ref.[201] we have checked, using the relations between the two tensorial structures reported in ???, that our result is in agreement with the one presented in ref.[198].

### 6.3.3 Calculation of the $p_T$ -expanded virtual corrections

The two-loop triangle diagrams can also be interpreted as an expansion in  $p_T$ , but this expansion terminates at  $\mathcal{O}(p_T^2)$ , rather being an infinite series. Hence, in this section we concentrate on the two-loop box diagrams  $p_T$ -expansion <sup>1</sup>.

Similar to the two-loop triangle diagrams, the box diagrams amplitudes were generated projected through the same pipeline. After the contraction of the epsilon tensors the diagrams were expanded as described in subsection 6.1.1, keeping only  $\mathcal{O}(p_T^4)$  terms. They were reduced to MI's using FIRE [276] and LiteRed [277]. The resulting MI's were identical to the one for Higgs pair production [203]. Nearly all of them are expressed in terms of generalised harmonic polylogarithms with the exception of two elliptic integrals [278, 279]. The renormalisation and IR pole subtraction procedure was carried out like prescribed subsection 6.3.1.

As a control, the two-loop box diagrams were also computed in the LME up to  $\mathcal{O}(1/m_t^6)$ . Since this expansion should be included within the  $p_T$ -expansion. We have retained the LME analytic expression by further expanding the  $p_T$ -expanded amplitude in small  $\hat{s}/m_t^2$ . Providing an additional cross-check for the validity of the  $p_T$ -expansion.

## 6.4 Results and conclusions

The virtual corrections to the gluon fusion  $Zh$  production have been implemented in a FORTRAN code using `handyG` [280], for the evaluation of generalised harmonic polylogarithms, `Chaplin` [281] for the harmonic polylogarithms appearing in the triangle two-loop

---

<sup>1</sup>The calculation of the box diagrams has been done mainly by my collaborators, the co-authors of [204]

$\hat{s}/m_t^2$	$\hat{t}/m_t^2$	ref.[202]	$\mathcal{O}(p_T^6)$
1.707133657190554	-0.441203767016323	35.429092(6)	35.430479
3.876056604162662	-1.616287256345735	4339.045(1)	4340.754
4.130574250302561	-1.750372271104745	6912.361(3)	6915.797
4.130574250302561	-2.595461551488002	6981.09(2)	6984.20

**Table 6.2.** Comparison of  $\mathcal{V}_{fin}4/(\alpha_s^2 \alpha^2)$  with the numerical results of ref.[202]. This plot has been already published in [204].

functions while the elliptic integrals are evaluated using the routines of ref.[279]. Since the result is analytic, the code is significantly faster than the numerical evaluation of the two-loop amplitude [202], with evalution time of ca. 0.5 min per one phase space point on a personal laptop.

In order to facilitate the comparison of our results with the ones presented in the literature, we define the finite part of the virtual corrections as in ref.[201]<sup>2</sup>

$$\begin{aligned} \mathcal{V}_{fin} = & \frac{G_F^2 m_Z^2}{16} \left( \frac{\alpha_s}{\pi} \right)^2 \left[ \sum_i \left| \mathcal{A}_i^{(0)} \right|^2 \frac{C_A}{2} \left( \pi^2 - \log^2 \left( \frac{\mu_R^2}{\hat{s}} \right) \right) \right. \\ & \left. + 2 \sum_i \text{Re} \left[ \mathcal{A}_i^{(0)} \left( \mathcal{A}_i^{(1)} \right)^* \right] \right] \end{aligned} \quad (6.36)$$

and in the numerical evaluation of eq.(6.36) we fixed  $\mu_R = \sqrt{\hat{s}}$ . Triangle and LME box topologies were validated against the results of refs.[198, 201] finding perfect agreement at the form-factor level, i.e.  $\mathcal{A}_i^{(1)}$ .

The virtual part of the partonic cross-section from the finite part of the virtual corrections in eq.(6.36) is defined by

$$\Delta \hat{\sigma}_{virt} = \int_{\hat{t}^-}^{\hat{t}^+} d\hat{t} \frac{\alpha_s}{16\pi^2} \frac{1}{\hat{s}^2} \mathcal{V}_{fin} \quad (6.37)$$

This function is used to confront  $p_T$ -expanded results. Starting with low  $M_{Zh}$  we have compared the  $p_T$ -expanded with the LME  $\mathcal{V}_{fin}$ , finding a good numerical agreement. It is important to note that, at the same order in the expansion, the  $p_T$ -expanded terms are more accurate than the LME ones, although computationally more demanding. Additional checks have been done using the numerical evaluation of the NLO amplitude by [202], where they have evaluated the exact two-loop MI's using `pySecDec` [282, 283]. Table 6.2 shows a comparison between our  $p_T$ -expanded  $\mathcal{V}_{fin}4/(\frac{\alpha_s^0}{4\pi} \alpha^2)$  versus the exact numerical result of [202] for several phase space points. As can be seen from the table the relative difference between the two results is less than half a permille.

In Figure 6.5, the dashed lines show the different orders of the expansion. For all

<sup>2</sup>The definition of the matrix elements here differs by a factor of  $\frac{1}{\hat{s}}$  from ref.[201], cf. also ??.

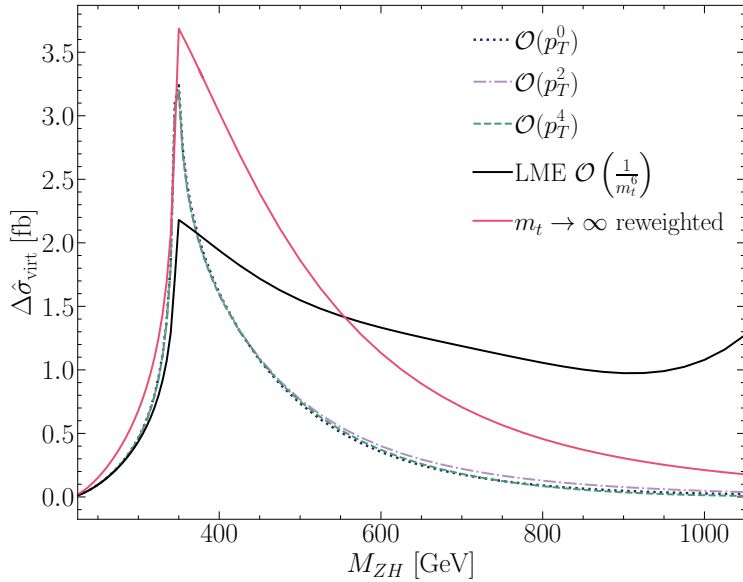


**Figure 6.5.**  $\Delta\hat{\sigma}_{\text{virt}}$  defined by eq.(6.37), shown as a function of  $M_{ZH}$ . The various orders of the  $p_T$ -expansion are plotted as dashed lines, while the black and red continuous lines stand for the LME and reweighted  $m_t \rightarrow \infty$  results, respectively. This plot has been already published in [204].

parts of the matrix elements the best results available, i.e. both  $\mathcal{A}^{(0)}$  were used and the double-triangle contribution are evaluated exactly, while for  $\mathcal{A}^{(1)}$  we use the various orders in the  $p_T$ -expansion. For comparison, the results are shown were  $\mathcal{A}^{(1)}$  is replaced by the one computed in LME up to  $\mathcal{O}(1/m_t^6)$  (full black line), which as mentioned before is valid up to  $M_{ZhH} < 2m_t$ . We observe that within the validity of the LME our results agree well with it. Furthermore, the results in the infinite top mass limit reweighted by the full amplitudes squared can be seen as the full red line in the plot, corresponding to the approach of ref.[196], keeping though the double triangle contribution in full top mass dependence. Differently from the LME line, the  $m_t \rightarrow \infty$  reweighted one shows a behaviour, for  $M_{Zh} \gtrsim 400$  GeV, similar to the behaviour of the  $p_T$  lines. Still, the difference between the reweighted result and the  $p_T$ -expanded ones is significant. The  $p_T$ -expanded results show very good convergence. The zero order in our expansion agrees extremely well with the higher orders in the expansion, and all the three results are very close up to  $M_{Zh} \sim 500$  GeV.

The calculation of the virtual two-loop corrections to the  $gg \rightarrow Zh$  is done using exact results for the triangle and double-triangle topologies, and in the  $p_T$ -expansion for the box one. The result of the calculation showed that we get the exact same MI's that was found for Higgs pair production [203], mostly these MI's are expressed in terms of generalised harmonic polylogarithms with the exception of two elliptic integrals. Using the LO calculation, we have shown the validity of the  $p_T$ -expansion covering the invariant mass interval  $M_{Zh} \lesssim 750$  GeV which covers  $\sim 98\%$  of the total phase space for 13 – 14

TeV energies.

The  $p_T$ -expansion agrees with per mill level with the numerical results found in [202]. However, it allows for fast computation of the amplitude with circa one second per phase space point using a modern laptop with mid-range specifications. Additionally, the integration over the  $\hat{t}$  variable in eq.(6.37) converges very well. The flexibility of our analytic results, an application to beyond-the-Standard Model is certainly possible.

Finally, it should be noted that this calculation complements nicely the results obtained in ref.[201] using a high-energy expansion, that according to the authors provides precise results for  $p_T \gtrsim 200$  GeV. The merging of the two analyses is going to provide a result that covers the whole phase space, can be easily implemented into a Monte Carlo code using Padé approximants, which is currently a work in progress in [Cite the new paper here-later](#)



## **Part III**

# **Higgs Pair at Hadron Colliders**



## 7 Overview of Higgs pair production at colliders

The dominant process for Higgs pair production at the LHC (and hadron colliders in general) is the gluon gluon fusion (ggF) via a heavy quark loop  $Q$ , mainly the top and beauty quark, with the latter contributing only to about 1%, see figure 7.1. This process

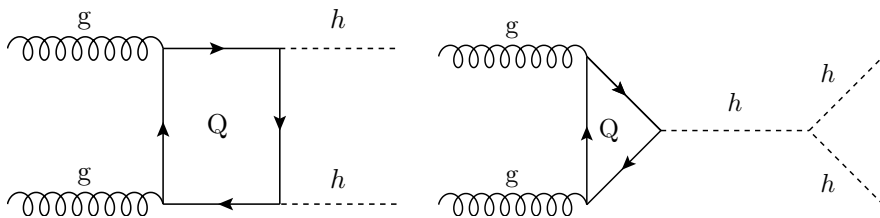
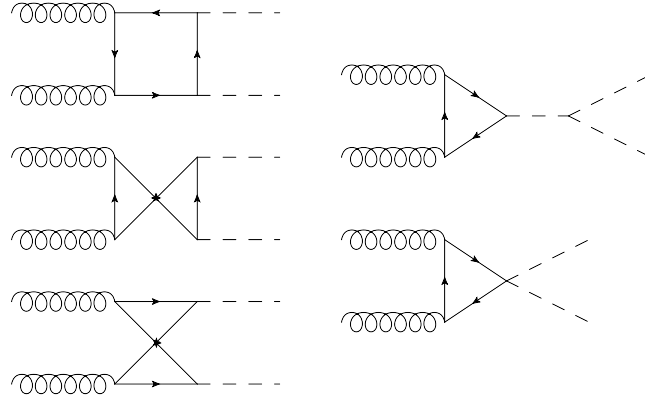


Figure 7.1. Feynman diagrams for the ggF process of Higgs pair production in the SM.

is well-studied at leading order (LO) analytically [284–287]. The next-to-leading QCD order (NLO) was initially computed using infinite top mass limit ( $m_t \rightarrow \infty$ ) using the Higgs effective field theory (HEFT) and implemented in the programme `Hpair` [110]. However, this approximation is not suitable for obtaining distributions, and using numerical methods [288–290] the full NLO results were obtained. In [291], parton shower effects were included in the NLO calculations, allowing the use of the NLO in event generators such as `PYTHIA` and `POWHEG`. Analytical calculations for the NLO corrections using small Higgs transverse momentum  $p_{T,h} \rightarrow 0$  yielded a good estimation for the numerical result [203]. The use of Padé approximation obtained also analytical results for the NLO result and a description for the three-loop (NNLO) form factors [292]. The NNLO cross section with top mass effects has been computed numerically in [293].

In this work, we have calculated the  $\sqrt{s} = 14$  TeV LO ggF inclusive cross-section and distributions with modified light Yukawa couplings by including the light quark loops and the coupling  $hhq\bar{q}$  described in the last diagram in figure 8.2. The calculation was carried out using a FORTRAN code utilising the `VEGAS` integration algorithm, and NNPDF30 parton distribution functions (PDF's)[294] implemented via `LHAPDF-6` package[295]. For the loop integrals (see Appendix), we have used the `COLLIER` library [296] for regularisation of the IR divergent light quark loops, that were assumed massless. A  $K$ -factor, for the NNLO correction were used according to the Higgs cross section working group recommended values [297, 298]:

$$K = \frac{\sigma_{NNLO}}{\sigma_{LO}}, \quad K_{14\text{TeV}} \approx 1.71. \quad (7.1)$$



**Figure 7.2.** The one-loop diagrams calculated in the ggF with modified Yukawa couplings

Since the cross-section is not expected to change a lot by changing the light Yukawa couplings, we use the same NNLO K-factor for all values of the scalings. The renormalisation  $\mu_R$  and factorisation  $\mu_F$  scales of the  $\alpha_s$  and PDF running are set to  $\mu_0 = 0.5 M_{hh}$ , and  $\alpha_s(M_Z) = 0.118$ . In our calculations, we did not consider the quark mass running, as the later will be accounted for in the K-factor.

### Theoretical systematic uncertainties

There are three main sources of theoretical *systematic* uncertainties:

1. Scale uncertainty: coming form the arbitrariness of scales choice.
2. PDF uncertainties : coming form the uncertainty in the PDF fitting and model.
3.  $\alpha_s$  running uncertainty: originating from the initial value (i.e.  $\alpha_s(M_Z)$ ).

In order compute these uncertainties, we follow the recommendations of the Higgs cross-section working group for the value and uncertainty of  $\alpha_s$

$$\alpha_s(M_Z) = 0.1180 \pm 0.0015, \quad (7.2)$$

and the methods described in [299, 300]. for PDF and  $\alpha_s$  uncertainties. In order to calculate the scale uncertainties, the cross-section was computed with different  $\mu_R$  and  $\mu_F$  values ranging between:

$$\frac{M_{hh}}{4} \leq \mu_R/\mu_F \leq M_{hh} \quad (7.3)$$

The scale uncertainty for the LO total cross-section was found to be  $+20\%, -16\%$ . Moreover, the PDF+ $\alpha_s$  uncertainty was  $\pm 6.8\%$ .

	$\sigma$ [fb]	Scale [fb]	PDF+ $\alpha_s$ [fb]	Total [fb]
SM HEFT (LO)	18.10	—	—	—
SM running mass (LO)	16.96	—	—	—
SM (LO)	21.45	+4.29 -3.43	$\pm 1.46$	+4.53 -3.73
SM (NLO) [301]	33.89	+6.17 -4.98	+2.37 -2.01	+6.61 -5.37
SM (NNLO) [293]	36.69	+0.77 -1.83	$\pm 1.10$ ( $g_{h\bar{q}\bar{q}} = g_{h\bar{b}\bar{b}}^{SM}$ )	+1.66 -6.43 (incl. $m_t$ uncertainty)
( $g_{h\bar{q}\bar{q}} = g_{h\bar{b}\bar{b}}^{SM}$ ) (ggF-LO)	21.84	+4.38 -3.51	$\pm 1.49$	+4.62 -3.81

**Table 7.1.** Gluon fusion (ggF) Higgs pair production cross-section with theoretical systematic uncertainties, for infinite top mass limit (SM HEFT), running mass, LO, NLO and NNLO QCD corrections. The NLO and NNLO results are taken from the references cited in the table. We also state the benchmark point ( $g_{h\bar{q}\bar{q}} = g_{h\bar{b}\bar{b}}^{SM}$ ) cross section result (all the light Yukawa couplings are scaled to the SM beauty Yukawa )

## results

The total cross sections with their uncertainties is shown in table ??.

## 7.1 Overview of Light Yukawa searches

There are additional measurements of the light-quark Yukawa couplings that might become relevant at HL-LHC or FCC-hh, a careful study of which is beyond the scope of the current work. Yet we attempt to include a discussion here, so as to provide a comparison with our study and to put it into proper context, or to serve as proposal for further studies.

The channel  $pp \rightarrow h+j$  has been suggested as a probe for charm Yukawa coupling [302] with charm-tagged jet having a potential bound of  $\kappa_c \sim 1$  for the HL-LHC, depending on the charm-tagging scheme. This process could be used for the first and second generations Yukawa couplings by looking at the shapes of kinematic distributions, the most important one being the  $p_T$  distribution [303–305]. The expected HL-LHC 95% CL bounds are  $\kappa_c \in [-0.6, 3.0]$ ,  $|\kappa_u| \lesssim 170$  and  $|\kappa_d| \lesssim 990$ . The use of  $h+j$  process along with other single Higgs processes have also been suggested as indirect probes for Higgs self coupling [112–116, 118], due to the contribution of the trilinear coupling to NLO electroweak corrections to these processes. In addition, experimental fits have been carried out for the trilinear coupling from single Higgs observables [147, 306].

It seems that for the HL-LHC, an optimal bound for the trilinear coupling can be obtained by combining both the data from single-Higgs process as well as Higgs pair production [146], with 68% CL bound on  $\kappa_\lambda \in [0.1, 2.3]$ , compared to the expected bound of  $\kappa_\lambda \in [0.0, 2.5] \cup [4.9, 7.4]$  coming from using di-Higgs measurements alone. Moreover, single Higgs processes, namely  $Zh$  and  $W^\pm h$  production, could also be useful in probing charm-Yukawa coupling using a mixture of  $b$ - and  $c$ -tagging schemes leveraging the mistagging probability of  $c$ -jets as  $b$ -jets in  $b$ -tagging working points, and vice-versa,

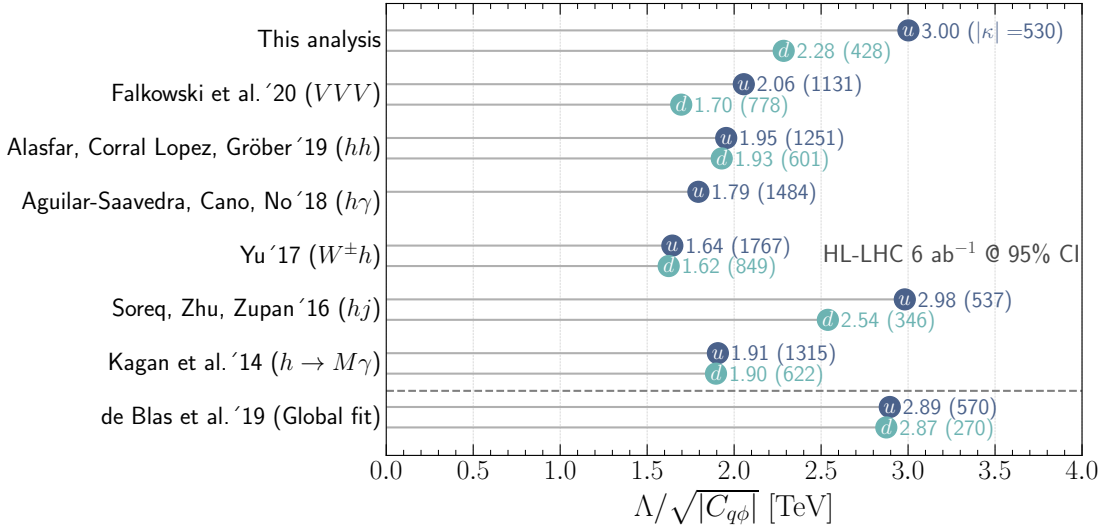


**Figure 7.3.** Summary of the 95% CI/CL sensitivity bounds on the SMEFT Wilson coefficients  $C_{u\phi}$  (blue), and  $C_{d\phi}$  (green). The bounds are interpreted in terms of the NP scale  $\Lambda$  that can be reached through the measurements of the Wilson coefficient at the HL-LHC at  $6 \text{ ab}^{-1}$ , the corresponding  $\kappa_q$ 's are shown inside the parentheses. Single parameter fit 95% CI bounds are used from this analysis for comparison with previous studies.

in order to break the degeneracy in the signal strength [307]. The use of this technique could probe  $\kappa_c \sim 1$  in the FCC-hh. Of course, for the charm-Yukawa coupling, the constraints are set to improve significantly, as there has been recent direct observation of  $h \rightarrow c\bar{c}$  [104]. Therefore, from here on, we will mainly concentrate on the process with more potential for constraining Yukawa couplings of the first generation quarks.

Rare Higgs decays to mesons,  $h \rightarrow M + V$ ,  $M = \Upsilon, J/\Psi, \phi \dots$ , were also suggested as a probe for light-quark Yukawa couplings [308–310], and there have been experimental searches for these decays [104, 311] with bounds on the branching ratios,  $\mathcal{B}(h \rightarrow X, \gamma, X = \Upsilon, J/\Psi, \phi) \sim 10^{-4} - 10^{-6}$  at 95% CL. It was shown in Ref. [312], that the charge asymmetry of the process  $pp \rightarrow hW^+$  vs  $pp \rightarrow hW^-$  can be used as a probe for light-quark Yukawa couplings as well as to break the degeneracy amongst quark flavours. Moreover, the rare process  $pp \rightarrow h\gamma$  is also a possible way to distinguish between enhancements of the up- and down-Yukawa couplings [313] where the authors have estimated the bounds on the up-Yukawa coupling of  $\kappa_u \sim 2000$  at the HL-LHC. Despite some processes appearing more sensitive than others, one should think of these processes as complementary to each other.

One of the main features of the effective couplings  $hhq\bar{q}$  and  $hhhq\bar{q}$  emerging from SMEFT operator  $\mathcal{O}_{q\phi}$ , or the Chiral Lagrangian for that matter, is that these couplings are either free from propagator suppression for  $hhq\bar{q}$  or scale with energy for  $hhhq\bar{q}$  while being safe from strong unitarity constraints. This feature gives processes with multiple Higgs and/or vector bosons  $V = W^\pm, Z$  an advantage in constraining  $\mathcal{O}_{q\phi}$ . The latter constraints come from the longitudinal degrees of freedom of the gauge bosons which

can be understood from the Goldstone boson equivalence theorem. The use of the final state  $VV$  as a probe for  $\mathcal{O}_{q\phi}$  is difficult due to the large SM background. However, the three-boson final state  $VVV$  was shown to give strong projected bounds for light-quark Yukawa couplings for HL-LHC with 95% CL bounds on  $\kappa_u \sim 1600$ , and  $\kappa_d \sim 1100$ . A ten fold improvement is expected at FCC-hh [314] with bounds of order  $\kappa_d \sim 30$ . Higgs pair production has a smaller SM background compared to  $VV$  production, but it has a significantly smaller cross section too, even when compared to  $VVV$ , as the latter process has already been observed at the LHC [315, 316].

On the contrary, Higgs pair production is inaccessible with the runs I-III of the LHC, but it is potentially accessible at the HL-LHC [317] having a  $\sigma \cdot BR \sim 1\text{fb}^{-1}$ . However, Higgs pair production, particularly the channel  $h \rightarrow b\bar{b}\gamma\gamma$ , is of significant interest as it has unique features. The first being the ability to constrain the trilinear and light-quark Yukawa couplings simultaneously, as we show in this work. Secondly, Higgs pair production could probe non-linear relations between Yukawa interaction and  $hhq\bar{q}$  couplings [318, 319]. Lastly, Higgs pair production is expected to be significant enhanced in certain models involving modification of light-quark Yukawa couplings (cf. [320–322])

For future colliders, like the FCC-hh at 100 TeV, in addition to Higgs pair production triple Higgs production might be an interesting channel for constraining the operators with Wilson coefficient  $C_{u\phi}$  and  $C_{d\phi}$  due to the energy increase of a Feynman diagram coupling the quarks to three Higgs bosons. In this case, a similar study to ours should be performed to see whether also in this case it will be important to do a combined fit on the light quark Yukawa couplings together with the trilinear and quartic Higgs self-couplings.<sup>1</sup>

Finally, we note that there are also non collider signatures for enhanced light-quark Yukawa couplings, manifesting in frequency shifts in atomic clocks from Higgs forces at the atomic level [324].

---

<sup>1</sup>In [323], it was shown that  $\sim \mathcal{O}(1)$  bounds on the quartic Higgs self-coupling can be reached at the FCC-hh.



# 8 Higgs pair as a probe for light Yukawas

## 8.1 Introduction

After the Higgs boson discovery the era of precision measurements of Higgs properties has begun. While the Higgs boson couplings to vector bosons and third generation fermions have been measured at the LHC and agree with their Standard Model (SM) prediction at the level of 10% – 20% [325], the situation for the Higgs self-couplings and couplings to first and second generation fermions is quite different. Current bounds on the trilinear Higgs self-coupling range from  $-5.0 < \lambda_{hhh}/\lambda_{hhh}^{SM} < 12.0$  [326] and are still above the limits of perturbative unitarity [52] or vacuum stability [167]. The quartic Higgs self-coupling is out of reach of the high-luminosity-LHC (HL-LHC) [317, 327]. Upper limits on the Higgs boson decays to muons are  $g_{h\bar{\mu}\mu}/g_{h\bar{\mu}\mu}^{SM} < 1.53$  [325], while current bounds on the Higgs coupling to electrons,  $g_{h\bar{e}e}/g_{h\bar{e}e}^{SM} < 611$ , are far away from the SM [328].

For the Yukawa couplings to the first and second generation quarks, henceforth denoted as light quark Yukawa couplings, the current best limits are obtained from a global fit to Higgs data [309, 329]. For instance for the HL-LHC, ref. [330] obtained for a projection on the coupling strength modification,  $\kappa_i = g_{h\bar{q}_i q_i}/g_{h\bar{q}_i q_i}^{SM}$ , where  $g_{h\bar{q}_i q_i}$  denotes the  $i = u, d, s, c$  Higgs Yukawa coupling to quarks, in a global fit

$$|\kappa_u| < 570, \quad |\kappa_d| < 270, \quad |\kappa_s| < 13, \quad |\kappa_c| < 1.2. \quad (8.1)$$

The determination of the light quark Yukawa couplings in a global fit is plagued by the fact that the Higgs boson width can only be measured at the LHC under certain assumptions.<sup>1</sup> The global fit can therefore not be considered to be completely model-independent. A more direct way of constraining the light Yukawa couplings is hence welcome.

Searches for exclusive decays of the Higgs boson to a vector meson and a photon  $h \rightarrow X\gamma$  with  $X = \rho, \omega, \phi, J/\psi$ <sup>2</sup> as a probe of light Yukawa couplings have been proposed in [308] and can be even used to probe flavour-off-diagonal Yukawa couplings [309] for instance in Higgs boson rare decays such as  $h \rightarrow MW^\pm$  or  $h \rightarrow MZ$ , with  $M$  denoting generically a scalar or pseudoscalar vector meson. From the experimental side, ATLAS and CMS have reported upper bounds on the decays  $h \rightarrow \rho\gamma$ ,  $h \rightarrow \phi\gamma$  in [336] and to  $h \rightarrow J/\psi\gamma$  in [337, 338]. The charm Yukawa coupling can also be constrained

---

<sup>1</sup>The width determination due to on- and off-shell measurements [331, 332] of Higgs boson couplings [333] is for instance made under the assumption that the couplings do not depend on the energy scale [334].

<sup>2</sup>In addition,  $h \rightarrow \Upsilon\gamma$  allows to probe the bottom Yukawa coupling [335].

to a factor of a few times its SM value at the HL-LHC making use of charm tagging in  $pp \rightarrow W/Zh$  with subsequent decay of the Higgs boson to  $c\bar{c}$  [307] (see [108, 339] for first experimental results) or in  $pp \rightarrow hc$  [302].

Another possibility for constraining the light quark Yukawa couplings is from Higgs kinematics. If the Higgs boson is produced with an associated jet, the transverse momentum distribution changes with respect to the SM one in the presence of enhanced quark Yukawa couplings of the second and first generation. For the second generation quarks, the main effect stems from log-enhanced contributions due to interference between top and light quark loop diagrams. This allows to set a bound on  $\kappa_c \in [-0.6, 3.0]$  at 95% C.L. at the HL-LHC [304]. Instead in the presence of significantly enhanced first generation quark Yukawa couplings the Higgs boson can be directly produced from initial state quarks, which again would alter the Higgs  $p_T$ -distribution [303]. For non-collider probes of the light Yukawa couplings see ref. [324].

In this paper, we will study the potential to constrain light quark Yukawa couplings from Higgs pair production. As for Higgs plus jet production, we can make use of kinematical information. We will mainly consider the case in which the modifications of the light Yukawa couplings can be described by a dimension six effective operator, denoted schematically by

$$\mathcal{O}_f = (\phi^\dagger \phi)(\bar{Q}_L \phi q_R). \quad (8.2)$$

The left-handed quark  $SU(2)$  doublet has been denoted by  $Q_L$ , the right-handed quark  $SU(2)$  singlet by  $q_R$ , while  $\phi$  is the scalar Higgs doublet field. In the presence of such an operator, both a shift in the Yukawa coupling to one Higgs boson as well as a new coupling of two Higgs bosons to two fermions modifies the Higgs pair production cross section. In the case of the top quark it was shown that such a new coupling can lead to large enhancements of the double Higgs production process [318, 340–342]. For the light quark Yukawa couplings this was shown in [320] under the assumption of universally enhanced light Yukawa couplings. We will consider more general scenarios and will show that indeed such an operator can also be constrained in di-Higgs production for the light generations of quarks. Under the assumption of linearly realised electroweak symmetry breaking we can then obtain a bound on the light quark Yukawa couplings which is competitive with the above mentioned ways of constraining them. We will also investigate how our bounds are modified if we allow for a modification of the trilinear Higgs self-coupling. Furthermore, we will discuss the possibility of charm tagging for di-Higgs final states, which will allow us to set bounds on the second generation quark Yukawa couplings.

The paper is structured as follows: in sect. 8.2 we will introduce our notation and point out under which circumstances scenarios considered in our analysis can be realised. In sect. 8.3 we present how the di-Higgs production process and the Higgs boson decays are modified in the presence of enhanced light quark Yukawa couplings. In sect. 8.4 we present the results of our analysis both in the presence of enhanced first and second generation Yukawa couplings. We also consider the potential reach of the HL-LHC by employing charm tagging. We conclude in sect. 8.5.

## 8.2 Effective Field Theory of light Yukawa couplings

Within the SM, the Higgs couplings to quarks are described by the Lagrangian

$$\mathcal{L}_y = -y_{ij}^u \bar{Q}_L^i \tilde{\phi} u_R^j - y_{ij}^d \bar{Q}_L^i \phi d_R^j + h.c., \quad (8.3)$$

with  $\tilde{\phi} = i\sigma_2\phi^*$ ,  $\sigma_2$  is the second Pauli matrix,  $\phi$  denotes the Higgs doublet,  $Q_L^i$  the left-handed  $SU(2)$  quark doublet of the  $i$ -th generation and  $u_R^j$  and  $d_R^j$  the right-handed up- and down-type fields of the  $j$ -th generation, respectively. Modifications of the SM from high-scale new physics can be described in a model-independent way by means of the SM effective field theory (SMEFT), in terms of higher dimensional operators. In particular, the couplings of the quarks to the fermions are modified by the operator

$$\Delta\mathcal{L}_y = \frac{\phi^\dagger \phi}{\Lambda^2} \left( c_{ij}^u \bar{Q}_L^i \tilde{\phi} u_R^j + c_{ij}^d \bar{Q}_L^i \phi d_R^j + h.c. \right), \quad (8.4)$$

where  $\Lambda$  denotes the cut-off of the effective field theory (EFT). The mass matrices of the up-type and down-type quarks are

$$M_{ij}^u = \frac{v}{\sqrt{2}} \left( y_{ij}^u - \frac{1}{2} c_{ij}^u \frac{v^2}{\Lambda^2} \right), \quad (8.5)$$

$$M_{ij}^d = \frac{v}{\sqrt{2}} \left( y_{ij}^d - \frac{1}{2} c_{ij}^d \frac{v^2}{\Lambda^2} \right). \quad (8.6)$$

They can be diagonalised by means of a bi-unitary transformation

$$m_{q_i} = \left( (V_L^{u/d})^\dagger M^{u/d} V_R^{u/d} \right)_{ii}, \quad (8.7)$$

while the CKM matrix is defined as  $V_{CKM} = (V_L^u)^\dagger V_L^d$ . By defining

$$\tilde{c}_{ij}^q = (V_L^q)_{ni}^* c_{nm}^q (V_R^q)_{mj}, \quad \text{with} \quad q = u, d, \quad (8.8)$$

we can write the couplings of one and two Higgs boson to fermions with

$$\mathcal{L} \supset g_{h\bar{q}_i q_j} \bar{q}_i q_j h + g_{h\bar{q}_i q_j} \bar{q}_i q_j h^2 \quad (8.9)$$

as

$$g_{h\bar{q}_i q_j} : \quad \frac{m_{q_i}}{v} \delta_{ij} - \frac{v^2}{\Lambda^2} \frac{\tilde{c}_{ij}^q}{\sqrt{2}}, \quad g_{hh\bar{q}_i q_j} : \quad -\frac{3}{2\sqrt{2}} \frac{v}{\Lambda^2} \tilde{c}_{ij}^q. \quad (8.10)$$

In the following, we will also use for the diagonal couplings alternatively the notation

$$g_{h\bar{q}_i q_i} = \kappa_q g_{h\bar{q}_i q_i}^{\text{SM}}, \quad g_{hh\bar{q}_i q_i} = -\frac{3}{2} \frac{1-\kappa_q}{v} g_{h\bar{q}_i q_i}^{\text{SM}}, \quad (8.11)$$

in a slight abuse of language of the  $\kappa$ -framework used often in experimental analyses.

Flavour-changing Higgs couplings are strongly constrained from low-energy flavour observables, such as meson-antimeson mixing. The bounds are of order  $|\tilde{c}_{uc/ds}| \lesssim 10^{-5} \Lambda^2/v^2$  and  $|\tilde{c}_{db/sb}| \lesssim 10^{-4} \Lambda^2/v^2$  [343]. Given that, a common assumption for the Wilson coefficients in eq. (10.1) is that of minimal flavour violation (MFV) [344], where

$$c_{ij}^u = \bar{c}_u y_{ij}^u, \quad c_{ij}^d = \bar{c}_d y_{ij}^d, \quad (8.12)$$

with flavour universal  $\bar{c}_u$  and  $\bar{c}_d$ . Hence, under the assumption of MFV the Yukawa matrices  $y_u$  ( $y_d$ ) and the Wilson coefficients  $c^u$  ( $c^d$ ) are simultaneously diagonalisable and no flavour changing Higgs interactions with quarks exist. We refrain though from making the assumption of MFV, due to the reason that with the Wilson coefficients being proportional to the Yukawa couplings, we introduce a strong hierarchy into the Higgs couplings to quarks. Since we want to describe modifications of the order of the ones in eq. (8.1) we would need to assume very low values of the new physics scale  $\Lambda$  and/or large Wilson coefficients, rendering the validity of the EFT questionable and in potentially conflict with measurements of the third generation couplings to the Higgs boson.

Instead, we will consider the case in which the  $\tilde{c}_{ij}^q$  are diagonal, though not proportional to the Yukawa matrices. This can be realised by appropriate choice of the parameters. For instance,  $V_{L/R}^u = \mathbb{1}$ ,  $V_R^d = \mathbb{1}$ , and  $V_L^d = V_{CKM}$ , which keeps  $\tilde{c}^u$  flavour-diagonal if  $c^u$  is chosen flavour-diagonal. Flavour violation then originates only from the CKM matrix. We will refer to this as flavour alignment. However, from a UV-perspective there is no obvious symmetry argument to enforce this at low-energy.

A possible way of keeping  $\tilde{c}$  flavour-diagonal with symmetry arguments could be realised for flavour universal  $c^{u/d}$  and a left-right symmetry rendering  $V_L = V_R$ . Then by setting universal  $\tilde{c}^{u/d}/\Lambda^2 \approx 1/(3 \text{ TeV})^2$  we get for instance a modification of the up-quark coupling to the Higgs boson of a factor of 500, but only a modification of the top Yukawa coupling by 1%, which is still consistent with the current limits on the top Yukawa coupling [345, 346]. Note that doing so for the down-type quarks would of course be more difficult, as it would imply a larger deviation in the bottom quark Yukawa coupling, due to its smaller mass. Alternatively, one can chose  $\tilde{c}^f$  flavour-diagonal (or with strongly suppressed flavour-off-diagonal elements) by choosing horizontal symmetries. We refer to [320] for a model with vector-like quarks and strongly enhanced light quark Yukawa couplings. Another realisation of large first and second generation Yukawa couplings without tree-level flavour-changing neutral currents (FCNCs) has been discussed in [347], and is referred to as spontaneous flavour violation. The basic idea is to achieve this by breaking the quark family number symmetry via the RH up-type or down-type quark wave function renormalisation, leading to either enhanced up- or down-type quark Yukawa couplings. A concrete realisation of this idea for a two-Higgs doublet model was discussed in [348].

We would also like to stress that from a UV perspective it makes sense to assume that if there is a modification in the light quark Yukawa couplings with respect to the SM, deviations in the di-Higgs production process can be expected, which in the limit of heavy new physics can be traced back to a coupling of two Higgs boson to two fermions.

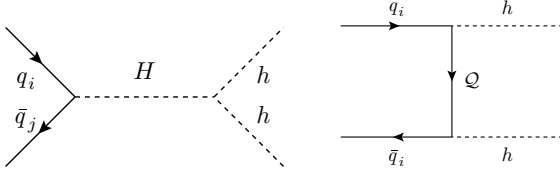


**Figure 8.1.** Examples of potential UV-complete models leading to a  $hh\bar{f}f$  coupling. The left Feynman diagram shows a heavy Higgs  $H$ , the right diagram a vector-like quark  $\mathcal{Q}$ .

We show this schematically in fig. 8.1 for a heavy new scalar and a heavy new vector-like fermion. The coupling of the SM-like Higgs boson in the models extended by a heavy new Higgs boson or a heavy new vector-like quark as shown in fig. 8.1 is modified due to a mixing with either the new Higgs boson, if it acquires a vacuum expectation value (VEV), or by the mixing between the quark and the new vector-like fermion. For the case of the heavy new scalar, the effective coupling of two SM-like Higgs bosons to fermions in the limit of  $m_H \gg E$ , with  $E$  denoting the energy scale of the process and  $m_H$  the Higgs mass of the heavy Higgs boson, can be written as

$$g_{hh\bar{q}q} \rightarrow -i \frac{g_{H\bar{q}q} g_{Hhh}}{m_H^2}. \quad (8.13)$$

A coupling  $g_{Hhh}$  always exist, if both of the Higgs fields acquire a VEV, since a portal term in the Lagrangian,  $(\phi^\dagger \phi)(\Phi^\dagger \Phi)$ , is always allowed by the symmetries. We denoted here the new Higgs multiplet by  $\Phi$  with neutral component  $H$ .

In the presence of new vector-like quarks that mix with the SM quarks, the coupling of two Higgs bosons to two fermions comes from  $\hat{t}/\hat{u}$  channel diagrams. If the mass of the new vector-like quark  $m_Q$  is  $m_Q \gg E$  one obtains for the coupling<sup>3</sup>

$$g_{hh\bar{q}q} \rightarrow -i \frac{g_{h\bar{q}\mathcal{Q}} g_{h\bar{\mathcal{Q}}q}}{m_Q}. \quad (8.14)$$

A more explicit consideration of models that realise large light Yukawa couplings is beyond the scope of this paper and we refer to existing work [320, 348].

We finally note that an alternative way of describing model-independent deviations from the SM Higgs couplings is by a non-linear effective Lagrangian (alternatively referred to as electroweak chiral Lagrangian) [349, 350]. While in SMEFT the Higgs boson is assumed to be part of an  $SU(2)$  doublet and the expansion is organised in terms of dimensionality of the operator, in the chiral Lagrangian the Higgs boson is assumed to be a singlet and the expansion is organised in terms of chiral dimension, where bosonic fields are assigned chiral dimension 0 and derivatives and fermion bi-linears chiral dimension 1. The Lagrangian responsible for a potential modification of the Yukawa couplings

<sup>3</sup>In Composite Higgs Models with vector-like quarks there is also a contribution from the non-linearities of the model.

can be written as [351]

$$\mathcal{L} = -\frac{v}{\sqrt{2}}(\bar{u}_L^i, \bar{d}_L^i)\Sigma \left( y_{q,ij} + k_{q,ij}\frac{h}{v} + k_{2q,ij}\frac{h^2}{v^2} + \dots \right) \begin{pmatrix} u_R^j \\ d_R^j \end{pmatrix} \quad (8.15)$$

with

$$\Sigma = e^{i\sigma^a \pi^a(x)/v}, \quad (8.16)$$

in terms of the Pauli matrices  $\sigma^a$  and the Goldstone bosons  $\pi^a$  with  $a = 1, 2, 3$ . The field  $\Sigma$  transforms linearly under the custodial symmetry  $SU(2)_L \times SU(2)_R$ . We note again as for the SMEFT that off-diagonal elements of  $k_q$  are strongly constrained. Compared to SMEFT the couplings of one or two Higgs boson to fermions are now uncorrelated, leading to different coefficients  $k_q$  and  $k_{2q}$ . In principle, the coefficients of the light fermion couplings to two Higgs bosons are yet unconstrained and di-Higgs production is the place to test if there exists a correlation among those and hence whether a linear or non-linear EFT prescription is to be preferred. While in the following we will mainly concentrate on the case of SMEFT we shall shortly comment also on the case of non-linear EFT.

### 8.3 Higgs pair production and Higgs decays with modified light Yukawa couplings

In this section we will describe how the Higgs pair production process for modified light quark Yukawa couplings is affected. While in the SM Higgs pair production is dominantly mediated by gluons fusing into a heavy quark loop coupling to the Higgs boson, for large first and second generation quark Yukawa couplings also quark annihilation becomes relevant. For a phenomenological analysis we also need to take into account the Higgs boson decays, which we describe in the last part of the section.

#### 8.3.1 Higgs pair production via gluon fusion

The dominant process for Higgs pair production at the LHC in the SM is the gluon fusion process (ggF) via a heavy quark loop  $Q$ , where  $Q$  stands mainly for the top quark. The bottom quark contributes with less than 1%. We show the Feynman diagrams for the process in fig. 7.1. The process has been known since long at leading order (LO) in full mass dependence [284–287]. The next-to-leading order (NLO) in the strong coupling constant was initially computed using the infinite top mass limit ( $m_t \rightarrow \infty$ ) and reweighted with the full LO results [110]. However, this approximation is only valid up to the top quark threshold. More recently, the NLO QCD corrections have been computed in full top mass dependence, showing that the infinite top mass limit overestimates the full result by 14% [288–290].<sup>4</sup> For distributions, the approximation of infinite top

<sup>4</sup>The numerical NLO QCD results for the virtual corrections were cross-checked by employing different analytic expansions [203, 352, 353].

mass is even worse. At next-to-next-to leading order (NNLO) results are available in the infinite top mass limit [354, 355] and by including top mass effects for the double real radiation [293]. First steps towards an inclusion of top mass effects for the virtual corrections (for the triangle only) have been made in [292, 356] and for the light fermion triangle contributions the NNLO has been computed in [357].

For our analysis, we have calculated the  $\sqrt{s} = 14$  TeV LO ggF inclusive cross section and distributions with modified light Yukawa couplings by including the light quark loops and the coupling  $hhq\bar{q}$  shown in fig. 8.2. The calculation was carried out using a

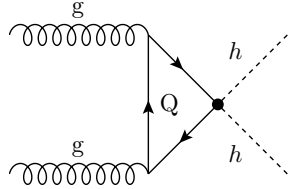


**Figure 8.2.** The new diagram for ggF emerging from the  $hhq\bar{q}$  coupling stemming from an effective dim-6 operator.

private FORTRAN implementation of the LO cross section utilising the VEGAS integration algorithm, and NNPDF30 parton distribution functions (PDF's)[294] implemented via the LHAPDF-6 package [295]. For the one-loop integrals appearing in the form factors of the box and triangle diagrams, we have used the COLLIER library [296] to ensure numerical stability of the loop integral calculation for massless quarks inside the loops. A  $K$ -factor for the NNLO correction was used following the recommendations by the Higgs cross section working group [298]

$$K = \frac{\sigma_{NNLO}}{\sigma_{LO}}, \quad K_{14 \text{ TeV}} = 1.72. \quad (8.17)$$

For differential distributions in the invariant mass of the Higgs boson pair,  $M_{hh}$ , we extract a differential  $K$ -factor from [293]. As a reference cross section at NNLO [293] for the analysis in sect. 8.4 we use

$$\sigma_{NNLO}^{\text{SM}} = 36.69^{+1.99}_{-2.57} \text{ fb}. \quad (8.18)$$

The uncertainty stems from the scale choice, the PDF+ $\alpha_s$  error and the uncertainty associated to the usage of the infinite top mass limit in parts of the calculation. Since we found that the cross section does not change much once the effects of the modified light Yukawa couplings are included, we use the same NNLO  $K$ -factor for all values of the scalings. The renormalisation,  $\mu_R$ , and factorisation scales,  $\mu_F$ , are set to  $\mu_0 = M_{hh}/2$  as has been pointed out as an optimal choice in ref. [358], and  $\alpha_s(M_Z) = 0.118$ .

## Results

For comparison of the results with modified Yukawa couplings with the SM results, we define as a benchmark point the case where all first and second generation quark Yukawa

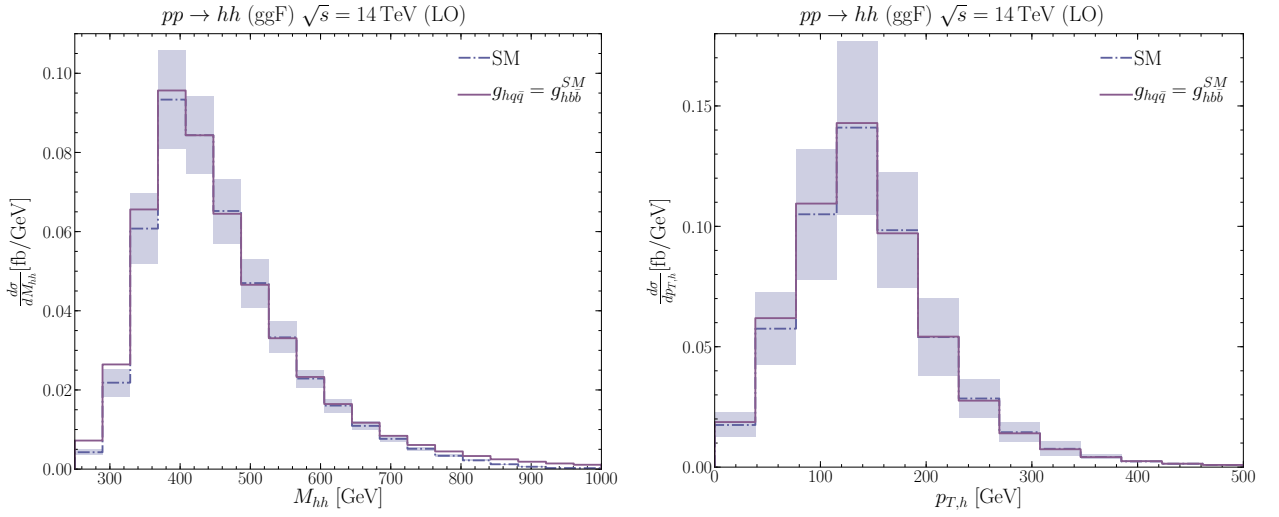


**Figure 8.3.** *Left:* The di-Higgs invariant mass differential cross section  $d\sigma/dM_{hh}$  for the SM at LO and the benchmark point toy. The error boxes denote the total scale, PDF and  $\alpha_s$  uncertainties. *Right:* The same but for the Higgs transverse momentum  $p_{T,h}$  distribution.

couplings are scaled to the SM bottom Yukawa coupling, which we will refer to in plots and tables as  $g_{h\bar{q}\bar{q}} = g_{h\bar{b}\bar{b}}^{\text{SM}}$ . This means we scale the Yukawa couplings by  $\kappa_q = g_{h\bar{q}\bar{q}}/g_{h\bar{q}\bar{q}}^{\text{SM}}$  with

$$\kappa_u = 1879, \quad \kappa_d = 889, \quad \kappa_s = 44, \quad \kappa_c = 3.3, \quad (8.19)$$

and use only flavour-diagonal modifications of the quark Yukawa couplings. This benchmark is inspired by ref. [320].

Figure 8.3 shows the di-Higgs invariant mass  $M_{hh}$ - and the  $p_{T,h}$ -distributions for the computed LO process. From the distributions it is evident, that the change of the ggF process in the presence of enhanced light Yukawa couplings is quite small. The reason is that the box contribution which is the major part of the cross section has two fermion coupling insertions and hence is strongly suppressed for all the light quarks with respect to the top quark loop diagrams. The bottom quark contribution to the ggF process in the SM is less than 1% and comes mainly from the triangle diagram, so adding several contributions from similar size does not change the cross section by much. Also the new diagrams (*cf.* fig. 8.2) are suppressed compared to the box diagrams of the top quark. In the presence of enhanced light quark Yukawa couplings the Higgs boson pair can though be directly produced by quark annihilation. We turn to discuss this process in the next part. In the meanwhile we can conclude that for the ggF process we can improve on the LO predictions by using SM  $K$ -factors and that the effects of light Yukawa coupling modifications for the ggF process are small for the still allowed modifications.

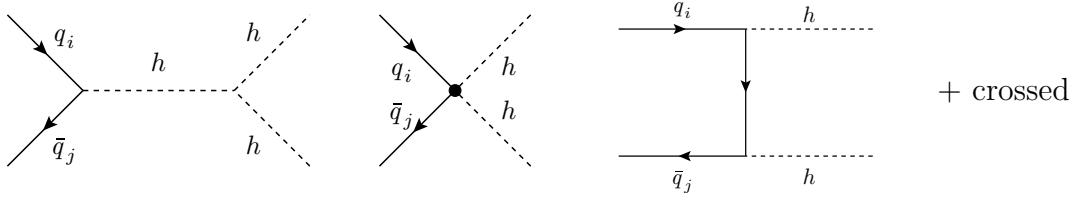


Figure 8.4. Feynman diagrams for the qqA Higgs pair production.

### 8.3.2 Higgs pair production via quark anti-quark annihilation

If the Yukawa couplings of the light quark generations are sufficiently increased, the Higgs bosons will be produced directly from the constituents of the proton with a sizeable rate. The quark anti-quark annihilation (qqA) process becomes then relevant for Higgs pair production. The qqA process has four Feynman diagrams shown in the fig. 8.4.

The differential cross section given by

$$\frac{d\hat{\sigma}_{q_i\bar{q}_j}}{d\hat{t}} = \frac{1}{16\pi} \frac{1}{12\hat{s}} \left[ \left| 2g_{hhq_i\bar{q}_j} + \frac{g_{hhh} g_{hq_i\bar{q}_j}}{\hat{s} - m_h^2 - im_h\Gamma_h} \right|^2 + \mathcal{O}(g_{hq_i\bar{q}_j}^4) \right]. \quad (8.20)$$

We neglect here the  $\hat{t}$  and  $\hat{u}$  channel diagrams, as their contribution is typically only  $\sim 0.1\%$  of the total cross section.

The hadronic cross section is then obtained by

$$\sigma_{\text{hadronic}} = \int_{\tau_0}^1 d\tau \int_{\hat{t}_-}^{\hat{t}_+} d\hat{t} \sum_{i,j} \frac{d\mathcal{L}^{q_i\bar{q}_j}}{d\tau} \frac{d\hat{\sigma}_{q_i\bar{q}_j}}{d\hat{t}}, \quad (8.21)$$

with  $\tau_0 = 4m_h^2/s$ ,  $\hat{s} = \tau s$  and

$$\hat{t}_\pm = m_h^2 - \frac{\hat{s}(1 \mp \beta)}{2} \quad \text{and} \quad \beta = \sqrt{1 - \frac{4m_h^2}{\hat{s}}}. \quad (8.22)$$

The parton luminosity is given by

$$\frac{d\mathcal{L}^{q_i\bar{q}_j}}{d\tau} = \int_\tau^1 \frac{dx}{x} \left[ f_{q_i}(x/\tau, \mu_F^2) f_{\bar{q}_j}(x, \mu_F^2) + f_{\bar{q}_j}(x/\tau, \mu_F^2) f_{q_i}(x, \mu_F^2) \right]. \quad (8.23)$$

We neglected all the kinematical masses in accordance with the 5-flavour scheme of the PDFs while the coupling of the Higgs boson to the light quarks (for flavour diagonal couplings) is

$$g_{hq_i\bar{q}_j} = \frac{m_q^{\overline{MS}}(\mu_R)}{v} \kappa_q \delta_{ij}, \quad (8.24)$$

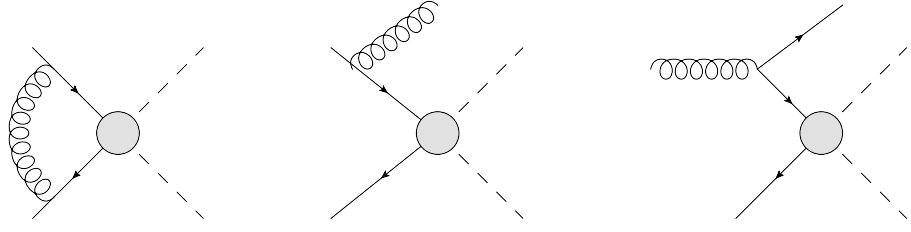


**Figure 8.5.** Generic form of the QCD corrections of order  $\mathcal{O}(\alpha_s)$  to the  $qqA$  Higgs pair production.

and analogously for the  $g_{hhq_i\bar{q}_j}$  coupling.<sup>5</sup>

### NLO QCD correction

Since NLO QCD corrections are sizeable, we will take them into account in our analysis. For this purpose, we will detail here how we obtained them. Since the  $\hat{t}$  and  $\hat{u}$  channel diagrams are strongly suppressed we can take the NLO QCD corrections over from  $b\bar{b} \rightarrow h$  in the 5-flavour scheme [359–361]<sup>6</sup> by some adjustments taking into account the modified LO cross section and the different kinematics of the process. The Feynman diagrams at NLO QCD are shown in fig. 8.5. For convenience and for making our adjustments explicit we report here the formulae from [364]

$$\sigma(q\bar{q} \rightarrow h) = \sigma_{LO} + \Delta\sigma_{q\bar{q}} + \Delta\sigma_{qg} \quad (8.25a)$$

$$\Delta\sigma_{q\bar{q}} = \frac{\alpha_s(\mu_R)}{\pi} \int_{\tau_0}^1 d\tau \sum_q \frac{d\mathcal{L}^{q\bar{q}}}{d\tau} \int_{\tau}^1 dz \hat{\sigma}_{LO}(Q^2 = z\tau s) \omega_{q\bar{q}}(z) \quad (8.25b)$$

$$\Delta\sigma_{qg} = \frac{\alpha_s(\mu_R)}{\pi} \int_{\tau_0}^1 d\tau \sum_{q,\bar{q}} \frac{d\mathcal{L}^{qg}}{d\tau} \int_{\tau}^1 dz \hat{\sigma}_{LO}(Q^2 = z\tau s) \omega_{qg}(z) \quad (8.25c)$$

and

$$\hat{\sigma}_{LO}(Q^2) = \int_{\hat{t}_-}^{\hat{t}_+} \frac{d\hat{\sigma}_{q_i\bar{q}_j}}{d\hat{t}} \quad (8.26)$$

with  $z = \tau_0/\tau$ ,  $\sigma_{LO} = \sigma_{\text{hadronic}}$  of eq. (8.21), and the  $\omega$  factors are given by

$$\begin{aligned} \omega_{q\bar{q}}(z) &= -P_{qg}(z) \ln \frac{\mu_F^2}{\tau s} + \frac{4}{3} \left\{ \left( 2\zeta_2 - 1 + \frac{3}{2} \ln \frac{\mu_R^2}{M_{hh}^2} \right) \delta(1-z) \right. \\ &\quad \left. + (1+z^2) \left[ 2\mathcal{D}_1(z) - \frac{\ln z}{1-z} \right] + 1-z \right\}, \end{aligned} \quad (8.27a)$$

$$\omega_{qg}(z) = -\frac{1}{2} P_{qg}(z) \ln \left( \frac{\mu_F^2}{(1-z)^2 \tau s} \right) - \frac{1}{8} (1-z)(3-7z), \quad (8.27b)$$

<sup>5</sup>We note that there is no inconsistency with such an assumption since in scenarios of modified Yukawa couplings, the masses of the quarks need not to be generated by electroweak symmetry breaking.

<sup>6</sup>Note that the NLO and NNLO QCD corrections for  $b\bar{b}hh$  have been given in [362, 363].

with  $\zeta_2 = \frac{\pi^2}{6}$ . The Altarelli Parisi splitting functions  $P_{qq}(z)$  and  $P_{qg}(z)$  [365–367] are given by

$$P_{qq}(z) = \frac{4}{3} \left[ 2\mathcal{D}_0(z) - 1 - z + \frac{3}{2} \delta(1-z) \right], \quad (8.28a)$$

$$P_{qg} = \frac{1}{2} \left[ z^2 + (1-z)^2 \right], \quad (8.28b)$$

and the ‘plus’ distribution is

$$\mathcal{D}_n(z) := \left( \frac{\ln(1-z)^n}{1-z} \right)_+. \quad (8.29)$$

We have chosen the renormalisation scale  $\mu_R = M_{hh}$  and the factorisation scale  $\mu_F = M_{hh}/4$ , as central values. We define the NLO  $K$ -factor, as

$$K_{NLO} = \frac{\sigma_{NLO}}{\sigma_{LO}} = 1.28 \pm 0.02, \quad (8.30)$$

with the error denoting the theoretical uncertainty. The  $K$ -factor does not depend on the scaling of the couplings, nor the flavour of the initial  $q\bar{q}$  since the LO cross section factors out (with exception of the different integration in the real contributions).

## Results

While in the SM, the contribution from quark annihilation to a Higgs boson pair is below 0.11 fb at NLO, it scales like  $\sim \kappa_q^2 m_q^2/v^4$ , dominated by the  $hh\bar{q}q$  diagram as can be seen from eq. (8.20), hence showing significant enhancement for enhanced Yukawa couplings. For our benchmark scenario ( $g_{h\bar{q}q} = g_{h\bar{b}b}^{\text{SM}}$ ) we find for the cross section

$$\sigma_{NLO}^{qqA} = 284 \pm 25 \text{ fb}, \quad (8.31)$$

and therefore a significantly larger cross section as for the ggF process. In fig. 8.6 we compare the ggF process (black line) for rescaled charm coupling to the Higgs boson(s) with the qqA process for different scalings of the light quark Yukawa couplings (different coloured, dashed, dotted solid and dashed dotted lines). We find that for sufficiently large scaling of the Yukawa couplings still allowed by current data, qqA can be even the dominant di-Higgs production channel. Note that in the figure we scale the Yukawa couplings for the different quark mass eigenstates differently. For the up and down quark Yukawa coupling the scaling is the same, hence the effect from rescaling the down Yukawa coupling is larger even though the up quark is more abundant in the proton. The plot shows nicely for which values of the coupling modifications the qqA process surpasses ggF.

We would also like to give a qualitative argument for the dominance of qqA for large  $\kappa_q$ . The dominant term for the qqA comes from the  $hh\bar{q}q$  vertex diagram, such that the

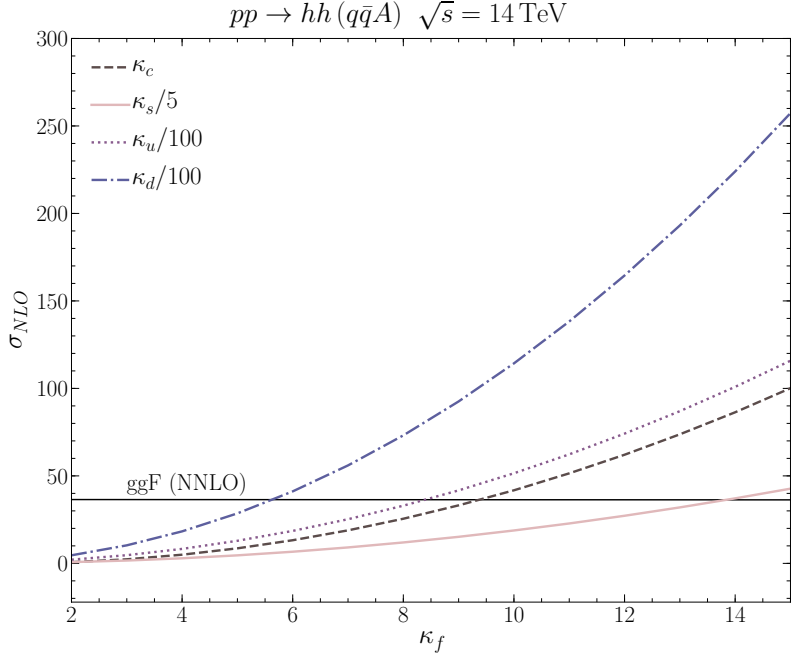


**Figure 8.6.** The NLO cross section for the  $q\bar{q}A$  process for different scalings of the quark Yukawa couplings. The solid black line shows the NNLO ggF process width rescaled charm Yukawa coupling, whose effect though is unrecognisable in the plot.

$q\bar{q}A$  cross section behaves for large values of  $\kappa$  as (assuming that  $\sigma_{SM}^{q\bar{q}A} \sim 0$ )

$$(\sigma^{q\bar{q}A} - \sigma_{SM}^{q\bar{q}A}) \sim g_{hhq\bar{q}}^2 \sim v^{-4} m_q^2 \kappa_q^2. \quad (8.32)$$

The ggF cross section instead gets contributions from light quark loops from the diagram in fig. 8.2 interfering with top quark loops in the triangle SM diagram, leading to a scaling of

$$(\sigma^{ggF} - \sigma_{SM}^{ggF}) \sim \kappa_q \frac{m_q^2}{v^2 M_{hh}^2} \ln^2 \left( \frac{M_{hh}}{m_q} \right). \quad (8.33)$$

Taking the ratio we get

$$\frac{(\sigma^{q\bar{q}A} - \sigma_{SM}^{q\bar{q}A})}{(\sigma^{ggF} - \sigma_{SM}^{ggF})} \sim \frac{\kappa_q}{v^2 \left( \frac{\ln^2 \left( \frac{M_{hh}}{m_q} \right)}{M_{hh}^2} \right)}. \quad (8.34)$$

This ratio approaches one (neglecting effects from different PDFs) when

$$\kappa_q^{qqA=ggF} \sim \frac{v^2 \ln^2 \left( \frac{M_{hh}}{m_q} \right)}{M_{hh}^2}. \quad (8.35)$$

Using this order of magnitude estimate, we see that the two cross sections are roughly equal if  $\kappa_c^{qqA=ggF} \sim 1$ ,  $\kappa_s^{qqA=ggF} \sim 10$  and  $\kappa_u^{qqA=ggF} \sim \kappa_d^{qqA=ggF} \sim 10^3$ . The actual values of  $\kappa_q^{qqA=ggF}$  can be read from fig. 8.6. We observe that  $\kappa_q^{qqA=ggF}$  values are not yet excluded, particularly for the first family.

In fig. 8.7 we show the di-Higgs invariant mass normalised differential cross section distributions for the  $g_{hq\bar{q}} = g_{hb\bar{b}}^{\text{SM}}$  benchmark point at NLO compared to the NNLO SM ggF cross section extracted from [293]. We notice a considerable shape difference, with shifted peak to the left, and a larger tail. This will allow us later on to use kinematical information to extract the light quark Yukawa couplings.

### 8.3.3 Higgs decays

The light fermion decay channels will no longer be negligible for enhanced light Yukawa couplings. The decay channels  $h \rightarrow gg$ ,  $h \rightarrow \gamma\gamma$  and  $h \rightarrow Z\gamma$  containing fermion loops

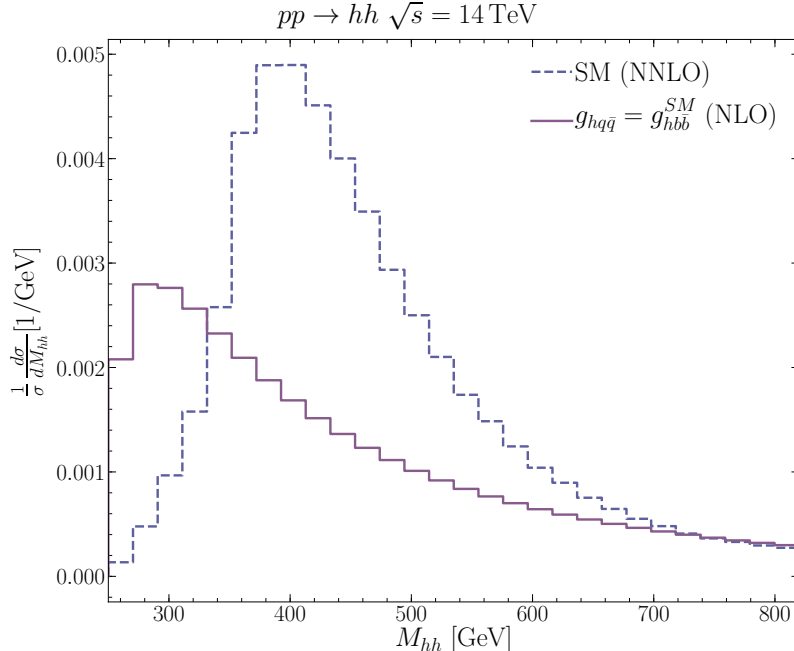


**Figure 8.7.** The qqA normalised NLO invariant mass differential cross section distribution for the benchmark point ( $g_{hq\bar{q}} = g_{hb\bar{b}}^{\text{SM}}$ ) (solid line) and the NNLO SM ggF cross section obtained from [293] (dashed line).

will get modified, but similarly to the production, the modification is  $\sim 2\kappa_q(m_q^2/m_h^2) \ln^2(m_q/m_h)$ . Thus, the main effect on the Higgs boson branching ratios and width is the ‘opening’ of the new light fermion channels.

In order to compute the Higgs partial widths and branching ratios (BR) at higher orders in QCD, we have modified the FORTRAN programme HDECAY [368, 369] to include the light fermion decay channels and loops in the above-mentioned decays. In the SM, light fermion BRs are of order  $\mathcal{O}(10^{-4})$  for  $h \rightarrow c\bar{c}$ ,  $\mathcal{O}(10^{-6})$  for  $h \rightarrow s\bar{s}$  and  $< \mathcal{O}(10^{-9})$  for the first generation quarks [298]. In our benchmark point ( $g_{h\bar{q}\bar{q}} = g_{h\bar{b}\bar{b}}^{\text{SM}}$ ) these would increase to  $\sim 18\%$ . Correspondingly, the BRs for  $h \rightarrow b\bar{b}/VV/\tau^+\tau^-$  decrease due to the increased Higgs width in the model.

In fig. 8.8 we show the BRs, denoted by  $\mathcal{B}$  in the following, of the Higgs boson pair with the best prospects for discovering Higgs pair production,  $hh \rightarrow b\bar{b}b\bar{b}$ ,  $hh \rightarrow b\bar{b}\gamma\gamma$  and  $hh \rightarrow b\bar{b}\tau^+\tau^-$  [326], and in addition we show for later purpose also  $hh \rightarrow c\bar{c}\gamma\gamma$ . Once we increase the light quark Yukawa couplings (shown for the different quarks by the different coloured lines) the BRs to  $b\bar{b}b\bar{b}$ ,  $b\bar{b}\gamma\gamma$  and  $b\bar{b}\tau^+\tau^-$  decrease due to the increased Higgs width. Instead the  $\mathcal{B}(hh \rightarrow c\bar{c}\gamma\gamma)$  first increases with increasing  $\kappa_c$ , but starts decreasing after reaching a maximum around  $\kappa_c \approx 8$ , where the  $\mathcal{B}(h \rightarrow c\bar{c})$  asymptotically reaches 1 while the  $\mathcal{B}(h \rightarrow \gamma\gamma)$  continues decreasing.

In fig. 8.9 we show the signal strength modifier defined here as

$$\mu_i := \frac{\sigma \mathcal{B}_i}{\sigma^{\text{SM}} \mathcal{B}_i^{\text{SM}}} \quad (i = b, c), \quad (8.36)$$

for final states with bottom (left hand side) and charm quarks (right hand side) for first generation (plots in the upper row) and second generation (plots in the lower row) modified Yukawa couplings. For the first generation, we obtain enhancement of both of the signal strengths  $\mu_c$  and  $\mu_b$ , as seen plots in the top of fig. 8.9. The second generation signal strength is instead reduced with respect to the SM for the channels with bottom quarks in the final state  $\mu_b := \sigma \mathcal{B}_b / \sigma^{\text{SM}} \mathcal{B}_b^{\text{SM}}$  when scaling the charm and strange Yukawa couplings, as seen in the lower left plot of fig. 8.9. Nevertheless, when considering channels with charm quarks in the final state the signal strength  $\mu_c := \sigma \mathcal{B}_c / \sigma^{\text{SM}} \mathcal{B}_c^{\text{SM}}$  is enhanced due to both enhancements from the cross section and BRs. The increased cross section in the presence of enhanced light quark Yukawa couplings has to compete with the decreased BRs for the standard search channels for di-Higgs production. We shall notice however, that while the increase of the cross section comes mainly from the  $q\bar{q}hh$  vertex diagram, the decrease of the BRs stems from the increased width which would be in good approximation (for flavour-diagonal couplings)

$$\Gamma_H \approx \Gamma_{\text{SM}} + \sum_{q=c,s,u,d} \frac{g_{h\bar{q}_iq_i}^2}{(g_{h\bar{q}_iq_i}^{\text{SM}})^2} \Gamma_q, \quad (8.37)$$

where  $\Gamma_q$  stands generically for the partial width of the Higgs boson decaying to light quarks. In a non-linear EFT as briefly discussed in sect. 8.2, the couplings of one Higgs

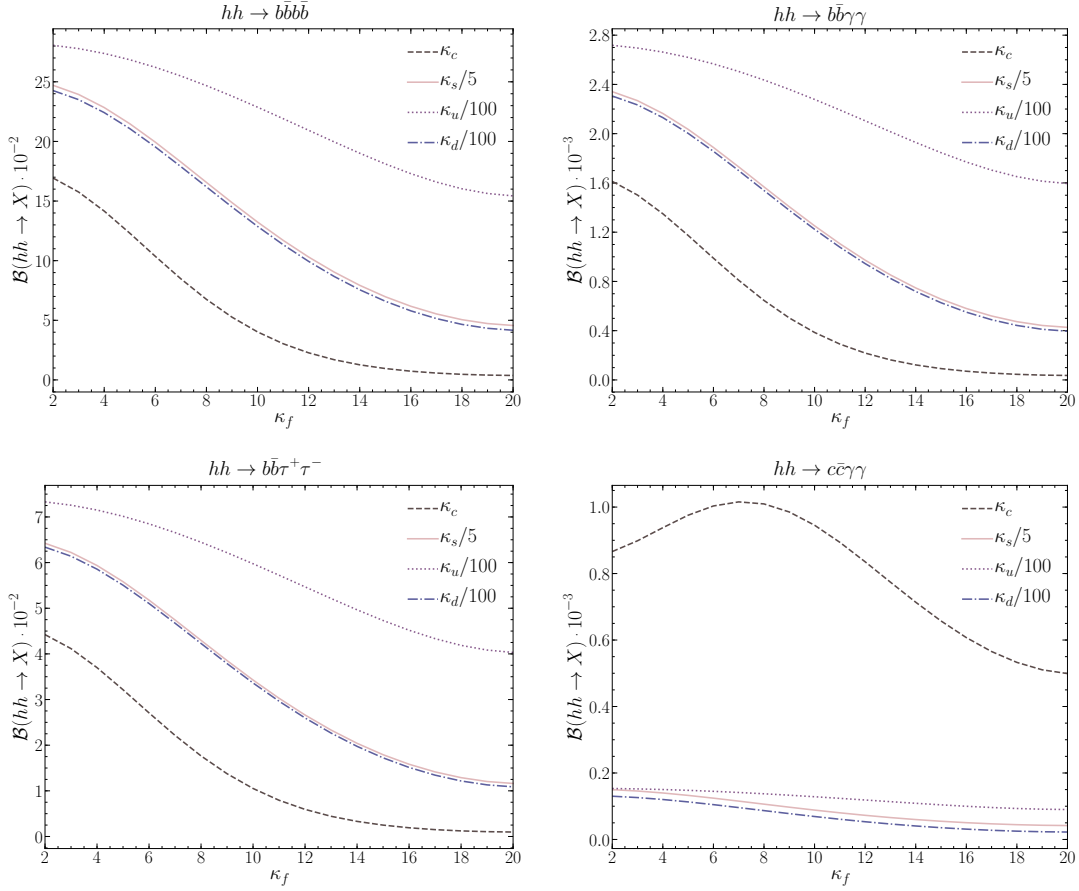


**Figure 8.8.** Different Higgs pair final states BRs including state-of-the-art QCD corrections as functions of the coupling modification factors  $\kappa_f$ . *Top left:*  $hh \rightarrow b\bar{b}b\bar{b}$ . *Top right:*  $hh \rightarrow b\bar{b}\gamma\gamma$ . *Bottom left:*  $hh \rightarrow b\bar{b}\tau^+\tau^-$ . *Bottom right:*  $hh \rightarrow c\bar{c}\gamma\gamma$ .

boson to quarks and two Higgs bosons to quarks are uncorrelated. So an increase of the cross section for  $hh$  production in the presence of modified light quark Yukawa couplings does not need to go hand in hand with a decrease of the BRs in the final states with bottom quarks (or at least the decrease could be in-proportional).

## 8.4 Phenomenological analysis

In this section we will investigate whether enhanced light quark Yukawa couplings can be measured in Higgs pair production. As we have seen in the previous section, we can get an enhancement in the signal strengths for first generation quarks from the enhanced cross sections while BRs in the standard di-Higgs search channels decrease. We have also seen that final states with charm quarks might be worth studying further for enhanced second generation Yukawa couplings. Here in this section, we will perform

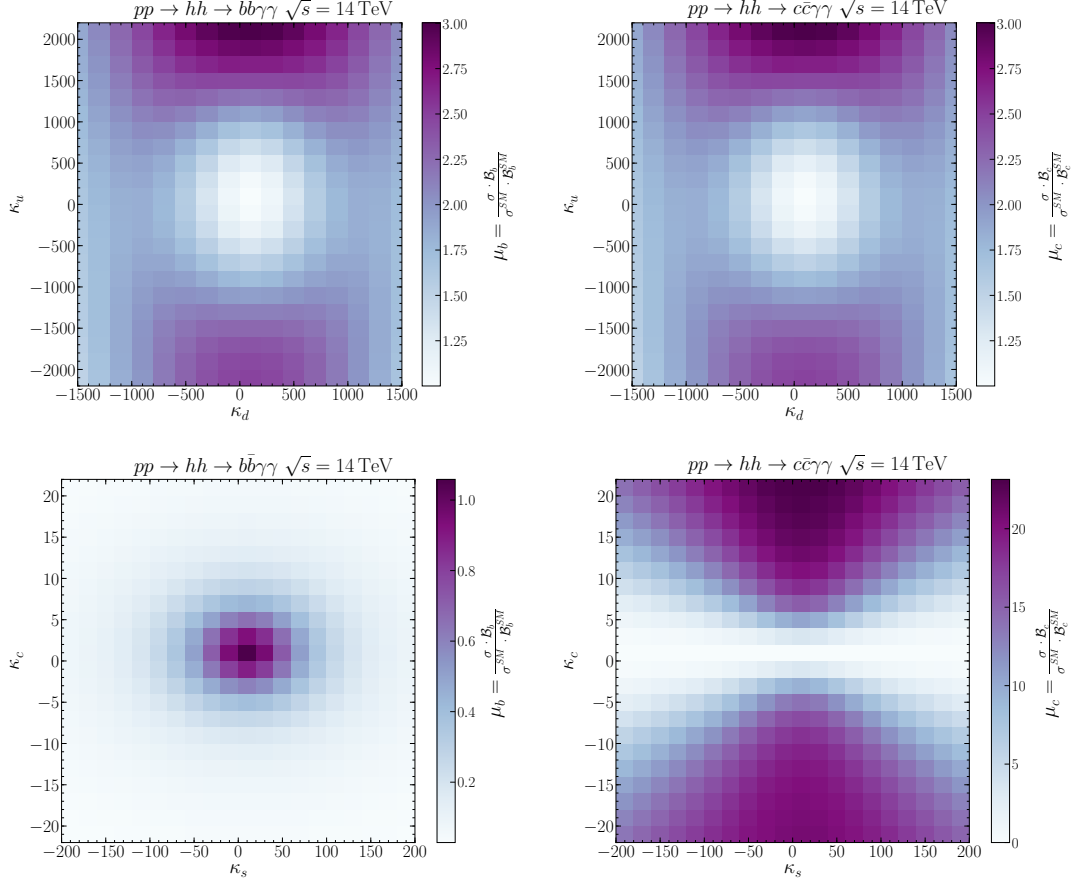


**Figure 8.9.** Signal strength modifier  $\mu = \sigma \mathcal{B}(hh \rightarrow X) / (\sigma^{SM} \mathcal{B}^{SM}(hh \rightarrow X))$  fits for bottom quark (left plots) and charm quark (right plots) final states for first (upper row) and second (lower row) generations quark Yukawa modifications.

a phenomenological analysis to see if the HL-LHC has potential to constrain the light quark Yukawa couplings in di-Higgs channels. The first part of the section is devoted to the analysis strategy, before we discuss the bounds from final states with bottom quarks. We will be focussing in particular on the  $b\bar{b}\gamma\gamma$  final state as it holds promising prospects [301, 370–374] despite the low BR of 0.27% in the SM for the Higgs boson pair. At the end of the section we take a closer look at the  $c\bar{c}\gamma\gamma$  final state, which is in particular interesting for enhanced charm Yukawa couplings.

For our phenomenological analysis we do not assume that the efficiency is constant for the new physics hypothesis with respect to the SM efficiency. Hence, we use the full definition of the signal strength  $\mu$  as the ratio of the number of events measured or expected given the new physics hypothesis over the number of events expected by the

SM (null) hypothesis

$$\mu = \frac{N_{\text{exp}}}{N_{\text{exp}}^{\text{SM}}}. \quad (8.38)$$

The number of expected events  $N_{\text{exp}}$  at a hadron collider with integrated luminosity  $L$  and selection efficiency  $\epsilon_{\text{SEL}}$  in the narrow width approximation for a process  $pp \rightarrow R$  with subsequent decay of  $R \rightarrow X$  is given by the formula

$$N_{\text{exp}} = \sigma(pp \rightarrow R) \mathcal{B}(R \rightarrow X) L \epsilon_{\text{SEL}}. \quad (8.39)$$

The selection efficiency can be written in terms of several factors by

$$\epsilon_{\text{SEL}} = \epsilon_{\text{Acc}} \cdot \epsilon_{\text{Rec}} \cdot \epsilon_{\text{Trig}} \cdot \epsilon_{\text{cut}}, \quad (8.40)$$

with  $\epsilon_{\text{Acc}}$  being the detector acceptance efficiency,  $\epsilon_{\text{Rec}}$  the efficiency from reconstruction,  $\epsilon_{\text{Trig}}$  the trigger efficiency and  $\epsilon_{\text{cut}}$  the efficiency obtained from the applied kinematical cuts on the signal. For the ATLAS and CMS experiments, the acceptance for the Higgs pair production is close to 100% due to the complete coverage of the pseudorapidity range of  $2.5 < |\eta| < 5$ , so we use  $\epsilon_{\text{Acc}} = 1$ . The other efficiencies will be discussed in more detail in subsect. 8.4.2.

### 8.4.1 Event generation

The parton showering and hadronisation of the process  $pp \rightarrow hh \rightarrow b\bar{b}\gamma\gamma$  has been simulated using **Pythia** 6.4 [375] with the settings detailed in appendix ???. The cross section of the Higgs pair production (ggF and qqA both at LO multiplied by a  $K$ -factor as described in subsect. 8.3.1 and 8.3.2) is fed to **Pythia** which decays the two Higgs bosons and then performs the parton showering. We have accounted for the correct BRs by using the values obtained as described in subsect. 8.3.3 from **HDECAY**. We have turned on initial and final state QCD and QED radiation and multiple interactions. The generated events were written to a ROOT file via **RootTuple** tool [376] for further analysis.

### 8.4.2 Analysis strategy

The analysis strategy follows the one performed in [370] allowing us to use their backgrounds. Note that the analysis was based on the SM simulated events, meaning that the significances could be potentially improved performing a dedicated new physics analysis. In order to satisfy the minimal reconstruction requirements of the LHC we select only events with

$$p_T(\gamma/j) > 25 \text{ GeV}, \quad |\eta(\gamma/j)| < 2.5. \quad (8.41)$$

Moreover, we veto events with hard leptons

$$p_T(\ell) > 20 \text{ GeV}, \quad |\eta(\ell)| < 2.5, \quad (8.42)$$

cut	$\epsilon_{\text{cut}}$	$\delta\epsilon_{\text{cut}}$
$p_T$ cuts in eq. (8.43)	0.35	0.07
$\Delta R$ cuts in eq. (8.44)	0.69	0.21
total	0.16	0.05

**Table 8.1.** The cuts used in the analysis with their efficiency  $\epsilon_{\text{cut}}$  and uncertainties on these efficiencies  $\delta\epsilon_{\text{cut}} = \sqrt{\epsilon(1-\epsilon)N}$ , where  $N$  is the total number of events. The analysis was performed on 100K SM simulated events.

corresponding of an expected  $\epsilon_{\text{Trig}} = 0.9$ . Jets were clustered using `fastjet` [377] with the anti-kt algorithm with a radius parameter of  $R = 0.5$ .

We have used a  $b$ -tagging efficiency of  $\epsilon_b = 0.7$ <sup>7</sup>. The contamination probability of  $\epsilon_{j \rightarrow b} < 1\%$  is found to be consistent with ATLAS and CMS performance [379–381]. For the photon reconstruction efficiency we used  $\epsilon_\gamma = 0.8$  as reported by ATLAS and CMS in [381, 382]. The selection cuts we used are the same ones as in [370], starting with the cuts of the transverse momentum  $p_T$  of the photons and  $b$ -tagged jets. The two hardest photons/ $b$ -tagged jets, with transverse momentum  $p_{T>}$ , and the softer ones with  $p_{T<}$  are selected to satisfy

$$p_{T>} (b/\gamma) > 50 \text{ GeV}, \quad \text{and} \quad p_{T<} (b/\gamma) > 30 \text{ GeV}. \quad (8.43)$$

In order to ensure well-separation of the photons and  $b$ -jets, we require the following cuts on the jet radius,

$$\Delta R(b, b) < 2, \quad \Delta R(\gamma, \gamma) < 2, \quad \Delta R(b, \gamma) > 1.5. \quad (8.44)$$

While the majority of the signal lies within this region, these cuts significantly reduce the backgrounds.

We choose a wide  $m_{\gamma\gamma}$  window (see eq. (8.45)) corresponding to 2-3 times the photon resolution of ATLAS and CMS [381, 382] which does not cause any significant loss. As for the Higgs mass window reconstructed from 2  $b$ -jets  $m_{b\bar{b}}$ , the mass window chosen in eq. (8.45) corresponds to the given  $b$ -tagging efficiency. The mass windows used are then

$$105 \text{ GeV} < m_{b\bar{b}} < 145 \text{ GeV}, \quad 123 \text{ GeV} < m_{\gamma\gamma} < 130 \text{ GeV}. \quad (8.45)$$

The selection cuts are summarised in table 8.1 with their corresponding efficiency. In table 8.2 we summarise all the efficiencies used in the analysis.

The major backgrounds for the considered final state are the  $b\bar{b}\gamma\gamma$  continuum background,  $\gamma\gamma jj$  with two mistagged jets,  $t\bar{t}h$ ,  $Zh$  and  $b\bar{b}h$  in the order of importance after the cuts in eq. (8.43). The number of background events (surviving the cuts) is taken from [370]. The backgrounds are illustrated in the fig. ?? in which we show the number of events for the SM Higgs pair signal in light blue and the most relevant backgrounds

<sup>7</sup>We have explicitly cross checked the number by doing a mass-drop tagger analysis [378].

Type	efficiency
$\epsilon_{\text{Acc}}$	$\sim 1$
$\epsilon_{\text{Rec}}$	0.31
$\epsilon_{\text{Trig}}$	0.90
$\epsilon_{\text{Cut}}$	0.16
total	0.044

**Table 8.2.** Values of the efficiencies calculated/used in this analysis.

in other colors. It should be noted that the background  $h(\rightarrow \gamma\gamma)Z(\rightarrow b\bar{b})$  is modified in the presence of enhanced light quark Yukawa couplings. We checked though explicitly that scaling the Yukawa couplings to the values of our benchmark point only changes the NLO cross section by less than 1%, making this effect negligible. The analysis was carried out for varying values of  $\kappa_f$  for the different flavours. Due to the change in the kinematical distributions (cf. fig. ??) resulting from the PDFs of the different flavours, the efficiencies depend on the flavour of the quarks. For  $\kappa_f \gg 1$  the  $\kappa_f$  dependence factors out of the cross section such that for the values considered in the analysis of the distributions no dependence on the concrete value of  $\kappa_f$  is seen. The flavour-specific efficiency ratio  $\epsilon_f$  is given by

$$\epsilon_f = \frac{\sigma_{ggF} \epsilon_{ggF} + \sigma_{q\bar{q}} \epsilon_{qq}}{\sigma_{gg} + \sigma_{q\bar{q}}}, \quad (8.46)$$

with  $\sigma_{ggF}$  being the gluon fusion cross section,  $\sigma_{q\bar{q}}$  the quark annihilation cross section and  $\epsilon_{ggF} = 0.044$ . We give the values for the qqA efficiency  $\epsilon_{qq}$  in table 8.3.

In fig. ?? we show for the SM and for our benchmark point  $g_{hq\bar{q}} = g_{hb\bar{b}}^{\text{SM}}$  the  $M_{hh}$  distribution. The lower panels in the plot show the efficiencies. These plots illustrate how the efficiency depends on the shape of the distribution, and hence the flavour  $f$  that is scaled by  $\kappa_f$ .

$\delta\kappa$	$\epsilon_{qq}$
$\kappa_u$	0.050
$\kappa_d$	0.049
$\kappa_u \& \kappa_d$	0.053
$\kappa_c$	0.034
$\kappa_s$	0.037
$\kappa_c \& \kappa_s$	0.039

**Table 8.3.** The dependence of  $\epsilon_{qq}$  on the flavour of the Yukawa couplings' scalings.

### 8.4.3 Statistical analysis

We have used the likelihood ratio test statistic  $q_\mu$  in order to estimate the HL-LHC sensitivity, and set projected limits on the scalings of the light Yukawa couplings. A (log)–likelihood was constructed from the signal and background events in each bin of the histogram in fig. ??,

$$-\ln \mathcal{L}(\mu) = \sum_{i \in \text{bins}} (N_{bi} + \mu N_{si}) - n_i \ln(N_{bi} + \mu N_{si}), \quad (8.47)$$

with  $N_{bi}$  and  $N_{si}$  being the number of background and signal events in the  $i$ th  $M_{hh}$  distribution, respectively. In order to include the theoretical uncertainties on the expected number of signal events, the above likelihood was extended by a gaussian distribution for  $N_{si}$  in which the mean equals to the central value of the bin values and standard deviation  $\sigma$  equals to its theoretical uncertainty. The signal strength  $\mu$  was then estimated by minimising  $-\ln \mathcal{L}(\mu)$  to obtain the estimator for  $\hat{\mu}$  by injecting SM signal + background events  $n_i$ . The test statistic is then given by

$$q_\mu = 2(\ln \mathcal{L}(\mu) - \ln \mathcal{L}(\hat{\mu})), \quad (8.48)$$

following the procedure described in [383].

In order to set bounds on the scalings, we have fitted the signal strength inclusively by a function depending on the scaling of the Yukawa couplings

$$\mu(\kappa_1, \kappa_2) = \left\{ \frac{1}{Z} \left[ A_0 \left( \kappa_1^2 \frac{m_{q1}^2}{M_{hh}^2} \ln^2 \left( \frac{M_{hh}}{m_{q1}} \right) \right) + A_1 \left( \kappa_2^2 \frac{m_{q2}^2}{M_{hh}^2} \ln^2 \left( \frac{M_{hh}}{m_{q2}} \right) \right) \right] + B_2 \right\} \epsilon_f, \quad (8.49)$$

with

$$Z = \frac{\kappa_1^2 m_{q1}^2 + \kappa_2^2 m_{q2}^2 + B_0}{m_{q1}^2 + m_{q2}^2 + B_1} \quad (8.50)$$

and  $m_{q1}$  and  $m_{q2}$  denoting the  $\overline{\text{MS}}$  masses of the quarks.

Taking  $M_{hh} \approx 300$  GeV, we could perform a fit for the signal strength for each of the quark generations scalings separately. Note that one could of course also extend the model to include the dependence of the signal strength on four Yukawa coupling modifications, taking into account the correlation between them when fitting the likelihood in eq. (8.47).

The expected HL-LHC sensitivity for the signal strength at 95% (68 %) CL is found to be  $\mu = 2.1(1.6)$ .

### 8.4.4 Results for the $b\bar{b}\gamma\gamma$ final state

We have performed a scan on the first generation Yukawa coupling scalings  $\kappa_u$  and  $\kappa_d$  in order to obtain exclusion limits, derived from the likelihood contours shown in fig. 8.10. The individual  $\kappa_q$  expected upper bounds at 68% and 95% CL are obtained by profiling the likelihood over the other first generation  $\kappa_q$ . Doing so, we obtain the following upper

bounds for HL-LHC

$$-571 < \kappa_d < 575, \text{ (68\% CL)}, \quad -853 < \kappa_d < 856, \text{ (95\% CL)}, \quad (8.51)$$

and

$$-1192 < \kappa_u < 1170, \text{ (68\% CL)}, \quad -1771 < \kappa_u < 1750, \text{ (95\% CL)}. \quad (8.52)$$

Note that these bounds are not directly comparable to the standard  $\kappa$  formalism bounds since we relate with  $\kappa$  the Yukawa couplings  $g_{hq\bar{q}}$  and the new coupling  $g_{hhq\bar{q}}$ . For the second generation quarks we were not able to obtain similar bounds due to the reduction of  $\mu/\mu_{\text{SM}}$  with increasing  $\kappa_s$  and  $\kappa_c$  away from the SM, which stems from the decrease of the branching ratio  $\mathcal{B}(hh \rightarrow b\bar{b}\gamma\gamma)$  as new decay channels open, while the cross section is not as much enhanced as for up and down quarks due to the charm and strange quark being less abundant in the proton. This leads to signal strength modifiers  $\mu/\mu_{\text{SM}} < 1$  (*cf.* fig. 8.9). We will analyse the second generation Yukawa couplings instead for the final state  $hh \rightarrow c\bar{c}\gamma\gamma$ , in which we observe significant enhancement of the relative signal strength modifier  $\mu/\mu_{\text{SM}}$  (*cf.* fig. 8.9). Before turning to a different final state though, we will reanalyse the  $b\bar{b}\gamma\gamma$  final state under the point of view of a non-linear effective field theory, hence leaving the couplings  $g_{hq\bar{q}}$  and  $g_{hhq\bar{q}}$  independent.

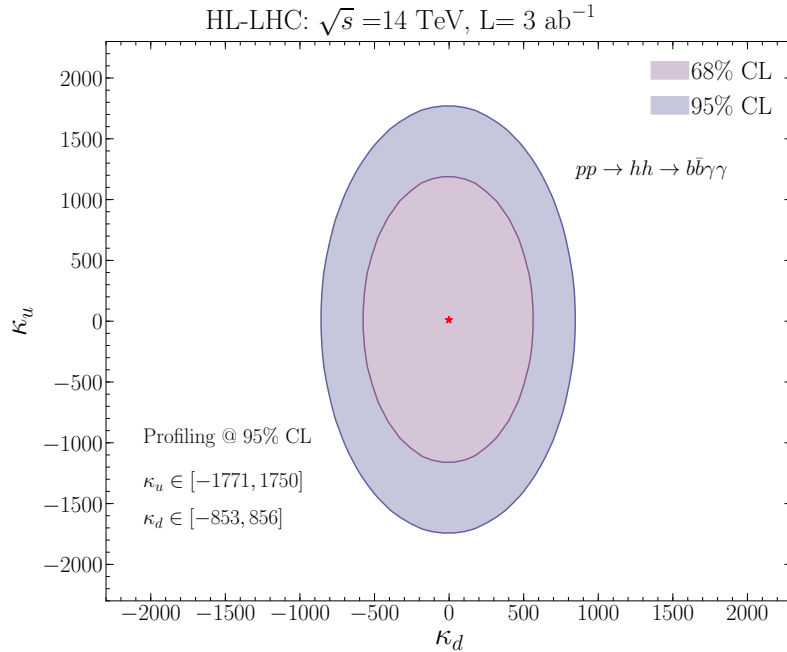


**Figure 8.10.** The expected sensitivity likelihood contours at 68% and 95% CL of the HL-LHC for the first generation Yukawa coupling scalings.

## Results for non-linear EFT

We will consider in this part a non-linear EFT as introduced in eq. (8.15). By expanding in the chiral modes, taking the 0th mode and the flavour diagonal terms, we get

$$-\mathcal{L} = \bar{q}_L \frac{m_q}{v} \left( v + c_q h + \frac{c_{qq}}{v} h^2 + \dots \right) q_R + h.c., \quad (8.53)$$

where we rescaled the coefficients  $k_q$  and  $k_{2q}$  of eq. (8.15) as  $k_{q,ii} = \sqrt{2}c_q m_q/v$  and  $k_{2q,ii} = \sqrt{2}c_{qq} m_q/v^2$ . Unlike the linear EFT, the Wilson coefficients  $c_q$  and  $c_{qq}$  are independent of each other. Using the previous analysis, it is possible to set bounds on these coefficients separately, as seen in fig. 8.11. We observe that without the  $hh\bar{q}q$

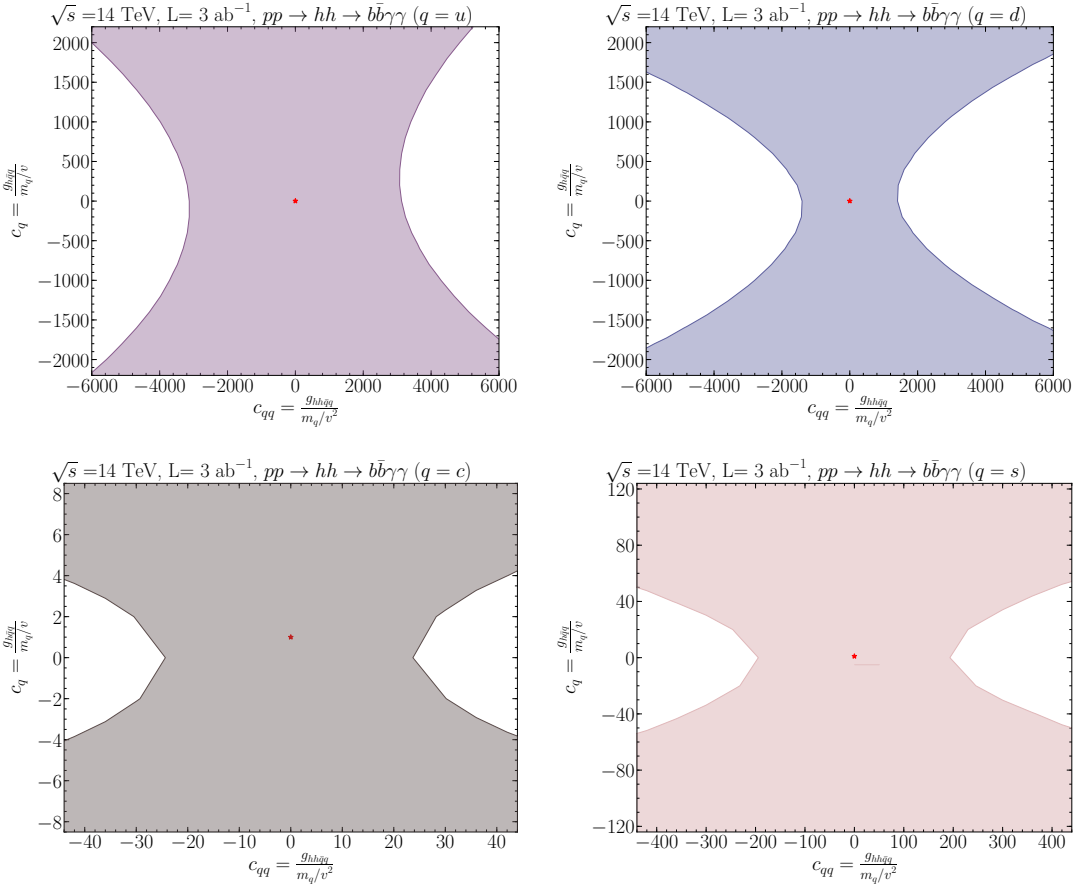


**Figure 8.11.** 95% CL likelihood contours for the non-linear EFT Wilson coefficients  $c_{qq}$  and  $c_q$  for up (upper left), down (upper right), charm (lower left) and strange quarks (lower right).

interaction, one cannot set bounds on any of the light Yukawa couplings from Higgs pair production. We remark though that in case any deviation in the light Yukawa couplings is observed, the di-Higgs channel can distinguish whether electroweak symmetry breaking

Detector	Cuts (1st, 2nd) $b$ -jets	$\epsilon_{c/b}^{\text{b-tag}}{}^2$
CMS	Med1-Med1	0.18
CMS	Med1-Loose	0.23
ATLAS	Med-Med	$8.2 \cdot 10^{-2}$
ATLAS	Tight-Tight	$5.9 \cdot 10^{-3}$

**Table 8.4.** The  $b$ -tagging working points used in the analysis, for CMS [385] and ATLAS [386].

is realised linearly or non-linearly.

#### 8.4.5 Charm-tagging and second generation bounds

In order to set bounds on the second generation Yukawa couplings, we use the method developed in [329, 384] that re-analyses final states with  $b$ -quarks based on the mistagging of  $c$ -jets as  $b$ -jets in associated  $VH$  production. The analysis relies on the current CMS [385] and ATLAS [386] working points for  $b$ -tagging, as illustrated in the table 8.4. The signal strength estimator when considering the mistagging probability of  $b$ -jets to  $c$ -jets (i.e.  $c$ -jet contamination of  $b$ -tagged jets)  $\epsilon_{b \rightarrow c}$  is

$$\hat{\mu} = \frac{\sigma_{hh} \mathcal{B}_b \epsilon_{b1} \epsilon_{b2} \epsilon_f + \sigma_{hh} \mathcal{B}_c \epsilon_{b \rightarrow c,1} \epsilon_{b \rightarrow c,2} \epsilon_f}{\sigma_{hh}^{\text{SM}} \mathcal{B}_b^{\text{SM}} \epsilon_{b1} \epsilon_{b2}}, \quad (8.54)$$

with  $\epsilon_f$  being the efficiency ratio in eq. (8.46). The above expression simplifies to

$$\hat{\mu} = \mu_b \epsilon_f + 0.05 \cdot \left( \epsilon_{c/b}^{\text{b-tag}} \right)^2 \epsilon_f \cdot \mu_c, \quad (8.55)$$

for  $\mathcal{B}_c^{\text{SM}} / \mathcal{B}_b^{\text{SM}} \approx 0.05$ . The signal strength modifier of the  $b\bar{b}\gamma\gamma$  final state is denoted by  $\mu_b$  and the one of the  $c\bar{c}\gamma\gamma$  final state by  $\mu_c$ . The ratio of tagging efficiencies is defined as

$$\left( \epsilon_{c/b}^{\text{b-tag}} \right)^2 = \frac{\epsilon_{b \rightarrow c,1} \epsilon_{b \rightarrow c,2}}{\epsilon_{b1} \epsilon_{b2}}. \quad (8.56)$$

One  $b$ -tagging working point could only constrain either  $\mu_b$  or  $\mu_c$ . In order to resolve the flat direction several  $b$ -tagging working points  $\left( \epsilon_{c/b}^{\text{b-tag}} \right)^2$  are needed. This is illustrated in fig. 8.12, where the working points fitting contours are combined using Fisher's method [387]. We thus obtain an upper projected limit on the charm final state signal strength after profiling over  $\mu_b$ ,

$$\mu_c(\text{up}) = 36.6 \text{ (68\% CL)}, \quad \mu_c(\text{up}) = 74.8 \text{ (95\% CL)}. \quad (8.57)$$

However, the obtained sensitivity is not sufficient to set any better limits at 95% CL than the existing ones (or projected ones in other channels) for the Yukawa coupling modifiers  $\kappa_c$ , and  $\kappa_s$ . Instead, we can improve on them by introducing  $c$ -tagging working

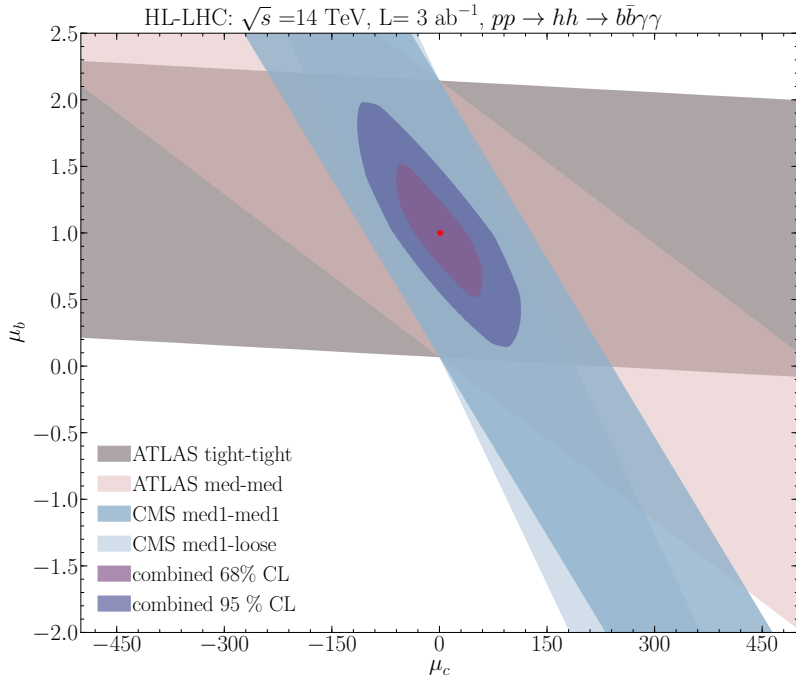


**Figure 8.12.** The 95 % CL contours of  $\mu_b$  vs  $\mu_c$ , obtained from fitting of the signal strength for several CMS and ATLAS  $b$ -tagging working points. Their combination with the 68% and 95% CL upper limits on  $\mu_b$  and  $\mu_c$  are shown.

points  $(\epsilon_{c/b}^{c\text{-tag}})^2$

$$\left(\epsilon_{c/b}^{c\text{-tag}}\right)^2 = \frac{\epsilon_{c1}\epsilon_{c2}}{\epsilon_{c\rightarrow b,1}\epsilon_{c\rightarrow b,2}}, \quad (8.58)$$

mixed with the  $b$ -tagging ones. We denoted the contamination of  $c$ -jets with  $b$ -jets by  $\epsilon_{c\rightarrow b}$ . For mixed tagging, the signal strength estimator becomes

$$\hat{\mu} = \frac{\sigma_{hh} \mathcal{B}_b \epsilon_{b1} \epsilon_{b2} \epsilon_f + \sigma_{hh} \mathcal{B}_c \epsilon_{c1} \epsilon_{c2} \epsilon_f}{\sigma_{hh}^{\text{SM}} \mathcal{B}_b^{\text{SM}} \epsilon_{b1} \epsilon_{b2} + \sigma_{hh}^{\text{SM}} \mathcal{B}_c^{\text{SM}} \epsilon_{c1} \epsilon_{c2}}, \quad (8.59)$$

where now  $\epsilon_b$  is either  $\epsilon_b$  or  $\epsilon_{c\rightarrow b}$  and  $\epsilon_c$  either  $\epsilon_c$  or  $\epsilon_{b\rightarrow c}$ . This simplifies to

$$\hat{\mu} = \frac{\mu_b + 0.05 \epsilon_{c/b}^2 \mu_c}{1 + 0.05 \epsilon_{c/b}^2} \epsilon_f. \quad (8.60)$$

The working point  $\epsilon_{c/b}^2$  could be the  $b$ -tagging or  $c$ -tagging working point. Assuming that  $c$ -tagging and  $b$ -tagging are uncorrelated, and working with the methods discussed in [307, 329], i.e. combining the ATLAS medium cuts (med.) for  $b$ -tagging with the  $c$ -tagging working points in order to break the degeneracy, we could improve the 95% CL sensitivity on  $\mu_c$ . We start by the  $c$ -tagging working point used by the ATLAS

<i>c</i> -tagging working point	$\epsilon_c$	$\epsilon_{c \rightarrow b}$	$\mu_c$ (up)	95% CL
<i>c</i> -tag I [388, 389]	19%	13%	10.1	
<i>c</i> -tag II [390, 391]	30%	20%	8.2	
<i>c</i> -tag III [390, 391]	50%	20%	3.8	

**Table 8.5.** The *c*-tagging working points with the expected 95% CL upper limit (sensitivity) of  $\mu_c$  obtained after profiling over  $\mu_b$ .

collaboration in Run I searches for top squarks decays to charm and neutralino [388, 389], which we refer to as *c*-tagging I. Further *c*-tagging working points from the HL-LHC upgrade are used: with the expected insertable B-layer (IBL) sub-detector that is to be installed during the ATLAS HL-LHC upgrade [390, 391], the new *c*-tagging II and III points, as illustrated in table 8.5, can be identified. In fig. ?? we used them to obtain in combination with the ATLAS med *b*-tagging expected 95% CL upper limits on  $\mu_c$  for the HL-LHC from an analysis of the final state  $b\bar{b}\gamma\gamma$ . Fitting signal strengths with varying  $\kappa_c, \kappa_s$  for charm and bottom final states (*cf.* eq. (8.49)) for constructing the likelihood  $\mathcal{L}(\kappa_c, \kappa_s)$ , we can set limits from the anticipated charm tagging working points as shown in fig. 8.13. These projected limits are an improvement compared to the current direct bound and prospects for HL-LHC, particularly for charm quark Yukawa modifications [307, 329]. Again, it should be kept in mind that the bounds on  $\kappa_q$  do not just correspond to the scaling of the Yukawa coupling, but also to the new coupling  $g_{hhq\bar{q}}$  arising in SMEFT.

## 8.5 Conclusion

The couplings to the first and second generation fermions remain among the less well measured couplings of the Higgs boson. In this paper we investigated the possibility of measuring light quark Yukawa couplings in Higgs pair production. For enhanced Yukawa couplings of the first generation quarks, we found that limits can be set when considering quark annihilation with subsequent decay of the Higgs boson pair to  $b\bar{b}\gamma\gamma$ . In an effective theory description with dimension 6 operators that modify the quark Yukawa couplings, there exists also a coupling of two Higgs bosons to two fermions. This coupling increases the Higgs pair production cross section and hence allows to set bounds on the light quark Yukawa coupling modifications. For the HL-LHC we found a sensitivity of  $|\kappa_u| \lesssim 1170$  and  $|\kappa_d| \lesssim 850$ , *cf.* fig. 8.10, which is comparable to the sensitivity of other channels that can directly probe the light quark Yukawa couplings though being weaker than the results from a global fit. Further improvements could be possible with a more dedicated analysis. We note though that the bounds we find stem mostly due to the diagram involving the coupling of two Higgs bosons to two quarks, as we showed explicitly also by considering a non-linear effective theory in which the coupling of one and two Higgs boson to fermions are uncorrelated. This channel can hence also be used to distinguish between a linear vs non-linear Higgs EFT hypothesis

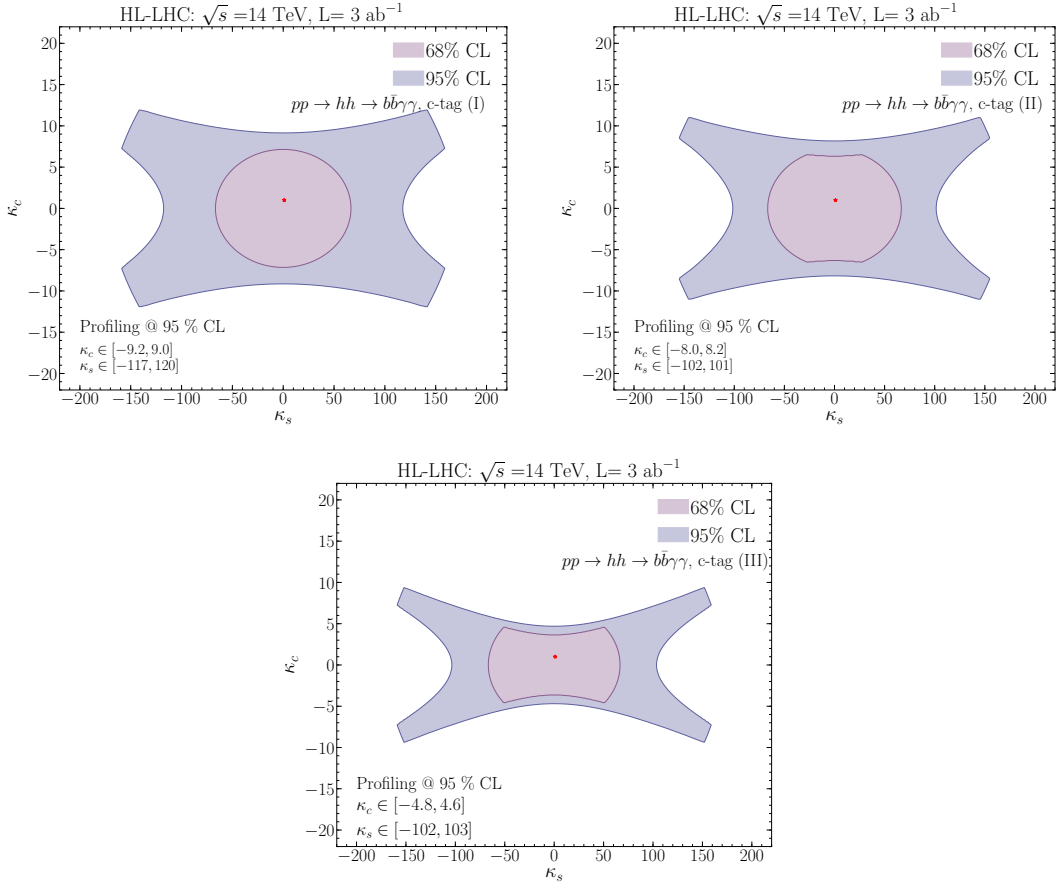


**Figure 8.13.** The expected sensitivity likelihood contours at 68% CL and 95% CL for an integrated luminosity  $L = 3000 \text{ fb}^{-1}$  for modified second generation quark Yukawa couplings, using the c-tagging I (upper pannel, left), II (upper pannel, right) and III (lower pannel) working points.

in the light quark sector. The LHC experiments should hence consider the Higgs pair production process in addition to other channels for probing the light quark Yukawa couplings.

For the second generation quarks we found that at the HL-LHC in the di-Higgs channel we will be able to set competitive bounds on the charm Yukawa coupling if final states with tagged charm quarks are considered. We were in particular considering the final state  $c\bar{c}\gamma\gamma$ , in which we found a sensitivity of  $|\kappa_c| \lesssim 5$  and  $|\kappa_s| \lesssim 100$ , *cf.* fig. 8.13, where the first prospective limit is comparable to the prospects from charm tagging in the  $Vh$  channel [307].

# 9 Optimised search for Higgs pair via Interpretable machine learning

## 9.1 Introduction

The primary objectives of this work are as follows:

- We show some well motivated BSM scenarios where light-quark Yukawas can be enhanced simultaneously with the Higgs trilinear coupling.
- We perform an interpretable machine learning analysis based on boosted decision trees and Shapley values, a measure derived from Coalition Game Theory to extract signal significance to get a better handle on the measurement of light-quark Yukawas.
- We perform simultaneous fits for several combinations of light-quark Yukawa couplings and the Higgs trilinear coupling.

We show in [section 8.2](#) the relevant EFT operators for the di-Higgs processes, discuss flavor bounds and minimal flavor violation (MFV). Then we introduce in [section 10.2](#) the concept of aligned flavor violation (AFV), and various "concrete" examples realising large enhancement to light yukawa while evading flavor bounds. We then study the leading contributing channels with simulation details explained in [section 9.2](#). Further we discuss in [section 9.3](#) the multivariate analysis and interpretable machine learning approach we adopt. We present prospected results in [section 9.4](#) at the HL-LHC and FCC. In [section 9.5](#) we summarize our main findings.

In the general framework of SMEFT, additional assumptions on UV-motivated flavor structure avoids stringent low energy FCNC and EDM bounds, making collider probe on the Yukawa and related Wilson coefficients competitive and relevant. See a recent overview of Yukawa coupling bounds from flavor and collider Higgs data, in the SMEFT framework given certain flavor structure. [[392](#)]

The single Higgs production and decay channels as measured currently already provide indirect bounds on the light quark Yukawa couplings from global fit. The main sensitivity comes from enhancement to the production when  $q\bar{q}$  fusion of the Higgs become comparable to ggF channel when the corresponding light-quark Yukawa is sufficiently enhanced. Secondly, there is additional overall "dilution" factor from the modified Higgs total width, for a final state of a specific (non-"light-jet") decay channel. In the case of di-Higgs, the  $q\bar{q}hh$  contact interaction become important for the di-Higgs production, and could become dominant production channel over the SM gluon fusion channel

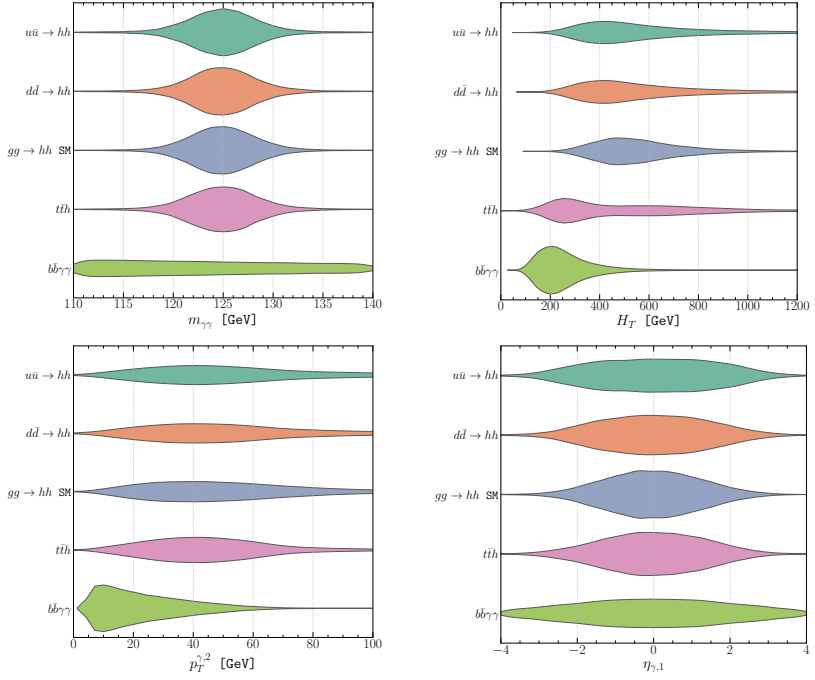


**Figure 9.1.** The .

through loop. The sensitivity thus achieved to the corresponding light-quark Yukawa in the SMEFT framework is better compared to that from single Higgs inclusive observable, and could even be competitive to single Higgs differential studies, as will be shown from our study.

### 9.1.1 Considerations of experimental constraints

For the 2HDM model, there are three main scenarios from the experimental searches point of view, in which one can obtain enhancements to light-quark Yukawa couplings. In the first scenario, the heavy Higgs  $H$  has a small mass  $m_H < 2$  TeV. Experimental resonance searches rules out this scenario where the resonant Higgs pair production is enhanced significantly due to the decay  $H \rightarrow hh$ , as the trilinear  $Hhh$  coupling scales as [322]

$$g_{Hhh} \approx \frac{m_H^2}{v^2} \cos(\beta - \alpha). \quad (9.1)$$

In the second scenario, we have a heavier  $H$  but a large  $Hq\bar{q}$  coupling. Here, the dijet resonance searches from  $H \rightarrow jj$  decay, provides the strongest constraints. Lastly, when we consider a heavy  $H$  and  $Hq\bar{q}$  not excluded by di-jet searches we lie within the EFT limit and non-resonant Higgs pair production discussed in this paper gives us the dominant constraints.

In the 2HDM with AFV or SFV, there is an interplay between light quark Yukawa and

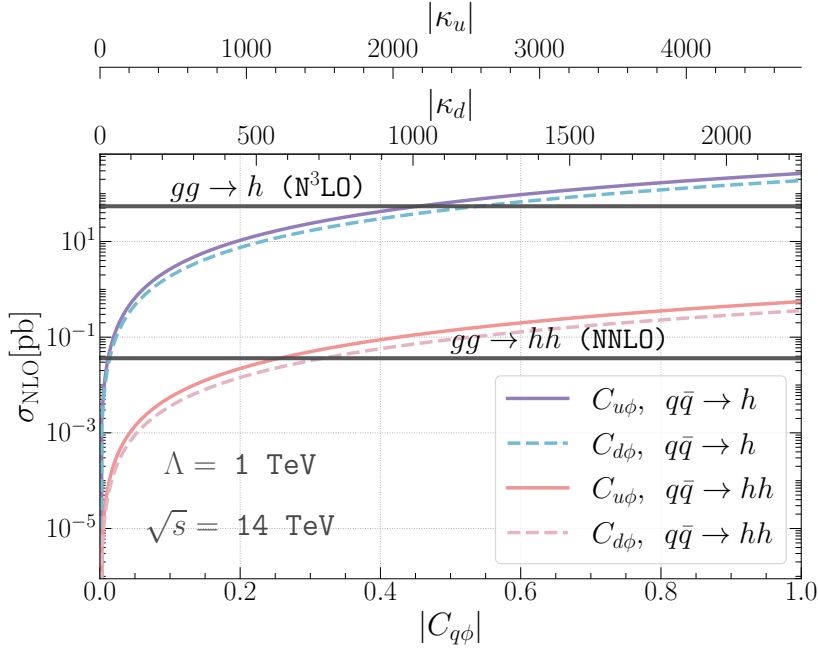


**Figure 9.2.** The production cross-section of single Higgs and di-Higgs at 14 TeV from the quark anti-quark annihilation  $q\bar{q}A$  as a function of the Wilson coefficients  $C_{u\phi}$  and  $C_{d\phi}$  versus the SM gluon fusion cross-sections (the horizontal solid line for  $gg \rightarrow h$  and the dashed-dotted one for  $gg \rightarrow hh$ ). One can observe that for values of  $C_{u\phi} = 0.22(0.43)$  and  $C_{d\phi} = 0.26(0.47)$  the  $q\bar{q}A$  channel becomes the dominant di-Higgs (single Higgs) production channel. The UV scale is set to  $\Lambda = 1 \text{ TeV}$ .

the Higgs trilinear self-coupling. This comes from the alignment parameters  $\alpha$  and  $\beta$ , as we see in equations (10.25) and (10.26). For example, when the mass of  $H$  is allowed to be very large  $m_H > 4 \text{ TeV}$ , enhancement to light-quark Yukawa couplings would be completely constrained from the bound on the Higgs self-coupling provided the 2HDM potential is tuned to avoid triviality and perturbativity bounds.

From the discussion in this section we see that several models are present in the literature that are able to accommodate for large deviations of the light-quark Yukawa couplings from their SM values while avoiding excessive contributions to FCNCs that are well measured and particularly limiting for models with additional flavour structures due to the implementation of AFV or SFV. The primary new physics deviation, complementary to direct searches, in the presented models will show up in the modification of the light quark Yukawa couplings. Armed with this knowledge, we motivate a study of how light-quark Yukawa couplings can be constrained at future experiments from Higgs pair production.

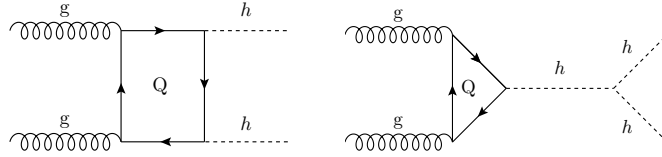


**Figure 9.3.** The cross-section of the  $ggF$  channel can be decomposed into three subprocesses based on its dependence on the trilinear coupling  $\lambda$ . The triangle topology depends on  $\lambda^2$ , the box one does not depend on it and the interference amongst the latter two is linear in  $\lambda$ .

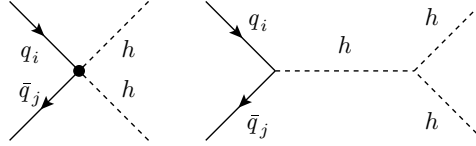


**Figure 9.4.** The dominant Feynman diagrams for the quark anti-quark annihilation ( $q\bar{q}A$ ) production of Higgs pair, via the SMEFT operator  $\mathcal{O}_{q\phi}$ .

## 9.2 Events simulation for HL-LHC and FCC-hh

We consider the final state  $b\bar{b}\gamma\gamma$ , as this channel has the most potential for Higgs pair searches [191]. It has the ‘‘clean’’  $h \rightarrow \gamma\gamma$  decay, but also the other Higgs decay to  $b$ -quark pair is a channel with large branching ratio  $\sim 58\%$  and b-tagging capabilities for ATLAS and CMS are continuously improving.

Channel	LO $\sigma$ [fb]	NLO $K$ -fact	$6 \text{ ab}^{-1}$ [#evt @ NLO]
$y_b^2$	0.0648	1.5	583
$y_b y_t$	-0.00829	1.9	-95
$y_t^2$	0.123	2.5	1,840
$Z h$	0.0827	1.3	645
$\sum b\bar{b}h$	0.262	-	2,970
$b\bar{b}\gamma\gamma$	12.9	1.5	116,000
$t\bar{t}h$	1.156	1.2	6,938

**Table 9.1.** SM cross-section for the main background processes at 14 TeV with  $6 \text{ ab}^{-1}$  data at the HL-LHC, and the number of events after the basic cuts as defined in Equation 9.3. For  $b\bar{b}h$  production, the Higgs boson is decayed to a pair of photons. The total production of Higgs associated with  $b\bar{b}$  is denoted by  $\sum b\bar{b}h$  and is the sum of the top four channels.

To be able to study the effects of enhanced light-quark Yukawa couplings or Higgs trilinear coupling, we need to simulate events for HL-LHC and FCC-hh which we use to train a machine learning model to identify the signal from the background. We consider the  $b\bar{b}h$ ,  $t\bar{t}h$ ,  $b\bar{b}\gamma\gamma$  processes as the main sources of background for the  $hh$  signal. For the  $b\bar{b}h$  processes, the contributions proportional to  $y_b^2$ ,  $y_b y_t$  and  $y_t^2$  are simulated separately with  $y_b$  running effects. The details of the simulation can be found in Ref. [393]. The  $Z h, Z \rightarrow b\bar{b}$  events are generated at leading order (LO), then scaled to NLO by  $K$ -

Channel	LO $\sigma$ [fb]	$K$ -fact.	Order	$6 \text{ ab}^{-1}$ [#evt @ order]
$hh_{\text{tri}}^{\text{ggF}}$	$7.288 \cdot 10^{-3}$	2.28		96
$hh_{\text{box}}^{\text{ggF}}$	0.054	1.98	NNLO	680
$hh_{\text{int}}^{\text{ggF}}$	-0.036	2.15		-460
$u\bar{u}\text{A}$ ( $C_{d\phi} = 0.1$ )	2.753	1.29	NLO	28
$d\bar{d}\text{A}$ ( $C_{u\phi} = 0.1$ )	4.270	1.30		43

**Table 9.2.** The LO cross-section for di-Higgs production at the HL-LHC for  $6 \text{ ab}^{-1}$  of data multiplied by the  $hh \rightarrow b\bar{b}\gamma\gamma$  branching ratio,  $K$ -factors (taken from [156] for the gluon channels and [319] for the quark channels) and the number of events after the basic cuts for the separated gluon fusion (ggF) and quark annihilation ( $q\bar{q}\text{A}$ ) at  $\sqrt{s} = 14 \text{ TeV}$ .

factors, defined as the ratio of higher order cross section over its LO counterpart. The  $K$ -factors were taken from  $t\bar{t}h$  [394],  $b\bar{b}\gamma\gamma$  [395],  $Zh$  [396] and the remaining part of the  $b\bar{b}h$  processes from [397]. The Higgs particles are further decayed to  $\gamma\gamma$  following the Higgs cross-section working group recommendations [153]. The parton-level results are showered using **Pythia 8.3** [398] and a detector simulation is done using **Delphes 3** [399]. To be inclusive and to explore the capabilities and importance of the full detector coverage, no generator-level cuts were applied on these processes except for the  $b\bar{b}\gamma\gamma$  processes to avoid divergences. These minimal generator-level cuts for  $b\bar{b}\gamma\gamma$  are

$$\begin{aligned} Xp_T^b &> 20 \text{ GeV}, \\ \text{generator level cuts: } &\eta_\gamma < 4.2, \Delta R_{b\gamma} > 0.2, \\ &100 < m_{\gamma\gamma} (\text{GeV}) < 150. \end{aligned} \quad (9.2)$$

Here  $Xp_T$  implies a minimum  $p_T$  cut for at least one  $b$ -jet. After the showering and detector simulation, further basic selection cuts were applied to select events with

$$\begin{aligned} \text{basic cuts: } &n_{\text{eff}}^{b\text{jet}} \geq 1, n_{\text{eff}}^{\gamma\text{jet}} \geq 2, \\ &p_T^{b\text{jet}} > 30 \text{ GeV}, p_T^{\gamma\text{jet}} > 5 \text{ GeV}, \\ &\eta_{b\text{jet}, \gamma\text{jet}} < 4, 110 \text{ GeV} < m_{\gamma_1\gamma_2} < 140 \text{ GeV}, \end{aligned} \quad (9.3)$$

and  $n_{\text{eff}}^{b/\gamma\text{jet}}$  representing the number of  $b/\gamma$ -jets that pass the basic selection. The cross-section,  $K$ -factors, number of events with  $6\text{ab}^{-1}$  luminosity at 14 TeV are given in [Table 9.1](#).

While the backgrounds are generated using **MadGraph\_aMC@NLO** [213], the  $hh$  signal is separated into two main channels. The first is the gluon-fusion (ggF) channel which is the dominant channel in the SM and which can be further decomposed into three subprocesses based on their dependence on the Higgs trilinear self-interaction,  $\lambda$ , as seen in [Figure 9.3](#). Amongst these subprocesses, the first is the amplitude squared of the contribution from the triangle diagram. It is proportional to  $\lambda^2$ . The second is the squared amplitude of the contribution from the box diagram that does not depend on

the trilinear coupling. The third is the contribution from the interference between the triangle and box diagrams, which is proportional to  $\lambda$ . Using this separation allows us to remove the dependence of the total  $K$ -factor for  $hh$  production on rescaling of the trilinear Higgs coupling [291]. The individual  $K$ -factors for each of the subprocesses are independent of the rescaling of the trilinear Higgs coupling making our analysis computationally much simpler. The  $ggF$  process is generated using the  $HH$  production program implemented in **POWHEG** [157, 291, 400], which has been modified to separate the individual contributions from the three diagrams. The cross-section for these individual contributions and the corresponding  $K$ -factors can be found in [Table 9.2](#).

The other main process, the quark anti-quark annihilation ( $q\bar{q}A$ ), is strongly suppressed in the SM for first generation quarks since the SM Yukawa couplings are proportional to the mass of the considered quark flavour. However, since this channel is a tree-level process, with sufficient large enhancement factors of the light quark Yukawa coupling, it becomes dominant as shown in [Figure 9.2](#). The  $q\bar{q}A$  cross section scales like  $\tilde{C}_{q\phi}^2/\Lambda^4$ , while the gluon fusion production cross-section remains almost unchanged. Therefore, for constraining enhancements of the light-quark Yukawa, we consider this channel as the signal and the  $ggF$  channel as part of the background. The  $q\bar{q}A$  process is generated with **MadGraph\_aMC@NLO** with a UFO model created with **FeynRules** [228]. Samples for both up- and down-quark initiated  $q\bar{q}A$  processes is generated. For all the  $hh$  signals, the samples are generated at LO and later scaled by the NLO  $K$ -factors given in [Table 9.2](#). The  $K$ -factors are obtained from ref. [154] for the gluon fusion process in EFT and adapted from [359–361] as described in [319] for the  $q\bar{q}A$  channel. Moreover, the two Higgs bosons are decayed to  $b\bar{b}$  and  $\gamma\gamma$  respectively, with **Pythia 8.3** and then showered. The same detector simulation and basic cuts as for the background are then performed. In addition, the same sets of parton distribution function (`NNPDF31_nlo_as_0118_nf_4`) are used for the signal and the background, implemented via **LHAPDF** [295]. The calculation of the Higgs full width and branching ratios is done using a modified version of **Hdecay** [368, 369] to include the new SMEFT operators  $\mathcal{O}_{q\phi}$ . It should be noted, that in both di-Higgs production and decay calculation, the light-quark masses are set to zero. However, when converting between SMEFT and  $\kappa$ -formalism, the  $\overline{\text{MS}}$  quark masses are used, in accordance to the PDG.

For FCC-hh, almost everything is done similarly after setting the energy to 100 TeV and the luminosity to  $30 \text{ ab}^{-1}$ . Since we do not have all  $K$ -factors available at a collider energy of 100 TeV we rescaled the LO samples by the same ones as for HL-LHC. We note that we explicitly checked that at least within the SM, for Higgs pair production via gluon fusion the difference is of  $\mathcal{O}(1\%)$  [177] and hence small.

### 9.3 Exploring higher dimensional kinematic distributions

After detector simulation and jet definition, we have a final state of two photon jets and at least one  $b$ -jet, where the two photons reconstruct back to a real scalar Higgs mass for all the  $b\bar{b}h$  channels. We first define and evaluate a comprehensive set of kinematic observables as the following:

- $p_T^{b_1}$ ,  $p_T^{b_2}$ ,  $p_T^{\gamma_1}$ ,  $p_T^{\gamma\gamma}$ ,
- $\eta_{b_{j1}}$ ,  $\eta_{b_{j2}}$ ,  $\eta_{\gamma_1}$ ,  $\eta_{\gamma\gamma}$ ,
- $n_{bjet}$ ,  $n_{jet}$ ,  $\Delta R_{\min}^{b\gamma}$ ,  $\Delta\varphi_{\min}^{bb}$ ,
- $m_{\gamma\gamma}$ ,  $m_{bb}$ ,  $m_{b_1 h}$ ,  $m_{b\bar{b}h}$ ,  $H_T$ .

$p_T^{b/\gamma_{1,2}}$  and  $\eta^{b/\gamma_{1,2}}$  are the  $p_T$  and rapidity for the tagged leading and sub-leading  $b/\gamma$ -jets (in our definition the subleading  $b$ -jet could be a null four-vector since we require one  $b$ -jet inclusive),  $n_{bj}$  is the number of tagged and passed  $b$ -jets.  $\Delta R_{\min}^{b\gamma}$  and  $\Delta\varphi_{\min}^{bb}$  are the minimum  $R$ -distance and  $\varphi$ -angle between a tagged  $b$ -jet and a photon jet. The remaining variables are the invariant masses and  $H_T$  is the scalar sum of the transverse mass of the system. We shall show in what follows, that it is not necessary to be very selective about the kinematic variables one chooses to use in the analysis. What is necessary is that all possibly useful kinematic variables are included. As can be seen from the list above, some of the variables seem to be interdependent and, probably, highly correlated. The beauty of using interpretable machine learning is that a hierarchy of importance for the variables will be built during the analysis using an over-complete basis of collider observables from which the most important ones can be chosen to fine tune the analysis.

### 9.3.1 Interpretable machine learning

Rule-based machine learning algorithms have for long been used as the gold standard for signal to background discrimination in a wide variety of particle physics analyses. They are known to outperform neural networks in terms of simplicity of implementation, computational resources required and accuracy in modelling the underlying distributions.<sup>1</sup> In addition, rule-based algorithms, such as decision trees, are more transparent as far as the signal vs. background separation is concerned. Placing emphasis on interpretability in multivariate analyses, we chose to work with Boosted Decision Trees (BDT). However, interpretability of a machine learning algorithm requires more than just a choice of an interpretable model. The conditions are:

- A variable set that is easily interpretable in terms of the dynamics being studied.
- A machine learning algorithm that is more transparent and not a complete black box.
- A method for interpreting the model and attribute variable importance to understand how the algorithm models the underlying distributions.

Choosing to work with BDTs just satisfies the second condition. We work with the BDT algorithm implemented in XGBoost [402], a publicly available scalable end-to-end boosting system for decision trees. We follow the normal procedures for training

---

<sup>1</sup>Nevertheless, we tested a deep neural network built with Tensorflow [401] and found no improvement in the classification accuracy.

and testing the BDT with simulated data. To satisfy the first condition we chose to work with high level kinematic variables that are representative of the process instead of working with four-vectors. The disadvantage of working with kinematic variable is that a complete set cannot be defined for a particular process unlike the four-vectors associated with the process. So, in principle, a large number of kinematic variables can be formulated and used in a multivariate analysis. While the number is never too large for any implementation of BDTs, having a large set of variables clouds the understanding of which ones are important for orchestrating the signal separation from the background. This is where the third point listed above is important. Variable importance attribution is a way to “short-list” only those variable that play an important role in predictive power of the classification (or regression) problem. There are several measures of variable importance used in machine learning like Gini or permutation based measures [403, 404], local explanations with surrogate models [405] etc., to name a few. However, these suffer from inconsistencies or fail to provide a global explanation of the model [406].

To build a mathematically consistent procedure for variable importance attribution we use Shapley values [407] from Coalition Game Theory. Formulated by Shapley in the mid-20<sup>th</sup> century, Shapley values formulate an axiomatic prescription for fairly distributing the payoff of a game amongst the players in a  $n$ -player cooperative game. When applied to machine learning, Shapley values tell us how important the presence of a variable is in determining a certain category (like signal or background) when compared to its absence from the multivariate problem being addressed. The process naturally and mathematically lends itself to studying the correlations between different variables since all possible combinations of variables can be taken out of the game to check the outcome.<sup>2</sup> A more detailed discussion of the application of Shapley values to signal vs. background classification problems for particle physics can be found in Refs. [393, 409, 410]. In this work we follow the same basic procedure as discussed in Ref. [393]. The importance of a variable in determining the outcome of a classification will be quantified by the mean of the absolute Shapley value,  $\overline{|S_v|}$ , larger values signifying higher importance. We will use the SHAP (SHapley Additive exPlanations) [406] package implemented in python based on Shapley values calculated exactly using tree-explainers [411, 412].

## 9.4 The $hh$ channel at future hadron colliders

We would like to study the bounds on three specific couplings in this work. The first one being the Higgs trilinear coupling quantified by  $C_\phi$  defined in Equation 10.1 and the other two being the deformation of the first-family SM Yukawa coupling to the up and down quark defined as  $C_{u\phi}$  and  $C_{d\phi}$  in Equation 10.12 with  $i = j = 1$ . We will not consider modifications of the second generation of quarks as their effects in di-Higgs production would be suppressed by the small parton distribution functions and are hence expected to be more pronounced using other methods for constraining them. For ease of interpretation we will also present our results in terms of  $\kappa_\lambda$ ,  $\kappa_u$  and  $\kappa_d$  which are

---

<sup>2</sup>More clarity on Shapley values and interpretable machine learning in general, along with their application can be found in [Interpretable Machine Learning](#) by Christoph Molnar [408].

simply the rescaling of the SM trilinear coupling and the light-quark Yukawa couplings of the up and down quarks, respectively.

In the BDT analysis we combine the  $b\bar{b}h$ , ( $h \rightarrow \gamma\gamma$ ) and  $t\bar{t}H$ , ( $h \rightarrow \gamma\gamma$ ) channels into one category calling it  $Q\bar{Q}h$  while the other (continuum) background channel,  $b\bar{b}\gamma\gamma$ , is treated as a separate category. For any analysis involving  $C_\phi$ , we need three separate categories for the triangle, box and interference terms of the  $ggF$   $hh$  production which we shall refer to as  $hh_{\text{tri}}^{\text{ggF}}$ ,  $hh_{\text{box}}^{\text{ggF}}$  and  $hh_{\text{int}}^{\text{ggF}}$ , respectively. The  $q\bar{q}A$  channels stands for two other categories, one each for probing the Wilson coefficients  $C_{u\phi}$  and  $C_{d\phi}$ , respectively. However, the  $q\bar{q}A$  channels are not the only channels sensitive to  $C_{u\phi}$  and  $C_{d\phi}$ . In fact the decay  $h \rightarrow \gamma\gamma$ , the production of the Higgs in the  $ggF$  channel and the width of the Higgs are modified by the size of  $C_{u\phi}$  and  $C_{d\phi}$  [319]. Hence, these as well need to be taken into account. In what follows, we will refer to the two  $q\bar{q}A$  channels as  $u\bar{u}A$  and  $d\bar{d}A$  explicitly.

As we progress through the analysis we study the modification of one, two and three Wilson coefficients at a time. To extract just  $C_\phi$  from the data we need to perform a five channel classification (two signal and three background modes including the  $hh_{\text{box}}^{\text{ggF}}$  contribution that is insensitive to modifications of  $C_\phi$ ). To extract either  $C_{u\phi}$  or  $C_{d\phi}$  we have to perform a four channel classification taking the  $ggF$  channel as a single background mode. To extract  $C_\phi$  and one of  $C_{u\phi}$  or  $C_{d\phi}$  we need to perform a six channel classification. Lastly, to extract all three Wilson coefficients we will need a seven channel classification. All the codes and data necessary to reproduce the results we got from this interpretable machine learning framework are made available at a **Github** repository: <https://github.com/talismbrandi/IML-diHiggs.git>.

To set the stage, we will define our measure of significance and how we estimate it. We first construct a confusion matrix from the predictions of the trained BDT. This is a  $n \times n$  matrix, for  $n$  channels. The sum of the elements in the  $i^{\text{th}}$  row,  $\sum_j N_{ij}$ , gives the actual number of events produced in channel  $i$  that would be generated in a pseudo-experiment with the projected luminosity corresponding to the actual experiment. The sum of the  $j^{\text{th}}$  column,  $\sum_i N_{ij}$ , gives the number of events from channel  $j$  predicted (including correct classifications and misclassifications) by the BDT in this pseudo-experiment. Hence the  $(i, j)$  element of the matrix gives the number of events of the  $i^{\text{th}}$  class that is classified as belonging to the  $j^{\text{th}}$  class with  $i \neq j$  signifying a misclassification. The significance of the  $j^{\text{th}}$  channel given by  $S/\sqrt{S+B}$ ,  $S$  being signal and  $B$  being background, can be defined as

$$\mathcal{Z}_j = \frac{|N_{jj}|}{\sqrt{\sum_i N_{ij}}}, \quad (9.4)$$

where  $i$  is the row index and  $j$  is the column index.

The fact that machine learning algorithms can far outperform cut-and-count analyses is a bygone conclusion. Preliminary estimates of the HL-LHC reach for SM di-Higgs production can be found in [191] and range from  $4\sigma$  to  $4.5\sigma$  signal significance combining several channels and both the ATLAS and CMS measurements. The  $b\bar{b}\gamma\gamma$  final state alone allows for a  $\sim 2.7\sigma$  measurement. In [413] a more refined machine learning procedure using Bayesian Optimization has been suggested and it has been shown that,

indeed, the measurement of a di-Higgs signal can be further improved over preliminary estimates made by ATLAS and CMS using the  $b\bar{b}\gamma\gamma$  final state alone. A sensitivity of about  $5\sigma$  can be achieved using their procedure with the caveat that they use  $S/\sqrt{B}$  as the definition of significance with very low number of signal and background events. As an exercise we repeated the BDT analysis with our framework and estimated a  $\sim 3.4\sigma$  signal significance for SM di-Higgs production, which is similar to the estimate made in [413] without using any optimization.

A better portrayal of the advantages gained by using a multivariate analysis can be made by comparing the constraints set on  $C_{u\phi}$ , or  $\kappa_u$ , and  $C_{d\phi}$ , or  $\kappa_d$ , from a cut-and-count (CC) analysis and a multivariate (MV) analysis allowing for the variation of only one Wilson coefficient at a time. The projected  $1\sigma$  bounds at HL-LHC for  $6\text{ ab}^{-1}$  of luminosity for a CC are given in [319] and compare to our results as follows

$$\begin{aligned} C_{u\phi}^{MV}(\kappa_u^{MV}) &= [-0.09, 0.10] \quad([-466, 454]), & C_{u\phi}^{CC}(\kappa_u^{CC}) &= [-0.18, 0.17] \quad([-841, 820]), \\ C_{d\phi}^{MV}(\kappa_d^{MV}) &= [-0.16, 0.16] \quad([-360, 360]), & C_{d\phi}^{CC}(\kappa_d^{CC}) &= [-0.18, 0.18] \quad([-405, 405]). \end{aligned} \quad (9.5)$$

From this we clearly see a factor of  $\sim 2$  improvement in the bounds on  $C_{u\phi}$  and  $\mathcal{O}(10\%)$  improvement in the determination of  $C_{d\phi}$ . The projected bounds on these operators at FCC-hh with  $30\text{ ab}^{-1}$  of data using our framework are

$$\begin{aligned} C_{u\phi}^{MV}(\kappa_u^{MV}) &= [-0.012, 0.011] \quad([-57.8, 54.7]), \\ C_{d\phi}^{MV}(\kappa_d^{MV}) &= [-0.012, 0.012] \quad([-26.3, 28.4]). \end{aligned} \quad (9.6)$$

These projected bounds for FCC-hh are an order of magnitude better than those for HL-LHC. In addition, the bounds on  $C_{u\phi}$  and  $C_{d\phi}$  are numerically the same displaying a much greater improvement in the bounds on  $C_{d\phi}$  than on  $C_{u\phi}$  at the higher energy collider.

#### 9.4.1 Constraints on $C_\phi$ at the HL-LHC and FCC-hh

First, we will show the projections of the limits that can be set on  $C_\phi$  (or equivalently,  $\kappa_\lambda$ ) from HL-LHC and FCC-hh. In Table 9.3 we provide the output of the BDT classification for  $6\text{ ab}^{-1}$  of data collected at HL-LHC and in Table 9.4 we provide the same for  $30\text{ ab}^{-1}$  of data at FCC-hh. It can be seen from these matrices that while the  $b\bar{b}\gamma\gamma$  QCD-QED channel is the dominant background, the BDT performs better in separating it from the signal channels than separating  $Q\bar{Q}h$ . This is due to the kinematic similarities between the signal and the  $Q\bar{Q}h$  background.

In Figure 9.5 we present the constraints on  $C_\phi$  (or  $\kappa_\lambda$ ) that can be set from HL-LHC in the left panel and FCC-hh in the right panel. The  $hh_{\text{box}}^{\text{ggF}}$  topology is not modified by  $C_\phi$  and serves as a background to the measurement of  $C_\phi$ . We separate the constraints from the  $hh_{\text{tri}}^{\text{ggF}}$ , which is quadratic in  $C_\phi$  from the  $hh_{\text{int}}^{\text{ggF}}$  which is linear in  $C_\phi$ . The combination of the two is given by the red dot-dashed line and is asymmetric around

Predicted no. of events at HL-LHC							
Actual no. of events	Channel	$hh_{\text{tri}}^{\text{ggF}}$	$hh_{\text{tri}}^{\text{ggF}}$	$hh_{\text{box}}^{\text{ggF}}$	$Q\bar{Q}h$	$b\bar{b}\gamma\gamma$	total
	$hh_{\text{tri}}^{\text{ggF}}$	28	14	18	38	10	108
	$hh_{\text{int}}^{\text{ggF}}$	89	80	129	178	41	517
	$hh_{\text{box}}^{\text{ggF}}$	77	105	266	265	50	763
	$Q\bar{Q}h$	177	98	191	5,457	1,835	7,758
	$b\bar{b}\gamma\gamma$	1,743	845	1,074	30,849	287,280	321,791
	$\mathcal{Z}_j$	0.61	2.37	6.49	28.45	534.1	

**Table 9.3.** Trained BDT classification (confusion matrix) of the five channel used to extract constraints on  $C_\phi$  (or  $\kappa_\lambda$ ) at HL-LHC with  $6 \text{ ab}^{-1}$  luminosity (ATLAS+CMS), assuming SM signal injection. The right-most column gives the total number of events expected in each channel in the SM and the bottom-most row gives the signal significance.

Predicted no. of events at FCC-hh							
Actual no. of events	Channel	$hh_{\text{tri}}^{\text{ggF}}$	$hh_{\text{tri}}^{\text{ggF}}$	$hh_{\text{box}}^{\text{ggF}}$	$Q\bar{Q}h$	$b\bar{b}\gamma\gamma$	total
	$hh_{\text{tri}}^{\text{ggF}}$	3,579	1,303	2,372	4,697	337	12,288
	$hh_{\text{int}}^{\text{ggF}}$	13,602	7,300	17,075	24,716	1523	64,216
	$hh_{\text{box}}^{\text{ggF}}$	14,534	11,416	35,988	415,26	1,996	105,460
	$Q\bar{Q}h$	29,611	12,355	23,279	1,238,266	214,564	1,518,075
	$b\bar{b}\gamma\gamma$	45,574	22,290	26,213	150,935	227,142	24,317,657
	$\mathcal{Z}_j$	10.95	31.22	111.1	737.7	4,743	

**Table 9.4.** Trained BDT classification (confusion matrix) of the five channel used to extract constraints on  $C_\phi$  (or  $\kappa_\lambda$ ) at FCC-hh with  $30 \text{ ab}^{-1}$  luminosity, assuming SM signal injection. The right-most column gives the total number of events expected in each channel in the SM and the bottom-most row gives the signal significance.

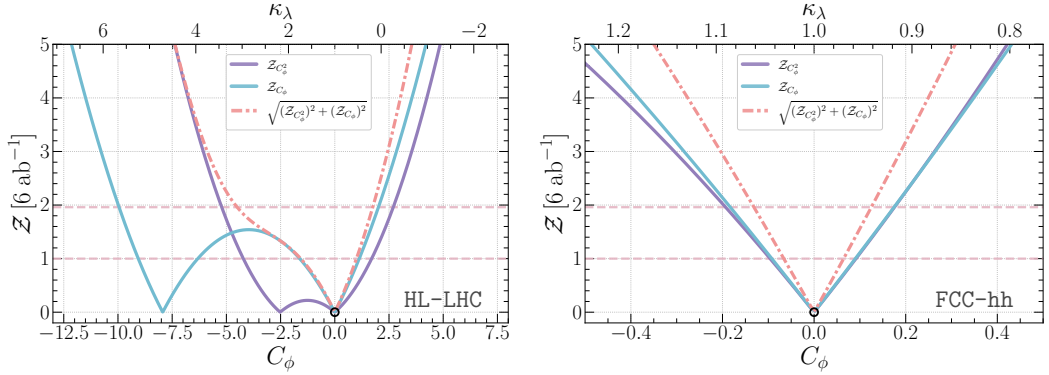


**Figure 9.5.** Bounds on  $C_\phi$  (or  $\kappa_\lambda$ ) at the HL-LHC (left panel) and the FCC-hh (right panel). The solid blue lines are the constraints coming from the  $hh_{\text{int}}^{\text{ggF}}$  contribution which scales linearly with the modified coupling and the solid purple line is that from the  $hh_{\text{tri}}^{\text{ggF}}$  contribution that scales quadratically with the modified coupling. The red dashed line is the combination of the quadratic and linear channel. The horizontal light red dashed lines marks the 68% and 95% confidence intervals.

the best fit point, for SM signal injection,  $C_\phi = 0$  ( $\kappa_\lambda = 1$ ). The projected  $1\sigma$  bound on  $C_\phi$  is  $[-1.57, 1.00]$  at HL-LHC. There is a vast improvement projected for the FCC-hh which is not only due to increased luminosity but also due to the measurement being at a higher energy. The projected  $1\sigma$  bound is  $C_\phi = [-0.066, 0.064]$ . The latter corresponds to a 3% bound on  $\kappa_\lambda$ .

#### 9.4.2 Two and three parameter constraints on $C_\phi$ , $C_{u\phi}$ and $C_{d\phi}$

The primary focus of this work is to move beyond just looking at constraints on  $C_\phi$  from di-Higgs production and to shed light on how simultaneous modifications of the light-quark Yukawa couplings due to non-zero contributions from  $C_{u\phi}$  and  $C_{d\phi}$  can change the constraints on  $C_\phi$ . The modifications of the light-quark Yukawa couplings manifest themselves in two different ways. Firstly, non-zero  $C_{u\phi}$  and  $C_{d\phi}$  open up the  $q\bar{q} \rightarrow hh$  production mode through a point interaction (see Figure 9.4) thus changing the production cross-section of the di-Higgs channel. This increase in the production cross-section sets the tightest constraints on  $C_{u\phi}$  and  $C_{d\phi}$  from di-Higgs production. Secondly, the modification of the light-quark Yukawa couplings also modify the branching fraction of  $h \rightarrow \gamma\gamma$  and the width of the Higgs. The latter modifies the channels that are also sensitive to  $C_\phi$ , thus modifying the constraints that can be set on  $C_\phi$  from future measurements. Such constraints are the subdominant ones on  $C_{u\phi}$  and  $C_{d\phi}$  but they are necessary for a holistic picture.

In the two parameter fits, we consider three possible scenarios. Firstly, one can assume that the trilinear Higgs coupling is not modified and only the light-quark Yukawa couplings are. Two other possibilities are the simultaneous modification of the  $C_\phi$  and one of  $C_{u\phi}$  and  $C_{d\phi}$ . These are the three constraints that we show in Figure 9.6. As

Operators	$C_{u\phi}$	$C_{d\phi}$	$C_\phi$		$\kappa_u$	$\kappa_d$	$\kappa_\lambda$
HL-LHC 14 TeV 6 ab $^{-1}$							
$\mathcal{O}_\phi$	—	—	[-1.57, 1.00]		—	—	[0.53, 1.73]
$\mathcal{O}_{u\phi}$	[-0.09, 0.10]	—	—		[-477, 431]	—	—
$\mathcal{O}_{d\phi}$	—	[-0.16, 0.16]	—		—	[-360, 360]	—
$\mathcal{O}_{u\phi} \& \mathcal{O}_\phi$	[-0.087, 0.091]	—	[-2.42, 0.79]		[-434, 417]	—	[0.63, 2.13]
$\mathcal{O}_{d\phi} \& \mathcal{O}_\phi$	—	[-0.17, 0.17]	[-2.73, 0.77]		—	[-381, 379]	[0.63, 2.27]
$\mathcal{O}_{u\phi} \& \mathcal{O}_{d\phi}$	[-0.065, 0.069]	[-0.12, 0.12]	—		[-331, 312]	[-268, 272]	—
All	[-0.077, 0.084]	[-0.160, 0.162]	[-2.77, 0.43]		[-400, 369]	[-362, 359]	[0.79, 2.30]
FCC-hh 100 TeV 30 ab $^{-1}$							
$\mathcal{O}_\phi$	—	—	[-0.066, 0.064]		—	—	[0.97, 1.03]
$\mathcal{O}_{u\phi}$	[-0.012, 0.011]	—	—		[-57.8, 54.7]	—	—
$\mathcal{O}_{d\phi}$	—	[-0.012, 0.011]	—		—	[-26.3, 28.4]	—
$\mathcal{O}_{u\phi} \& \mathcal{O}_\phi$	[-0.010, 0.011]	—	[-0.091, 0.042]		[-52, 49]	—	[0.98, 1.04]
$\mathcal{O}_{d\phi} \& \mathcal{O}_\phi$	—	[-0.010, 0.012]	[-0.092, 0.041]		—	[-24, 26]	[0.98, 1.04]
$\mathcal{O}_{u\phi} \& \mathcal{O}_{d\phi}$	[-0.008, 0.009]	[-0.008, 0.009]	—		[-42, 39]	[-19, 19]	—
All	[-0.009, 0.010]	[-0.009, 0.010]	[-0.105, 0.023]		[-47, 44]	[-21, 21]	[0.99, 1.05]

**Table 9.5.** The  $1\sigma$  bounds on  $C_{u\phi}$ ,  $C_{d\phi}$  and  $C_\phi$  from one-, two- and three-parameter fits for HL-LHC with  $6\text{ab}^{-1}$  of data and FCC-hh with  $30\text{ab}^{-1}$  of data. The corresponding bounds on the rescaling of the effective couplings,  $\kappa_u$ ,  $\kappa_d$  and  $\kappa_\lambda$  are presented on the right side of the table.

before, the constraints have been obtained by training the BDT to separate the relevant signal channels from the background, the signal used being the one corresponding to the pair of Wilson coefficients that we intend to constrain. The confusion matrices for all the three cases can be found in the [Github](#) repository for this analysis. The left panels of Figure 9.6 show the projected constraints for HL-LHC and right panels for the FCC-hh.

Comparing with the constraints on  $C_\phi$  given in subsection 9.4.1 and Figure 9.5, it can be seen from the top and middle left panels of Figure 9.6 that, indeed, the constraints on  $C_\phi$  are diluted when the light-quark Yukawa couplings are allowed to vary. This effect is somewhat more prominent for  $C_{d\phi}$  than for  $C_{u\phi}$  and stems from the fact that away from  $C_{u\phi,d\phi} = 0$  larger negative values of  $C_\phi$  are allowed by the crescent shaped curves in Figure 9.6. For  $C_{d\phi}$  vs.  $C_\phi$  the  $3\sigma$  region is unbounded in the domain  $|C_{d\phi}| \gtrsim 0.6$ . The bounds on  $C_{u\phi}$  and  $C_{d\phi}$  from the fit with two-parameters including  $C_\phi$  remain the same as the bounds on these Wilson coefficient from the single parameter  $C_{u\phi,d\phi}$  fits. We summarize the results in Table 9.5.

It should be noted that the two-parameter fit for  $C_{u\phi}$  and  $C_{d\phi}$  provide a stronger bound on the two parameters than the fit done individually. While this might be a bit counter-intuitive considering constraints from fits tend to deteriorate with the increasing number of parameters, we found that is not the case here. The reason is that the two-parameter fit is performed with the predictions made by the BDT trained with simulated events for both  $u\bar{u}A$  and  $d\bar{d}A$ . Between these two channels, each form the background for the other when separating them through a confusion matrix. Since the training also give the proportion of mistagged events, both the signal and the backgrounds are modified by

the Wilson coefficients leading to a greater deformation of the likelihood in a favourable direction such that the constraints on the Wilson coefficients in the two-parameter fit is better than for the case in which they were separated from other  $b\bar{b}\gamma\gamma$  backgrounds individually.

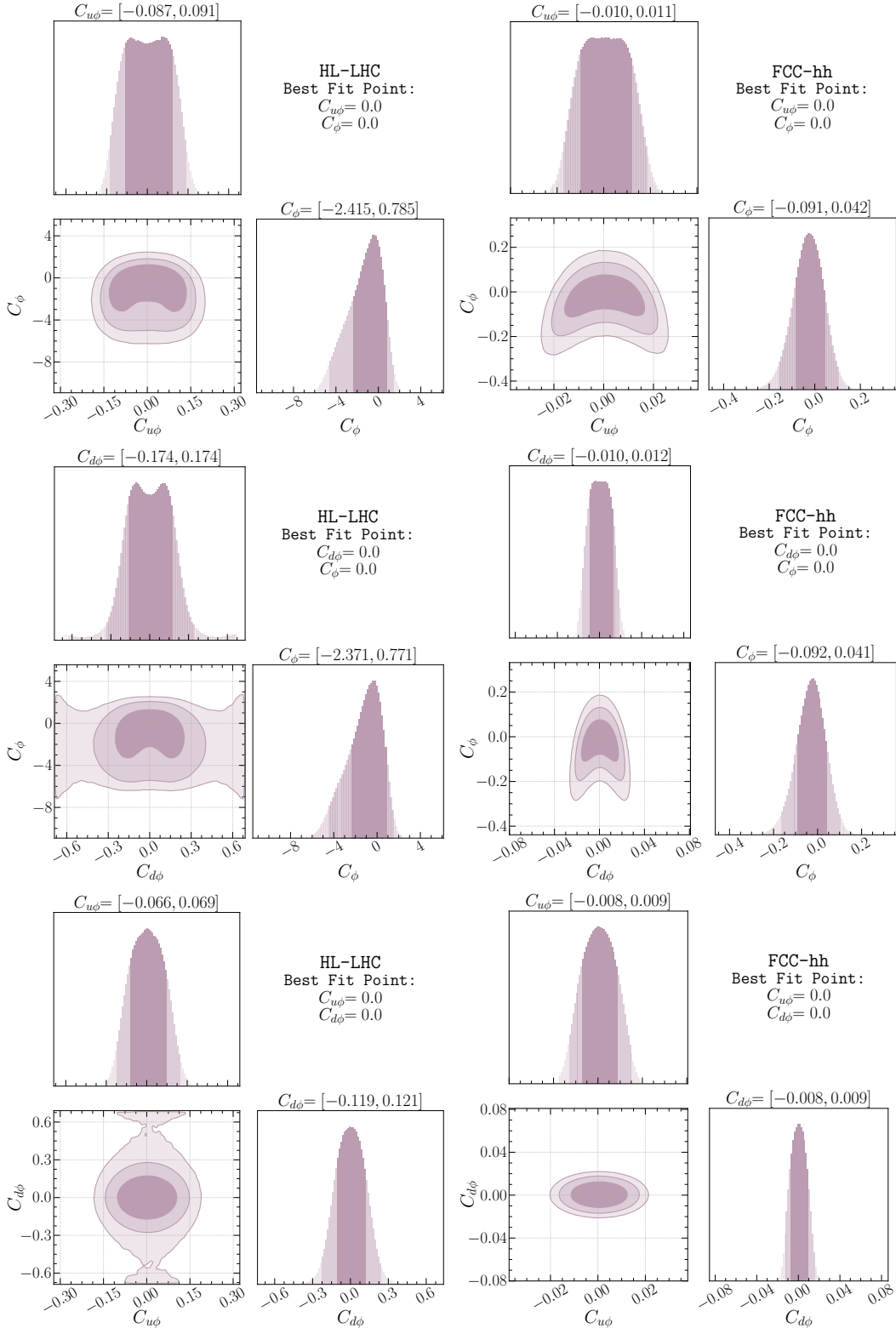


**Figure 9.6.** Constraints on pairs of Wilson coefficients for  $C_\phi$ ,  $C_{u\phi}$  and  $C_{d\phi}$ . The panels of the left are for HL-LHC with  $6 \text{ ab}^{-1}$  of luminosity and the ones on the right are for FCC-hh with  $30 \text{ ab}^{-1}$  of luminosity.

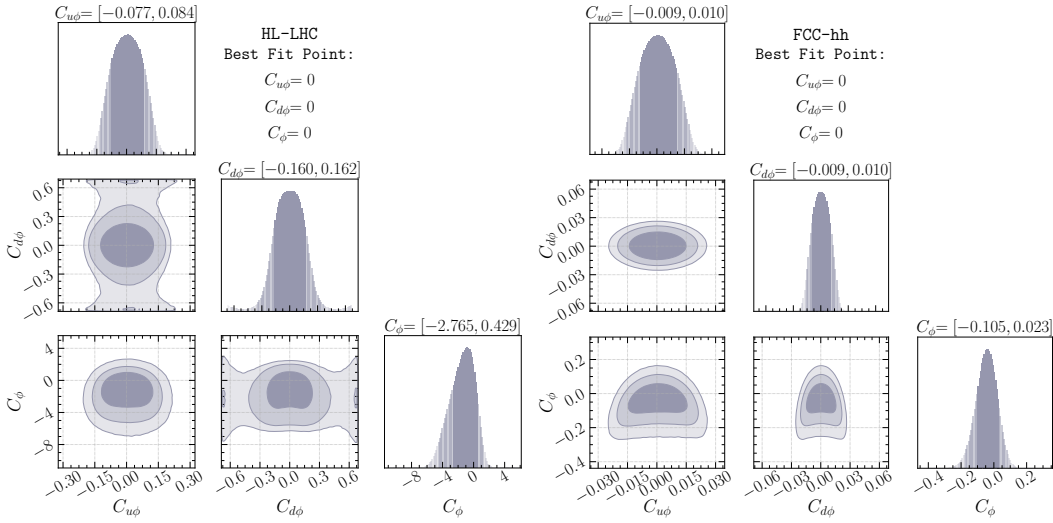


**Figure 9.7.** Three parameter fits with  $C_{u\phi}$ ,  $C_{d\phi}$  and  $C_\phi$ ,  $6\text{ab}^{-1}$  of luminosity at 14 TeV for HL-LHC (left panel) and  $30\text{ab}^{-1}$  of luminosity at 100 TeV for FCC-hh (right panel).

Finally, we perform a combined three-parameter fit including  $C_{u\phi}$ ,  $C_{d\phi}$  and  $C_\phi$ , with the results shown in Figure 9.7. For the same reason as explained before, the bounds on  $C_{u\phi}$  and  $C_{d\phi}$  are somewhat better than the two-parameter fits of these operators individually with  $C_\phi$ . The HL-LHC and FCC-hh projected bounds on  $C_\phi$  remain nearly the same as those from the corresponding two-parameter fits. In Table 9.5 we also provide the bounds on  $\kappa_u$ ,  $\kappa_d$  and  $\kappa_\lambda$  for comparison.

#### 9.4.3 Interpretation of Shapley values

Finally, we want to demonstrate the interpretability of the machine learning framework we use and discuss the physics that allows for the separation of the signal channels from the background channels. The advantage of using an interpretable multivariate framework is that one can easily understand which of the kinematic variables are important for orchestrating this separation in a manner that significantly improves upon a cut-and-count analysis. As described previously, we use a measure derived from Shapley values,  $|S_v|$ , to understand the importance of each kinematic variable and, henceforth, understand the differences in kinematic shapes that separate the signal from the background.

To give a feeling of what the values of  $S_v$  mean, let us examine a single event. Assuming we have trained the BDT with  $n$  kinematic variables, each event with  $n \times m$  Shapley values associated with it,  $m$  being the number of channels (signal and background channels). For a particular channel,  $j$  and kinematic variable,  $i$ ,  $S_v$  can be positive or negative. A positive value implies that it is more likely that the event belongs to channel  $j$  according to the value of the kinematic variable  $i$ . Conversely, a negative value implies that the event is less likely to belong to channel  $j$  given the value of the kinematic variable  $i$ . So regardless of whether  $S_v$  is positive or negative it helps in the sorting of events

into various channels. Hence,  $\overline{|S_v|}$  for a particular variable represents the strength of the variable to distinguish between channels. When summed over all channels this gives an overall picture of how good a discriminant a kinematic variable is for the processes involved. This is what is shown in [Figure 9.8](#) which we will now elaborate upon.

To begin with, we take a look at the  $\overline{|S_v|}$  computed for the five channel analysis performed for separating  $hh_{\text{tri}}^{\text{ggF}}$  and  $hh_{\text{int}}^{\text{ggF}}$  channels from  $hh_{\text{box}}^{\text{ggF}}$ ,  $Q\bar{Q}h$  and  $b\bar{b}\gamma\gamma$  QCD-QED background. In [Figure 9.8](#) we see the hierarchy plots for HL-LHC (top left panel) and FCC-hh (top right panel) generated from the predictions made by the BDT for this five channel analysis. For both the colliders,  $H_T$  is the most important variable that is bringing about separation of the  $hh_{\text{tri}}^{\text{ggF}}$  and  $hh_{\text{int}}^{\text{ggF}}$  channels from the dominating  $b\bar{b}\gamma\gamma$  QCD-QED background. The second most important variable is  $m_{\gamma\gamma}$ . The importance of  $m_{\gamma\gamma}$  accentuates the separation of the background by a greater degree at FCC-hh than at HL-LHC.

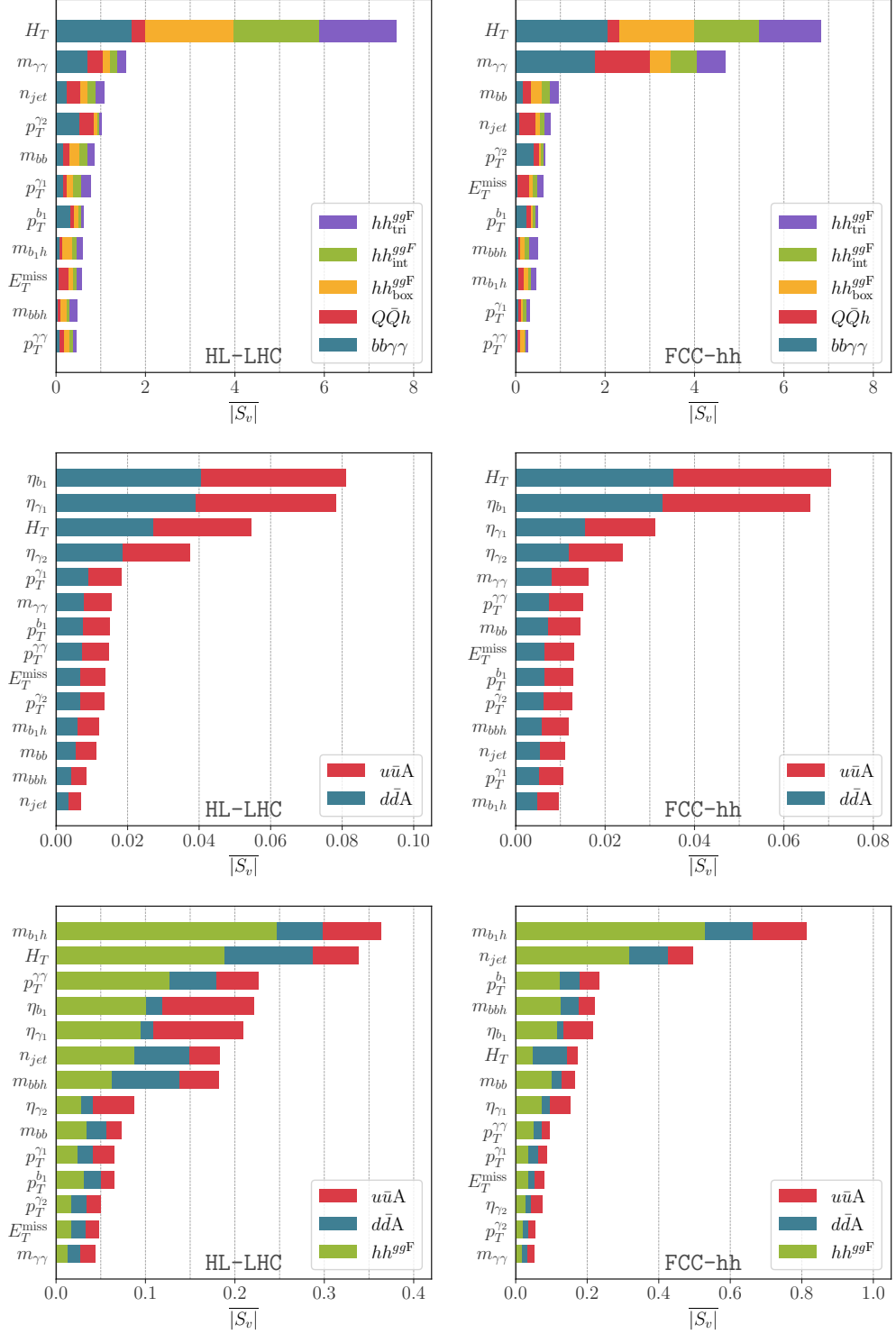


**Figure 9.8.** Top panels: The hierarchy of variables important for the separation of  $hh^{ggF}_{tri}$  from  $hh^{ggF}_{int}$  events from  $hh^{ggF}_{box}$ ,  $Q\bar{Q}h$  and  $bb\gamma\gamma$  QCD-QED background at HL-LHC (left panel) and FCC-hh (right panel). Middle panels: The hierarchy of variables important for the separation of  $u\bar{u}A$  from  $d\bar{d}A$  events at HL-LHC (left panel) and FCC-hh (right panel). Lower panels: The hierarchy of variables important for the separation of  $hh^{ggF}$ ,  $u\bar{u}A$  and  $d\bar{d}A$  events at HL-LHC (left panel) and FCC-hh (right panel). The higher the value of  $|S_v|$  is, the more important the kinematic variable is in separating the different channels.

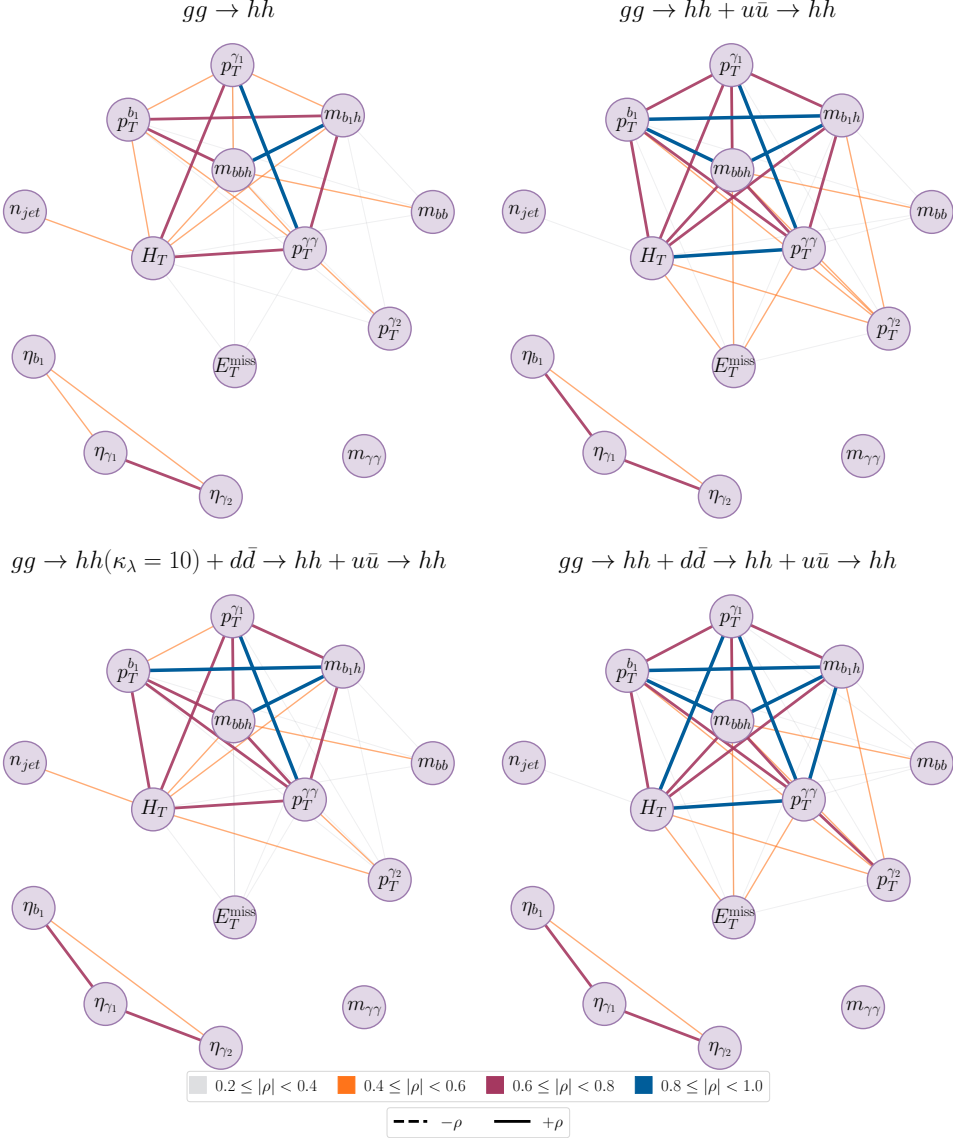


**Figure 9.9.** Network diagrams visualization of correlations ( $\rho$ ) amongst the kinematic variables used in the analysis. Top left: Only the gluon-gluon fusion channel. Top right: The  $ggF$  channel along with the  $u\bar{u}A$  channel with  $\kappa_u = 1600$ . Bottom right: The  $d\bar{d}A$  channel with  $\kappa_d = 800$  added to the channels in the top right panel. Bottom left: The same channels as in the bottom right panel but with  $\kappa_\lambda = 10$ .

For the separation between the two  $q\bar{q}A$  channels the story is very different. From the middle panels of Figure 9.8 we see that the separation of  $u\bar{u}A$  and  $d\bar{d}A$  is truly a multivariate problem. Not surprisingly, the picture is very different for HL-LHC and FCC-hh. The differences between the two channels are driven by the differences in the parton distribution functions (PDF) of the up and down quarks. Since the PDF

for the quarks change significantly from 14 TeV to 100 TeV, the variables that effect the separation of the two channels also change. Thus  $|S_v|$  give us a true picture of how distributions of several kinematic variables determine the separation of different channels that are mostly similar. When comparing the abscissa of the top two panels with the middle two panels one will also notice that  $|S_v|$  assumes much smaller values in the separation of  $u\bar{u}A$  and  $d\bar{d}A$ . This clearly shows that the two channels are distributed quite identically and are difficult to separate.

Lastly, in the bottom panels of Figure 9.8 we show the variables that are important in separating the  $q\bar{q}A$  channels from the  $ggh$  Higgs pair production channel. The invariant mass of the leading  $b$ -jet and  $h$ ,  $m_{b_1 h}$  is the most important variable at both HL-LHC and FCC-hh. However the hierarchy of variables below  $m_{b_1 h}$  are quite different for HL-LHC and FCC-hh. Both  $H_T$  and  $p_T^{\gamma\gamma}$  are far less important at FCC-hh than at HL-LHC. This displays the clear advantage that machine learning algorithms have over a cut-and-count analysis where separate cut strategies would have to be built for the two colliders leading to two separate analysis that can, instead, be done with the same framework when using machine learning.

The correlation plots in Figure 9.9 show how the linear correlations amongst the variables evolve when different channels are added. The top left panel are events sampled from the  $ggF$  distribution. One can already see a clustering in some of the variables related to momenta and invariant mass. The other cluster is of the pseudorapidity of the particles in the final state. This correlation structure evolves when one adds the  $u\bar{u}A$  channel when  $E_T^{\text{miss}}$  gets connected to the upper cluster in the top right panel. The correlation is now stronger between  $\eta_{\gamma_1}$  and  $\eta_{b_1}$  and several correlations in the upper cluster are much stronger too. The change in the correlations continue as one keeps adding channels as can be seen from the bottom right and bottom left panels. It is the capture of this change in the correlations (and higher-order correlations) that enhances the capabilities of the machine learning algorithms to distinguish between the various channels. While  $m_{\gamma\gamma}$  by its shape alone allows for the separation between  $b\bar{b}\gamma\gamma$  and the other channels, the correlations between the other kinematic variables aid in the separation of the channels with one or two Higgs in the final state.

## 9.5 Summary

In this work we walk through an analysis of how kinematic shapes can be used to glean information about the nuances of various production modes with the same final states but deformed differentially by the existence of degrees of freedom beyond the Standard Model. We show that this information can be extracted by using an interpretable machine learning framework which is not only very effective separating these differences in kinematic shapes, but also yields itself to interpretations in terms of physics that is known and well understood. The example we chose is Higgs pair production in the  $b\bar{b}\gamma\gamma$  final state. We emphasized that probing Higgs pair production is an important next step for an understanding of the model underlying the fundamental interactions of particles and hence a potential gateway to new physics. We show that even beyond the trilinear

Higgs couplings, the light-quark Yukawa couplings can be probed through this production mode. In fact, the  $q\bar{q}A$  channel opens up only in the presence of BSM physics and well motivated models of new dynamics bring about the simultaneous modification of the trilinear Higgs coupling and the light-quark Yukawa couplings. Indeed, we motivated our study by showing that in different frameworks large modifications of the light quark Yukawa couplings can be obtained. Knowing the difficulty of measuring these couplings we propose an interpretable machine learning framework that significantly outperforms traditional cut-based analyses.

As opposed to using black-box models, the interpretable framework allows us to gain physics insights into how signal and background separation can be brought into effect, pointing to kinematic variables like  $H_T$  and  $m_{\gamma\gamma}$  as being important variables that instrument this separation. As a result we find enhanced sensitivities to  $C_\phi$  or  $\kappa_\lambda$  that quantify the modification to the Higgs trilinear coupling. Furthermore, we see that the measurement of the light-quark Yukawa couplings is aided by using the methods we advocate bringing about far greater sensitivities than would be possible with a cut-based analysis at the HL-LHC and the FCC-hh. The advantage of using an interpretable framework using Shapley values is that it provides added confidence to the robustness of the multivariate analyses that we perform using simulated data.

The salient results of this work are:

- The modification of the Higgs trilinear coupling can be measured at  $\mathcal{O}(1)$  precision at the HL-LHC and at  $\mathcal{O}(1\%)$  precision at the FCC-hh.
- The rescaling of the light-quark Yukawa couplings,  $\kappa_u$  and  $\kappa_d$ , can be measured to  $\mathcal{O}(100)$  at the HL-LHC and  $\mathcal{O}(10)$  at FCC-hh. This translates to  $C_{u\phi}$  and  $C_{d\phi}$  constrained at  $\mathcal{O}(10\%)$  at the HL-LHC and  $\mathcal{O}(1\%)$  at FCC-hh.
- The measurement of  $C_\phi$ , or  $\kappa_\lambda$ , is significantly diluted once the light-quark Yukawa couplings are allowed to vary. Hence, in a joint fit, the bounds on  $C_\phi$  are much weaker.
- There are theoretical models that motivate the simultaneous modification of the trilinear Higgs coupling and the light-quark Yukawa couplings. Hence, the dilution of the bounds on  $C_\phi$  due to the presence of NP in the light-quark Yukawa sector should be taken into consideration in future phenomenological extraction of  $C_\phi$ .
- The bounds obtained with the interpretable machine learning framework that we use not only outperforms cut-based analyses by far, but also allows for physics insights into kinematic distributions of the various channels that helps distinguish them in an experiment.

In conclusion, we stress that the interplay between the Yukawa sector and the Higgs trilinear coupling is non-trivial and requires careful consideration. Future experiments at the HL-LHC and FCC-hh will bring significant improvements in the sensitivities to  $C_\phi$ ,  $C_{u\phi}$  and  $C_{d\phi}$  through the Higgs pair production channel. In particular, the bounds on the light-quark Yukawa couplings from Higgs pair production can possibly be the most stringent bounds amongst all other experimental probes of the light quark Yukawa couplings.

## 9.6 Discussion of theoretical and systematic uncertainties

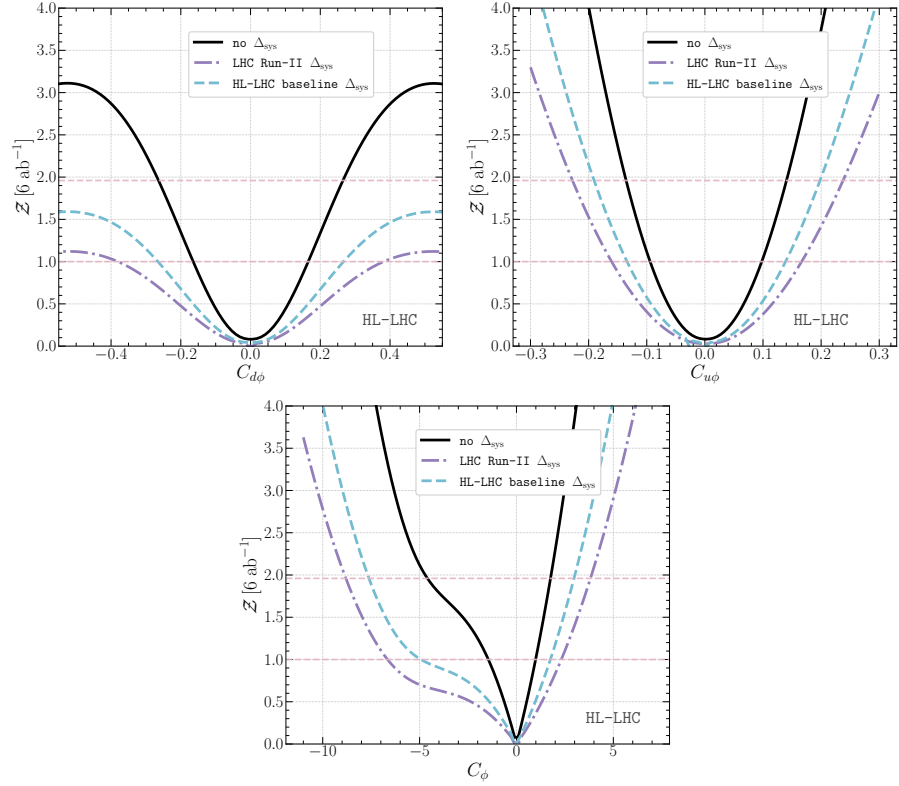


**Figure 9.10.** The significance  $Z$  from a single parameter fit for  $C_{d\phi}$  (upper left panel) ,  $C_{u\phi}$  (upper right panel) and  $C_\phi$  (lower center panel) for the HL-LHC with no systematic uncertainties (black) and two ansätze for systematic uncertainties. The first is the current Run-II 8.2% in violet and the HL-LHC baseline 5.3% estimated by ATLAS in blue, including theoretical uncertainties without top mass renormalisation scheme.

In this section we present an estimate of the systematic uncertainties that can affect the measurements discussed in this work at the HL-LHC. We do not present these estimates for the FCC-hh for lack of sufficient information or the ability to project such uncertainties far into the future. We use two scenarios for systematic uncertainties: the first is a 8.2% uncertainty which corresponds to the current systematic uncertainty that ATLAS has reported for their Run-II search for Higgs pair production [414]. The second scenario is the ATLAS HL-LHC baseline systematic uncertainty of 5.3% reported in [415]. For LHC run-II, statistical uncertainties remain the dominant part of the uncertainty budget for di-Higgs analysis. Regarding the systematic uncertainties, experimental sources remain the dominant part in comparison to the theoretical ones. The story flips for the HL-LHC where the main source of uncertainties is expected to be coming from theoretical uncertainties. The current theoretical uncertainty estimate of the SM gluon fusion process at NNLO is  $^{+6\%}_{-23\%}$  for  $\sqrt{s} = 14$  TeV and  $^{+4\%}_{-21\%}$  for

$\sqrt{s} = 100\text{TeV}$  [416]. The largest part of the uncertainty stems from the uncertainty due to the renormalization scheme choice of the top quark mass. This uncertainty can, for the moment, only be estimated at NLO since no full mass dependent results at NNLO are available. Moreover, the top quark mass renormalization scheme uncertainty is not included in the estimated HL-LHC (nor LHC Run II) uncertainties schemes that we have considered.

In Figure 9.10 we show the significance  $\mathcal{Z}$  for the three Wilson coefficient,  $C_\phi$ ,  $C_{u\phi}$  and  $C_{d\phi}$ , at the HL-LHC from single parameter fits with no systematic uncertainties (black), LHC Run-II (violet) and HL-LHC baseline (blue) systematic uncertainties ansatze. We observe that for the current Run-II ansatz, the bounds for all three Wilson coefficients is diluted by 100% or more. As for the HL-LHC baseline, the bounds are diluted by  $\sim 70\%$ . However, it should be noted, that both systematic uncertainties scenarios are rather conservative. It is likely that the HL-LHC detector upgrade and new theoretical developments in higher-order corrections to di-Higgs cross-section will reduce the systematic uncertainties from the baseline.

## 9.7 Light-quark Yukawa and Self Coupling at Future Lepton Colliders

Future high energy lepton colliders [251, 254, 417] offer further alternative and clean signals for measurement of Higgs properties. For example, Higgs decays to “un-tagged” light jets including  $u, d, s$  quarks can be further disentangled from  $H \rightarrow gg$  using event shape analysis [418] and can reach a sensitivity of  $\kappa_d \approx 90$  and  $\kappa_u \approx 192$  at 250 GeV with  $5\text{ab}^{-1}$  data compared with a sensitivity of  $\kappa_d \approx 470$  and  $\kappa_u \approx 900$  at the  $6\text{ab}^{-1}$  HL-LHC [303, 419].

The sensitivity to Higgs self-coupling comes indirectly for center of mass energy below 250 GeV from the precision measurement of the  $Zh$  production channel ( $\delta\kappa_\lambda$  ( $1\sigma$ ) 0.4 at 250 GeV), and at 500 GeV directly from the  $Zhh$  channel ( $\delta\kappa_\lambda$  ( $1\sigma$ ) 0.27 at 500 GeV), and from vector boson fusion like production to  $hh\nu\nu$  when 1 TeV or higher energy scales are available ( $\delta\kappa_\lambda$  ( $1\sigma$ ) 10% at 1 TeV). The prospective sensitivity depends on the collider setup, mainly the integrated luminosity and polarization of initial lepton beams. Given the updated prospects of future machine designs [330], we list a short summary in Table 9.6 of the expected sensitivities on the individual parameters in the  $\kappa$  framework. These numbers are all assuming one-parameter fits in  $\kappa$  or (translated from) SMEFT framework. No simultaneous fit including both  $\kappa_q$  and  $\kappa_\lambda$  (or using the corresponding SMEFT operators) have been performed yet.

Collider	$ \kappa_u $	$ \kappa_d $	$\delta\kappa_\lambda$ ( $1\sigma$ )
240 GeV $5\text{ab}^{-1}$ (CECP/FCC)	192 [418]	90 [418]	100% (Indirect[168])
350 GeV $1.5\text{ ab}^{-1}$ (FCCee)	310[330]	140[330]	40% (Indirect[168])
500 GeV $4\text{ ab}^{-1}$ (ILC)	330[330]	160[330]	27% [251]
1 TeV $8\text{ ab}^{-1}$ (ILC)	—	—	10% [330]
3 TeV $1\text{ ab}^{-1}$ (CLIC)	430[330]	200[330]	10% [330]
10 TeV $10\text{ ab}^{-1}$ (Muon)	—	—	3% [330]

**Table 9.6.** Prospective light-quark Yukawa and Higgs self-coupling sensitivities at future lepton colliders. The light-quark Yukawa bounds are 95% CL, while the self-coupling bounds are  $1\sigma$  or 68% CL sensitivity reach.

## Part IV

# Flavour physics



# 10 Higgs and flavour

## 10.1 Effective Field Theory for Higgs pair production

The potential deformations of the SM in a model-independent manner can be accomplished by means of an EFT description parametrising new physics (NP) with higher-dimensional operators suppressed by some large energy scale  $\Lambda$ . A complete basis for the higher-dimensional operators has been given in Refs. [126, 131]. In this work we are interested in probing the Higgs trilinear and light-quark Yukawa couplings. Starting with the dimension-six operators modifying the Higgs self-couplings, we see that they are given by

$$\mathcal{L} \supset \frac{C_{\phi\Box}}{\Lambda^2} (\phi^\dagger \phi) \Box (\phi^\dagger \phi) + \frac{C_{\phi D}}{\Lambda^2} (\phi^\dagger D_\mu \phi)^* (\phi^\dagger D^\mu \phi) + \frac{C_\phi}{\Lambda^2} |\phi^\dagger \phi|^3. \quad (10.1)$$

where  $\phi$  denotes the Higgs-doublet which, in the unitary gauge, can be written as  $\phi = 1/\sqrt{2}(0, v + h)^T$ . It is common to quote the constraints on the Higgs couplings in terms of rescaling to the SM coupling prediction, typically denoted by  $\kappa$ :

$$\kappa = \frac{g_h}{g_h^{\text{SM}}}. \quad (10.2)$$

If the new physics contributions do not generate new Lorentz structures there is a possible translation between the Wilson coefficients in the SMEFT Warsaw basis discussed above, and the  $\kappa$  formalism usually used by experimentalists. In particular, taking the rescaling of the trilinear coupling,  $\kappa_\lambda$ , the translation is given by

$$\kappa_\lambda = 1 - \frac{v^4}{m_h^2} \frac{C_\phi}{\Lambda^2} + 3c_{\phi,\text{kin}}, \quad (10.3)$$

where  $c_{\phi,\text{kin}}$  is given by

$$c_{\phi,\text{kin}} = \left( C_{\phi\Box} - \frac{1}{4} C_{\phi D} \right) \frac{v^2}{\Lambda^2}. \quad (10.4)$$

The latter Wilson coefficients modify all the Higgs couplings, and are strongly constrained by electroweak precision observables (e.g. the  $T$  parameter constrains  $C_{\phi D}$ ). Therefore, we set  $c_{\phi,\text{kin}} = 0$  from now on.

Before discussing the SMEFT operators modifying the coupling between the Higgs boson and light quarks, we start by a review of the SM couplings between them, i.e. the Yukawa interaction

$$-\mathcal{L}_y = y_{ij}^u \bar{q}_L^i \tilde{\phi} u_R^j + y_{ij}^d \bar{q}_L^i \phi d_R^j + h.c., \quad (10.5)$$

Here,  $q_L^i$  is the left-handed  $SU(2)$  quark doublet of the  $i^{th}$  generation and  $u_R^j$  and  $d_R^j$ , the right-handed up- and down-type fields of the  $j^{th}$  generation, respectively, and  $\tilde{\phi} = i\sigma_2\phi^*$ . The  $3 \times 3$  Yukawa matrices are the SM **spurions** that break the flavour symmetry of the SM  $U(3)_{Q_L} \otimes U(3)_{u_R} \otimes U(3)_{d_R}$  to the baryon number and the gauged hypercharge groups, i.e.  $U(1)_B \otimes U(1)_Y$ . In the ground state, the the Lagrangian (10.5) gives the quark masses. Thus, defining a diagonal *mass basis* as opposed to a generic *interaction basis* that eq (10.5) is written in it. The transformation of the yukawa matrices  $y^{u/d}$  from generic flavour basis to the mass basis  $Y^{u/d} = \text{diag}(y_1^{u/d}, y_2^{u/d}, y_3^{u/d})$  is performed by means of a bi-unitary transformation. To illustrate this we show the singular-value decomposition of the Yukawa matrices

$$\begin{aligned} (y^u)_{ij} &= (\mathcal{U}_L^u)_{li}(Y^u)_{ll}(\mathcal{U}_R^u)_{lj}^\dagger, \\ (y^d)_{ij} &= (\mathcal{U}_R^d)_{li}^\dagger(Y^d)_{ll}(\mathcal{U}_L^d)_{lj}. \end{aligned} \quad (10.6)$$

This decomposition is not unique and only defined upto a  $U(1)^5$  and a  $U(1)_B$  phases. However, this transformation freedom does not hold for CKM matrix, defined as

$$V_{CKM} = (\mathcal{U}_L^u)^T(\mathcal{U}_L^d)^*, \quad (10.7)$$

where we can only rotate by  $U(1)_B$ . This manifests in Flavour-changing charged currents at tree-level. But no Flavour-changing neutral currents (FCNC) are allowed at tree-level in the SM. Additionally, the loop-induced FCNC's are CKM suppressed

In a similar manner, the SMEFT introduces new flavour spurions via the dimension-six operators

$$\mathcal{L} \supset \frac{\phi^\dagger \phi}{\Lambda^2} \left( (C_{u\phi})_{ij} \bar{q}_L^i \tilde{\phi} u_R^j + (C_{d\phi})_{ij} \bar{q}_L^i \phi d_R^j + h.c. \right), \quad (10.8)$$

The mass matrices of the up- and down-type quarks are obtained from the Yukawa and the new SMEFT coupling

$$\begin{aligned} M_{ij}^u &= \frac{v}{\sqrt{2}} \left( y_{ij}^u - \frac{1}{2} (C_{u\phi})_{ij} \frac{v^2}{\Lambda^2} \right), \\ M_{ij}^d &= \frac{v}{\sqrt{2}} \left( y_{ij}^d - \frac{1}{2} (C_{d\phi})_{ij} \frac{v^2}{\Lambda^2} \right). \end{aligned} \quad (10.9)$$

The Wilson coefficients' matrices  $C_{q\phi}$  need not to be simultaneously diagonalisable with the SM Yukawa's  $y^q$ . However, we need to have a diagonal mass basis like the SM ones, here we will be having new set of bi-unitary transformations  $\mathcal{V}_{L/R}^{u/d}$  such that we could write  $C_{q\phi}$  in terms of the mass basis ones  $\tilde{C}_{q\phi}$  in a similar ways to eq (10.6)

$$\begin{aligned} (C_{u\phi})_{ij} &= (\mathcal{V}_L^u)_{li}(\tilde{C}_{u\phi})_{lm}(\mathcal{V}_R^u)_{mj}^\dagger, \\ (C_{d\phi})_{ij} &= (\mathcal{V}_R^d)_{li}^\dagger(\tilde{C}_{d\phi})_{lm}(\mathcal{V}_L^d)_{mj}. \end{aligned} \quad (10.10)$$

where  $\mathcal{V}_{L/R}^{u/d}$  are only guaranteed to diagonalise the mass matrices  $M_{ij}^{u/d}$  in general<sup>1</sup>. The couplings of one and two Higgs boson to fermions can be defined as (in the mass basis)

$$\mathcal{L} \supset g_{h\bar{q}_iq_j} \bar{q}_i q_j h + g_{h\bar{q}_iq_j} \bar{q}_i q_j h^2, \quad (10.11)$$

with

$$g_{h\bar{q}_iq_j} := \frac{m_{q_i}}{v} \delta_{ij} - \frac{v^2}{\Lambda^2} \frac{(\tilde{C}_{q\phi})_{ij}}{\sqrt{2}}, \quad g_{hh\bar{q}_iq_j} := -\frac{3}{2\sqrt{2}} \frac{v}{\Lambda^2} (\tilde{C}_{q\phi})_{ij}. \quad (10.12)$$

A similar relation exists for the rescalings of the quark Yukawa couplings  $\kappa_q$

$$\kappa_q = 1 - \frac{v^3}{\sqrt{2}m_q} \frac{C_{q\phi}}{\Lambda^2}. \quad (10.13)$$

However, one should be careful while interpreting results quoted in terms of Wilson coefficients in the SMEFT framework extracted from di-Higgs, multi-Higgs or multi-vector bosons searches, as these results include couplings that are not present in the SM. For example, the  $hh\bar{q}\bar{q}$  coupling, though being linearly related to the quark Yukawa coupling  $h\bar{q}\bar{q}$ , is not a rescaling of any SM Higgs coupling. With this in mind, one can strictly remain within a linear EFT and link the rescaling of the quark Yukawa,  $\kappa_q$ , to the  $hh\bar{q}\bar{q}$  coupling through

$$g_{h\bar{q}\bar{q}}^{\text{linear-EFT}} = -\frac{3}{2} \frac{1 - \kappa_q}{v} g_{h\bar{q}\bar{q}}^{\text{SM}}. \quad (10.14)$$

This relation will no longer hold once a non-linear EFT is used. Hence, the  $\kappa$ -formalism, in a strict sense, is not applicable to multi-Higgs studies.

Here, we see that the new Wilson coefficients introduce tree-level FCNC, or even if a tree-level ones are suppressed the loop-level ones will not have the SM CKM suppression. Generically, such a construction leads to flavour-changing neutral currents (FCNCs) which are strongly constrained from low-energy measurements of flavour observables. The bounds are of order  $|(\tilde{C}_{u\phi,d\phi})_{12}| \lesssim 10^{-5} \Lambda^2/v^2$  and  $|(\tilde{C}_{u\phi,d\phi})_{13}| \lesssim 10^{-4} \Lambda^2/v^2$  and stem from  $\Delta F = 2$  transitions [343, 420]. Given that FCNCs need to be suppressed, a popular way of realising this is by imposing minimal flavour violation (MFV) [344], where all sources of flavour violation are proportional to the SM Yukawa couplings

$$(C_{u\phi})_{ij} = \bar{a}_u y_{ij}^u + \bar{b}_u (y_u y_u^\dagger)(y_u)_{ij} + \bar{c}_u (y_d y_d^\dagger)(y_u)_{ij} + \dots, \\ (C_{d\phi})_{ij} = \bar{a}_d y_{ij}^d + \bar{b}_d (y_d y_d^\dagger)(y_d)_{ij} + \bar{c}_d (y_u y_u^\dagger)(y_d)_{ij} + \dots. \quad (10.15)$$

Here  $\bar{a}, \bar{b}$  and  $\bar{c}$  are generic flavour universal  $\mathcal{O}(1)$  coefficients

The assumption of MFV introduces a strong hierarchy amongst the Higgs couplings to quarks, due to the proportionality of the Wilson coefficients to the Yukawa couplings.

---

<sup>1</sup>The CKM matrix with this extended flavour sector will not longer guaranteed to be unitary, however unitarity violation will be typically of order  $m_q^2/\Lambda^2$ .

Since we want to explore rather large modifications of the light-quark Yukawa couplings, in MFV models very low values of the NP scale  $\Lambda$  and/or large Wilson coefficients need to be assumed, rendering the validity of the EFT questionable. Furthermore, this would potentially generate conflict with measurements of the third generation couplings to the Higgs boson. Hence, we refrain from assuming MFV and instead assume *flavour alignment*. We will discuss in the next section how this can be concretely realized. Moreover, we choose setting  $\Lambda = 1 \text{ TeV}$  throughout the remainder of this paper, staying well within the SMEFT validity region and in order to simplify the presentation of the results.

## 10.2 Models of flavour alignment and large light-quark Yukawa couplings

A systematic generalisation of flavour alignment is provided by aligned flavour violation (AFV) [347, 348]. In order to introduce more flavour violation in than (MFV), AFV introduces more spurions, with the constraint that these spurions are invariant under the  $U(1)^5$  transformations mentioned above. This leaves only the CKM matrix transforming non-trivially under the  $U(1)^5$ . In AFV, it is possible to write these spurions, for example, the extra couplings to up-type and down-type quarks,  $k_u$  and  $k_d$  respectively, as an expansion in the CKM matrix  $V_{CKM}$ , known as the alignment expansion

$$k_u = \mathcal{V}_L^u \left( K_{0,u} + K_{1,u} V_{CKM}^* K_{2,u} V_{CKM}^T K_{3,u} + \mathcal{O}(V_{CKM}^4) \right) (\mathcal{V}_R^u)^\dagger, \quad (10.16)$$

$$(k_d)^\dagger = \mathcal{V}_L^d \left( K_{0,d} + K_{1,d} V_{CKM}^T K_{2,d} V_{CKM}^* K_{3,d} + \mathcal{O}(V_{CKM}^4) \right) (\mathcal{V}_R^d)^\dagger, \quad (10.17)$$

where  $K_{a,u}$  and  $K_{a,d}$  are complex  $3 \times 3$  diagonal matrices, that are arbitrarily flavour invariant, and the transformation matrices are similar to the ones appearing in eq (10.10), they are a generalisation to the SM bi-unitary transformations. The AFV condition necessitates that the alignment coefficients  $K_{a,q}$  to be diagonal, such that the expansion is invariant under the  $U(1)^5$  transformation. We have omitted generation indices here for readability.

applying AFV to the SMEFT case is rather straightforward, in a generic flavour basis we have.

$$(k_q)_{ij} = \frac{(C_{q\phi})_{ij}}{\Lambda^2}. \quad (10.18)$$

This formalism is stable under renormalisation group (RGE) evolution as only the matrices  $K_{i,d}$  will contribute to the RGE and flavour alignment is maintained.

### 10.2.1 Model realizations

It should be noted that from a UV perspective there is no well-motivated symmetry argument for the realization of AFV, given the fact that the  $U(1)^5$  symmetry is only an auxiliary group used when redefining the quark mass eigenstates. Concrete realisations

in UV models are rather fine-tuned and other mechanisms might be required for the realisation of flavour alignment.

Flavour alignment can be realized in various models, for instance SUSY [421, 422], two or multi-Higgs doublet models [423, 424] and models with vector-like quarks (VLQ) [320]. In the latter, FCNCs are avoided by imposing horizontal flavour symmetries leading to AFV. The mixing between the SM quarks and the VLQ's  $Q \sim (\mathbf{3}_{SU(3)_C}, \mathbf{2}_{SU(2)_L}, 1/6_Y)$ ,  $U \sim (\mathbf{3}, \mathbf{1}, 2/3)$  and  $D \sim (\mathbf{3}, \mathbf{1}, -1/3)$  is given by the Lagrangian

$$\mathcal{L} = -\lambda_{Qu}\bar{Q}_L\tilde{\phi}u_R - \lambda_{Qd}\bar{Q}_L\phi d_R - \lambda_{Uq}\bar{q}_L\tilde{\phi}U_R - \lambda_{Dq}\bar{q}_L\phi D_R - \lambda_{QD}\bar{Q}_L\phi D_R - \lambda_{UQ}\bar{Q}_L\tilde{\phi}U_R + h.c. \quad (10.19)$$

The matrices  $\lambda$  are the new spurions in this mode, and they do not need to be diagonal, but they are, by virtue of a horizontal symmetry and particular charge assignment, can be made to obey the AFV assumptions. If all the new VLQ's have the same mass scale  $M$ , we could write the enhancement of the light quarks-Higgs coupling  $\delta g_{h\bar{q}q}$  in terms of these matrices

$$\delta g_{h\bar{u}u} \approx \frac{v^2}{m_Q^2}(\lambda_{Uq}\lambda_{UQ}\lambda_{Qu}) \quad \text{and} \quad \delta g_{h\bar{d}d} \approx \frac{v^2}{M^2}(\lambda_{Dq}\lambda_{DQ}\lambda_{Qd}), \quad (10.20)$$

here, the flavour indices are also dropped. While the exact proposal of [320] foresees Yukawa couplings of the first and second generation quarks up to the value of the bottom quark Yukawa coupling, it requires masses of the VLQs of around 1.5 TeV. For less significant enhancements, the scale of the VLQs could reach  $> 2$  TeV and hence be well within the EFT limit and in accordance with bounds from direct searches of VLQs. The VLQs would also modify Higgs production in gluon fusion and the loop-induced Higgs decays. The contributions would scale like

$$\frac{\alpha_s}{\pi} \frac{\lambda_{QU}}{m_Q^2} \phi^\dagger \phi G^{\mu\nu} G_{\mu\nu} \quad (10.21)$$

which with  $\mathcal{O}(1)$   $\lambda_{QU}$  is suppressed strongly compared to the top quark contributions. The VLQs can in principle contribute to flavour observables through loop contributions, where they would couple with the charged currents. The mixing can be fine-tuned such that the loop contributions of the VLQs in flavour observables can be strongly suppressed.

Another concrete realisation of models with large light quark Yukawa couplings has been provided by the framework of spontaneous flavour violation (SFV) [347], where the tuning necessary in general AFV is avoided by promoting the flavour violating spurions to the wavefunctions of the quark [347]. The wavefunction renormalisation constants come from tree-level diagrams involving interaction between the SM quarks, new set of VLQs and scalars. Unlike general AFV, large deviations from their SM values are possible only for either up-type or down-type Yukawa couplings but not both in the SFV framework. Also, it requires the introduction of a discrete symmetry in order to

prevent the VLQ from interacting with the SM degrees of freedom directly. A UV-complete model with SFV has been proposed in Refs. [322, 348] based on a two-Higgs doublet model. Deviations in light quark Yukawa coupling can be achieved by having a second Higgs doublet coupling to fermions via flavour diagonal matrices  $K_{0,q}$  ( $q = u, d$ ) as defined in (10.17). In particular in order to have only the first/second generation deviating from its SM value the corresponding diagonal element in  $K_{0,q}$  is supposed to be non-zero. These matrices are then not proportional to the SM Yukawa couplings. SFV is realized either only in the down or only in the up sector, assuming that the flavour mixing that generates the CKM matrix correspondingly stems from the other sector. Assuming that the mass eigenstates of the two Higgs neutral states are

$$h = \sin(\beta - \alpha)h_1 + \cos(\beta - \alpha)h_2 \quad (10.22)$$

$$H = -\cos(\beta - \alpha)h_1 + \sin(\beta - \alpha)h_2 \quad (10.23)$$

where  $h_1$  and  $h_2$  are the CP-even neutral interaction eigenstates, the large Yukawa couplings of  $h_2$  appear in  $g_{h\bar{q}_iq_i}$ , the Yukawa coupling of the SM-like Higgs boson, via the mixing of  $h_1$  and  $h_2$  with the mixing angle  $\beta - \alpha$ . Working in the Higgs basis in which  $h_1$  takes a vacuum expectation value, the couplings of the Higgs boson to quarks  $g_{h\bar{q}_iq_i}$  then become

$$g_{h\bar{q}_iq_i} = \frac{m_{q_i}}{v} \sin(\beta - \alpha) + (K_q)_{ii} \cos(\beta - \alpha). \quad (10.24)$$

where  $(K_q)_{ii}$  is the  $i$ th matrix element of the matrices  $K_{0,d}$  or  $K_{0,u}$  appearing in eq (10.17), and the  $q$  indicates either up or down-type quarks. Note that the new matrix  $K_q$  is simultaneously diagonalisable with the SM Yukawa. Clearly, the deviation of the Higgs to quark couplings become more pronounced away from the alignment limit  $\cos(\beta - \alpha) \rightarrow 0$ . This automatically leads to a deviation in the Higgs couplings, for instance, to vector bosons proportional to  $\cos(\beta - \alpha)$  but not potentially enhanced by large  $K_q$ 's as in case of the Higgs couplings to light quarks. We note that while there is freedom to chose values for  $K_q$ 's in the diagonal, a potential  $\mathcal{O}(1)$  choice would lead to much larger modification factors for first and second generation as for the third generation where the first term in eq. (10.24) would dominate. Large  $K_q$ 's lead also to large couplings of the second Higgs doublet with light quarks

$$g_{H\bar{q}_i\bar{q}_i} \approx (K_q)_{ii} \sin(\beta - \alpha). \quad (10.25)$$

We note that if we want to achieve large deviations to light quarks, the alignment parameter given by

$$\cos(\beta - \alpha) = -\lambda_6 \frac{v^2}{m_H^2} \left[ 1 + \mathcal{O}(v^4/m_H^4) \right], \quad (10.26)$$

where  $m_H$  denotes the heavy Higgs mass and  $\lambda_6$  is the 2HDM potential parameter of the operator  $\phi_1^\dagger \phi_1 \phi_1^\dagger \phi_2$ , cannot be too small. This implies that the heavy Higgs boson

cannot be too heavy if requiring perturbative  $\lambda_6$ . Given this, the model is constrained from heavy Higgs boson searches as well as meson mixing due to diagrams involving heavy charged Higgs bosons.



# 11 Flavour anomalies and Electroweak precision tests

## 11.1 Introduction

In the era of the Large Hadron Collider (LHC) an intense program aimed at probing the Standard Model (SM) at the TeV scale has been established. At the same time, one of the most valuable sources for the study of new physics (NP) above the electroweak (EW) scale is provided by indirect tests of the SM via the so-called the EW precision observables (EWPO). These include, in particular, the very precise measurements at the  $Z$  pole performed at the Large Electron-Positron (LEP) collider and the Stanford Linear Collider (SLC). In corroboration with the Higgs-boson discovery and the experimental information collected at LHC and Tevatron, they provide strong constraints on theories beyond the SM (BSM) that lead to important deformations of the standard EW sector [26, 139, 141, 223, 425–430]. Intriguingly, the interplay between the TeV region under scrutiny at the LHC and the NP probes represented by EW precision tests may be of fundamental importance for the study of the *B-physics anomalies* [431–438].

The outcome of LHCb and Belle analyses in the study of semileptonic  $B$  decays points to the possible presence of NP in the measured ratios  $R_{K^{(*)}} \equiv Br(B \rightarrow K^{(*)}\mu^+\mu^-)/Br(B \rightarrow K^{(*)}e^+e^-)$  at low dilepton mass [439–442]. The averaged experimental values deviate from unity at the  $\sim 2.5\sigma$  level, hinting at lepton universality violation (LUV). A statistically significant inference of LUV in  $b \rightarrow s\ell\ell$  ( $\ell = e, \mu$ ) transitions can be translated into a strong case for the evidence of BSM physics [443–445].

The interpretation of these experimental results as an imprint of heavy new dynamics has primarily been assessed in a model-independent fashion via the language of effective field theories (EFT) in [446–450] and more recently revisited in refs. [436, 437, 451–455]. Furthermore, the NP picture depicted by these global analyses could also accommodate a set of tensions related to the well-measured muonic channel of these  $B$  decays, in particular, to the angular analysis of  $B \rightarrow K^*\mu^+\mu^-$  [456, 457]. These measurements have very recently been updated by the LHCb collaboration [458].

The set of tensions not related to LUV tests would specifically connect NP effects to muon-flavoured couplings. However, long-distant effects present in the amplitude of these processes [459–463] – involving hadronic contributions that are theoretically difficult to handle [464–467] – make such a conclusion debatable, see, e.g. [468, 469]. From this point of view, the LUV information extracted from ratios of branching ratios and from observables like the ones considered in [470–473] remain the most promising avenue in the future for a more precise assessment of the overall tension seen in  $b \rightarrow s\ell\ell$  measurements [474]. Eventually, while a tighter upper limit has been recently obtained

by LHCb on the branching ratio of  $B_s \rightarrow e^+ e^-$  [475], the combined experimental average for the  $Br(B_s \rightarrow \mu^+ \mu^-)$  [476–478] also shows some tension with the SM prediction [479] as can be seen from the findings in [436, 437].

A broader discussion on  $B$ -physics anomalies should also include the LUV information stemming from another class of rare  $B$  decays, namely  $b \rightarrow c$  semileptonic transitions [480–483]. Indeed, a combined resolution of  $R_{K^{(*)}}$  anomalies with the long-standing deviations observed in  $R_{D^{(*)}} \equiv Br(B \rightarrow D^{(*)}\tau\nu)/Br(B \rightarrow D^{(*)}\ell\nu)$  originally found at Babar [484] and subsequently measured at Belle [485] and LHCb [486], has triggered a lot of interest in the theory community. In particular, in order for NP effects to simultaneously account for a  $\sim 20\%$  deviation in tree-level charged-weak decays and in loop-level flavour-changing neutral currents (FCNC), models with a highly non-trivial flavour structure are required [487–496], often being at the edge of flavour physics constraints [497, 498] and collider bounds [499, 500]. So far, model building has been mainly put forward in the direction of UV-completing low-energy leptoquark benchmarks identified, for instance, in refs. [434, 435, 438, 501, 502].

It is important to acknowledge that the most up-to-date measurements of  $R_{D^{(*)}}$  from the Belle collaboration – obtained by fully reconstructing the  $\tau$  particle via the hadronic [503] and, more notably, leptonic [504] decay modes – turns out to be in good agreement with the SM [505–508]. This fact may cast some doubt on the effective role one should really attribute to  $b \rightarrow c$  transitions in the interpretation of the depicted *B-physics crisis*.

Therefore, in light of the recent results from Belle and LHCb, it is timely for us to focus again on the  $b \rightarrow s\ell\ell$  conundrum and reassess the solutions to  $B$ -physics anomalies that can be realized at one loop without any new source of flavour violation. The simplest resolution of these anomalies has been proposed in ref. [509], extending the SM with a single new Abelian gauge group, together with the presence of top- and muon-partners, resulting in a topophilic  $Z'$  boson capable of evading present collider constraints [510] and responsible for the required LUV signatures.

Such a minimal model actually falls into a larger category pointed out in ref. [433] through the language of the Standard Model Effective Field Theory (SMEFT), and subsequently elaborated upon in greater detail in the phenomenological study of ref. [511].

At the basis of this class of proposals, the notable attempt is twofold:

- i) Addressing the deviations in these FCNC processes with NP effects entering at one-loop level, as for SM amplitudes. This reduces the original multi-TeV domain of NP for  $B$  anomalies [512] to energies closer to present and future collider reach.
- ii) Avoiding the introduction of new sources of flavour violation beyond the SM Yukawa couplings, relaxing in this way, any restrictive flavour probe of NP in a fashion similar to what is predicted in Minimal Flavour Violation (MFV) [344, 513, 514].

The aforementioned proposal shows a strong tension with  $Z$ -pole precision observables [511, 515]. In ref. [436] it has been shown that even in the presence of large hadronic effects in the amplitude of  $B \rightarrow K^* \mu^+ \mu^-$ , a tension of at the  $3\sigma$  level at least

would persist between  $B$  data and EWPO for muonic LUV effects, and an even stronger tension would be found in the case of LUV scenarios involving electron couplings.

This fact has been brought to light recently [516] to abandon *ii*), and reformulate the original proposal addressing  $B$  anomalies at one loop adding specific BSM sources of flavour violation in order to reconcile  $B$  data with EW precision tests in this context. However, as briefly advertised in ref. [436], an important caveat of this EW tension versus  $B$  anomalies concerns the assumption of no tree-level NP contributions to EWPO.

In this work, we attempt, for the first time, to provide a broad exploration of the possible cross-talk of NP in the EW sector and in the flavour playground for  $b \rightarrow s\ell\ell$  transitions. Firstly, we revisit the standard EW analysis in the presence of leading-log one-loop contributions from the renormalization group equations (RGE) evolution of the operators in the SMEFT [231, 232]. Then, we perform a joint fit to the comprehensive experimental set that includes EWPO in conjugation with the state-of-the-art measurements of semileptonic  $B$  decays. Our EFT analysis targets heavy new dynamics that contributes to  $b \rightarrow s\ell\ell$  at the loop level only through SMEFT RGE, involving the SM Yukawa couplings as the only sources of flavour violation in the resolution of  $B$  anomalies.

Within our study, we systematically review novel correlations among gauge-invariant dimension-six operators that help us shed new light on the one-loop solutions to  $B$  anomalies. Continuing in the spirit of the previous work done by some of us [436, 449, 465, 468, 517–519], we shall furnish our results in both a conservative and optimistic approach to the non-perturbative hadronic contributions which can significantly affect the conclusions on the NP effects at hand.

On the basis of the SMEFT picture obtained from our combined inspection of EW and flavour data, we proceed to refine simple UV models already considered in the literature [433, 509, 510]. We corner the interesting parameter space of this refined class of models where EWPO are respected while  $B$  anomalies can be addressed at one loop without introducing new sources of flavour violation. Eventually, we go on to discuss the complementary probes offered by collider searches.

The paper is organized as follows: in section 11.2 we review the ingredients of our EFT analysis; in section 11.3 we detail the strategy adopted for our combined EW+flavour fit in the SMEFT, the results from which are collected in section 11.4; in section 11.5 we discuss the most economic viable  $Z'$  model in relation to our EFT results and also mention possible alternative leptoquark scenarios. Our conclusions are summarized in section 11.6.

## 11.2 Theoretical preamble

Previous global analyses of  $b \rightarrow s\ell\ell$  anomalies have highlighted the appearance of new dynamics at a scale of  $\mathcal{O}(10)$  TeV for  $\mathcal{O}(1)$  effective couplings encoding NP effects at the tree level [446–450]. The mass gap with the weak scale, characterized by the Higgs vacuum expectation value (VEV)  $v \approx 246$  GeV, justifies the BSM translation of these results in the gauge-invariant formalism of the SMEFT [126, 520]. At dimension six, in

an operator product expansion in inverse powers of the NP scale  $\Lambda$ , and working in the Warsaw basis [126], the operators of interest for the explanation of these  $B$  anomalies are [433, 436, 437]:

$$\begin{aligned} O_{\ell\ell 23}^{LQ(1)} &= \bar{L}_\ell \gamma_\mu L_\ell \bar{Q}_2 \gamma^\mu Q_3 , \\ O_{\ell\ell 23}^{LQ(3)} &= \bar{L}_\ell \gamma_\mu \tau^A L_\ell \bar{Q}_2 \gamma^\mu \tau^A Q_3 , \\ O_{23\ell\ell}^{Qe} &= \bar{Q}_2 \gamma_\mu Q_3 \bar{e}_\ell \gamma^\mu e_\ell , \\ O_{\ell\ell 23}^{Ld} &= \bar{L}_\ell \gamma_\mu L \bar{d}_2 \gamma^\mu d_3 , \\ O_{\ell\ell 23}^{ed} &= \bar{d}_2 \gamma_\mu d_3 \bar{e}_\ell \gamma^\mu e_\ell , \end{aligned} \quad (11.1)$$

where weak doublets are represented in upper case,  $SU(2)_L$  singlets in lower case, and Pauli matrices  $\tau^A$  characterize  $SU(2)_L$  triplet currents. Within available light-cone sumrule results on long-distance effects in  $B \rightarrow K^* \mu^+ \mu^-$  [459, 463], data point to the presence of both the operators with  $b \rightarrow s$  left-handed and right-handed currents with muonic flavour ( $\ell = 2$ ) in eq. (11.1) [436, 451–453]. However, it is important to observe that:

- The current statistical significance for the need of right-handed  $b \rightarrow s$  couplings remain small, hinted only by the ratio  $R_{K^*}/R_K \neq 1$  at the  $1\sigma$  level [436, 450]. Hence, the present  $B$  anomalies can be essentially addressed by  $O_{2223}^{LQ(1,3)}$  and  $O_{2322}^{Qe}$ .
- Within a conservative approach to hadronic uncertainties [464–466], the preference for muonic NP effects in global analyses gets mitigated to a large extent and electro-philic scenarios become viable too [449]; moreover, the fully left-handed operator(s)<sup>1</sup>  $O_{\ell\ell 23}^{LQ(1,3)}$  offers the minimal model-independent resolution to  $b \rightarrow s$  anomalies [436].

Interestingly, with a leading expansion in the top-quark Yukawa coupling of the RGE computed in [231, 232], the Wilson coefficients associated to  $O_{2223}^{LQ}$  and  $O_{2322}^{Qe}$  can be generated at one loop by two distinct sets of dimension-six operators [433] that can lead to LUV effects in  $b \rightarrow s\ell\ell$  amplitudes without flavour violation in the quark current. A first set involves operators built of Higgs and leptonic currents:

$$\begin{aligned} O_{\ell\ell}^{HL(1)} &= (H^\dagger i \overset{\leftrightarrow}{D}_\mu H)(\bar{L}_\ell \gamma^\mu L_\ell) , \\ O_{\ell\ell}^{HL(3)} &= (H^\dagger i \overset{\leftrightarrow}{D}_\mu^A H)(\bar{L}_\ell \gamma^\mu \tau^A L_\ell) , \\ O_{\ell\ell}^{He} &= (H^\dagger i \overset{\leftrightarrow}{D}_\mu H)(\bar{e}_\ell \gamma^\mu e_\ell) . \end{aligned} \quad (11.2)$$

A second one corresponds to semileptonic four-fermion (SL-4F) operators with right-

---

<sup>1</sup>The most promising observables that will allow to genuinely disentangle NP effects in the future in the fully left-handed operator  $O_{\ell\ell 23}^{LQ(3)}$  from the ones of  $O_{\ell\ell 23}^{LQ(1)}$ , are  $B \rightarrow K^{(*)}\nu\bar{\nu}$  decays [521–523].

handed top-quark currents:

$$\begin{aligned} O_{\ell\ell 33}^{Lu} &= (\bar{L}_\ell \gamma_\mu L_\ell)(\bar{u}_3 \gamma^\mu u_3), \\ O_{\ell\ell 33}^{eu} &= (\bar{e}_\ell \gamma_\mu e_\ell)(\bar{u}_3 \gamma^\mu u_3). \end{aligned} \quad (11.3)$$

Solving the RGE in a leading-logarithmic approximation, the matching conditions for the left-handed quark-current operators in eq. (11.1) at the scale  $\mu_{\text{EW}} \sim v$  are:<sup>2</sup>

$$\begin{aligned} C_{\ell\ell 23}^{LQ(1)} &= V_{ts}^* V_{tb} \left( \frac{y_t}{4\pi} \right)^2 \log \left( \frac{\Lambda}{\mu_{\text{EW}}} \right) (C_{\ell\ell 33}^{Lu} - C_{\ell\ell}^{HL(1)}), \\ C_{\ell\ell 23}^{LQ(3)} &= V_{ts}^* V_{tb} \left( \frac{y_t}{4\pi} \right)^2 \log \left( \frac{\Lambda}{\mu_{\text{EW}}} \right) C_{\ell\ell}^{HL(3)}, \\ C_{23\ell\ell}^{Qe} &= V_{ts}^* V_{tb} \left( \frac{y_t}{4\pi} \right)^2 \log \left( \frac{\Lambda}{\mu_{\text{EW}}} \right) (C_{\ell\ell 33}^{eu} - C_{\ell\ell}^{He}). \end{aligned} \quad (11.4)$$

In terms of vectorial and axial currents typically discussed in the context of the weak effective theory at low energies [526–528], the operators in eq. (11.4) are matched to

$$\begin{aligned} O_{9V,\ell} &= \frac{\alpha_e}{8\pi} (\bar{s}\gamma_\mu(1-\gamma_5)b)(\bar{\ell}\gamma^\mu\ell), \\ O_{10A,\ell} &= \frac{\alpha_e}{8\pi} (\bar{s}\gamma_\mu(1-\gamma_5)b)(\bar{\ell}\gamma^\mu\gamma_5\ell), \end{aligned} \quad (11.5)$$

so that the matching conditions at the scale  $\mu_{\text{EW}}$  for the set of operators in eq. (11.2) - (11.3) follow:

$$\begin{aligned} C_{9,\ell}^{\text{NP}} &= \frac{\pi v^2}{\alpha_e \Lambda^2} \left( \frac{y_t}{4\pi} \right)^2 \log \left( \frac{\Lambda}{\mu_{\text{EW}}} \right) (C_{\ell\ell}^{HL(3)} - C_{\ell\ell}^{HL(1)} - C_{\ell\ell}^{He} + C_{\ell\ell 33}^{Lu} + C_{\ell\ell 33}^{eu}), \\ C_{10,\ell}^{\text{NP}} &= \frac{\pi v^2}{\alpha_e \Lambda^2} \left( \frac{y_t}{4\pi} \right)^2 \log \left( \frac{\Lambda}{\mu_{\text{EW}}} \right) (C_{\ell\ell}^{HL(1)} - C_{\ell\ell}^{HL(3)} - C_{\ell\ell}^{He} - C_{\ell\ell 33}^{Lu} + C_{\ell\ell 33}^{eu}) \end{aligned} \quad (11.6)$$

where  $\alpha_e \equiv e^2/(4\pi)$ ,  $e$  being the electric charge, and the overall normalization in the weak Hamiltonian follows the standard conventions adopted in refs. [436, 449, 465].

As anticipated in the Introduction, the set of operators of interest for the study of  $R_{K(*)}$  in eq. (11.4) is also probed by EW precision data. Indeed, operators involving the Higgs field and lepton bilinears in the SMEFT induce modifications to EW-boson couplings that have been precisely measured at LEP/SLC, providing also an important test bed for lepton universality [428, 515]. Modifications of the  $Z$  couplings to the leptons can be induced also at loop level through the top-loop contribution [223]. In the leading-log approximation and at the leading order in the top Yukawa coupling, LUV effects can

---

<sup>2</sup>In this work, for one-loop effects, we assume the NP scale to be  $\Lambda = 1$  TeV. We also set  $\mu_{\text{EW}} = m_t \simeq v/\sqrt{2}$  to minimize the matching-scale dependence with the inclusion of next-to-leading corrections [524, 525].

be generated by:

$$\begin{aligned}\Delta g_{Z,L}^{\ell\ell} \Big|_{\text{LUV}} &= -\frac{1}{2} \left( C_{\ell\ell}^{HL(1)} + C_{\ell\ell}^{HL(3)} \right) \frac{v^2}{\Lambda^2} - 3 \left( \frac{y_t v}{4\pi\Lambda} \right)^2 \log \left( \frac{\Lambda}{\mu_{\text{EW}}} \right) C_{\ell\ell 33}^{Lu}, \\ \Delta g_{Z,R}^{\ell\ell} \Big|_{\text{LUV}} &= -\frac{1}{2} C_{\ell\ell}^{He} \frac{v^2}{\Lambda^2} - 3 \left( \frac{y_t v}{4\pi\Lambda} \right)^2 \log \left( \frac{\Lambda}{\mu_{\text{EW}}} \right) C_{\ell\ell 33}^{eu},\end{aligned}\quad (11.7)$$

where  $\Delta g_{Z,L(R)}^{\ell\ell} \equiv g_{Z,L(R)}^{\ell\ell} - g_{Z,L(R)}^{\ell\ell,\text{SM}}$  is the deviation with respect to the left-handed (right-handed) leptonic couplings to the  $Z$  boson in the SM theory.

Motivated by the previous observations, we would like to perform an EFT analysis of new physics models that can explain the flavour anomalies in the above-mentioned fashion, but exploring more generally the interplay of such SM extensions with EWPO. For that purpose, we consider an EFT analysis of new physics with the following assumptions:

- The solution to the flavour anomalies is obtained via radiative effects, such as those described in eq. (11.6).
- Such NP can also contribute to EWPO at tree-level, in a flavour non-universal way.
- Other effects that could enter in the previous observables via renormalization group (RG) mixing are either small or can be constrained better via other processes.

As we will see in section 11.5, and can also be deduced using the results in [258], it is not difficult to construct minimal BSM models where the previous conditions are satisfied. From an EFT point of view, fulfilling these considerations requires the enlarging of the set of operators considered in eq. (11.2) and also including the corresponding dimension-six interactions modifying the neutral and charged quark currents:

$$\begin{aligned}O_{qq}^{HQ(1)} &= (H^\dagger i \overleftrightarrow{D}_\mu H)(\bar{Q}_q \gamma^\mu Q_q), \\ O_{qq}^{HQ(3)} &= (H^\dagger i \overleftrightarrow{D}_\mu^A H)(\bar{Q}_q \gamma^\mu \tau^A Q_q), \\ O_{qq}^{Hu} &= (H^\dagger i \overleftrightarrow{D}_\mu H)(\bar{u}_q \gamma^\mu u_q), \\ O_{qq}^{Hd} &= (H^\dagger i \overleftrightarrow{D}_\mu H)(\bar{d}_q \gamma^\mu d_q),\end{aligned}\quad (11.8)$$

where  $q = 1, 2, 3$  identifies quark generations.<sup>3</sup> In this regard, we note that EWPO cannot separate in a clean way contributions from the first family quarks, in particular in the  $d$  sector. Therefore, and analogously to what was done in ref. [529], we identify deviations in the couplings of the EW bosons to the first and second family of the quarks via  $C_{11}^{HQ(1,3)} = C_{22}^{HQ(1,3)}$ ,  $C_{11}^{Hu} = C_{22}^{Hu}$ , and  $C_{11}^{Hd} = C_{22}^{Hd}$ . This implicit  $U(2)^3$  symmetry

---

<sup>3</sup>In our SMEFT analysis we require these quark operators to be diagonal in a basis that is aligned, as much as possible, with the down-quark physical basis. This will be convenient to avoid possible dangerous tree-level FCNC effects [498]. Similarly, we also assume lepton-flavour alignment with the charged-lepton mass basis.

in the quark sector would in general also help to mitigate large contributions to FCNC. Note that, even in this situation, not all the Wilson coefficients related to eq. (11.8) can be well constrained with the EWPO. This is the case for the Wilson coefficient of  $O_{33}^{Hu}$ , which modifies the right-handed top quark coupling to the  $Z$ . This cannot be probed at tree level by  $Z$ -pole measurements.

Introducing eq. (11.8) also modifies the EW couplings of the  $Z$  to all fermions at the one-loop level, and in particular the leptonic couplings,  $g_{Z,L(R)}^{\ell\ell}$ . These are, however, flavour-universal effects. In our study, we propagate the leading  $y_t$  effects of this kind, coming from the RG mixing with  $O_{33}^{HQ(1)}$ . As we will see, given the comparatively weaker bound on the Wilson coefficient of that operator compared to the leptonic ones, these effects can be sizeable in the fit. It must be noted that, at the same order in the perturbative expansions we are considering, similar effects from  $O_{33}^{Hu}$  could also have a non-negligible phenomenological impact. However, as explained before,  $C_{33}^{Hu}$  cannot be directly bound in the EWPO fit. Hence, to avoid flat directions in our EFT analysis, we assume the RGE boundary condition  $C_{33}^{Hu} = 0$  to hold true. Excluding  $O_{33}^{Hu}$  and taking into account the aforementioned assumptions in the quark sector, eq. (11.8) adds a total of 7 new degrees of freedom into our EFT analysis.

Finally, for completeness, we also consider the effects of the four-lepton operator:

$$O_{1221}^{LL} = (\bar{L}_1 \gamma^\mu L_2)(\bar{L}_2 \gamma_\mu L_1) , \quad (11.9)$$

which contributes to the muon decay amplitude, and therefore alters the extraction of the value of the Fermi constant,  $G_F$ , which is one of the inputs of the SM EW sector.

The operators in eqs. (11.2), (11.8) and (11.9), with the assumptions mentioned before, saturate all the 17 degrees of freedom, i.e. combinations of operators, that can be constrained in a fit to EWPO in the dimension-six SMEFT framework <sup>4</sup>, while keeping flavour changing neutral currents in the light quark sector under control. Together with the 4 four-fermion operators from eq. (11.3), this completes a total of 21 operators, which we include in the fit setup described in the next section.

## 11.3 Analysis strategy

We now proceed to discuss in more detail our EFT analysis. Our aim is to pin down the picture that should address the present  $B$  anomalies via one-loop SM RGE effects of flavour-conserving dimension-six operators, and respect at the same time the constraints from EW precision. We can achieve this goal with a comprehensive global analysis that

---

<sup>4</sup>In this regard, we should mention that at dimension six, in the Warsaw basis, EW observables are also affected by two more operators not discussed so far:  $O_{HWB} = (H^\dagger \tau^A H) W_{\mu\nu}^A B^{\mu\nu}$  and  $O_{HD} = |H^\dagger D_\mu H|^2$ . Contrary to the set in eqs. (11.2) and (11.8), these operators only induce oblique, and therefore flavour-universal, corrections in EW observables. Given our focus on LUV effects, we assume for  $O_{HWB}$  and  $O_{HD}$  that the corresponding Wilson coefficients are not generated by the NP at the scale  $\Lambda$ .

aims at combining EWPO and  $b \rightarrow s\ell\ell$  data.<sup>5</sup>

We perform a Bayesian analysis on the most recent set of  $b \rightarrow s\ell\ell$  measurements together with the state-of-the-art theoretical information already implemented and described in ref. [436]. We include in our study EW physics following what originally done in ref. [426] and, more recently, in ref. [428]. In particular, we adopt the list of observables reported in Table 1 of this reference, and allow for lepton non-universal contributions from heavy BSM physics in EWPO [515, 529] within the framework described in section 11.2.

For this purpose we adopt the publicly available `HEPfit` [242] package, a Markov Chain Monte Carlo (MCMC) framework built using the Bayesian Analysis Toolkit [533].<sup>6</sup> In our analyses we vary  $\mathcal{O}(100)$  parameters including nuisance parameters. The data that we use for the fits can be categorized as follows:

- The set of EWPO including the  $Z$ -pole measurements from LEP/SLD, the measurements of the  $W$  properties at LEP-II, as well as several related inputs from the Tevatron and LHC measurements of the properties of the EW bosons [11, 13, 534–538]. The following lists the bulk of the EWPO included in the fits:

$$\begin{aligned} M_H, m_t, \alpha_S(M_Z), \Delta\alpha_{\text{had}}^{(5)}(M_Z), \\ M_Z, \Gamma_Z, R_{e,\mu,\tau}, \sigma_{\text{had}}, A_{FB}^{e,\mu,\tau}, A_{e,\mu,\tau}, A_{e,\tau}(P_\tau), R_{c,b}, A_{FB}^{c,b}, A_{s,c,b}, R_{u+c}, \\ M_W, \Gamma_W, \text{BR}_{W \rightarrow e\nu, \mu\nu, \tau\nu}, \Gamma_{W \rightarrow cs}/\Gamma_{W \rightarrow ud+cs}, |V_{tb}|; \end{aligned}$$

- The angular distribution of  $B \rightarrow K^{(*)}\ell^+\ell^-$  decays for both  $\mu$  and  $e$  final states in the large-recoil region.<sup>7</sup> These include data from ATLAS [539], Belle [472], CMS [540, 541] and LHCb [458, 542]; we also include the branching fractions from LHCb [543], and of  $B \rightarrow K^*\gamma$ <sup>8</sup> for which we use the HFLAV average [545];
- Branching ratios for  $B^{(+)} \rightarrow K^{(+)}\mu^+\mu^-$  decays in the large-recoil region measured by LHCb [546];
- The angular distribution of  $B_s \rightarrow \phi\mu^+\mu^-$  [547] and the branching ratio of the decay  $B_s \rightarrow \phi\gamma$  [548], measured by LHCb;
- The lepton universality violating ratios  $R_K$  [441] and  $R_{K^*}$  [440] from LHCb and Belle [442];
- Branching ratio of  $B_{(s)} \rightarrow \mu^+\mu^-$  measured by LHCb [477], CMS [476], and ATLAS [478]; we also use the upper limit on  $B_s \rightarrow e^+e^-$  decay reported recently by

<sup>5</sup>See ref. [530] for another recent analysis where  $b \rightarrow s\ell\ell$  data and EW measurements have been combined, with the different scope of resolving tensions in the determination of the Cabibbo angle [531, 532].

<sup>6</sup>All code and configuration files can be made available upon request.

<sup>7</sup>We do not consider in this work low-recoil data, plagued by broad charmonium resonances, implying very large hadronic uncertainties. For analogous reasoning, we do not attempt to study here the baryon rare decay  $\Lambda_b \rightarrow \Lambda\mu^+\mu^-$  as well.

<sup>8</sup>NP effects from dipole operators are strongly constrained as extensively investigated in ref. [544]. However, radiative exclusive  $B$  decays still provide relevant information about hadronic effects [468].

LHCb [475].

For the  $B \rightarrow K^*\ell^+\ell^-$  channel, as in previous works [436, 449, 468, 517–519], we consider two different scenarios for hadronic contributions stemming from long-distance effects [459, 460, 464]. We take into account a conservative approach (Phenomenological Data Driven or PDD) as originally proposed in [465], and refined in ref. [468], and a more optimistic approach based on the results in [459] (Phenomenological Model Driven or PMD). For the PDD model, a quite generic model of hadronic contributions is simultaneously fitted to  $b \rightarrow s\ell\ell$  data together with the effects coming from NP. Within this approach, a net assessment of the presence of BSM physics is only possible via observables sensitive to LUV effects. See the discussion in ref. [436] for more details. For the PMD approach we use the dispersion relations specified in [459] to constrain the hadronic contributions in the entire large-recoil region considered in the analysis. This leads to much smaller hadronic effects in the  $B \rightarrow K^*\ell^+\ell^-$  amplitudes [517], which significantly affects NP results of global analysis [436].

We have characterized our study by considering several different scenarios for the SMEFT fit. In particular, we would like to clarify the sets of data and operators used in each of these fit scenarios, which are organized as follows:

- **EW:** In this fit we simultaneously vary the Wilson coefficients of the *17 operators* in eqs. (11.2), (11.8), and (11.9), as presented in section 11.2. This fit includes EW precision measurements only, and it is performed under the assumptions listed in section 11.2.
- **EW (SL-4F Only):** This refers to a fit done with the Wilson coefficients of the *SL-4F operators* involving the right-handed top current, reported in eq. (11.3). This scenario incorporates the assumption that BSM enters the modifications of the  $Z$  couplings to muons and electrons through top-quark loops only.
- **EW & Flavour:** In these fits we vary the Wilson coefficients of all the *21 operators* given in eq. (11.2), (11.8), and eq. (11.9), together with eq. (11.3). We use all the EW data and include all the flavour observables listed at the beginning of this section. This scenario comes in two varieties, PDD and PMD, as explained above.
- **Flavour:** These fits exclusively include the Wilson coefficients of the *4 operators* (both electrons and muons) appearing in eq. (11.3), and are done including only flavour data, i.e. excluding EW measurements. Results are again distinguished for the PDD and PMD cases.

## 11.4 Results from the SMEFT

### 11.4.1 Analysis of EW and $b \rightarrow s\ell\ell$ data

As a first step in our analysis, we reproduced the outcome of the EW fit originally obtained in ref. [515] using `HEPfit`. Then, we expanded upon the standard EW results through the study of the **EW** scenario introduced in the previous section, yielding

constraints on the Wilson coefficients of the SMEFT operators involving, in particular, dimension-six operators with a Higgs-doublet current, and including also leading-loop effects under the working hypotheses stated in section 11.2. The subset of these operators containing leptonic currents can give rise to non-universal modifications of EW gauge-boson couplings. Assuming NP integrated out at the heavy scale  $\Lambda > v$ , these operators also contribute via RGE flow to  $b \rightarrow s\ell\ell$  observables at one loop, see eq. (11.4).

On the left side of Figure 11.1, we show in orange the bounds from the **EW** fit on the Wilson coefficients of the operators with leptonic currents in terms of mean and standard deviation of the marginalized posterior probability density function. We observe compatibility with the SM within the  $2\sigma$  level. Note that EW data strongly correlate the operators under consideration among themselves, as can be seen in the correlation matrix presented

in

Figure

11.2.

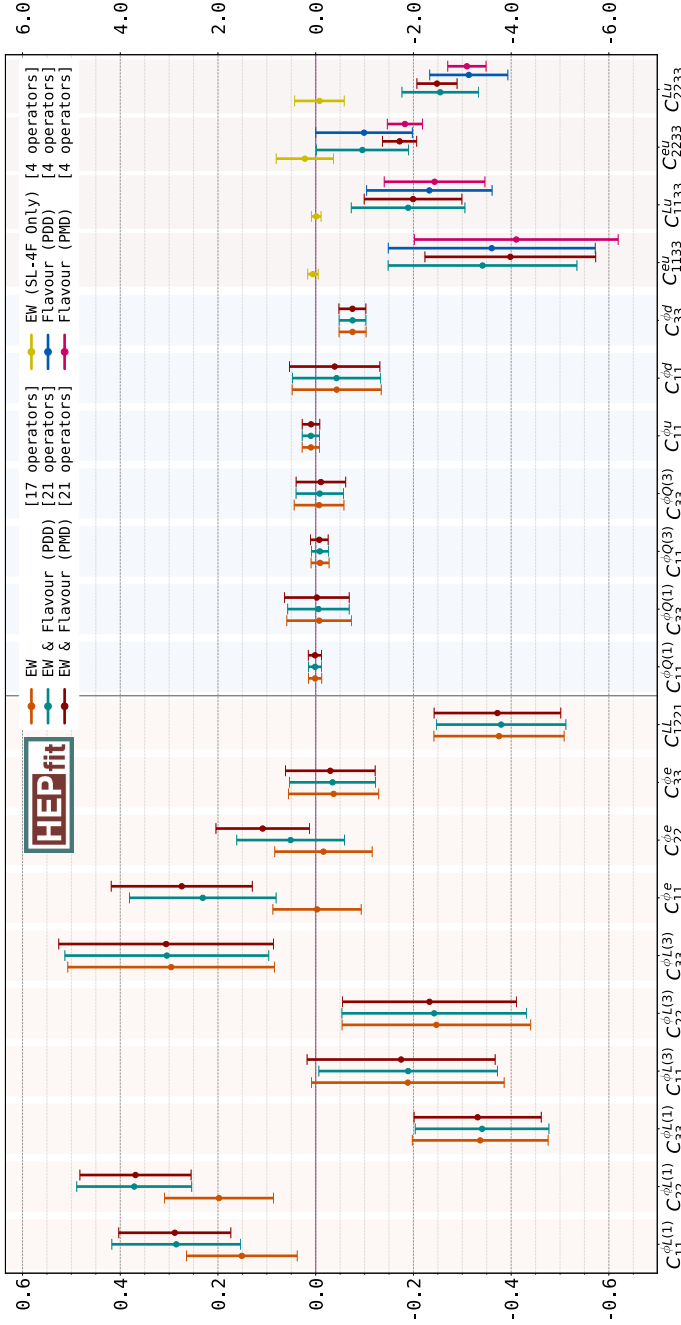


**Figure 11.1.** Mean and standard deviation of the marginalized posterior distributions for each of the Wilson coefficients (in  $\text{TeV}^{-2}$ ) considered in the different fits described in section 11.3. Note that each fit assumes a different set of non-zero operators: EW – 17 operators presented in eqs. (11.2), (11.8) and (11.9); EW(SL-4F Only) – four-fermion operators in eq.(11.3); Flavour (PDD) and (PMD) are the fits with the operators in eq.(11.3), where (PDD) and (PMD) refer to the various assumptions on the hadronic long-distance effects in the flavour sector; EW & Flavour (PDD) and (PMD) stand for the fits including the 21 operators in eqs. (11.3), (11.2), (11.3), (11.8) and (11.9). (Note the different scaling in the axes quantifying the size of the bounds presented in each half of the figure.)

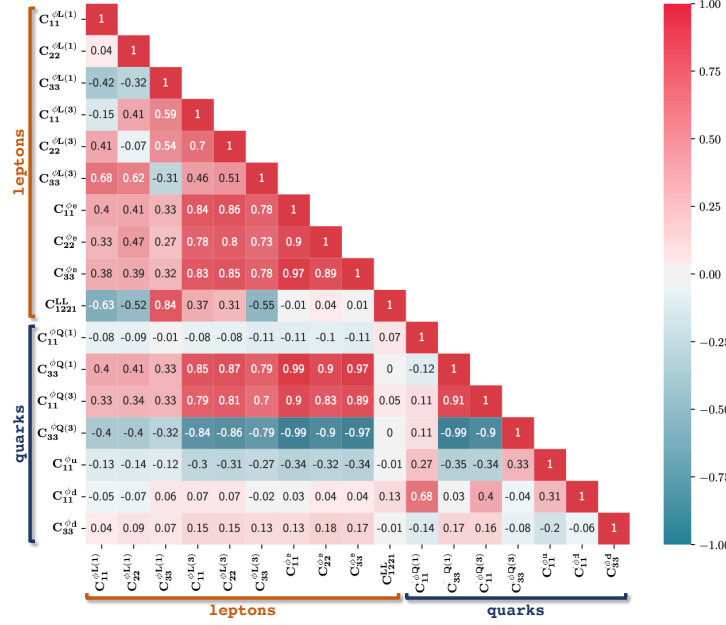


**Figure 11.2.** The correlation matrix extracted from the SMEFT analysis of the set of independent operators in eqs. (11.2), (11.8), (11.9) in the **EW** scenario introduced in section 11.3. The two distinct groups of Wilson coefficients associated to leptonic and quark interactions are remarked as “leptons” and “quarks”, respectively.

where away from the photon pole,  $R_{K^{(*)}}^{\text{SM}}$  are predicted to be unity at percent level [445].

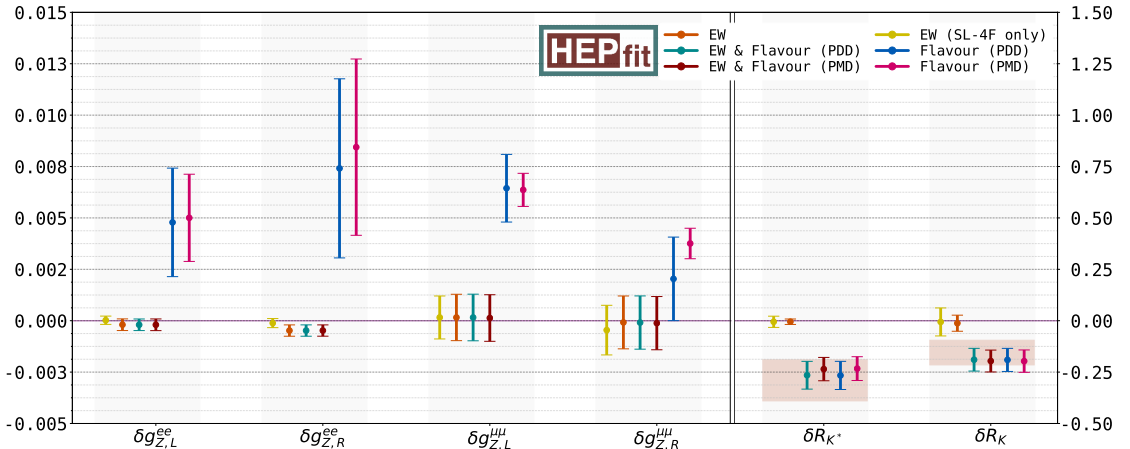


**Figure 11.3.** Mean and standard deviation of the marginalized posterior of the key set of observables for this work, in relation to the tension between  $b \rightarrow s\ell\ell$  anomalies and LEP/SLD measurements. In particular, the left panel shows the deviations in the effective  $Z\ell\ell$  couplings, normalized by SM values. The right panel, on the other hand, shows the deviation from the nominal SM values of the lepton universality violating ratios, see eq. (11.10), with the red boxes indicating the region selected by the experimental measurements of  $R_{K,(K^*)}$ .

In particular, the strong correlation between the operators with quarks and leptons is introduced by the non-negligible one-loop universal contribution of the operator  $\mathcal{O}_{33}^{HQ(1)}$  to all the EW couplings, as anticipated at the end of section 11.4. With the direct bound on  $C_{33}^{HQ(1)}$  being relatively weak compared to the limits on the leptonic operators, such effects in the leptonic couplings can be sizable.

This leads to a relaxation of the naive bounds on  $C_{\ell\ell}^{HL(1)}$ ,  $C_{\ell\ell}^{HL(3)}$  and  $C_{\ell\ell}^{He}$  that one would obtain in a tree-level analysis. To illustrate this, we present in section 11.7 a comparison with the results from such a tree level analysis of the EW fit. The results in Figure 11.2 can then be compared to those in Figure 11.8 where, as it is apparent, there is a substantial decoupling between the dimension-six operators made of Higgs doublets and quark bilinears from the leptonic ones.

The impact of these operators on the key observables for the present discussion is reported in Figure 11.3. There, we collect mean and standard deviation on the shift in the  $Z$  coupling to light leptons (normalized to the corresponding SM value), and on the effect on  $R_{K^{(*)}}$  in the dilepton-mass range  $[1.0, 6.0]$  GeV<sup>2</sup>:

$$\delta g_{Z,L(R)}^{ee(\mu\mu)} \equiv g_{Z,L(R)}^{ee(\mu\mu)}/g_{Z,L(R)}^{ee(\mu\mu),SM} - 1 , \quad \delta R_{K^{(*)}} \equiv R_{K^{(*)}} - R_{K^{(*)}}^{SM} , \quad (11.10)$$

Note that EW measurements tightly constrain NP effects modifying the EW gauge boson couplings to electrons, and also forbid deviations beyond the per-mille level in the case of couplings to muons. This translates into strong bounds on the Wilson coefficients  $C_{\ell\ell}^{HL(1,3),He}$ . Hence, the one-loop contribution to  $R_{K^{(*)}}$  from  $\mathcal{O}_{\ell\ell}^{HL(1,3),He}$  comes out to be tiny. We can then move our attention to the **EW (SL-4F Only)** scenario, reported in yellow in Figure 11.1 and Figure 11.3, and find a similar conclusion. Indeed, EW data once again strongly constrain the NP Wilson coefficients related to  $\mathcal{O}_{\ell\ell 33}^{eu,Lu}$  – the SL-4F operators – implying all the four NP Wilson coefficients to be compatible with 0. However, note that unlike the previous case,  $C_{\ell\ell 33}^{Lu,eu}$  only contribute at one loop to  $\delta g_{Z,L(R)}^{\ell\ell}$  and  $\delta R_{K^{(*)}}$  in eq. (11.10). Consequently, the resulting impact on  $b \rightarrow s\ell\ell$  flavour observables can be larger than the one in the **EW** scenario. As depicted in Figure 11.3, however, there is still an overall tension between EWPO bounds (in yellow) and the experimental measurements of  $R_K$  and  $R_{K^*}$  (indicated by the shaded red boxes in the right side of the figure) at the  $3\sigma$  level.

To frame this tension from a different perspective, let us now focus on the set of flavour measurements as previously done in ref. [436]. In Figure 11.1 we also show the constraints on the four Wilson coefficients of eq. (11.3) coming from  $b \rightarrow s\ell\ell$  data, in what we dubbed as the **Flavour** scenario. We present the PMD case, corresponding to an optimistic approach to QCD power corrections, in pink, while the more conservative PDD case is shown in blue. We observe that in both cases a muonic solution to  $B$  anomalies stands out, with  $C_{2233}^{Lu}$  different from 0 at more than  $3\sigma$  in the PDD case, and at roughly  $6\sigma$  in the PMD one.

We stress that the difference between the results obtained in the PMD and in the PDD case is substantially driven by the angular analysis of  $B \rightarrow K^*\mu\mu$ . In particular, only within the PDD approach the fully left-handed solution to  $B$  anomalies,  $C_{9,\ell} = -C_{10,\ell}$ ,

is favoured by data (signalled here by the Wilson coefficient of  $O_{\ell\ell 33}^{eu}$  being compatible with 0 at  $1\sigma$ , see the results in blue in Figure 11.1). In addition, an electron resolution of  $B$  anomalies is, once again, viable only within PDD [436, 449].

In the **Flavour** scenario one can also predict the induced shift in the  $Z$ -boson couplings according to eq. (11.7), and these are shown in Figure 11.3. As can be seen,  $\delta g_{Z,L,R}^{\ell\ell}$  would receive large contributions at one loop from  $O_{\ell\ell 33}^{Lu,eu}$  in correspondence to the one-loop MFV-like resolution of  $B$  anomalies. Such contribution would be, however, now in tension with the results from EW precision tests. In particular, as a reflection of the main role played by  $O_{2233}^{Lu}$  in the **Flavour** fit to the four NP Wilson coefficients considered,  $g_{Z,L}^{\mu\mu}$  shows the most important deviation from the SM value. Also, the prediction of  $g_{Z,L(R)}^{\mu\mu}$  becomes indirectly sensitive to the underlying treatment of hadronic uncertainties adopted for the study of  $b \rightarrow s$  data. Therefore, we observe that within the PMD approach, the inconsistency between what is needed to address  $B$  anomalies and what is required by EW measurements is even more severe than the  $3\sigma$  established in the **EW (SL-4F Only)** scenario, and imprinted also in the **Flavour** fit with the PDD approach. In fact, we stress once again that adopting light-cone sum-rule results [459] for the long-distant effects in  $B \rightarrow K^*\ell\ell$  decay, the tension between  $B$  anomalies and EW data reaches the  $6\sigma$  level.

So, how do we reach a consensus between  $b \rightarrow s\ell\ell$  measurements and EWPO?

Succinctly, an obvious solution which satisfies these constraints is a class of models where  $R_{K(*)}$  anomalies are addressed at tree level and where modifications to  $Z$ -lepton-lepton vertices are at the same time suppressed. However, these models would not offer a solution to  $B$  anomalies of the MFV type envisaged so far, namely they would rely on the existence of sizeable new sources of flavour violation. At this point, we would like to emphasize that a combined fit of EW and flavour observables offers a new insight into this matter: it highlights strong correlations between the dimension-six operators  $O_{\ell\ell 33}^{Lu(eu)}$  and  $O_{\ell\ell}^{HL(1)(He)}$  as is evident from Figure 11.4. This figure presents a pictorial representation of the correlations between the leptonic operators included in the different fits.

Apart from the fits introduced in the previous section, for illustration purposes we also show in Figure 11.4 the correlations obtained in a variant of the **EW** fit including also the four-fermion operators  $O_{\ell\ell 33}^{Lu(eu)}$ , labelled as **EW (including SL-4F operators)**. This is shown in the upper-right corner of the figure. As can be seen in that panel, and one could deduce from the relations in eq. (11.7), in a pure EW fit adding the four-fermion operators would simply introduce 4 flat directions. These are illustrated by the links connecting the  $C_{\ell\ell 33}^{eu}$  ( $C_{\ell\ell 33}^{Lu}$ ) and  $C_{\ell\ell}^{He}$  ( $C_{\ell\ell}^{HL(1)}$ ) operators, corresponding to 100% anti-correlation. Such flat directions are lifted upon the introduction of the flavour measurements of  $R_K$  and  $R_{K^*}$ , as can be seen in the lower panels of Figure 11.4 for the **EW & Flavour** fits. Even then, due again to relations in eq. (11.4) and (11.7) and the comparatively different precision of the EW and flavour measurements, sizable correlations remain.

In Figure 11.1 the imprint of these correlations is a shift of central values and an increase on the bounds on the corresponding Wilson coefficients, with red and green bars

representing the outcome of the fit in the **EW & Flavour** scenario within the **PMD** and **PDD** approaches, respectively. The interplay between  $O_{\ell\ell 33}^{Lu(eu)}$  and  $O_{\ell\ell}^{HL(1)(He)}$  is evident when comparing the reported red and green bounds versus the orange EW constraints on  $C_{\ell\ell}^{HL(1)(He)}$ , and the yellow ones for  $C_{\ell\ell 33}^{Lu(eu)}$ . Consequently, as clearly depicted in Figure 11.3, looking at the red and green ranges reported for the **EW & Flavour** scenario,  $R_{K^{(*)}}$  puzzles are solved with EW precision being respected. It is important to emphasize that, despite the significant correlation between quark and lepton operators introduced by the one-loop effects of  $C_{33}^{HQ(1)}$ , quark operators play no significant role in reconciling the EWPO constraints with the solution to  $B$  anomalies. This will become clearer in the next section, but can be easily understood from the fact that, as mentioned before, quark and lepton constraints are somewhat uncorrelated in the tree-level EW fit, and the fact that the one-loop corrections effect induced by  $C_{33}^{HQ(1)}$  are flavour universal.

### 11.4.2 A minimal EFT picture

Finally, let us draw what would be the minimal picture for NP out of the general analysis obtained with the 21 operators considered in the **EW & Flavour** scenario. Indeed, a simpler picture will serve as a guideline for the UV models discussed in section 11.5. As mentioned before, given the hadronic uncertainties at hand, the most economic explanation addressing in particular  $R_{K^{(*)}}$  anomalies resides in the NP contribution from the fully left-handed operator,  $O_{\ell\ell 23}^{LQ}$ . In the present context this operator is generated at one loop by  $O_{\ell\ell 33}^{Lu}$ , according to eq. (11.4).

Then, in Figure 11.5 we show in orange the overall constraint from  $b \rightarrow s\ell\ell$  data on  $C_{\ell\ell 33}^{Lu}$  within the most conservative approach to long-distance effects, i.e. the PDD one. In particular, in the left (right) panel we report the constraint on the muonic (electronic) scenario. In the same figure, we highlight with the vertical gray band the bound derived from the full correlated set of EWPO on the same operator. From the comparison of the orange and gray single-operator bounds, the tension between flavour and EW measurements is manifest at the  $3\sigma$  level in the left panel of Figure 11.5. It gets even more pronounced in the right panel due to the precise probe of NP that EW gauge-boson couplings to electrons provide. In the same Figure 11.5, we also show with the horizontal gray band the result of the EWPO constraints applied this time on the NP contribution coming exclusively from the operator  $C_{\ell\ell}^{HL(1)}$ . Note that this operator would also contribute to  $R_{K^{(*)}}$  at one loop, but the size needed would be  $\mathcal{O}(1)$  and it is out of scale in the vertical axis of the plot.

Most importantly, in the same figure we display in (dashed) magenta the  $1(2)\sigma$  contour where EW data are reconciled with the one-loop MFV explanation of  $B$  anomalies when a combined fit of the NP contributions from these two operators is performed. Therefore, heavy BSM degrees of freedom that, once integrated out, generate sizeable contributions both to the Wilson coefficient of  $O_{\ell\ell}^{HL(1)}$  and of  $C_{\ell\ell 33}^{Lu}$  are the key aspect of this scenario that addresses  $B$  anomalies without requiring sources of flavour violation beyond SM ones.

Finally, note that the role played here by  $O_{\ell\ell 33}^{Lu}$  could be shared, in part, with  $O_{\ell\ell 33}^{eu}$ ,

depending on how much departure is actually required from the fully left-handed solution to  $B$  anomalies. As already noted, this fact critically depends on the information stemming from  $B \rightarrow K^* \mu\mu$  [436]. On general grounds, to relieve the bounds from EWPO, the presence of  $O_{\ell\ell 33}^{eu}$  would also necessitate sizeable NP effects from  $O_{\ell\ell}^{He}$ .

As a last comment of this section we would also like to highlight that in the class of models considered the prediction for the LUV observable  $R_K$  is always close to the one for  $R_{K^*}$ : any hint of NP coming from  $R_{K^*}/R_K \neq 1$  [443, 444, 450, 549] would not be addressed within the NP models considered here, mainly involving the operators in eq. (11.2) and (11.3). In the following sections we will put our focus on the economic EFT scenario captured in Figure 11.5 to build up simple UV scenarios realizing the EFT picture here delineated.

## 11.5 Directions for UV models

In this section we discuss how the lesson derived from the SMEFT picture illustrated, in particular, in Figure 11.5, can be realized in a minimal extension of the SM. Here, we explicitly show how models involving a new  $Z'$  gauge boson around the TeV scale provide the most economic example of the correlations advertised in the previous section. This can be achieved if we have a  $Z'$  coupled both to top and lepton SM fields. These couplings can be obtained introducing vector-like top and muon/electron partners reasonably close to the EW scale [509, 510], making this class of models potentially interesting also from the point of view of naturalness in the Higgs sector. Finally, we will also briefly comment on possible alternative scenarios that can be obtained with leptoquarks.

### 11.5.1 $Z'$ with vector-like partners

Let us start with the baseline presented originally in ref. [509]. A simple extension of the SM, able to address  $B$  anomalies, and that does not introduce any explicit new source of flavour violation, can be conceived as follows:

- The SM gauge group,  $SU(3)_c \otimes SU(2)_L \otimes U(1)_Y$ , is extended by a new Abelian gauge group,  $U(1)_X$ , under which SM fields are neutral;
- There is a new complex scalar field  $\mathcal{S}$  that spontaneously breaks  $U(1)_X$ , giving a mass to the gauge boson  $X_\mu$  equal to  $m_{Z'} = g_X \langle \mathcal{S} \rangle$ ;
- A coloured vector-like top partner,  $\mathcal{T}$ , properly charged under  $U(1)_X$  and  $U(1)_Y$  can mix with the right-handed top-quark field  $u_3$  via a Yukawa interaction with  $\mathcal{S}$ ;
- A vector-like muonic partner,  $\mathcal{M}$ , doublet of  $SU(2)_L$  and charged under  $U(1)_{X,Y}$ , can mix with the muonic doublet  $L_2$  via another Yukawa coupling of  $\mathcal{S}$ ;

- The couplings controlling the kinetic-mixing term,  $X_{\mu\nu}B^{\mu\nu}$ , and the quadratic scalar mixing,  $\mathcal{S}^\dagger S H^\dagger H$ , are set to be phenomenologically negligible.<sup>9</sup>

Then, the UV model is completely characterized by eight new parameters: the gauge coupling  $g_X$ , the mass  $\mu_S$  and quartic  $\lambda_S$  of the renormalizable potential of  $\mathcal{S}$ , the new Yukawa couplings  $Y_{\mathcal{T},\mathcal{M}}$ , here taken to be real, and the vector-like mass-term parameters  $M_{\mathcal{T},\mathcal{M}}$ . In particular, the Lagrangian of the model contains the following terms:

$$M_{\mathcal{T}} \overline{\mathcal{T}_R} \mathcal{T}_L + M_{\mathcal{M}} \overline{\mathcal{M}_R} \mathcal{M}_L + Y_t \bar{u}_3 \tilde{H}^\dagger Q_3 + Y_{\mathcal{T}} \bar{u}_3 \mathcal{T}_L \mathcal{S} + Y_\mu \bar{e}_2 H^\dagger L_2 + Y_{\mathcal{M}} \overline{\mathcal{M}_R} L_2 \mathcal{S} + \text{h.c.} , \quad (11.11)$$

that characterize the mixing pattern of SM fields and vector-like partners.<sup>10</sup> Symmetry breaking of  $U(1)_X$  is triggered by  $\langle \mathcal{S} \rangle^2 = -\mu_S^2/(2\lambda_S) \equiv \eta^2 \neq 0$ , that implies the following fermionic mixing patterns:

$$\begin{aligned} \text{top sector: } & \left( \begin{array}{cc} \bar{u}_3 & \overline{\mathcal{T}}_R \end{array} \right) \left( \begin{array}{cc} \frac{Y_t v}{\sqrt{2}} & \frac{Y_{\mathcal{T}} \eta}{\sqrt{2}} \\ 0 & M_{\mathcal{T}} \end{array} \right) \left( \begin{array}{c} U_3 \\ \mathcal{T}_L \end{array} \right) + \text{h.c.} , \\ \text{muon sector: } & \left( \begin{array}{cc} \bar{e}_2 & \overline{\mathcal{M}}_R \end{array} \right) \left( \begin{array}{cc} \frac{Y_\mu v}{\sqrt{2}} & 0 \\ \frac{Y_{\mathcal{M}} \eta}{\sqrt{2}} & M_{\mathcal{M}} \end{array} \right) \left( \begin{array}{c} E_2 \\ \mathcal{M}_L \end{array} \right) + \text{h.c.} , \end{aligned} \quad (11.12)$$

where  $U_i$  ( $E_i$ ) indicates the  $Q_i$ -component ( $L_i$ -component) with weak isospin  $1/2$  ( $-1/2$ ). Using the determinant and trace of the squared mass matrices, one can easily show that the eigenvalues  $m_{t,\mathcal{T}}$  and  $m_{\mu,\mathcal{M}}$  must satisfy [509]:

$$\begin{aligned} m_{t,\mu} m_{\mathcal{T},\mathcal{M}} &= \frac{1}{\sqrt{2}} Y_{t,\mu} v M_{\mathcal{T},\mathcal{M}} , \\ m_{t,\mu}^2 + m_{\mathcal{T},\mathcal{M}}^2 &= M_{\mathcal{T},\mathcal{M}}^2 + \frac{1}{2} (Y_{t,\mu} v)^2 + \frac{1}{2} (Y_{\mathcal{T},\mathcal{M}} \eta)^2 , \end{aligned} \quad (11.13)$$

that in the decoupling limit clearly yield:  $m_{t,\mu} \simeq Y_{t,\mu} v / \sqrt{2}$ ,  $m_{\mathcal{T},\mathcal{M}} \simeq M_{\mathcal{T},\mathcal{M}}$ .

Defining for the top sector the rotation matrix from the interaction to the mass basis following the convention:

$$\left( \begin{array}{c} t_{R(L)} \\ \mathcal{T}'_{R(L)} \end{array} \right) = \left( \begin{array}{cc} \cos \theta_{R(L)}^t & -\sin \theta_{R(L)}^t \\ \sin \theta_{R(L)}^t & \cos \theta_{R(L)}^t \end{array} \right) \left( \begin{array}{c} u_3(U_3) \\ \mathcal{T}_{R(L)} \end{array} \right) , \quad (11.14)$$

and doing similarly for the muonic sector, the mixing angles between SM fields,  $t$  and  $\mu$ , and their partner mass eigenstates,  $\mathcal{T}'$  and  $\mathcal{M}'$ , can be conveniently expressed in terms

<sup>9</sup>Using naive dimensional analysis, both kinetic and scalar quadratic mixing should appear beyond the tree level suppressed at least by a loop factor and the corresponding SM-partner rotation angles.

<sup>10</sup>Note that upon an opposite  $U(1)_X$  charge assignment for the vector-like fermionic partners than the one implicitly assumed, one should replace in eq. (11.11)  $\mathcal{S}$  with  $\mathcal{S}^\dagger$ .

of the dimensionless ratios  $\xi_{\mathcal{T},\mathcal{M}}$  and  $\varepsilon_{t,\mu}$ :

$$\begin{aligned}\tan 2\theta_R^t &= \frac{2\xi_{\mathcal{T}}}{\xi_{\mathcal{T}}^2 - \varepsilon_t^2 - 1}, \quad \tan 2\theta_L^t = \frac{2\varepsilon_t}{\xi_{\mathcal{T}}^2 - \varepsilon_t^2 + 1}, \text{ with } \varepsilon_t \equiv \frac{Y_t v}{Y_{\mathcal{T}} \eta}, \quad \xi_{\mathcal{T}} \equiv \frac{\sqrt{2} M_{\mathcal{T}}}{\eta Y_{\mathcal{T}}}; \\ \tan 2\theta_R^\mu &= \frac{2\varepsilon_\mu}{\xi_{\mathcal{M}}^2 - \varepsilon_\mu^2 + 1}, \quad \tan 2\theta_L^\mu = \frac{2\xi_{\mathcal{M}}}{\xi_{\mathcal{M}}^2 - \varepsilon_\mu^2 - 1}, \text{ with } \varepsilon_\mu \equiv \frac{Y_\mu v}{Y_{\mathcal{M}} \eta}, \quad \xi_{\mathcal{M}} \equiv \frac{\sqrt{2} M_{\mathcal{M}}}{\eta Y_{\mathcal{M}}}.\end{aligned}\quad (11.15)$$

In a perturbative expansion in  $\varepsilon_{t,\mu}$ , eq. (11.15) clearly shows that the mixing in the top sector proceeds mainly through  $\tan \theta_R^t \simeq 1/\xi_{\mathcal{T}}$ , while in the muonic sector one has  $\tan \theta_L^\mu \simeq 1/\xi_{\mathcal{M}}$  and very tiny  $\tan \theta_R^\mu$ .

Hence, for  $\varepsilon_{t,\mu}/\xi_{\mathcal{T},\mathcal{M}} = Y_{t,\mu} v / \sqrt{2} M_{\mathcal{T},\mathcal{M}} < 1$ , the leading couplings of the  $Z'$  boson to the SM fields correspond to right-handed tops and to left-handed muons as well as neutrinos according to:<sup>11</sup>

$$g_{Z't_R} = g_X \sin^2 \theta_R^t = \frac{g_X}{1 + \xi_{\mathcal{T}}^2} + \mathcal{O}(\varepsilon_t^2/\xi_{\mathcal{T}}^2), \quad (11.16)$$

$$g_{Z'\mu_L(\nu)} = g_X \sin^2 \theta_L^\mu = \frac{g_X}{1 + \xi_{\mathcal{M}}^2} + \mathcal{O}(\varepsilon_\mu^2/\xi_{\mathcal{M}}^2), \quad (11.17)$$

with  $g_{Z't_L(\mu_R)}$  being non-negligible only at order  $\varepsilon_{t(\mu)}^2/\xi_{\mathcal{T}(\mathcal{M})}^2$ . Consequently, integrating out the  $Z'$  relevantly generates the operator  $O_{2233}^{Lu}$  with Wilson coefficient:

$$C_{2233}^{Lu} = -\frac{g_{Z't_R} g_{Z'\mu_L}}{m_{Z'}^2} \simeq -\frac{1}{(1 + \xi_{\mathcal{T}}^2)(1 + \xi_{\mathcal{M}}^2)\eta^2}, \quad (11.18)$$

together with four-fermion operators built of  $t_R$  or  $\mu_L, \nu$  fields that can be potentially probed at collider and by experimental signatures like  $\nu$ -trident production.

From eq. (11.18) it is clear that in order to have  $|C_{2233}^{Lu}| \sim 2 \text{ TeV}^{-2}$  as highlighted in Figure 11.5, one needs to rely on a relatively low symmetry-breaking scale  $\eta \lesssim \text{TeV}$ ;<sup>12</sup> for  $m_{Z'} \sim \text{TeV}$  this implies  $g_X \gtrsim 1$ . In Figure 11.6 we show the  $1\sigma$  region corresponding to the explanation of  $B$  anomalies via eq. (11.18) in the parameter space  $\xi_{\mathcal{T},\mathcal{M}}$ , fixing the gauge coupling  $g_X = m_{Z'}/\eta$  for a tentative  $Z'$  gauge boson at the TeV scale and the VEV of the new scalar field  $\mathcal{S}$  set to  $\eta = 250 \text{ GeV}$  and  $\eta = 500 \text{ GeV}$  in the left and right panel, respectively. In the same plot, we re-interpret in our scenario the most relevant collider constraints originally identified in ref. [511].

For small values of  $\xi_{\mathcal{M}}$ , the measurement of neutrino-trident production performed in [550] is effective, and its constraint is reported at the  $2\sigma$  level with the orange vertical band. Under the reasonable assumption that the  $Z'$  boson is mainly produced at tree level in association with the  $t\bar{t}$  pair, in the blue region we show the 95% high- $p_T$  constraint stemming from the recasting of the  $pp \rightarrow \mu^-\mu^+\bar{t}t$  search at ATLAS [551], while in cyan we report the expected constraint on the model from the 4-tops analysis of CMS [552], see ref. [511] for further details. From the same work, we also adopt the expected collider

<sup>11</sup>In what follows, for  $\eta \sim \mathcal{O}(v)$  we will have  $\xi_{\mathcal{T}} \sim \mathcal{O}(1)$ ; consequently,  $\varepsilon_t \sim \mathcal{O}(v/M_{\mathcal{T}})$ .

<sup>12</sup>Note that even for masses as low as  $\mu_{\mathcal{S}} \sim \mathcal{O}(v)$ , for  $\eta \simeq v$  and  $\lambda_{\mathcal{S}} \sim \mathcal{O}(1)$ , the interactions of  $\mathcal{S}$  do not alter the phenomenology discussed here since the largest  $\mathcal{S}$ -generated effects are still suppressed as  $\mathcal{O}(\varepsilon_t^2/\xi_{\mathcal{T}}^2)$ .

constraints for future projected luminosity corresponding to  $300 \text{ fb}^{-1}$ , shown with dashed lines. Note that these projections become of fundamental importance when it comes to probe the interesting  $1\sigma$  region connected to  $B$  anomalies. In particular, the right panel in Figure 11.6 captures the benchmark for a promising discovery at the High-Luminosity LHC.

Finally, in the same figure, fixing the partner Yukawa coupling to  $\mathcal{O}(1)$  values as reported in the two panels, we mark in gray the region corresponding to the bound on the mass of the vector-like partner expected from collider, taken to be  $m_T = 1.4 \text{ TeV}$  from the search at ATLAS in ref. [553], and  $m_M = 0.8 \text{ TeV}$  from the CMS analysis of ref. [554].

As already discussed, the scenario depicted in Figure 11.6 remains viable under the lens of EW precision as long as we also have some heavy new dynamics yielding at the EW scale an imprint of  $O_{22}^{HL(1)}$  consistently with the correlation obtained in the left panel of Figure 11.5.

A simple way to obtain such NP contribution would be to consider the joint effect that the leptonic mixing of the vector-like partner would have together with the kinetic mixing of the  $Z'$ , so far neglected. The  $Z$ - $Z'$  mixing could also originate from charging the new scalar field  $S$  under both Abelian gauge groups, introducing a small misalignment with the standard hypercharge  $U(1)_Y$  in the UV. However, the required mixing of the  $Z'$  would end up mediating light-quark pair annihilation into muons: the typical size of the Wilson coefficient of this four-fermion operator would be  $\mathcal{O}(g_Y^2/m_{Z'}^2)$ , in net tension with the di-muon bound from ATLAS [551], probing NP scales as high as 20 - 40 TeV for  $\mathcal{O}(1)$  (dimensionless) couplings. Hence, we rule out here this possibility.

Interestingly, it is still possible to generate  $O_{22}^{HL(1)}$  without relying on the  $Z$ - $Z'$  mixing, but rather invoking the presence in the UV theory of additional new vector-like leptonic states [555, 556]. These ones may be phenomenologically interesting in relation to the problem of the origin of neutrino masses as well as for the prediction of the anomalous magnetic moment  $(g-2)_\mu$  [557], and may give peculiar multi-lepton signatures at colliders [558, 559].

In the most economic scenario, we may consider the presence in the UV theory of a pair of new vector-like muonic partners: a singlet of  $SU(2)_L, S_Y$ , and a triplet of  $SU(2)_L, T_Y$ , where in both cases the subscript  $Y$  denotes the hypercharge of the fermion. These fields would have their own mass terms controlled by the parameters  $M_{S_Y, T_Y}$ , and interact with the SM doublet  $L_2$  via the Yukawa couplings  $\mathcal{Y}_{S_Y, T_Y}$  according to:

$$\mathcal{Y}_{S_0} \bar{S}_{0,R} \tilde{H}^\dagger L_2 + \mathcal{Y}_{T_0} \bar{T}_{0,R}^A \tau^A \tilde{H}^\dagger L_2 + \text{h.c.}, \quad (11.19)$$

where we have reported the case of vector-like muonic partners with hypercharge  $Y = 0$ . We assume the new Yukawa couplings to be real. Another possibility of interest may be the one of replacing in eq. (11.19)  $\tilde{H} = i\tau^2 H^*$  with the Higgs doublet,  $H$ , and involve then the pair of vector-like partners with hypercharge  $Y = 1$ .

Integrating out these vector-like states from the theory would generate contributions

related to  $\mathcal{O}^{HL(1,3)}$  [556, 557] of the form:

$$\begin{aligned} C_{22}^{HL(1)} &= \frac{\mathcal{Y}_{S_0}^2}{4M_{S_0}^2} - \frac{\mathcal{Y}_{S_1}^2}{4M_{S_1}^2} + \frac{3\mathcal{Y}_{T_0}^2}{4M_{T_0}^2} - \frac{3\mathcal{Y}_{T_1}^2}{4M_{T_1}^2}, \\ C_{22}^{HL(3)} &= -\frac{\mathcal{Y}_{S_0}^2}{4M_{S_0}^2} - \frac{\mathcal{Y}_{S_1}^2}{4M_{S_1}^2} + \frac{\mathcal{Y}_{T_0}^2}{4M_{T_0}^2} + \frac{\mathcal{Y}_{T_1}^2}{4M_{T_1}^2}. \end{aligned} \quad (11.20)$$

Clearly, in order to have  $C_{22}^{HL(1)} \sim 0.1$  and negligible  $C_{22}^{HL(3)}$ <sup>13</sup>, one would need to rely on a tuning of the  $Y = 0$  triplet Wilson coefficient with one of the contributions coming from the singlet vector-like muonic partner. However, once generated at the NP scale  $\Lambda \sim \mathcal{O}(M_{T_0}) \gg v$ , we observe that the relation established between the triplet and singlet contributions to  $\mathcal{O}^{HL(1,3)}$  would be stable under the RG flow of the SMEFT.

A final comment is needed for the electron scenario reported in the right panel of Figure 11.5, that involves opposite signs for the Wilson coefficients of  $\mathcal{O}^{Lu}$  and  $\mathcal{O}^{HL(1)}$  discussed so far. For the former, we note that the sign highlighted in the matching in eq. (11.18) follows from having assumed the same sign for the charge of the vector-like top and muon partners under  $U(1)_X$ . Hence, assuming the vector-like electron partner to have the opposite  $U(1)_X$  charge of the top-partner one would be sufficient to accomplish  $C_{1133}^{Lu} > 0$ . (Of course, this would also imply a distinct use in eq. (11.11) of  $\mathcal{S}$  and  $\mathcal{S}^\dagger$  couplings in the Yukawa terms of the vector-like partners involved to keep the theory invariant under  $U(1)_X$ .) For what concerns the generation of  $C_{11}^{HL(1)} < 0$ , according to eq. (11.20) one needs to correlate once again the contribution stemming from  $S_0$ , or from  $S_1$ , with the effect coming from a  $SU(2)_L$  triplet, that now needs to be identified with  $T_1$ , namely the triplet of hypercharge  $Y = 1$ .

Eventually, we wish also to comment on the possible role of the  $\mathcal{O}^{eu}$  operator, so far neglected in this discussion, but of potential relevance more in general. In fact, as mentioned earlier, the presence of  $\mathcal{O}^{eu}$  would be particularly needed in the case where hadronic corrections entering in the amplitude of  $B \rightarrow K^* \ell \ell$  would be of the size originally estimated in [459]. In that case, a solution to flavour anomalies would be preferred in the muonic channel with NP Wilson coefficient  $C_{2233}^{eu}$  also substantially deviating from 0, as already discussed in subsection 11.4.1. Then, one would need to involve also the operator  $\mathcal{O}_{11,22}^{He}$  to relieve possible tensions with EW precision. In a general picture, the required NP effects from  $\mathcal{O}_{11,22}^{He}$  can be obtained integrating out heavy vector-like  $SU(2)_L$  leptonic doublets.

### 11.5.2 Leptoquark scenarios

An alternative way to reproduce the minimal EFT scenario of Figure 11.5 would be via *leptoquarks* (LQ), particles generically predicted in grand unified theories (GUTs) [560, 561]. Notoriously, LQ-induced dimension-six operators could be potentially dangerous

---

<sup>13</sup>We have indeed verified that a scenario involving at the same time  $C^{Lu}$  and  $C^{HL(1,3)}$  would not alter what already highlighted in Figure 11.5, with the best-fit value for  $|C^{HL(3)}|$  turning out to be of  $\mathcal{O}(10^{-2})$ .

as they would lead to proton decay at tree level, forcing to push their scale up to the GUT scale. However, the outcome may drastically change in models where the couplings of the LQs would be non-universal with respect to lepton and/or quark flavours. In such a case their mass could be much lower than what typically expected in GUTs and their signatures may actually be probed at present colliders. Interestingly, such LQs are candidates that could explain the lepton flavour universality violation – even at the loop level here considered [511, 516] – hinted in the recent LHCb and Belle data. However, this would imply generically a rather non-trivial flavour structure in the theory [562]. For a comprehensive survey of LQ models, see for instance [258, 502, 563–565].

Here, we limit ourselves to the case of toy models that specifically generate the operators of interest, namely  $C_{\ell\ell 33}^{Lu}$  and  $C_{\ell\ell 33}^{eu}$ , for  $\ell = 1$  (electron) or  $\ell = 2$  (muon). In these peculiar LQ models we then assume that couplings between right-handed top quarks and light leptons are the only ones that actually matter for TeV phenomenology.

In Table 11.1 we list the vector and scalar LQs that constitute the potential LQ candidates able to generate the solutions for  $b \rightarrow s\ell\ell$  anomalies at one loop under scrutiny.

Vector LQ: $\mathcal{V}^\mu$	$SU(3)_c \otimes SU(2)_L \otimes U(1)_Y$	Comments
$\bar{L}_\ell \gamma_\mu (\tau^A) Q_3 \mathcal{V}^{\mu(A)}$	$(\bar{\mathbf{3}}, \mathbf{1} \text{ or } \mathbf{3}, -2/3)$	not of interest
$(\mathcal{V}^\mu)^\dagger \bar{e}_\ell^c \gamma_\mu Q_3$	$(\bar{\mathbf{3}}, \mathbf{2}, 5/6)$	not of interest
$\bar{L}_\ell^c \gamma_\mu u_3 i\tau^2 \mathcal{V}^\mu$	$(\bar{\mathbf{3}}, \mathbf{2}, -1/6)$	generates $C_{\ell\ell 33}^{Lu} > 0$
$\bar{e}_\ell \gamma_\mu u_3 \mathcal{V}^\mu$	$(\bar{\mathbf{3}}, \mathbf{1}, -5/3)$	generates $C_{\ell\ell 33}^{eu} < 0$
Scalar LQ: $\mathcal{S}$		
$\bar{L}_\ell (\tau^A) (i\tau^2) Q_3^c \mathcal{S}^{\dagger(A)}$	$(\bar{\mathbf{3}}, \mathbf{1} \text{ or } \mathbf{3}, 1/3)$	not of interest
$\bar{e}_\ell Q_3 i\tau^2 \mathcal{S}$	$(\bar{\mathbf{3}}, \mathbf{2}, -7/6)$	not of interest
$\bar{L}_\ell u_3 \mathcal{S}$	$(\bar{\mathbf{3}}, \mathbf{2}, -7/6)$	generates $C_{\ell\ell 33}^{Lu} < 0$
$\bar{e}_\ell^c u_3 \mathcal{S}$	$(\bar{\mathbf{3}}, \mathbf{1}, 1/3)$	generates $C_{\ell\ell 33}^{eu} > 0$

**Table 11.1.** Scalar and vector LQ interactions under scrutiny: LQs of interest for our analysis have to generate the dimension-six operators  $O_{\ell\ell 33}^{Lu,eu}$ .

Looking back at Figure 11.5, from the table above we recognize as the most economic LQ scenario for the resolution of  $B$  anomalies at one loop, the case of the vector LQ  $\mathcal{V}^\mu \sim (\bar{\mathbf{3}}, \mathbf{2}, -1/6)$  for LUV effects originating from electron couplings, and the scalar  $\mathcal{S} \sim (\bar{\mathbf{3}}, \mathbf{2}, -7/6)$  for the ones associated to muons. The interaction terms of interest are:

$$\mathcal{L}_{\mathcal{V}\bar{f}f} = \tilde{\lambda}_{te} \bar{L}_1^c \gamma_\mu u_3 i\tau^2 \mathcal{V}^\mu + \text{h.c.} , \quad \mathcal{L}_{\mathcal{S}\bar{f}f} = \lambda_{t\mu} \bar{L}_2 u_3 \mathcal{S} + \text{h.c.}, \quad (11.21)$$

leading to the corresponding matching condition:

$$C_{1133}^{Lu} = + \frac{|\tilde{\lambda}_{te}|^2}{M_{\mathcal{V}}^2} , \quad C_{2233}^{Lu} = - \frac{|\lambda_{t\mu}|^2}{2M_{\mathcal{S}}^2} . \quad (11.22)$$

In Figure 11.7 we report in (lighter) magenta the underlying  $1(2)\sigma$  region where  $B$  anomalies are addressed in concordance with the minimal EFT picture of Figure 11.5. In the same plot, we also show a conservative estimate of the present LHC constraint on the mass of the LQ states considered, based on the dedicated collider study of ref. [566].

We conclude noting that from the point of view of realizing the economic EFT result in Figure 11.5, these leptoquark models should again be supplied by the combination of a singlet and a triplet  $SU(2)_L$  muon/electron partners. Otherwise, in these models the leading contribution to  $C_{\ell\ell}^{HL(1)}$  would appear only at the loop level, in net distinction with the  $Z'$  scenario, where the  $Z$ - $Z'$  mixing could be a priori exploited.

## 11.6 Summary

In this work we have revisited the analysis of  $b \rightarrow s\ell\ell$  anomalies looking for NP solutions that generate these FCNC processes at one loop and do not involve any new source of flavour violation beyond the SM ones. To this end, we have performed a broad analysis with dimension-six operators in the SMEFT, combining the experimental data on  $B$ -physics with measurements of EWPO. The general outcome of our study is summarized in Figure 11.1 and, supported with Figure 11.3, shows that a resolution of  $B$  anomalies of the MFV nature can be made fully compatible with EW precision.

From the SMEFT results derived we have then proceeded to identifying a minimal EFT scenario as captured in Figure 11.5, that served as a simple guidance for SM UV completions. In this regard, we have explored in some detail the top-philic and muon/electron-philic  $Z'$ , interesting for direct searches at collider as highlighted in Figure 11.6. We have also commented on the viable leptoquark scenarios, collected in Table 11.1. For both  $Z'$  and leptoquark solutions we have found that additional contributions were necessary in order to maintain  $Z$  coupling measurements under control: in particular, we have shown that a correlated pair of vector-like leptons, a  $SU(2)_L$  singlet and a triplet, can realize the minimal EFT scenario depicted on Figure 11.5. We observe that the existence of these particles may be independently motivated by the heavy new dynamics underlying the origin of neutrino masses and/or by a tentative explanation of the  $(g-2)_\mu$  anomaly [557].

We conclude by noting that the measurement of  $B$  decays at the scale of a few GeV is expected to reach a precision regime with the completion of the future runs at LHC and SuperKEKB. Hence, better measurements of the LUV observables and angular distributions of  $b \rightarrow s\ell\ell$  will be available in the next few years from Belle II [474] and LHCb [567]. These will add a fundamental verification of the current interpretation of  $B$  anomalies and of the direction in our search for NP signatures. Along these lines, should these signals of LUV persist, their interplay with EW precision measurements could be further tested at future  $e^+e^-$  colliders. In particular, circular  $e^+e^-$  colliders running at the  $Z$  pole, such as the FCC-ee [568, 569] or CEPC [254], could test deviations in the lepton universality of neutral weak currents with more than one order of magnitude improvement in precision compared to current data. At linear colliders, like the ILC [251] or CLIC [256], where there is no proposed run at the  $Z$  pole, it would still be possible

to obtain a significant improvement in the measurements of EWPO via radiative return to the  $Z$  [570]. Furthermore, the high-energy regime achievable at linear colliders would allow, after crossing the  $t\bar{t}$  threshold, to directly test the effects of the interactions  $O_{1133}^{Lu,eu}$  via  $e^+e^- \rightarrow t\bar{t}$ . For the muon case, on the other hand, to test  $O_{2233}^{Lu,eu}$  one would still need to rely on more complicated signals, such as  $t\bar{t}\mu^+\mu^-$ , which would be in any case cleaner than at the LHC. (However, ideal optimal tests of these 4-fermion operators in 2-to-2 scattering processes would require a high-energy muon collider.) All of these could represent valuable additions from a “flavour” perspective in the interpretation of EW (and Higgs) measurements at these future machines within the EFT framework [330, 529].

## 11.7 Discussions on EW fits

Here we revisit the constraints set by EWPO on the parameter space of the SMEFT. We make minimal flavour assumptions and include all quark and lepton operators described in the **EW** fit presented in section 11.3. Measurements of EWPO have been extensively studied in the literature [141, 426, 427, 429, 515, 571–576] within the SMEFT framework. The purpose here is to provide further details on the correlation between quark and lepton sectors constrained by EWPO, illustrating some of the effects when going beyond the tree-level analysis.

The experimental inputs are the same considered for the **EW** fit in section 11.3, and include, in particular, the full set measurements taken at LEP/SLD at the  $Z$  pole, as well as the measurements of the  $W$  boson obtained at LEP II, the Tevatron and the LHC (e.g. mass, width, branching ratios as well as the determination of  $|V_{tb}|$  at the LHC <sup>14</sup>). For these fits we use the **HEPfit** package [242] as for the rest of the work.

We first consider the case of the **EW** fit at the tree level. In this case, the results of the fit reveal that while there is sizable correlation between the left-handed leptonic operators, as well as between the different quark operators, both sector are however decoupled to a good extent in the fit as can be seen from Figure 11.8.

For the main fits presented in section 11.4, however, we also consider the leading logarithmically enhanced contributions at one-loop level via RG running. For our purposes, and considering the size of the bounds on the different operators from the **EW** fit, the most important contribution comes from  $C_{33}^{HQ(1)}$ . This induces an universal contribution that propagates into all EWPO. As a result of this, and similar to what was seen between the leptonic operators and the 4-fermion operators due to their interplay in eqs. (11.7), a non-trivial pattern of correlations between the lepton and quark operator sectors in the **EW** fit arises, as shown in Figure 11.2. Similar to the change in the bounds on the leptonic operators in the **EW+Flavour** fit once we included the RG effects of the four-

<sup>14</sup>The extraction of  $|V_{tb}|$  could be, a priori, affected by other SMEFT effects entering in single-top production, e.g. 4-fermion operators. Such effects are neglected in our analysis. The only effect of this input in the EW fits in this paper is to lift a flat direction that would otherwise appear between  $C_{33}^{HQ(1)}$  and  $C_{33}^{HQ(3)}$ , had we excluded this measurement. Even with this input, these two coefficients are nearly 100% correlated, as can be seen in Figure 11.8.

fermion operators, the bounds on the leptonic operators also relax in the EW fit once we include the RG effects from  $C_{33}^{HQ(1)}$ . This is shown in Figure 11.9. However, unlike in the **EW+Flavour** fit, such effects do not induce a significant shift in the central values of the Wilson coefficients, which is simply due to the fact that the data selects  $C_{33}^{HQ(1)}$  to be centered around zero.

As can be seen in Figure 11.9, the relaxation of the bounds can be in some cases rather dramatic, which brings about the question of what could be the impact of further effects not included in our analysis. We estimated that including the main RG effects for all the other operators in the EW fit amounts to changes of at most  $\sim 25\%$ . One should also note that finite terms involving the Wilson coefficients of the quark coupling may become relevant at this point. As can be deduced from the full NLO results presented in [576], these are not expected to significantly change the picture. In any case, the overall conclusions on this paper regarding the reconciliation between EW data and  $B$  anomalies hold true.

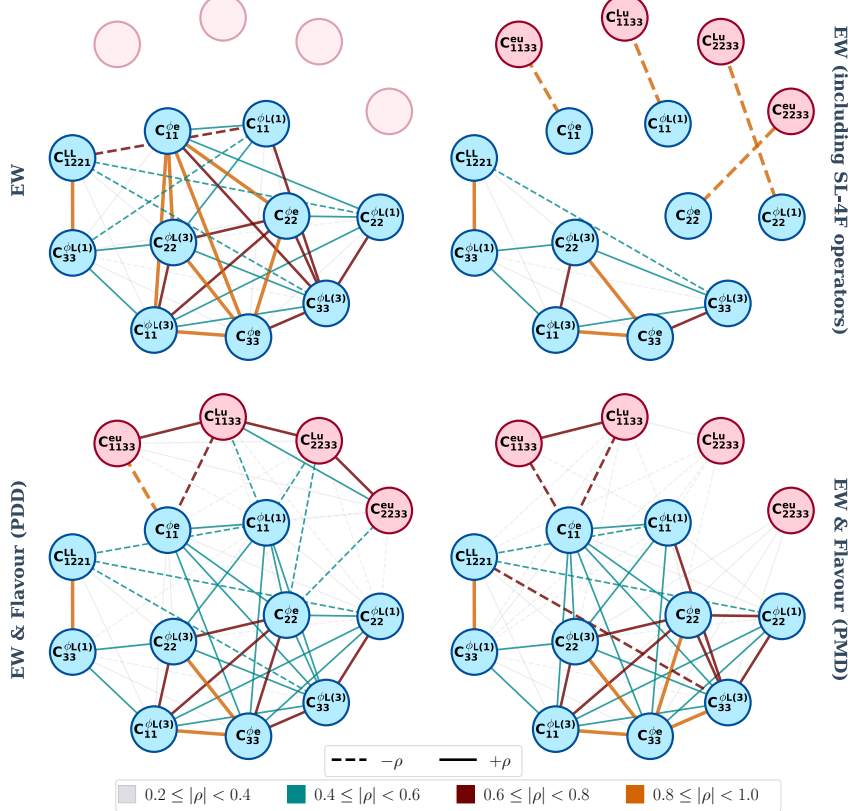


**Figure 11.4.** Correlations among dimension-six operators involving leptonic currents in different scenarios. In the upper side we show the **EW** fit (upper-left panel), and the scenario where in the same setup the **SL-4F** operators are also included (upper-right panel), highlighting the anti-correlation among the set of Wilson coefficients  $C_{\ell\ell}^{H(1)}$ ,  $C_{\ell\ell}^{He}$  and  $C_{\ell\ell 33}^{Lu,eu}$ . In the lower-side panels we show how  $b \rightarrow sll$  measurements break these degeneracies, showing the **Flavour** fit for the **PDD** case (lower-left panel), and the **PMD** one (lower-right panel).

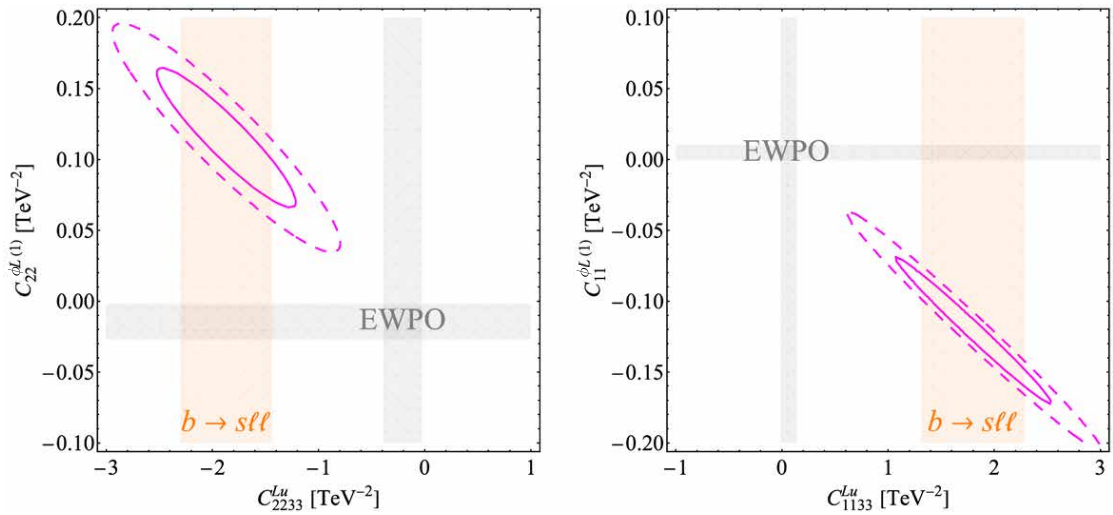


**Figure 11.5.** The most economic EFT picture where  $B$  anomalies can be reconciled at one loop with EWPO. In (dashed) magenta the  $1(2)\sigma$  correlation between the Wilson coefficients of the operators responsible of addressing  $B$  anomalies without any source of flavour violation beyond the Yukawa couplings of the SM. The minimal scenario involves LUV effects in the (electron) muon sector as highlighted by the  $1\sigma$  orange band in the (right) left panel, originated from  $b \rightarrow s\ell\ell$  data analyzed with a conservative approach to hadronic uncertainties. In same figure, the  $1\sigma$  region allowed by EWPO within a single-operator analysis, horizontal and vertical grey bands.

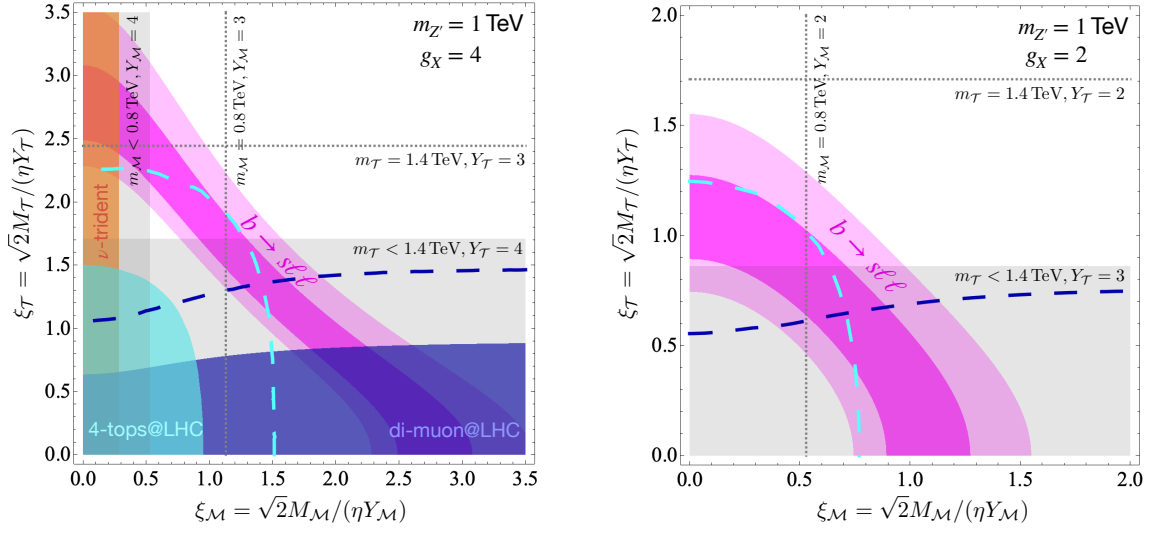


**Figure 11.6.** 68% (95%) probability region in (lighter) magenta for the minimal  $Z'$  model that addresses  $B$  anomalies in the parameter space identified by eq. (11.18), with  $\eta = m_{Z'}/4$  (left panel), and  $\eta = m_{Z'}/2$  (right panel), for  $m_{Z'} = 1$  TeV. Relevant LHC constraints are reported in blue and cyan regions according to the analysis originally performed in ref. [511], together with the corresponding collider projections at  $300 \text{ fb}^{-1}$ . Finally, the gray regions underlie the parameter space where the mass of the vector-like partner lies below current collider limits for a fixed Yukawa coupling as explicitly reported, while dashed lines show the corresponding shift of the limit due to a smaller value of the same type of Yukawa coupling.

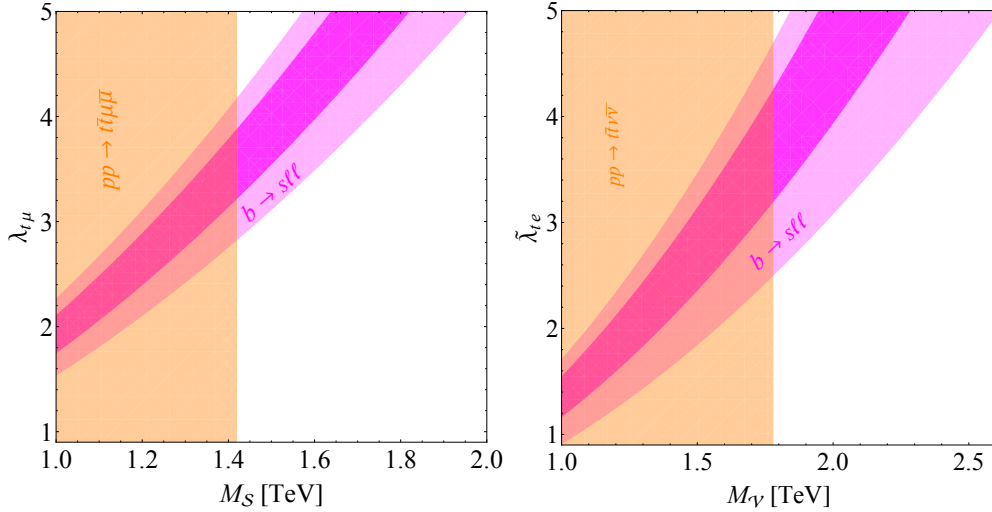


**Figure 11.7.** 68% (95%) probability region in magenta for the LQ candidates addressing  $b \rightarrow s\ell\ell$  anomalies at one loop. The scalar (vector) LQ corresponds to a solution with LUV effects related to muon (electron) couplings. A conservative bound on the corresponding LQ mass is reported according to the analysis of ref. [566].

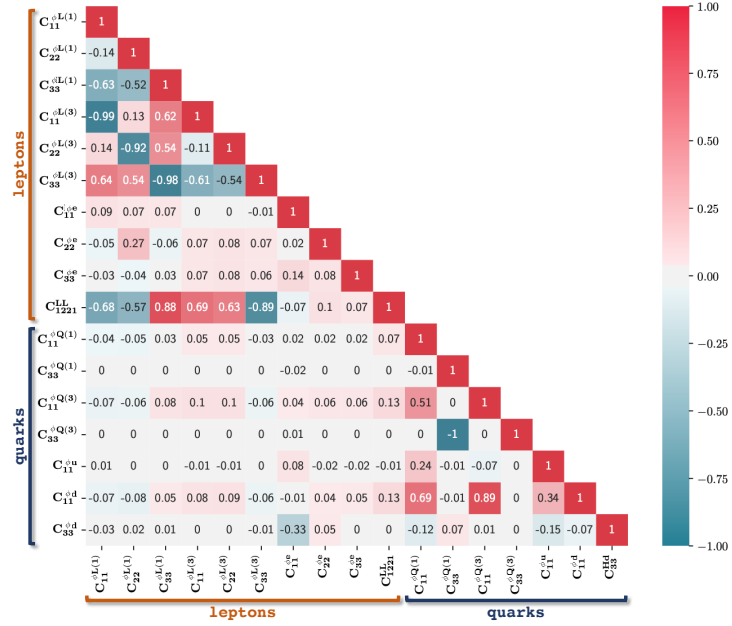


**Figure 11.8.** The correlation matrix extracted from the SMEFT analysis of the set of independent operators in eqs. (11.2), (11.8), (11.9), including only their effects at tree-level. The two distinct groups of correlated Wilson coefficients associated to leptonic and quark interactions are remarked as “leptons” and “quarks”, respectively. Note that, compared to Figure 11.2, in this tree-level analysis there is a significant decorrelation between the constraints on quarks and lepton operators.

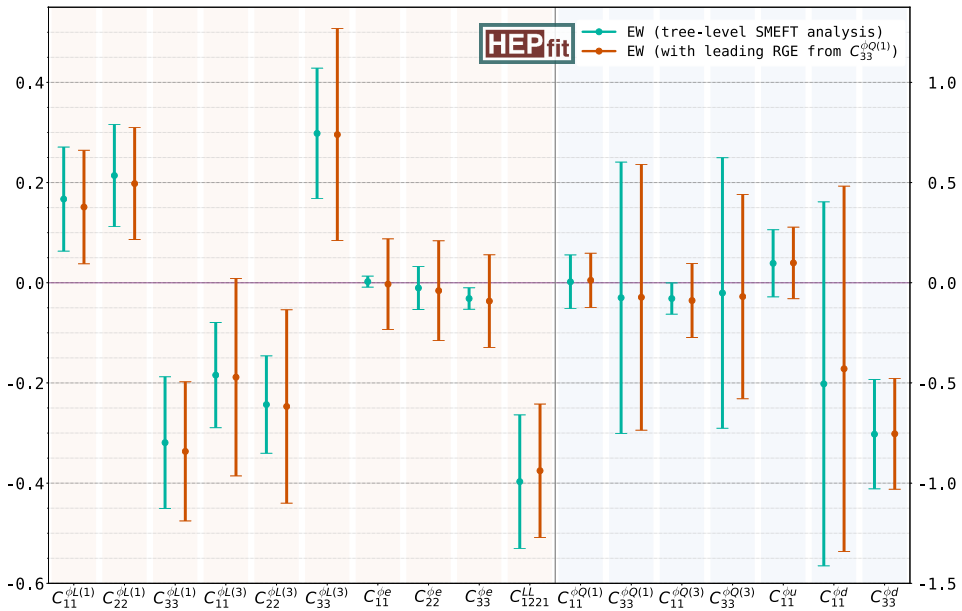


**Figure 11.9.** Comparison of the mean and standard deviation of the marginalized posterior for the Wilson coefficients (in  $\text{TeV}^{-2}$ ) of the operators included in the EW fit under two different approximations: in green the results from a pure tree-level analysis; in orange we show the result including the dominant log-enhanced one-loop terms. See text for details.



# Bibliography

- [1] R. A. Minlos, *Introduction to mathematical statistical physics*. No. 19. American Mathematical Soc., 2000.
- [2] M. Gell-Mann, “The eightfold way: A theory of strong interaction symmetry,” <https://www.osti.gov/biblio/4008239>.
- [3] C. N. Yang and R. L. Mills, “Conservation of isotopic spin and isotopic gauge invariance,” *Phys. Rev.* **96** (Oct, 1954) 191–195.  
<https://link.aps.org/doi/10.1103/PhysRev.96.191>.
- [4] **Particle Data Group** Collaboration, P. Zyla *et al.*, “Review of Particle Physics,” *PTEP* **2020** no. 8, (2020) 083C01.
- [5] D. S. Freed, “Lectures on topological quantum field theory,” 1993.
- [6] R. Dijkgraaf and E. Witten, “Topological gauge theories and group cohomology,” *Communications in Mathematical Physics* **129** no. 2, (1990) 393–429.
- [7] A. Salam and J. C. Ward, “On a gauge theory of elementary interactions,” *Il Nuovo Cimento (1955-1965)* **19** no. 1, (1961) 165–170.  
<https://doi.org/10.1007/BF02812723>.
- [8] A. Salam and J. C. Ward, “Weak and electromagnetic interactions,” *Il Nuovo Cimento (1955-1965)* **11** no. 4, (1959) 568–577.  
<https://doi.org/10.1007/BF02726525>.
- [9] S. Weinberg, “A model of leptons,” *Phys. Rev. Lett.* **19** (Nov, 1967) 1264–1266.  
<https://link.aps.org/doi/10.1103/PhysRevLett.19.1264>.
- [10] F. Capozzi, E. Lisi, A. Marrone, D. Montanino, and A. Palazzo, “Neutrino masses and mixings: Status of known and unknown  $3\nu$  parameters,” *Nucl. Phys. B* **908** (2016) 218–234, [arXiv:1601.07777 \[hep-ph\]](https://arxiv.org/abs/1601.07777).
- [11] **ALEPH, DELPHI, L3, OPAL, SLD, LEP Electroweak Working Group, SLD Electroweak Group, SLD Heavy Flavour Group** Collaboration, S. Schael *et al.*, “Precision electroweak measurements on the  $Z$  resonance,” *Phys. Rept.* **427** (2006) 257–454, [arXiv:hep-ex/0509008 \[hep-ex\]](https://arxiv.org/abs/hep-ex/0509008).
- [12] **SLD** Collaboration, K. Abe *et al.*, “First direct measurement of the parity violating coupling of the  $Z_0$  to the  $s$  quark,” *Phys. Rev. Lett.* **85** (2000) 5059–5063, [arXiv:hep-ex/0006019](https://arxiv.org/abs/hep-ex/0006019).

- [13] **CDF, D0** Collaboration, T. E. W. Group, “2012 Update of the Combination of CDF and D0 Results for the Mass of the W Boson,” [arXiv:1204.0042 \[hep-ex\]](https://arxiv.org/abs/1204.0042).
- [14] **ALEPH, DELPHI, L3, OPAL, LEP Electroweak** Collaboration, S. Schael *et al.*, “Electroweak Measurements in Electron-Positron Collisions at W-Boson-Pair Energies at LEP,” *Phys. Rept.* **532** (2013) 119–244, [arXiv:1302.3415 \[hep-ex\]](https://arxiv.org/abs/1302.3415).
- [15] **DØ** Collaboration, V. M. Abazov *et al.*, “Measurement of  $\sin^2 \theta_{\text{eff}}^\ell$  and Z-light quark couplings using the forward-backward charge asymmetry in  $p\bar{p} \rightarrow Z/\gamma^* \rightarrow e^+e^-$  events with  $\mathcal{L} = 5.0 \text{ fb}^{-1}$  at  $\sqrt{s} = 1.96 \text{ TeV}$ ,” *Phys. Rev. D* **84** (2011) 012007, [arXiv:1104.4590 \[hep-ex\]](https://arxiv.org/abs/1104.4590).
- [16] **CMS** Collaboration, V. Khachatryan *et al.*, “Measurement of the t-channel single-top-quark production cross section and of the  $|V_{tb}|$  CKM matrix element in pp collisions at  $\sqrt{s} = 8 \text{ TeV}$ ,” *JHEP* **06** (2014) 090, [arXiv:1403.7366 \[hep-ex\]](https://arxiv.org/abs/1403.7366).
- [17] **ATLAS** Collaboration, M. Aaboud *et al.*, “Measurement of the W-boson mass in pp collisions at  $\sqrt{s} = 7 \text{ TeV}$  with the ATLAS detector,” *Eur. Phys. J. C* **78** no. 2, (2018) 110, [arXiv:1701.07240 \[hep-ex\]](https://arxiv.org/abs/1701.07240). [Erratum: Eur.Phys.J.C 78, 898 (2018)].
- [18] Y. Nambu, “Quasi-particles and gauge invariance in the theory of superconductivity,” *Phys. Rev.* **117** (Feb, 1960) 648–663. <https://link.aps.org/doi/10.1103/PhysRev.117.648>.
- [19] J. Goldstone, “Field theories with superconductor solutions,” *Il Nuovo Cimento (1955-1965)* **19** no. 1, (1961) 154–164.
- [20] J. Goldstone, A. Salam, and S. Weinberg, “Broken symmetries,” *Phys. Rev.* **127** (Aug, 1962) 965–970. <https://link.aps.org/doi/10.1103/PhysRev.127.965>.
- [21] P. W. Anderson, “Plasmons, gauge invariance, and mass,” *Phys. Rev.* **130** (Apr, 1963) 439–442. <https://link.aps.org/doi/10.1103/PhysRev.130.439>.
- [22] F. Englert and R. Brout, “Broken symmetry and the mass of gauge vector mesons,” *Phys. Rev. Lett.* **13** (Aug, 1964) 321–323. <https://link.aps.org/doi/10.1103/PhysRevLett.13.321>.
- [23] P. W. Higgs, “Broken symmetries and the masses of gauge bosons,” *Phys. Rev. Lett.* **13** (Oct, 1964) 508–509. <https://link.aps.org/doi/10.1103/PhysRevLett.13.508>.
- [24] G. S. Guralnik, C. R. Hagen, and T. W. B. Kibble, “Global conservation laws and massless particles,” *Phys. Rev. Lett.* **13** (Nov, 1964) 585–587. <https://link.aps.org/doi/10.1103/PhysRevLett.13.585>.

- [25] G. S. Guralnik, “The History of the Guralnik, Hagen and Kibble development of the Theory of Spontaneous Symmetry Breaking and Gauge Particles,” *Int. J. Mod. Phys. A* **24** (2009) 2601–2627, [arXiv:0907.3466 \[physics.hist-ph\]](https://arxiv.org/abs/0907.3466).
- [26] J. Erler and M. Schott, “Electroweak Precision Tests of the Standard Model after the Discovery of the Higgs Boson,” *Prog. Part. Nucl. Phys.* **106** (2019) 68–119, [arXiv:1902.05142 \[hep-ph\]](https://arxiv.org/abs/1902.05142).
- [27] CMS Collaboration, S. Chatrchyan *et al.*, “Observation of a New Boson at a Mass of 125 GeV with the CMS Experiment at the LHC,” *Phys. Lett. B* **716** (2012) 30–61, [arXiv:1207.7235 \[hep-ex\]](https://arxiv.org/abs/1207.7235).
- [28] ATLAS Collaboration, G. Aad *et al.*, “Observation of a new particle in the search for the Standard Model Higgs boson with the ATLAS detector at the LHC,” *Phys. Lett. B* **716** (2012) 1–29, [arXiv:1207.7214 \[hep-ex\]](https://arxiv.org/abs/1207.7214).
- [29] N. Cabibbo, “Unitary symmetry and leptonic decays,” *Phys. Rev. Lett.* **10** (Jun, 1963) 531–533. <https://link.aps.org/doi/10.1103/PhysRevLett.10.531>.
- [30] M. Kobayashi and T. Maskawa, “CP-Violation in the Renormalizable Theory of Weak Interaction,” *Progress of Theoretical Physics* **49** no. 2, (02, 1973) 652–657, <https://academic.oup.com/ptp/article-pdf/49/2/652/5257692/49-2-652.pdf>. <https://doi.org/10.1143/PTP.49.652>.
- [31] R. E. Behrends, R. J. Finkelstein, and A. Sirlin, “Radiative corrections to decay processes,” *Phys. Rev.* **101** (Jan, 1956) 866–873. <https://link.aps.org/doi/10.1103/PhysRev.101.866>.
- [32] T. Kinoshita and A. Sirlin, “Radiative corrections to fermi interactions,” *Phys. Rev.* **113** (Mar, 1959) 1652–1660. <https://link.aps.org/doi/10.1103/PhysRev.113.1652>.
- [33] I. Mohammad and A. Donnachie, “Radiative Corrections to Radiative Muon Decay.”
- [34] T. van Ritbergen and R. G. Stuart, “Complete 2-loop quantum electrodynamic contributions to the muon lifetime in the fermi model,” *Phys. Rev. Lett.* **82** (Jan, 1999) 488–491. <https://link.aps.org/doi/10.1103/PhysRevLett.82.488>.
- [35] D. Ross and M. Veltman, “Neutral currents and the higgs mechanism,” *Nuclear Physics B* **95** no. 1, (1975) 135–147. <https://www.sciencedirect.com/science/article/pii/055032137590485X>.
- [36] A. Djouadi, “The Anatomy of electro-weak symmetry breaking. I: The Higgs boson in the standard model,” *Phys. Rept.* **457** (2008) 1–216, [arXiv:hep-ph/0503172](https://arxiv.org/abs/hep-ph/0503172).

## Bibliography

---

- [37] M. J. Dugan, H. Georgi, and D. B. Kaplan, “Anatomy of a composite higgs model,” *Nuclear Physics* **254** (1985) 299–326.
- [38] C. T. Hill and E. H. Simmons, “Strong Dynamics and Electroweak Symmetry Breaking,” *Phys. Rept.* **381** (2003) 235–402, [arXiv:hep-ph/0203079](https://arxiv.org/abs/hep-ph/0203079). [Erratum: Phys.Rept. 390, 553–554 (2004)].
- [39] M. Schwartz, *Quantum Field Theory and the Standard Model*. Quantum Field Theory and the Standard Model. Cambridge University Press, 2014.  
<https://books.google.nl/books?id=HbdEAgAAQBAJ>.
- [40] M. Peskin and D. Schroeder, *An Introduction To Quantum Field Theory*. Frontiers in Physics. Avalon Publishing, 1995.  
<https://books.google.de/books?id=EVeNNcslvXOC>.
- [41] M. Einhorn, D. Jones, and M. Veltman, “Heavy particles and the rho parameter in the standard model,” *Nuclear Physics B* **191** no. 1, (1981) 146–172.  
<https://www.sciencedirect.com/science/article/pii/0550321381902923>.
- [42] W. J. Marciano and J. L. Rosner, “Atomic parity violation as a probe of new physics,” *Phys. Rev. Lett.* **65** (Dec, 1990) 2963–2966.  
<https://link.aps.org/doi/10.1103/PhysRevLett.65.2963>.
- [43] M. E. Peskin and T. Takeuchi, “New constraint on a strongly interacting higgs sector,” *Phys. Rev. Lett.* **65** (Aug, 1990) 964–967.  
<https://link.aps.org/doi/10.1103/PhysRevLett.65.964>.
- [44] D. C. Kennedy and P. Langacker, “Erratum: “precision electroweak experiments and heavy physics: A global analysis [phys. rev. lett. 65, 2967 (1990)]”,” *Phys. Rev. Lett.* **66** (Jan, 1991) 395–395.  
<https://link.aps.org/doi/10.1103/PhysRevLett.66.395.2>.
- [45] M. E. Peskin and T. Takeuchi, “Estimation of oblique electroweak corrections,” 1991.
- [46] M. Golden and L. Randall, “Radiative corrections to electroweak parameters in technicolor theories,” *Nuclear Physics B* **361** no. 1, (1991) 3–23.  
<https://www.sciencedirect.com/science/article/pii/0550321391906144>.
- [47] B. Holdom and J. Terning, “Large corrections to electroweak parameters in technicolor theories,” *Physics Letters B* **247** no. 1, (1990) 88–92.  
<https://www.sciencedirect.com/science/article/pii/037026939091054F>.
- [48] G. Altarelli, R. Barbieri, and S. Jadach, “Toward a model-independent analysis of electroweak data,” *Nuclear Physics B* **369** no. 1, (1992) 3–32.  
<https://www.sciencedirect.com/science/article/pii/055032139290376M>.

- [49] R. S. Chivukula, S. B. Selipsky, and E. H. Simmons, “Nonoblique effects in the  $zbb^-$  vertex from extended technicolor dynamics,” *Phys. Rev. Lett.* **69** (Jul, 1992) 575–577. <https://link.aps.org/doi/10.1103/PhysRevLett.69.575>.
- [50] E. H. Simmons, R. S. Chivukula, and J. Terning, “Testing extended technicolor with R(b),” *Prog. Theor. Phys. Suppl.* **123** (1996) 87–96, [arXiv:hep-ph/9509392](https://arxiv.org/abs/hep-ph/9509392).
- [51] G. Valencia and S. Willenbrock, “Goldstone-boson equivalence theorem and the higgs resonance,” *Phys. Rev. D* **42** (Aug, 1990) 853–859. <https://link.aps.org/doi/10.1103/PhysRevD.42.853>.
- [52] L. Di Luzio, R. Gröber, and M. Spannowsky, “Maxi-sizing the trilinear Higgs self-coupling: how large could it be?,” *Eur. Phys. J. C* **77** no. 11, (2017) 788, [arXiv:1704.02311 \[hep-ph\]](https://arxiv.org/abs/1704.02311).
- [53] M. Lindner, “Implications of Triviality for the Standard Model,” *Z. Phys. C* **31** (1986) 295.
- [54] M. Sher, “Electroweak Higgs Potentials and Vacuum Stability,” *Phys. Rept.* **179** (1989) 273–418.
- [55] J. A. Casas, J. R. Espinosa, and M. Quiros, “Standard model stability bounds for new physics within LHC reach,” *Phys. Lett. B* **382** (1996) 374–382, [arXiv:hep-ph/9603227](https://arxiv.org/abs/hep-ph/9603227).
- [56] G. Isidori, G. Ridolfi, and A. Strumia, “On the metastability of the standard model vacuum,” *Nucl. Phys. B* **609** (2001) 387–409, [arXiv:hep-ph/0104016](https://arxiv.org/abs/hep-ph/0104016).
- [57] G. Degrassi, S. Di Vita, J. Elias-Miro, J. R. Espinosa, G. F. Giudice, G. Isidori, and A. Strumia, “Higgs mass and vacuum stability in the Standard Model at NNLO,” *JHEP* **08** (2012) 098, [arXiv:1205.6497 \[hep-ph\]](https://arxiv.org/abs/1205.6497).
- [58] J. Ellis, “Physics goals of the next century@ cern,” in *AIP Conference Proceedings*, vol. 542, pp. 267–292, American Institute of Physics. 2000.
- [59] “LHC-facts.” <http://www.lhc-facts.ch>.
- [60] “Weltmaschine- CERN und LHC.” [https://www.weltmaschine.de/cern\\_und\\_lhc/lhc/](https://www.weltmaschine.de/cern_und_lhc/lhc/).
- [61] “LHC Design Report Vol.1: The LHC Main Ring.”
- [62] “LHC long term schedule .” <https://lhc-commissioning.web.cern.ch/schedule/LHC-long-term.htm>.
- [63] “High-Luminosity Large Hadron Collider (HL-LHC) : Preliminary Design Report.”

- [64] “LHC preformance tracking.” <https://bpt.web.cern.ch/lhc/>.
- [65] “Taking a look at the LHC.”  
[https://www.lhc-closer.de/taking\\_a\\_closer\\_look\\_at\\_lhc/0.luminosity](https://www.lhc-closer.de/taking_a_closer_look_at_lhc/0.luminosity).
- [66] “ATLAS Run 2 luminosity public results .” <https://twiki.cern.ch/twiki/bin/view/AtlasPublic/LuminosityPublicResults>.
- [67] “CMS luminosity public results .”  
<https://twiki.cern.ch/twiki/bin/view/CMSPublic/LumiPublicResults>.
- [68] “ATLAS Run 2 luminosity public results .” <https://twiki.cern.ch/twiki/bin/view/AtlasPublic/LuminosityPublicResultsRun2>.
- [69] S. Fartoukh *et al.*, “LHC Configuration and Operational Scenario for Run 3,” tech. rep., CERN, Geneva, Nov, 2021. <https://cds.cern.ch/record/2790409>.
- [70] **CMS** Collaboration, A. M. Sirunyan *et al.*, “A measurement of the Higgs boson mass in the diphoton decay channel,” *Phys. Lett. B* **805** (2020) 135425, [arXiv:2002.06398 \[hep-ex\]](https://arxiv.org/abs/2002.06398).
- [71] **ATLAS** Collaboration, M. Aaboud *et al.*, “Measurement of the Higgs boson mass in the  $H \rightarrow ZZ^* \rightarrow 4\ell$  and  $H \rightarrow \gamma\gamma$  channels with  $\sqrt{s} = 13$  TeV  $pp$  collisions using the ATLAS detector,” *Phys. Lett. B* **784** (2018) 345–366, [arXiv:1806.00242 \[hep-ex\]](https://arxiv.org/abs/1806.00242).
- [72] **ATLAS, CMS** Collaboration, G. Aad *et al.*, “Combined Measurement of the Higgs Boson Mass in  $pp$  Collisions at  $\sqrt{s} = 7$  and 8 TeV with the ATLAS and CMS Experiments,” *Phys. Rev. Lett.* **114** (2015) 191803, [arXiv:1503.07589 \[hep-ex\]](https://arxiv.org/abs/1503.07589).
- [73] **CMS** Collaboration, A. M. Sirunyan *et al.*, “Measurements of properties of the Higgs boson decaying into the four-lepton final state in  $pp$  collisions at  $\sqrt{s} = 13$  TeV,” *JHEP* **11** (2017) 047, [arXiv:1706.09936 \[hep-ex\]](https://arxiv.org/abs/1706.09936).
- [74] P. M. Aronow and B. T. Miller, *Foundations of Agnostic Statistics*. Cambridge University Press, 2019.
- [75] J. De Blas, G. Durieux, C. Grojean, J. Gu, and A. Paul, “On the future of Higgs, electroweak and diboson measurements at lepton colliders,” *JHEP* **12** (2019) 117, [arXiv:1907.04311 \[hep-ph\]](https://arxiv.org/abs/1907.04311).
- [76] S. Banerjee, R. S. Gupta, O. Ochoa-Valeriano, and M. Spannowsky, “High energy lepton colliders as the ultimate Higgs microscopes,” [arXiv:2109.14634 \[hep-ph\]](https://arxiv.org/abs/2109.14634).

- [77] **ATLAS** Collaboration, M. Aaboud *et al.*, “Constraints on off-shell Higgs boson production and the Higgs boson total width in  $ZZ \rightarrow 4\ell$  and  $ZZ \rightarrow 2\ell 2\nu$  final states with the ATLAS detector,” *Phys. Lett. B* **786** (2018) 223–244, [arXiv:1808.01191 \[hep-ex\]](https://arxiv.org/abs/1808.01191).
- [78] **CMS** Collaboration, A. M. Sirunyan *et al.*, “Measurements of the Higgs boson width and anomalous  $HVV$  couplings from on-shell and off-shell production in the four-lepton final state,” *Phys. Rev. D* **99** no. 11, (2019) 112003, [arXiv:1901.00174 \[hep-ex\]](https://arxiv.org/abs/1901.00174).
- [79] **ATLAS** Collaboration, G. Aad *et al.*, “Study of the spin and parity of the Higgs boson in diboson decays with the ATLAS detector,” *Eur. Phys. J. C* **75** no. 10, (2015) 476, [arXiv:1506.05669 \[hep-ex\]](https://arxiv.org/abs/1506.05669). [Erratum: Eur.Phys.J.C 76, 152 (2016)].
- [80] **CMS** Collaboration, V. Khachatryan *et al.*, “Constraints on the spin-parity and anomalous  $HVV$  couplings of the Higgs boson in proton collisions at 7 and 8 TeV,” *Phys. Rev. D* **92** no. 1, (2015) 012004, [arXiv:1411.3441 \[hep-ex\]](https://arxiv.org/abs/1411.3441).
- [81] **CMS** Collaboration, V. Khachatryan *et al.*, “Measurement of differential and integrated fiducial cross sections for Higgs boson production in the four-lepton decay channel in pp collisions at  $\sqrt{s} = 7$  and 8 TeV,” *JHEP* **04** (2016) 005, [arXiv:1512.08377 \[hep-ex\]](https://arxiv.org/abs/1512.08377).
- [82] “Measurements of the total cross sections for Higgs boson production combining the  $H \rightarrow \gamma\gamma$  and  $H \rightarrow ZZ^* \rightarrow 4\ell$  decay channels at 7, 8 and 13 TeV center-of-mass energies with the ATLAS detector,”.
- [83] **CMS** Collaboration, A. M. Sirunyan *et al.*, “Measurement and interpretation of differential cross sections for Higgs boson production at  $\sqrt{s} = 13$  TeV,” *Phys. Lett. B* **792** (2019) 369–396, [arXiv:1812.06504 \[hep-ex\]](https://arxiv.org/abs/1812.06504).
- [84] **CMS** Collaboration, A. M. Sirunyan *et al.*, “Measurements of production cross sections of the Higgs boson in the four-lepton final state in proton–proton collisions at  $\sqrt{s} = 13$  TeV,” *Eur. Phys. J. C* **81** no. 6, (2021) 488, [arXiv:2103.04956 \[hep-ex\]](https://arxiv.org/abs/2103.04956).
- [85] **ATLAS** Collaboration, “Combined measurement of the total and differential cross sections in the  $H \rightarrow \gamma\gamma$  and the  $H \rightarrow ZZ^* \rightarrow 4\ell$  decay channels at  $\sqrt{s} = 13$  TeV with the ATLAS detector,”.
- [86] **ATLAS** Collaboration, “Measurements and interpretations of Higgs-boson fiducial cross sections in the diphoton decay channel using  $139\text{ fb}^{-1}$  of  $pp$  collision data at  $\sqrt{s} = 13$  TeV with the ATLAS detector,”.
- [87] **CMS** Collaboration, “Measurements of properties of the Higgs boson in the four-lepton final state in proton-proton collisions at  $\sqrt{s} = 13$  TeV,”.

- [88] N. Berger *et al.*, “Simplified Template Cross Sections - Stage 1.1,” [arXiv:1906.02754 \[hep-ph\]](https://arxiv.org/abs/1906.02754).
- [89] **ATLAS** Collaboration, “A combination of measurements of Higgs boson production and decay using up to  $139 \text{ fb}^{-1}$  of proton–proton collision data at  $\sqrt{s} = 13 \text{ TeV}$  collected with the ATLAS experiment,” Tech. Rep. ATLAS-CONF-2020-027, 2020.
- [90] **CMS** Collaboration, A. M. Sirunyan *et al.*, “Measurements of Higgs boson production cross sections and couplings in the diphoton decay channel at  $\sqrt{s} = 13 \text{ TeV}$ ,” *JHEP* **07** (2021) 027, [arXiv:2103.06956 \[hep-ex\]](https://arxiv.org/abs/2103.06956).
- [91] **CMS Collaboration** Collaboration, “Sensitivity projections for Higgs boson properties measurements at the HL-LHC,” tech. rep., CERN, Geneva, 2018. <https://cds.cern.ch/record/2647699>.
- [92] **CMS** Collaboration, “Combined Higgs boson production and decay measurements with up to  $137 \text{ fb}^{-1}$  of proton-proton collision data at  $\text{sqrt}s = 13 \text{ TeV}$ ,” Tech. Rep. CMS-PAS-HIG-19-005, 2020.
- [93] **CMS** Collaboration, “Measurement of Higgs boson production in association with a W or Z boson in the  $H \rightarrow WW$  decay channel,” Tech. Rep. CMS-PAS-HIG-19-017, 2021.
- [94] **ATLAS** Collaboration, “Combined measurements of Higgs boson production and decay using up to  $139 \text{ fb}^{-1}$  of proton-proton collision data at  $\sqrt{s} = 13 \text{ TeV}$  collected with the ATLAS experiment.”
- [95]
- [96] **CMS** Collaboration, A. M. Sirunyan *et al.*, “Search for associated production of a Higgs boson and a single top quark in proton-proton collisions at  $\sqrt{s} = 13 \text{ TeV}$ ,” *Phys. Rev. D* **99** no. 9, (2019) 092005, [arXiv:1811.09696 \[hep-ex\]](https://arxiv.org/abs/1811.09696).
- [97] **CMS** Collaboration, A. M. Sirunyan *et al.*, “Observation of Higgs boson decay to bottom quarks,” *Phys. Rev. Lett.* **121** no. 12, (2018) 121801, [arXiv:1808.08242 \[hep-ex\]](https://arxiv.org/abs/1808.08242).
- [98] **ATLAS** Collaboration, M. Aaboud *et al.*, “Observation of  $H \rightarrow b\bar{b}$  decays and  $VH$  production with the ATLAS detector,” *Phys. Lett. B* **786** (2018) 59–86, [arXiv:1808.08238 \[hep-ex\]](https://arxiv.org/abs/1808.08238).
- [99] **ATLAS** Collaboration, M. Aaboud *et al.*, “Measurement of VH,  $H \rightarrow b\bar{b}$  production as a function of the vector-boson transverse momentum in  $13 \text{ TeV}$  pp collisions with the ATLAS detector,” *JHEP* **05** (2019) 141, [arXiv:1903.04618 \[hep-ex\]](https://arxiv.org/abs/1903.04618).

- [100] **ATLAS** Collaboration, M. Aaboud *et al.*, “Cross-section measurements of the Higgs boson decaying into a pair of  $\tau$ -leptons in proton-proton collisions at  $\sqrt{s} = 13$  TeV with the ATLAS detector,” *Phys. Rev. D* **99** (2019) 072001, [arXiv:1811.08856 \[hep-ex\]](https://arxiv.org/abs/1811.08856).
- [101] **CMS** Collaboration, “Measurement of Higgs boson production and decay to the  $\tau\tau$  final state.”
- [102] **ATLAS** Collaboration, G. Aad *et al.*, “A search for the dimuon decay of the Standard Model Higgs boson with the ATLAS detector,” *Phys. Lett. B* **812** (2021) 135980, [arXiv:2007.07830 \[hep-ex\]](https://arxiv.org/abs/2007.07830).
- [103] **CMS** Collaboration, A. M. Sirunyan *et al.*, “Evidence for Higgs boson decay to a pair of muons,” *JHEP* **01** (2021) 148, [arXiv:2009.04363 \[hep-ex\]](https://arxiv.org/abs/2009.04363).
- [104] **ATLAS** Collaboration, “Direct constraint on the Higgs-charm coupling from a search for Higgs boson decays to charm quarks with the ATLAS detector.”
- [105] **ATLAS** Collaboration, G. Aad *et al.*, “Direct constraint on the Higgs-charm coupling from a search for Higgs boson decays into charm quarks with the ATLAS detector,” [arXiv:2201.11428 \[hep-ex\]](https://arxiv.org/abs/2201.11428).
- [106] **CMS** Collaboration, A. M. Sirunyan *et al.*, “A search for the standard model Higgs boson decaying to charm quarks,” *JHEP* **03** (2020) 131, [arXiv:1912.01662 \[hep-ex\]](https://arxiv.org/abs/1912.01662).
- [107] **ATLAS Collaboration** Collaboration, C. Bernius, “HL-LHC prospects from ATLAS and CMS,” tech. rep., CERN, Geneva, Mar, 2019.  
<https://cds.cern.ch/record/2666331>.
- [108] **ATLAS** Collaboration, “Prospects for  $H \rightarrow c\bar{c}$  using Charm Tagging with the ATLAS Experiment at the HL-LHC,” Tech. Rep. ATL-PHYS-PUB-2018-016, CERN, Geneva, Aug, 2018. [http://cds.cern.ch/record/2633635](https://cds.cern.ch/record/2633635).
- [109] **ATLAS** Collaboration, G. Aad *et al.*, “A search for the  $Z\gamma$  decay mode of the Higgs boson in  $pp$  collisions at  $\sqrt{s} = 13$  TeV with the ATLAS detector,” *Phys. Lett. B* **809** (2020) 135754, [arXiv:2005.05382 \[hep-ex\]](https://arxiv.org/abs/2005.05382).
- [110] S. Dawson, S. Dittmaier, and M. Spira, “Neutral Higgs boson pair production at hadron colliders: QCD corrections,” *Phys. Rev. D* **58** (1998) 115012, [arXiv:hep-ph/9805244](https://arxiv.org/abs/hep-ph/9805244).
- [111] A. Papaefstathiou and K. Sakurai, “Triple Higgs boson production at a 100 TeV proton-proton collider,” *JHEP* **02** (2016) 006, [arXiv:1508.06524 \[hep-ph\]](https://arxiv.org/abs/1508.06524).
- [112] M. McCullough, “An Indirect Model-Dependent Probe of the Higgs Self-Coupling,” *Phys. Rev. D* **90** no. 1, (2014) 015001, [arXiv:1312.3322 \[hep-ph\]](https://arxiv.org/abs/1312.3322). [Erratum: Phys.Rev.D 92, 039903 (2015)].

- [113] M. Gorbahn and U. Haisch, “Indirect probes of the trilinear Higgs coupling:  $gg \rightarrow h$  and  $h \rightarrow \gamma\gamma$ ,” *JHEP* **10** (2016) 094, [arXiv:1607.03773 \[hep-ph\]](https://arxiv.org/abs/1607.03773).
- [114] G. Degrassi, P. P. Giardino, F. Maltoni, and D. Pagani, “Probing the Higgs self coupling via single Higgs production at the LHC,” *JHEP* **12** (2016) 080, [arXiv:1607.04251 \[hep-ph\]](https://arxiv.org/abs/1607.04251).
- [115] W. Bizon, M. Gorbahn, U. Haisch, and G. Zanderighi, “Constraints on the trilinear Higgs coupling from vector boson fusion and associated Higgs production at the LHC,” *JHEP* **07** (2017) 083, [arXiv:1610.05771 \[hep-ph\]](https://arxiv.org/abs/1610.05771).
- [116] F. Maltoni, D. Pagani, A. Shivaji, and X. Zhao, “Trilinear Higgs coupling determination via single-Higgs differential measurements at the LHC,” *Eur. Phys. J. C* **77** no. 12, (2017) 887, [arXiv:1709.08649 \[hep-ph\]](https://arxiv.org/abs/1709.08649).
- [117] G. Degrassi and M. Vitti, “The effect of an anomalous Higgs trilinear self-coupling on the  $h \rightarrow \gamma Z$  decay,” *Eur. Phys. J. C* **80** no. 4, (2020) 307, [arXiv:1912.06429 \[hep-ph\]](https://arxiv.org/abs/1912.06429).
- [118] G. Degrassi, B. Di Micco, P. P. Giardino, and E. Rossi, “Higgs boson self-coupling constraints from single Higgs, double Higgs and Electroweak measurements,” *Phys. Lett. B* **817** (2021) 136307, [arXiv:2102.07651 \[hep-ph\]](https://arxiv.org/abs/2102.07651).
- [119] U. Haisch and G. Koole, “Off-shell Higgs production at the LHC as a probe of the trilinear Higgs coupling,” [arXiv:2111.12589 \[hep-ph\]](https://arxiv.org/abs/2111.12589).
- [120] S. Weinberg, “Phenomenological lagrangians,” *Physica A: Statistical Mechanics and its Applications* **96** no. 1, (1979) 327–340.  
<https://www.sciencedirect.com/science/article/pii/0378437179902231>.
- [121] S. Weinberg, “Baryon- and lepton-nonconserving processes,” *Phys. Rev. Lett.* **43** (Nov, 1979) 1566–1570.  
<https://link.aps.org/doi/10.1103/PhysRevLett.43.1566>.
- [122] L. Lehman, “Extending the Standard Model Effective Field Theory with the Complete Set of Dimension-7 Operators,” *Phys. Rev. D* **90** no. 12, (2014) 125023, [arXiv:1410.4193 \[hep-ph\]](https://arxiv.org/abs/1410.4193).
- [123] L. Lehman and A. Martin, “Low-derivative operators of the Standard Model effective field theory via Hilbert series methods,” *JHEP* **02** (2016) 081, [arXiv:1510.00372 \[hep-ph\]](https://arxiv.org/abs/1510.00372).
- [124] B. Henning, X. Lu, T. Melia, and H. Murayama, “2, 84, 30, 993, 560, 15456, 11962, 261485, ...: Higher dimension operators in the SM EFT,” *JHEP* **08** (2017) 016, [arXiv:1512.03433 \[hep-ph\]](https://arxiv.org/abs/1512.03433). [Erratum: JHEP 09, 019 (2019)].
- [125] J. A. Aguilar-Saavedra, “Effective four-fermion operators in top physics: A Roadmap,” *Nucl. Phys. B* **843** (2011) 638–672, [arXiv:1008.3562 \[hep-ph\]](https://arxiv.org/abs/1008.3562). [Erratum: Nucl.Phys.B 851, 443–444 (2011)].

- [126] B. Grzadkowski, M. Iskrzynski, M. Misiak, and J. Rosiek, “Dimension-Six Terms in the Standard Model Lagrangian,” *JHEP* **10** (2010) 085, [arXiv:1008.4884 \[hep-ph\]](https://arxiv.org/abs/1008.4884).
- [127] W. Buchmüller and D. Wyler, “Effective lagrangian analysis of new interactions and flavour conservation,” *Nuclear Physics B* **268** no. 3, (1986) 621–653.  
<https://www.sciencedirect.com/science/article/pii/0550321386902622>.
- [128] K. Hagiwara, S. Ishihara, R. Szalapski, and D. Zeppenfeld, “Low-energy effects of new interactions in the electroweak boson sector,” *Phys. Rev. D* **48** (1993) 2182–2203.
- [129] R. Alonso, E. E. Jenkins, A. V. Manohar, and M. Trott, “Renormalization Group Evolution of the Standard Model Dimension Six Operators III: Gauge Coupling Dependence and Phenomenology,” *JHEP* **04** (2014) 159, [arXiv:1312.2014 \[hep-ph\]](https://arxiv.org/abs/1312.2014).
- [130] G. F. Giudice, C. Grojean, A. Pomarol, and R. Rattazzi, “The Strongly-Interacting Light Higgs,” *JHEP* **06** (2007) 045, [arXiv:hep-ph/0703164](https://arxiv.org/abs/hep-ph/0703164).
- [131] R. Contino, M. Ghezzi, C. Grojean, M. Muhlleitner, and M. Spira, “Effective Lagrangian for a light Higgs-like scalar,” *JHEP* **07** (2013) 035, [arXiv:1303.3876 \[hep-ph\]](https://arxiv.org/abs/1303.3876).
- [132] J. Elias-Miró, C. Grojean, R. S. Gupta, and D. Marzocca, “Scaling and tuning of EW and Higgs observables,” *JHEP* **05** (2014) 019, [arXiv:1312.2928 \[hep-ph\]](https://arxiv.org/abs/1312.2928).
- [133] R. S. Gupta, A. Pomarol, and F. Riva, “BSM Primary Effects,” *Phys. Rev. D* **91** no. 3, (2015) 035001, [arXiv:1405.0181 \[hep-ph\]](https://arxiv.org/abs/1405.0181).
- [134] L. Alasfar, A. Azatov, J. de Blas, A. Paul, and M. Valli, “ $B$  anomalies under the lens of electroweak precision,” *JHEP* **12** (2020) 016, [arXiv:2007.04400 \[hep-ph\]](https://arxiv.org/abs/2007.04400).
- [135] M. Carena and H. Haber, “Higgs boson theory and phenomenology,” *Progress in Particle and Nuclear Physics* **50** no. 1, (2003) 63–152.  
<https://www.sciencedirect.com/science/article/pii/S0146641002001771>.
- [136] R. Contino, “The Higgs as a Composite Nambu-Goldstone Boson,” in *Theoretical Advanced Study Institute in Elementary Particle Physics: Physics of the Large and the Small*, pp. 235–306. 2011. [arXiv:1005.4269 \[hep-ph\]](https://arxiv.org/abs/1005.4269).
- [137] G. Panico and A. Wulzer, *The Composite Nambu-Goldstone Higgs*, vol. 913. Springer, 2016. [arXiv:1506.01961 \[hep-ph\]](https://arxiv.org/abs/1506.01961).
- [138] **ATLAS** Collaboration, “Methodology for EFT interpretation of Higgs boson Simplified Template Cross-section results in ATLAS.”

- [139] S. Dawson, S. Homiller, and S. D. Lane, “Putting SMEFT Fits to Work,” [arXiv:2007.01296 \[hep-ph\]](https://arxiv.org/abs/2007.01296).
- [140] **SMEFiT** Collaboration, J. J. Ethier, G. Magni, F. Maltoni, L. Mantani, E. R. Nocera, J. Rojo, E. Slade, E. Vryonidou, and C. Zhang, “Combined SMEFT interpretation of Higgs, diboson, and top quark data from the LHC,” *JHEP* **11** (2021) 089, [arXiv:2105.00006 \[hep-ph\]](https://arxiv.org/abs/2105.00006).
- [141] J. Ellis, C. W. Murphy, V. Sanz, and T. You, “Updated Global SMEFT Fit to Higgs, Diboson and Electroweak Data,” *JHEP* **06** (2018) 146, [arXiv:1803.03252 \[hep-ph\]](https://arxiv.org/abs/1803.03252).
- [142] S. Dawson and P. P. Giardino, “Flavorful Electroweak Precision Observables in the Standard Model Effective Field Theory,” [arXiv:2201.09887 \[hep-ph\]](https://arxiv.org/abs/2201.09887).
- [143] J. Ellis, M. Madigan, K. Mimasu, V. Sanz, and T. You, “Top, Higgs, Diboson and Electroweak Fit to the Standard Model Effective Field Theory,” *JHEP* **04** (2021) 279, [arXiv:2012.02779 \[hep-ph\]](https://arxiv.org/abs/2012.02779).
- [144] G. Degrassi, P. Gambino, and P. P. Giardino, “The  $m_W - m_Z$  interdependence in the Standard Model: a new scrutiny,” *JHEP* **05** (2015) 154, [arXiv:1411.7040 \[hep-ph\]](https://arxiv.org/abs/1411.7040).
- [145] G. D. Kribs, A. Maier, H. Rzehak, M. Spannowsky, and P. Waite, “Electroweak oblique parameters as a probe of the trilinear Higgs boson self-interaction,” *Phys. Rev. D* **95** no. 9, (2017) 093004, [arXiv:1702.07678 \[hep-ph\]](https://arxiv.org/abs/1702.07678).
- [146] S. Di Vita, C. Grojean, G. Panico, M. Riembau, and T. Vantalon, “A global view on the Higgs self-coupling,” *JHEP* **09** (2017) 069, [arXiv:1704.01953 \[hep-ph\]](https://arxiv.org/abs/1704.01953).
- [147] **ATLAS** Collaboration, “Constraints on the Higgs boson self-coupling from the combination of single-Higgs and double-Higgs production analyses performed with the ATLAS experiment,” Tech. Rep. ATLAS-CONF-2019-049, 2019.
- [148] R. Grober, M. Muhlleitner, and M. Spira, “Higgs Pair Production at NLO QCD for CP-violating Higgs Sectors,” *Nucl. Phys. B* **925** (2017) 1–27, [arXiv:1705.05314 \[hep-ph\]](https://arxiv.org/abs/1705.05314).
- [149] J. Gasser and H. Leutwyler, “Chiral perturbation theory to one loop,” *Annals of Physics* **158** no. 1, (1984) 142–210.  
<https://www.sciencedirect.com/science/article/pii/0003491684902422>.
- [150] J. Gasser and H. Leutwyler, “Chiral perturbation theory: Expansions in the mass of the strange quark,” *Nuclear Physics B* **250** no. 1, (1985) 465–516.  
<https://www.sciencedirect.com/science/article/pii/0550321385904924>.
- [151] G. Buchalla, O. Catà, and C. Krause, “Complete Electroweak Chiral Lagrangian with a Light Higgs at NLO,” *Nucl. Phys. B* **880** (2014) 552–573, [arXiv:1307.5017 \[hep-ph\]](https://arxiv.org/abs/1307.5017). [Erratum: Nucl.Phys.B 913, 475–478 (2016)].

- [152] G. Buchalla, O. Cata, A. Celis, and C. Krause, “Note on Anomalous Higgs-Boson Couplings in Effective Field Theory,” *Phys. Lett. B* **750** (2015) 298–301, [arXiv:1504.01707 \[hep-ph\]](https://arxiv.org/abs/1504.01707).
- [153] **LHC Higgs Cross Section Working Group** Collaboration, D. de Florian *et al.*, “Handbook of LHC Higgs Cross Sections: 4. Deciphering the Nature of the Higgs Sector,” [arXiv:1610.07922 \[hep-ph\]](https://arxiv.org/abs/1610.07922).
- [154] G. Buchalla, M. Capozi, A. Celis, G. Heinrich, and L. Scyboz, “Higgs boson pair production in non-linear Effective Field Theory with full  $m_t$ -dependence at NLO QCD,” *JHEP* **09** (2018) 057, [arXiv:1806.05162 \[hep-ph\]](https://arxiv.org/abs/1806.05162).
- [155] M. Capozi and G. Heinrich, “Exploring anomalous couplings in Higgs boson pair production through shape analysis,” *JHEP* **03** (2020) 091, [arXiv:1908.08923 \[hep-ph\]](https://arxiv.org/abs/1908.08923).
- [156] D. de Florian, I. Fabre, G. Heinrich, J. Mazzitelli, and L. Scyboz, “Anomalous couplings in Higgs-boson pair production at approximate NNLO QCD,” [arXiv:2106.14050 \[hep-ph\]](https://arxiv.org/abs/2106.14050).
- [157] G. Heinrich, S. P. Jones, M. Kerner, and L. Scyboz, “A non-linear EFT description of  $gg \rightarrow HH$  at NLO interfaced to POWHEG,” *JHEP* **10** (2020) 021, [arXiv:2006.16877 \[hep-ph\]](https://arxiv.org/abs/2006.16877).
- [158] K. Agashe, R. Contino, and A. Pomarol, “The minimal composite higgs model,” *Nuclear Physics B* **719** no. 1, (2005) 165–187.  
<https://www.sciencedirect.com/science/article/pii/S0550321305003445>.
- [159] W. D. Goldberger, B. Grinstein, and W. Skiba, “Distinguishing the higgs boson from the dilaton at the large hadron collider,” *Phys. Rev. Lett.* **100** (Mar, 2008) 111802. <https://link.aps.org/doi/10.1103/PhysRevLett.100.111802>.
- [160] K. Habaa, S. Matsuzaki, and K. Yamawaki, “Holographic Techni-dilaton, or Conformal Higgs,” in *International Workshop on Strong Coupling Gauge Theories in LHC Era: SCGT 09*, pp. 401–403. 2011. [arXiv:1003.2841 \[hep-ph\]](https://arxiv.org/abs/1003.2841).
- [161] A. Delgado, K. Lane, and A. Martin, “A Light Scalar in Low-Scale Technicolor,” *Phys. Lett. B* **696** (2011) 482–486, [arXiv:1011.0745 \[hep-ph\]](https://arxiv.org/abs/1011.0745).
- [162] J. Galloway, M. A. Luty, Y. Tsai, and Y. Zhao, “Induced Electroweak Symmetry Breaking and Supersymmetric Naturalness,” *Phys. Rev. D* **89** no. 7, (2014) 075003, [arXiv:1306.6354 \[hep-ph\]](https://arxiv.org/abs/1306.6354).
- [163] S. Chang, J. Galloway, M. Luty, E. Salvioni, and Y. Tsai, “Phenomenology of Induced Electroweak Symmetry Breaking,” *JHEP* **03** (2015) 017, [arXiv:1411.6023 \[hep-ph\]](https://arxiv.org/abs/1411.6023).

- [164] C. Hartmann and M. Trott, “Higgs Decay to Two Photons at One Loop in the Standard Model Effective Field Theory,” *Phys. Rev. Lett.* **115** no. 19, (2015) 191801, [arXiv:1507.03568 \[hep-ph\]](#).
- [165] A. Falkowski, B. Fuks, K. Mawatari, K. Mimasu, F. Riva, and V. Sanz, “Rosetta: an operator basis translator for Standard Model effective field theory,” *Eur. Phys. J. C* **75** no. 12, (2015) 583, [arXiv:1508.05895 \[hep-ph\]](#).
- [166] M. Gonzalez-Alonso, A. Greljo, G. Isidori, and D. Marzocca, “Pseudo-observables in Higgs decays,” *Eur. Phys. J. C* **75** (2015) 128, [arXiv:1412.6038 \[hep-ph\]](#).
- [167] A. Falkowski and R. Rattazzi, “Which EFT,” [arXiv:1902.05936 \[hep-ph\]](#).
- [168] S. Di Vita, G. Durieux, C. Grojean, J. Gu, Z. Liu, G. Panico, M. Riembau, and T. Vantalon, “A global view on the Higgs self-coupling at lepton colliders,” *JHEP* **02** (2018) 178, [arXiv:1711.03978 \[hep-ph\]](#).
- [169] M. Bonetti, K. Melnikov, and L. Tancredi, “Higher order corrections to mixed QCD-EW contributions to Higgs boson production in gluon fusion,” *Phys. Rev. D* **97** no. 5, (2018) 056017, [arXiv:1801.10403 \[hep-ph\]](#). [Erratum: *Phys. Rev. D* 97, 099906 (2018)].
- [170] X. Chen, T. Gehrmann, E. W. N. Glover, A. Huss, B. Mistlberger, and A. Pelloni, “Fully Differential Higgs Boson Production to Third Order in QCD,” *Phys. Rev. Lett.* **127** no. 7, (2021) 072002, [arXiv:2102.07607 \[hep-ph\]](#).
- [171] G. Billis, B. Dehnadi, M. A. Ebert, J. K. L. Michel, and F. J. Tackmann, “Higgs pT Spectrum and Total Cross Section with Fiducial Cuts at Third Resummed and Fixed Order in QCD,” *Phys. Rev. Lett.* **127** no. 7, (2021) 072001, [arXiv:2102.08039 \[hep-ph\]](#).
- [172] M. Bonetti, K. Melnikov, and L. Tancredi, “Three-loop mixed QCD-electroweak corrections to Higgs boson gluon fusion,” *Phys. Rev. D* **97** no. 3, (2018) 034004, [arXiv:1711.11113 \[hep-ph\]](#).
- [173] M. Bonetti, E. Panzer, V. A. Smirnov, and L. Tancredi, “Two-loop mixed QCD-EW corrections to  $gg \rightarrow Hg$ ,” *JHEP* **11** (2020) 045, [arXiv:2007.09813 \[hep-ph\]](#).
- [174] M. Becchetti, R. Bonciani, V. Del Duca, V. Hirschi, F. Moriello, and A. Schweitzer, “Next-to-leading order corrections to light-quark mixed QCD-EW contributions to Higgs boson production,” *Phys. Rev. D* **103** no. 5, (2021) 054037, [arXiv:2010.09451 \[hep-ph\]](#).
- [175] M. L. Czakon and M. Niggetiedt, “Exact quark-mass dependence of the Higgs-gluon form factor at three loops in QCD,” *JHEP* **05** (2020) 149, [arXiv:2001.03008 \[hep-ph\]](#).

- [176] M. Czakon, R. V. Harlander, J. Klappert, and M. Niggetiedt, “Exact Top-Quark Mass Dependence in Hadronic Higgs Production,” *Phys. Rev. Lett.* **127** no. 16, (2021) 162002, [arXiv:2105.04436 \[hep-ph\]](https://arxiv.org/abs/2105.04436).
- [177] F. Maltoni, E. Vryonidou, and M. Zaro, “Top-quark mass effects in double and triple Higgs production in gluon-gluon fusion at NLO,” *JHEP* **11** (2014) 079, [arXiv:1408.6542 \[hep-ph\]](https://arxiv.org/abs/1408.6542).
- [178] K. Kudashkin, K. Melnikov, and C. Wever, “Two-loop amplitudes for processes  $gg \rightarrow Hg$ ,  $qg \rightarrow Hq$  and  $q\bar{q} \rightarrow Hg$  at large Higgs transverse momentum,” *JHEP* **02** (2018) 135, [arXiv:1712.06549 \[hep-ph\]](https://arxiv.org/abs/1712.06549).
- [179] J. M. Lindert, K. Kudashkin, K. Melnikov, and C. Wever, “Higgs bosons with large transverse momentum at the LHC,” *Phys. Lett. B* **782** (2018) 210–214, [arXiv:1801.08226 \[hep-ph\]](https://arxiv.org/abs/1801.08226).
- [180] S. P. Jones, M. Kerner, and G. Luisoni, “Next-to-leading-order qcd corrections to higgs boson plus jet production with full top-quark mass dependence,” *Phys. Rev. Lett.* **120** (Apr, 2018) 162001.  
<https://link.aps.org/doi/10.1103/PhysRevLett.120.162001>.
- [181] V. Hankele, G. Klämke, D. Zeppenfeld, and T. Figy, “Anomalous higgs boson couplings in vector boson fusion at the cern lhc,” *Physical Review D* **74** no. 9, (2006) 095001.
- [182] T. Han, G. Valencia, and S. Willenbrock, “Structure function approach to vector boson scattering in p p collisions,” *Phys. Rev. Lett.* **69** (1992) 3274–3277, [arXiv:hep-ph/9206246](https://arxiv.org/abs/hep-ph/9206246).
- [183] T. Figy, C. Oleari, and D. Zeppenfeld, “Next-to-leading order jet distributions for Higgs boson production via weak boson fusion,” *Phys. Rev. D* **68** (2003) 073005, [arXiv:hep-ph/0306109](https://arxiv.org/abs/hep-ph/0306109).
- [184] E. L. Berger and J. M. Campbell, “Higgs boson production in weak boson fusion at next-to-leading order,” *Phys. Rev. D* **70** (2004) 073011, [arXiv:hep-ph/0403194](https://arxiv.org/abs/hep-ph/0403194).
- [185] M. Gomez-Bock, M. Mondragon, M. Muhlleitner, M. Spira, and P. M. Zerwas, “Concepts of Electroweak Symmetry Breaking and Higgs Physics,” in *4th CERN-CLAF School of High-Energy Physics*, pp. 177–238. 12, 2007. [arXiv:0712.2419 \[hep-ph\]](https://arxiv.org/abs/0712.2419).
- [186] P. Bolzoni, F. Maltoni, S.-O. Moch, and M. Zaro, “Higgs production via vector-boson fusion at NNLO in QCD,” *Phys. Rev. Lett.* **105** (2010) 011801, [arXiv:1003.4451 \[hep-ph\]](https://arxiv.org/abs/1003.4451).

- [187] A. Denner, S. Dittmaier, S. Kallweit, and A. Mück, “HAWK 2.0: A Monte Carlo program for Higgs production in vector-boson fusion and Higgs strahlung at hadron colliders,” *Comput. Phys. Commun.* **195** (2015) 161–171, [arXiv:1412.5390 \[hep-ph\]](https://arxiv.org/abs/1412.5390).
- [188] T. Han and S. Willenbrock, “QCD correction to the  $p\ p \rightarrow W\ H$  and  $Z\ H$  total cross-sections,” *Phys. Lett. B* **273** (1991) 167–172.
- [189] O. Brein, A. Djouadi, and R. Harlander, “NNLO QCD corrections to the Higgs-strahlung processes at hadron colliders,” *Phys. Lett. B* **579** (2004) 149–156, [arXiv:hep-ph/0307206](https://arxiv.org/abs/hep-ph/0307206).
- [190] S. Amoroso *et al.*, “Les Houches 2019: Physics at TeV Colliders: Standard Model Working Group Report,” in *11th Les Houches Workshop on Physics at TeV Colliders: PhysTeV Les Houches*. 3, 2020. [arXiv:2003.01700 \[hep-ph\]](https://arxiv.org/abs/2003.01700).
- [191] M. Cepeda *et al.*, “Report from Working Group 2: Higgs Physics at the HL-LHC and HE-LHC,” *CERN Yellow Rep. Monogr.* **7** (2019) 221–584, [arXiv:1902.00134 \[hep-ph\]](https://arxiv.org/abs/1902.00134).
- [192] C. Englert, M. McCullough, and M. Spannowsky, “Gluon-initiated associated production boosts Higgs physics,” *Phys. Rev. D* **89** no. 1, (2014) 013013, [arXiv:1310.4828 \[hep-ph\]](https://arxiv.org/abs/1310.4828).
- [193] C. Englert, R. Rosenfeld, M. Spannowsky, and A. Tonero, “New physics and signal-background interference in associated  $pp \rightarrow HZ$  production,” *EPL* **114** no. 3, (2016) 31001, [arXiv:1603.05304 \[hep-ph\]](https://arxiv.org/abs/1603.05304).
- [194] B. A. Kniehl, “Associated Production of Higgs and Z Bosons From Gluon Fusion in Hadron Collisions,” *Phys. Rev. D* **42** (1990) 2253–2258.
- [195] D. A. Dicus and C. Kao, “Higgs Boson -  $Z^0$  Production From Gluon Fusion,” *Phys. Rev. D* **38** (1988) 1008. [Erratum: Phys.Rev.D 42, 2412 (1990)].
- [196] L. Altenkamp, S. Dittmaier, R. V. Harlander, H. Rzehak, and T. J. Zirke, “Gluon-induced Higgs-strahlung at next-to-leading order QCD,” *JHEP* **02** (2013) 078, [arXiv:1211.5015 \[hep-ph\]](https://arxiv.org/abs/1211.5015).
- [197] R. V. Harlander, A. Kulesza, V. Theeuwes, and T. Zirke, “Soft gluon resummation for gluon-induced Higgs Strahlung,” *JHEP* **11** (2014) 082, [arXiv:1410.0217 \[hep-ph\]](https://arxiv.org/abs/1410.0217).
- [198] A. Hasselhuhn, T. Luthe, and M. Steinhauser, “On top quark mass effects to  $gg \rightarrow ZH$  at NLO,” *JHEP* **01** (2017) 073, [arXiv:1611.05881 \[hep-ph\]](https://arxiv.org/abs/1611.05881).
- [199] R. Harlander, J. Klappert, C. Pandini, and A. Papaefstathiou, “Exploiting the WH/ZH symmetry in the search for New Physics,” *Eur. Phys. J. C* **78** no. 9, (2018) 760, [arXiv:1804.02299 \[hep-ph\]](https://arxiv.org/abs/1804.02299).

- [200] B. Hespel, F. Maltoni, and E. Vryonidou, “Higgs and Z boson associated production via gluon fusion in the SM and the 2HDM,” *JHEP* **06** (2015) 065, [arXiv:1503.01656 \[hep-ph\]](https://arxiv.org/abs/1503.01656).
- [201] J. Davies, G. Mishima, and M. Steinhauser, “Virtual corrections to  $gg \rightarrow ZH$  in the high-energy and large- $m_t$  limits,” [arXiv:2011.12314 \[hep-ph\]](https://arxiv.org/abs/2011.12314).
- [202] L. Chen, G. Heinrich, S. P. Jones, M. Kerner, J. Klappert, and J. Schlenk, “ $ZH$  production in gluon fusion: two-loop amplitudes with full top quark mass dependence,” [arXiv:2011.12325 \[hep-ph\]](https://arxiv.org/abs/2011.12325).
- [203] R. Bonciani, G. Degrassi, P. P. Giardino, and R. Gröber, “Analytical Method for Next-to-Leading-Order QCD Corrections to Double-Higgs Production,” *Phys. Rev. Lett.* **121** no. 16, (2018) 162003, [arXiv:1806.11564 \[hep-ph\]](https://arxiv.org/abs/1806.11564).
- [204] L. Alasfar, G. Degrassi, P. P. Giardino, R. Gröber, and M. Vitti, “Virtual corrections to  $gg \rightarrow ZH$  via a transverse momentum expansion,” *JHEP* **05** (2021) 168, [arXiv:2103.06225 \[hep-ph\]](https://arxiv.org/abs/2103.06225).
- [205] F. Dulat, A. Lazopoulos, and B. Mistlberger, “iHixs 2 — Inclusive Higgs cross sections,” *Comput. Phys. Commun.* **233** (2018) 243–260, [arXiv:1802.00827 \[hep-ph\]](https://arxiv.org/abs/1802.00827).
- [206] S. Alioli, P. Nason, C. Oleari, and E. Re, “NLO Higgs boson production via gluon fusion matched with shower in POWHEG,” *JHEP* **04** (2009) 002, [arXiv:0812.0578 \[hep-ph\]](https://arxiv.org/abs/0812.0578).
- [207] P. Nason and C. Oleari, “NLO Higgs boson production via vector-boson fusion matched with shower in POWHEG,” *JHEP* **02** (2010) 037, [arXiv:0911.5299 \[hep-ph\]](https://arxiv.org/abs/0911.5299).
- [208] E. Bagnaschi, G. Degrassi, P. Slavich, and A. Vicini, “Higgs production via gluon fusion in the POWHEG approach in the SM and in the MSSM,” *JHEP* **02** (2012) 088, [arXiv:1111.2854 \[hep-ph\]](https://arxiv.org/abs/1111.2854).
- [209] J. M. Campbell, R. K. Ellis, R. Frederix, P. Nason, C. Oleari, and C. Williams, “NLO Higgs Boson Production Plus One and Two Jets Using the POWHEG BOX, MadGraph4 and MCFM,” *JHEP* **07** (2012) 092, [arXiv:1202.5475 \[hep-ph\]](https://arxiv.org/abs/1202.5475).
- [210] G. Luisoni, P. Nason, C. Oleari, and F. Tramontano, “ $HW^\pm/HZ + 0$  and 1 jet at NLO with the POWHEG BOX interfaced to GoSam and their merging within MiNLO,” *JHEP* **10** (2013) 083, [arXiv:1306.2542 \[hep-ph\]](https://arxiv.org/abs/1306.2542).
- [211] B. Jäger, F. Schissler, and D. Zeppenfeld, “Parton-shower effects on Higgs boson production via vector-boson fusion in association with three jets,” *JHEP* **07** (2014) 125, [arXiv:1405.6950 \[hep-ph\]](https://arxiv.org/abs/1405.6950).

- [212] H. B. Hartanto, B. Jager, L. Reina, and D. Wackerlo, “Higgs boson production in association with top quarks in the POWHEG BOX,” *Phys. Rev. D* **91** no. 9, (2015) 094003, [arXiv:1501.04498 \[hep-ph\]](https://arxiv.org/abs/1501.04498).
- [213] J. Alwall, R. Frederix, S. Frixione, V. Hirschi, F. Maltoni, O. Mattelaer, H. S. Shao, T. Stelzer, P. Torrielli, and M. Zaro, “The automated computation of tree-level and next-to-leading order differential cross sections, and their matching to parton shower simulations,” *JHEP* **07** (2014) 079, [arXiv:1405.0301 \[hep-ph\]](https://arxiv.org/abs/1405.0301).
- [214] “Higgs corss-sections working group.” <https://twiki.cern.ch/twiki/bin/view/LHCPhysics/LHCHWG?redirectTo=LHCPhysics.LHCHXSWG>.
- [215] C. Degrande, G. Durieux, F. Maltoni, K. Mimasu, E. Vryonidou, and C. Zhang, “Automated one-loop computations in the standard model effective field theory,” *Phys. Rev. D* **103** no. 9, (2021) 096024, [arXiv:2008.11743 \[hep-ph\]](https://arxiv.org/abs/2008.11743).
- [216] R. Frederix, D. Pagani, and M. Zaro, “Large NLO corrections in  $t\bar{t}W^\pm$  and  $t\bar{t}t\bar{t}$  hadroproduction from supposedly subleading EW contributions,” *JHEP* **02** (2018) 031, [arXiv:1711.02116 \[hep-ph\]](https://arxiv.org/abs/1711.02116).
- [217] **CMS** Collaboration, A. M. Sirunyan *et al.*, “Search for the production of four top quarks in the single-lepton and opposite-sign dilepton final states in proton-proton collisions at  $\sqrt{s} = 13$  TeV,” *JHEP* **11** (2019) 082, [arXiv:1906.02805 \[hep-ex\]](https://arxiv.org/abs/1906.02805).
- [218] **ATLAS** Collaboration, G. Aad *et al.*, “Evidence for  $t\bar{t}t\bar{t}$  production in the multilepton final state in proton–proton collisions at  $\sqrt{s} = 13$  TeV with the ATLAS detector,” *Eur. Phys. J. C* **80** no. 11, (2020) 1085, [arXiv:2007.14858 \[hep-ex\]](https://arxiv.org/abs/2007.14858).
- [219] **CMS** Collaboration, A. M. Sirunyan *et al.*, “Measurement of the cross section for  $t\bar{t}$  production with additional jets and b jets in pp collisions at  $\sqrt{s} = 13$  TeV,” *JHEP* **07** (2020) 125, [arXiv:2003.06467 \[hep-ex\]](https://arxiv.org/abs/2003.06467).
- [220] **ATLAS** Collaboration, “Measurements of fiducial and differential cross-sections of  $t\bar{t}$  production with additional heavy-flavour jets in proton-proton collisions at  $\sqrt{s} = 13$  TeV with the ATLAS detector,” Tech. Rep. ATLAS-CONF-2018-029, 2018.
- [221] J. D’Hondt, A. Mariotti, K. Mimasu, S. Moortgat, and C. Zhang, “Learning to pinpoint effective operators at the LHC: a study of the  $t\bar{t}b\bar{b}$  signature,” *JHEP* **11** (2018) 131, [arXiv:1807.02130 \[hep-ph\]](https://arxiv.org/abs/1807.02130).
- [222] N. P. Hartland, F. Maltoni, E. R. Nocera, J. Rojo, E. Slade, E. Vryonidou, and C. Zhang, “A Monte Carlo global analysis of the Standard Model Effective Field Theory: the top quark sector,” *JHEP* **04** (2019) 100, [arXiv:1901.05965 \[hep-ph\]](https://arxiv.org/abs/1901.05965).

- [223] J. de Blas, M. Chala, and J. Santiago, “Renormalization Group Constraints on New Top Interactions from Electroweak Precision Data,” *JHEP* **09** (2015) 189, [arXiv:1507.00757 \[hep-ph\]](https://arxiv.org/abs/1507.00757).
- [224] A. Dedes, W. Materkowska, M. Paraskevas, J. Rosiek, and K. Suxho, “Feynman rules for the Standard Model Effective Field Theory in  $R_\xi$ -gauges,” *JHEP* **06** (2017) 143, [arXiv:1704.03888 \[hep-ph\]](https://arxiv.org/abs/1704.03888).
- [225] H. Patel, “Package-X: A Mathematica package for the analytic calculation of one-loop integrals,” *Comput. Phys. Commun.* **197** (2015) 276–290, [arXiv:1503.01469 \[hep-ph\]](https://arxiv.org/abs/1503.01469).
- [226] P. Maierhöfer, J. Usovitsch, and P. Uwer, “Kira—A Feynman integral reduction program,” *Comput. Phys. Commun.* **230** (2018) 99–112, [arXiv:1705.05610 \[hep-ph\]](https://arxiv.org/abs/1705.05610).
- [227] T. Hahn, “Generating Feynman diagrams and amplitudes with FeynArts 3,” *Comput. Phys. Commun.* **140** (2001) 418–431, [arXiv:hep-ph/0012260](https://arxiv.org/abs/hep-ph/0012260).
- [228] A. Alloul, N. D. Christensen, C. Degrande, C. Duhr, and B. Fuks, “FeynRules 2.0 - A complete toolbox for tree-level phenomenology,” *Comput. Phys. Commun.* **185** (2014) 2250–2300, [arXiv:1310.1921 \[hep-ph\]](https://arxiv.org/abs/1310.1921).
- [229] A. Smirnov, “Algorithm FIRE – Feynman Integral REduction,” *JHEP* **10** (2008) 107, [arXiv:0807.3243 \[hep-ph\]](https://arxiv.org/abs/0807.3243).
- [230] S. Dawson and P. P. Giardino, “Higgs decays to  $ZZ$  and  $Z\gamma$  in the standard model effective field theory: An NLO analysis,” *Phys. Rev. D* **97** no. 9, (2018) 093003, [arXiv:1801.01136 \[hep-ph\]](https://arxiv.org/abs/1801.01136).
- [231] E. E. Jenkins, A. V. Manohar, and M. Trott, “Renormalization Group Evolution of the Standard Model Dimension Six Operators I: Formalism and lambda Dependence,” *JHEP* **10** (2013) 087, [arXiv:1308.2627 \[hep-ph\]](https://arxiv.org/abs/1308.2627).
- [232] E. E. Jenkins, A. V. Manohar, and M. Trott, “Renormalization Group Evolution of the Standard Model Dimension Six Operators II: Yukawa Dependence,” *JHEP* **01** (2014) 035, [arXiv:1310.4838 \[hep-ph\]](https://arxiv.org/abs/1310.4838).
- [233] R. Gauld, B. D. Pecjak, and D. J. Scott, “One-loop corrections to  $h \rightarrow b\bar{b}$  and  $h \rightarrow \tau\bar{\tau}$  decays in the Standard Model Dimension-6 EFT: four-fermion operators and the large- $m_t$  limit,” *JHEP* **05** (2016) 080, [arXiv:1512.02508 \[hep-ph\]](https://arxiv.org/abs/1512.02508).
- [234] G. Ossola, C. G. Papadopoulos, and R. Pittau, “Reducing full one-loop amplitudes to scalar integrals at the integrand level,” *Nucl. Phys. B* **763** (2007) 147–169, [arXiv:hep-ph/0609007](https://arxiv.org/abs/hep-ph/0609007).
- [235] G. Ossola, C. G. Papadopoulos, and R. Pittau, “CutTools: A Program implementing the OPP reduction method to compute one-loop amplitudes,” *JHEP* **03** (2008) 042, [arXiv:0711.3596 \[hep-ph\]](https://arxiv.org/abs/0711.3596).

- [236] G. Ossola, C. G. Papadopoulos, and R. Pittau, “On the Rational Terms of the one-loop amplitudes,” *JHEP* **05** (2008) 004, [arXiv:0802.1876 \[hep-ph\]](https://arxiv.org/abs/0802.1876).
- [237] R. D. Ball *et al.*, “Parton distributions with LHC data,” *Nucl. Phys. B* **867** (2013) 244–289, [arXiv:1207.1303 \[hep-ph\]](https://arxiv.org/abs/1207.1303).
- [238] I. Brivio, Y. Jiang, and M. Trott, “The SMEFTsim package, theory and tools,” *JHEP* **12** (2017) 070, [arXiv:1709.06492 \[hep-ph\]](https://arxiv.org/abs/1709.06492).
- [239] “Guidelines for extrapolation of cms and atlas lhc/hl-lhc couplings projections to he-lhc.” <https://twiki.cern.ch/twiki/bin/view/LHCPhysics/GuidelinesCouplingProjections2018#Details%20of%20the%20CMS%20projections>.
- [240] J. Salvatier, T. V. Wiecki, and C. Fonnesbeck, “Probabilistic programming in python using PyMC3,” *PeerJ Computer Science* **2** (Apr, 2016) e55. <https://doi.org/10.7717/peerj-cs.55>.
- [241] R. Kumar, C. Carroll, A. Hartikainen, and O. Martin, “Arviz a unified library for exploratory analysis of bayesian models in python,” *Journal of Open Source Software* **4** no. 33, (2019) 1143. <https://doi.org/10.21105/joss.01143>.
- [242] J. de Blas *et al.*, “**HEPfit**: a Code for the Combination of Indirect and Direct Constraints on High Energy Physics Models,” *Eur. Phys. J. C* **80** no. 5, (2020) 456, [arXiv:1910.14012 \[hep-ph\]](https://arxiv.org/abs/1910.14012).
- [243] I. Brivio, S. Bruggisser, F. Maltoni, R. Moutafis, T. Plehn, E. Vryonidou, S. Westhoff, and C. Zhang, “O new physics, where art thou? A global search in the top sector,” *JHEP* **02** (2020) 131, [arXiv:1910.03606 \[hep-ph\]](https://arxiv.org/abs/1910.03606).
- [244] C. Zhang, “Constraining  $qq\bar{t}$  operators from four-top production: a case for enhanced EFT sensitivity,” *Chin. Phys. C* **42** no. 2, (2018) 023104, [arXiv:1708.05928 \[hep-ph\]](https://arxiv.org/abs/1708.05928).
- [245] **ATLAS** Collaboration, “Search for Higgs boson pair production in the two bottom quarks plus two photons final state in  $pp$  collisions at  $\sqrt{s} = 13$  TeV with the ATLAS detector,” Tech. Rep. ATLAS-CONF-2021-016, 2021.
- [246] L. Alasfar, R. Gröber, C. Grojean, A. Paul, and Z. Qian, “Machine learning augmented probes of light-quark Yukawa and trilinear couplings from Higgs pair production,” *In preparation* (2021) .
- [247] J. Alison *et al.*, “Higgs boson potential at colliders: Status and perspectives,” *Rev. Phys.* **5** (2020) 100045, [arXiv:1910.00012 \[hep-ph\]](https://arxiv.org/abs/1910.00012).
- [248] **CMS** Collaboration, “Prospects for HH measurements at the HL-LHC,” *CMS-PAS-FTR-18-019* (2018) .

- [249] **FCC** Collaboration, A. Abada *et al.*, “FCC Physics Opportunities: Future Circular Collider Conceptual Design Report Volume 1,” *Eur. Phys. J. C* **79** no. 6, (2019) 474.
- [250] **FCC** Collaboration, A. Abada *et al.*, “FCC-ee: The Lepton Collider: Future Circular Collider Conceptual Design Report Volume 2,” *Eur. Phys. J. ST* **228** no. 2, (2019) 261–623.
- [251] P. Bambade *et al.*, “The International Linear Collider: A Global Project,” [arXiv:1903.01629 \[hep-ex\]](https://arxiv.org/abs/1903.01629).
- [252] **LCC Physics Working Group** Collaboration, K. Fujii *et al.*, “Tests of the Standard Model at the International Linear Collider,” [arXiv:1908.11299 \[hep-ex\]](https://arxiv.org/abs/1908.11299).
- [253] F. An *et al.*, “Precision Higgs physics at the CEPC,” *Chin. Phys. C* **43** no. 4, (2019) 043002, [arXiv:1810.09037 \[hep-ex\]](https://arxiv.org/abs/1810.09037).
- [254] **CEPC Study Group** Collaboration, M. Dong *et al.*, “CEPC Conceptual Design Report: Volume 2 - Physics & Detector,” [arXiv:1811.10545 \[hep-ex\]](https://arxiv.org/abs/1811.10545).
- [255] **CLICdp, CLIC** Collaboration, T. K. Charles *et al.*, “The Compact Linear Collider (CLIC) - 2018 Summary Report,” [arXiv:1812.06018 \[physics.acc-ph\]](https://arxiv.org/abs/1812.06018).
- [256] J. de Blas *et al.*, “The CLIC Potential for New Physics,” [arXiv:1812.02093 \[hep-ph\]](https://arxiv.org/abs/1812.02093).
- [257] G. Banelli, E. Salvioni, J. Serra, T. Theil, and A. Weiler, “The Present and Future of Four Top Operators,” *JHEP* **02** (2021) 043, [arXiv:2010.05915 \[hep-ph\]](https://arxiv.org/abs/2010.05915).
- [258] J. de Blas, J. C. Criado, M. Perez-Victoria, and J. Santiago, “Effective description of general extensions of the Standard Model: the complete tree-level dictionary,” *JHEP* **03** (2018) 109, [arXiv:1711.10391 \[hep-ph\]](https://arxiv.org/abs/1711.10391).
- [259] Anisha, S. D. Bakshi, S. Banerjee, A. Biekötter, J. Chakrabortty, S. K. Patra, and M. Spannowsky, “Effective limits on single scalar extensions in the light of recent LHC data,” [arXiv:2111.05876 \[hep-ph\]](https://arxiv.org/abs/2111.05876).
- [260] **ATLAS** Collaboration, M. Aaboud *et al.*, “Observation of  $H \rightarrow b\bar{b}$  decays and  $VH$  production with the ATLAS detector,” *Phys. Lett. B* **786** (2018) 59–86, [arXiv:1808.08238 \[hep-ex\]](https://arxiv.org/abs/1808.08238).
- [261] **CMS** Collaboration, A. M. Sirunyan *et al.*, “Observation of Higgs boson decay to bottom quarks,” *Phys. Rev. Lett.* **121** no. 12, (2018) 121801, [arXiv:1808.08242 \[hep-ex\]](https://arxiv.org/abs/1808.08242).

- [262] R. V. Harlander, S. Liebler, and T. Zirke, “Higgs Strahlung at the Large Hadron Collider in the 2-Higgs-Doublet Model,” *JHEP* **02** (2014) 023, [arXiv:1307.8122 \[hep-ph\]](https://arxiv.org/abs/1307.8122).
- [263] L. D. Landau, “On the angular momentum of a system of two photons,” *Dokl. Akad. Nauk SSSR* **60** no. 2, (1948) 207–209.
- [264] C.-N. Yang, “Selection Rules for the Dematerialization of a Particle Into Two Photons,” *Phys. Rev.* **77** (1950) 242–245.
- [265] G. Passarino and M. J. G. Veltman, “One Loop corrections for  $e^+e^-$  annihilation into  $\mu^+\mu^-$  in the Weinberg Model,” *Nucl. Phys.* **B160** (1979) 151.
- [266] S. Larin, “The Renormalization of the axial anomaly in dimensional regularization,” *Phys. Lett. B* **303** (1993) 113–118, [arXiv:hep-ph/9302240](https://arxiv.org/abs/hep-ph/9302240).
- [267] M. Spira, A. Djouadi, D. Graudenz, and P. M. Zerwas, “Higgs boson production at the LHC,” *Nucl. Phys. B* **453** (1995) 17–82, [arXiv:hep-ph/9504378](https://arxiv.org/abs/hep-ph/9504378).
- [268] U. Aglietti, R. Bonciani, G. Degrassi, and A. Vicini, “Analytic Results for Virtual QCD Corrections to Higgs Production and Decay,” *JHEP* **01** (2007) 021, [arXiv:hep-ph/0611266](https://arxiv.org/abs/hep-ph/0611266).
- [269] R. Mertig, M. Bohm, and A. Denner, “FEYN CALC: Computer algebraic calculation of Feynman amplitudes,” *Comput. Phys. Commun.* **64** (1991) 345–359.
- [270] V. Shtabovenko, R. Mertig, and F. Orellana, “New Developments in FeynCalc 9.0,” *Comput. Phys. Commun.* **207** (2016) 432–444, [arXiv:1601.01167 \[hep-ph\]](https://arxiv.org/abs/1601.01167).
- [271] H. H. Patel, “Package-X 2.0: A Mathematica package for the analytic calculation of one-loop integrals,” *Comput. Phys. Commun.* **218** (2017) 66–70, [arXiv:1612.00009 \[hep-ph\]](https://arxiv.org/abs/1612.00009).
- [272] P. Maierhöfer, J. Usovitsch, and P. Uwer, “Kira—A Feynman integral reduction program,” *Comput. Phys. Commun.* **230** (2018) 99–112, [arXiv:1705.05610 \[hep-ph\]](https://arxiv.org/abs/1705.05610).
- [273] R. Bonciani, P. Mastrolia, and E. Remiddi, “Master integrals for the two loop QCD virtual corrections to the forward backward asymmetry,” *Nucl. Phys. B* **690** (2004) 138–176, [arXiv:hep-ph/0311145](https://arxiv.org/abs/hep-ph/0311145).
- [274] S. Borowka and G. Heinrich, “Massive non-planar two-loop four-point integrals with SecDec 2.1,” *Comput. Phys. Commun.* **184** (2013) 2552–2561, [arXiv:1303.1157 \[hep-ph\]](https://arxiv.org/abs/1303.1157).

- [275] S. Borowka, G. Heinrich, S. P. Jones, M. Kerner, J. Schlenk, and T. Zirke, “SecDec-3.0: numerical evaluation of multi-scale integrals beyond one loop,” *Comput. Phys. Commun.* **196** (2015) 470–491, [arXiv:1502.06595 \[hep-ph\]](#).
- [276] A. V. Smirnov, “FIRE5: a C++ implementation of Feynman Integral REduction,” *Comput. Phys. Commun.* **189** (2015) 182–191, [arXiv:1408.2372 \[hep-ph\]](#).
- [277] R. N. Lee, “LiteRed 1.4: a powerful tool for reduction of multiloop integrals,” *J. Phys. Conf. Ser.* **523** (2014) 012059, [arXiv:1310.1145 \[hep-ph\]](#).
- [278] A. von Manteuffel and L. Tancredi, “A non-planar two-loop three-point function beyond multiple polylogarithms,” *JHEP* **06** (2017) 127, [arXiv:1701.05905 \[hep-ph\]](#).
- [279] R. Bonciani, G. Degrassi, P. P. Giardino, and R. Gröber, “A Numerical Routine for the Crossed Vertex Diagram with a Massive-Particle Loop,” *Comput. Phys. Commun.* **241** (2019) 122–131, [arXiv:1812.02698 \[hep-ph\]](#).
- [280] L. Naterop, A. Signer, and Y. Ulrich, “handyG —Rapid numerical evaluation of generalised polylogarithms in Fortran,” *Comput. Phys. Commun.* **253** (2020) 107165, [arXiv:1909.01656 \[hep-ph\]](#).
- [281] S. Buehler and C. Duhr, “CHAPLIN - Complex Harmonic Polylogarithms in Fortran,” *Comput. Phys. Commun.* **185** (2014) 2703–2713, [arXiv:1106.5739 \[hep-ph\]](#).
- [282] S. Borowka, G. Heinrich, S. Jahn, S. P. Jones, M. Kerner, J. Schlenk, and T. Zirke, “pySecDec: a toolbox for the numerical evaluation of multi-scale integrals,” *Comput. Phys. Commun.* **222** (2018) 313–326, [arXiv:1703.09692 \[hep-ph\]](#).
- [283] S. Borowka, G. Heinrich, S. Jahn, S. P. Jones, M. Kerner, and J. Schlenk, “A GPU compatible quasi-Monte Carlo integrator interfaced to pySecDec,” *Comput. Phys. Commun.* **240** (2019) 120–137, [arXiv:1811.11720 \[physics.comp-ph\]](#).
- [284] O. Eboli, G. Marques, S. Novaes, and A. Natale, “Twin higgs-boson production,” *Physics Letters B* **197** no. 1, (1987) 269–272.
- [285] E. Glover and J. van der Bij, “Higgs boson pair production via gluon fusion,” *Nuclear Physics B* **309** no. 2, (1988) 282–294.
- [286] D. A. Dicus, C. Kao, and S. S. D. Willenbrock, “Higgs Boson Pair Production From Gluon Fusion,” *Phys. Lett.* **B203** (1988) 457–461.
- [287] T. Plehn, M. Spira, and P. M. Zerwas, “Pair production of neutral Higgs particles in gluon-gluon collisions,” *Nucl. Phys.* **B479** (1996) 46–64, [arXiv:hep-ph/9603205 \[hep-ph\]](#). [Erratum: Nucl. Phys.B531,655(1998)].

- [288] S. Borowka, N. Greiner, G. Heinrich, S. P. Jones, M. Kerner, J. Schlenk, and T. Zirke, “Full top quark mass dependence in Higgs boson pair production at NLO,” *JHEP* **10** (2016) 107, [arXiv:1608.04798 \[hep-ph\]](https://arxiv.org/abs/1608.04798).
- [289] S. Borowka, N. Greiner, G. Heinrich, S. P. Jones, M. Kerner, J. Schlenk, U. Schubert, and T. Zirke, “Higgs Boson Pair Production in Gluon Fusion at Next-to-Leading Order with Full Top-Quark Mass Dependence,” *Phys. Rev. Lett.* **117** no. 1, (2016) 012001, [arXiv:1604.06447 \[hep-ph\]](https://arxiv.org/abs/1604.06447). [Erratum: *Phys. Rev. Lett.* 117,no.7,079901(2016)].
- [290] J. Baglio, F. Campanario, S. Glaus, M. Mühlleitner, M. Spira, and J. Streicher, “Gluon fusion into Higgs pairs at NLO QCD and the top mass scheme,” *Eur. Phys. J.* **C79** no. 6, (2019) 459, [arXiv:1811.05692 \[hep-ph\]](https://arxiv.org/abs/1811.05692).
- [291] G. Heinrich, S. P. Jones, M. Kerner, G. Luisoni, and L. Scyboz, “Probing the trilinear Higgs boson coupling in di-Higgs production at NLO QCD including parton shower effects,” *JHEP* **06** (2019) 066, [arXiv:1903.08137 \[hep-ph\]](https://arxiv.org/abs/1903.08137).
- [292] J. Davies, R. Gröber, A. Maier, T. Rauh, and M. Steinhauser, “Top quark mass dependence of the Higgs boson-gluon form factor at three loops,” *Phys. Rev. D* **100** no. 3, (2019) 034017, [arXiv:1906.00982 \[hep-ph\]](https://arxiv.org/abs/1906.00982).
- [293] M. Grazzini, G. Heinrich, S. Jones, S. Kallweit, M. Kerner, J. M. Lindert, and J. Mazzitelli, “Higgs boson pair production at NNLO with top quark mass effects,” *JHEP* **05** (2018) 059, [arXiv:1803.02463 \[hep-ph\]](https://arxiv.org/abs/1803.02463).
- [294] **NNPDF** Collaboration, R. D. Ball *et al.*, “Parton distributions from high-precision collider data,” *Eur. Phys. J.* **C77** no. 10, (2017) 663, [arXiv:1706.00428 \[hep-ph\]](https://arxiv.org/abs/1706.00428).
- [295] A. Buckley, J. Ferrando, S. Lloyd, K. Nordström, B. Page, M. Rüfenacht, M. Schönherr, and G. Watt, “LHAPDF6: parton density access in the LHC precision era,” *Eur. Phys. J.* **C75** (2015) 132, [arXiv:1412.7420 \[hep-ph\]](https://arxiv.org/abs/1412.7420).
- [296] A. Denner, S. Dittmaier, and L. Hofer, “COLLIER - A fortran-library for one-loop integrals,” *PoS LL2014* (2014) 071, [arXiv:1407.0087 \[hep-ph\]](https://arxiv.org/abs/1407.0087).
- [297] S. Dittmaier *et al.*, “Handbook of LHC Higgs Cross Sections: 2. Differential Distributions,” [arXiv:1201.3084 \[hep-ph\]](https://arxiv.org/abs/1201.3084).
- [298] **LHC Higgs Cross Section Working Group** Collaboration, D. de Florian *et al.*, “Handbook of LHC Higgs Cross Sections: 4. Deciphering the Nature of the Higgs Sector,” [arXiv:1610.07922 \[hep-ph\]](https://arxiv.org/abs/1610.07922).
- [299] A. D. Martin, W. J. Stirling, R. S. Thorne, and G. Watt, “Uncertainties on alpha(S) in global PDF analyses and implications for predicted hadronic cross sections,” *Eur. Phys. J.* **C64** (2009) 653–680, [arXiv:0905.3531 \[hep-ph\]](https://arxiv.org/abs/0905.3531).

- [300] F. Demartin, S. Forte, E. Mariani, J. Rojo, and A. Vicini, “The impact of PDF and alphas uncertainties on Higgs Production in gluon fusion at hadron colliders,” *Phys. Rev.* **D82** (2010) 014002, [arXiv:1004.0962 \[hep-ph\]](#).
- [301] J. Baglio, A. Djouadi, R. Gröber, M. M. Mühlleitner, J. Quevillon, and M. Spira, “The measurement of the Higgs self-coupling at the LHC: theoretical status,” *JHEP* **04** (2013) 151, [arXiv:1212.5581 \[hep-ph\]](#).
- [302] I. Brivio, F. Goertz, and G. Isidori, “Probing the Charm Quark Yukawa Coupling in Higgs+Charm Production,” *Phys. Rev. Lett.* **115** no. 21, (2015) 211801, [arXiv:1507.02916 \[hep-ph\]](#).
- [303] Y. Soreq, H. X. Zhu, and J. Zupan, “Light quark Yukawa couplings from Higgs kinematics,” *JHEP* **12** (2016) 045, [arXiv:1606.09621 \[hep-ph\]](#).
- [304] F. Bishara, U. Haisch, P. F. Monni, and E. Re, “Constraining Light-Quark Yukawa Couplings from Higgs Distributions,” *Phys. Rev. Lett.* **118** no. 12, (2017) 121801, [arXiv:1606.09253 \[hep-ph\]](#).
- [305] G. Bonner and H. E. Logan, “Constraining the Higgs couplings to up and down quarks using production kinematics at the CERN Large Hadron Collider,” [arXiv:1608.04376 \[hep-ph\]](#).
- [306] CMS Collaboration, “Constraints on the Higgs boson self-coupling from ttH+tH, H to gamma gamma differential measurements at the HL-LHC,” Tech. Rep. CMS-PAS-FTR-18-020, 2018.
- [307] G. Perez, Y. Soreq, E. Stamou, and K. Tobioka, “Prospects for measuring the Higgs boson coupling to light quarks,” *Phys. Rev.* **D93** no. 1, (2016) 013001, [arXiv:1505.06689 \[hep-ph\]](#).
- [308] G. T. Bodwin, F. Petriello, S. Stoynev, and M. Velasco, “Higgs boson decays to quarkonia and the  $H\bar{c}c$  coupling,” *Phys. Rev.* **D88** no. 5, (2013) 053003, [arXiv:1306.5770 \[hep-ph\]](#).
- [309] A. L. Kagan, G. Perez, F. Petriello, Y. Soreq, S. Stoynev, and J. Zupan, “Exclusive Window onto Higgs Yukawa Couplings,” *Phys. Rev. Lett.* **114** no. 10, (2015) 101802, [arXiv:1406.1722 \[hep-ph\]](#).
- [310] M. König and M. Neubert, “Exclusive Radiative Higgs Decays as Probes of Light-Quark Yukawa Couplings,” *JHEP* **08** (2015) 012, [arXiv:1505.03870 \[hep-ph\]](#).
- [311] CMS Collaboration, A. M. Sirunyan *et al.*, “Search for rare decays of Z and Higgs bosons to  $J/\psi$  and a photon in proton-proton collisions at  $\sqrt{s} = 13$  TeV,” *Eur. Phys. J. C* **79** no. 2, (2019) 94, [arXiv:1810.10056 \[hep-ex\]](#).

- [312] F. Yu, “Light Quark Yukawa Couplings and the  $W^\pm h$  Charge Asymmetry,” *Nucl. Part. Phys. Proc.* **285-286** (2017) 123–125.
- [313] J. A. Aguilar-Saavedra, J. M. Cano, and J. M. No, “More light on Higgs flavor at the LHC: Higgs boson couplings to light quarks through  $h + \gamma$  production,” *Phys. Rev. D* **103** no. 9, (2021) 095023, [arXiv:2008.12538 \[hep-ph\]](https://arxiv.org/abs/2008.12538).
- [314] A. Falkowski, S. Ganguly, P. Gras, J. M. No, K. Tobioka, N. Vignaroli, and T. You, “Light quark Yukawas in triboson final states,” *JHEP* **04** (2021) 023, [arXiv:2011.09551 \[hep-ph\]](https://arxiv.org/abs/2011.09551).
- [315] **ATLAS** Collaboration, A. Sciandra, “Measurement of Triboson Production and aQGCs with the ATLAS detector.”
- [316] **CMS** Collaboration, “Observation of heavy triboson production in leptonic final states in proton-proton collisions at  $\sqrt{s} = 13$  TeV.”
- [317] T. Binoth, S. Karg, N. Kauer, and R. Ruckl, “Multi-Higgs boson production in the Standard Model and beyond,” *Phys. Rev. D* **74** (2006) 113008, [arXiv:hep-ph/0608057 \[hep-ph\]](https://arxiv.org/abs/hep-ph/0608057).
- [318] R. Contino, M. Ghezzi, M. Moretti, G. Panico, F. Piccinini, and A. Wulzer, “Anomalous Couplings in Double Higgs Production,” *JHEP* **08** (2012) 154, [arXiv:1205.5444 \[hep-ph\]](https://arxiv.org/abs/1205.5444).
- [319] L. Alasfar, R. Corral Lopez, and R. Gröber, “Probing Higgs couplings to light quarks via Higgs pair production,” *JHEP* **11** (2019) 088, [arXiv:1909.05279 \[hep-ph\]](https://arxiv.org/abs/1909.05279).
- [320] S. Bar-Shalom and A. Soni, “Universally enhanced light-quarks Yukawa couplings paradigm,” *Phys. Rev. D* **98** no. 5, (2018) 055001, [arXiv:1804.02400 \[hep-ph\]](https://arxiv.org/abs/1804.02400).
- [321] M. Bauer, M. Carena, and A. Carmona, “Higgs Pair Production as a Signal of Enhanced Yukawa Couplings,” *Phys. Rev. Lett.* **121** no. 2, (2018) 021801, [arXiv:1801.00363 \[hep-ph\]](https://arxiv.org/abs/1801.00363).
- [322] D. Egana-Ugrinovic, S. Homiller, and P. Meade, “Multi-Higgs Production Probes Higgs Flavor,” *Phys. Rev. D* **103** (2021) 115005, [arXiv:2101.04119 \[hep-ph\]](https://arxiv.org/abs/2101.04119).
- [323] A. Papaefstathiou and K. Sakurai, “Triple Higgs boson production at a 100 TeV proton-proton collider,” *JHEP* **02** (Aug, 2015) 006. 10 p, [arXiv:1508.06524](https://arxiv.org/abs/1508.06524). <https://cds.cern.ch/record/2047255>. Corrected version of Figure 6.
- [324] C. Delaunay, R. Ozeri, G. Perez, and Y. Soreq, “Probing Atomic Higgs-like Forces at the Precision Frontier,” *Phys. Rev. D* **96** no. 9, (2017) 093001, [arXiv:1601.05087 \[hep-ph\]](https://arxiv.org/abs/1601.05087).

- [325] **ATLAS** Collaboration, G. Aad *et al.*, “Combined measurements of Higgs boson production and decay using up to  $80 \text{ fb}^{-1}$  of proton-proton collision data at  $\sqrt{s} = 13 \text{ TeV}$  collected with the ATLAS experiment,” *Phys. Rev. D* **101** no. 1, (2020) 012002, [arXiv:1909.02845 \[hep-ex\]](#).
- [326] **ATLAS** Collaboration, G. Aad *et al.*, “Combination of searches for Higgs boson pairs in  $pp$  collisions at  $\sqrt{s} = 13 \text{ TeV}$  with the ATLAS detector,” [arXiv:1906.02025 \[hep-ex\]](#).
- [327] T. Plehn and M. Rauch, “The quartic higgs coupling at hadron colliders,” *Phys. Rev. D* **72** (2005) 053008, [arXiv:hep-ph/0507321 \[hep-ph\]](#).
- [328] **CMS** Collaboration, V. Khachatryan *et al.*, “Search for a standard model-like Higgs boson in the  $\mu^+\mu^-$  and  $e^+e^-$  decay channels at the LHC,” *Phys. Lett. B* **744** (2015) 184–207, [arXiv:1410.6679 \[hep-ex\]](#).
- [329] G. Perez, Y. Soreq, E. Stamou, and K. Tobioka, “Constraining the charm Yukawa and Higgs-quark coupling universality,” *Phys. Rev. D* **92** no. 3, (2015) 033016, [arXiv:1503.00290 \[hep-ph\]](#).
- [330] J. De Blas *et al.*, “Higgs Boson Studies at Future Particle Colliders,” [arXiv:1905.03764 \[hep-ph\]](#).
- [331] **ATLAS** Collaboration, M. Aaboud *et al.*, “Constraints on off-shell Higgs boson production and the Higgs boson total width in  $ZZ \rightarrow 4\ell$  and  $ZZ \rightarrow 2\ell 2\nu$  final states with the ATLAS detector,” *Phys. Lett. B* **786** (2018) 223–244, [arXiv:1808.01191 \[hep-ex\]](#).
- [332] **CMS** Collaboration, A. M. Sirunyan *et al.*, “Measurements of the Higgs boson width and anomalous  $HVV$  couplings from on-shell and off-shell production in the four-lepton final state,” *Phys. Rev. D* **99** no. 11, (2019) 112003, [arXiv:1901.00174 \[hep-ex\]](#).
- [333] F. Caola and K. Melnikov, “Constraining the Higgs boson width with  $ZZ$  production at the LHC,” *Phys. Rev. D* **88** (2013) 054024, [arXiv:1307.4935 \[hep-ph\]](#).
- [334] C. Englert and M. Spannowsky, “Limitations and Opportunities of Off-Shell Coupling Measurements,” *Phys. Rev. D* **90** (2014) 053003, [arXiv:1405.0285 \[hep-ph\]](#).
- [335] M. König and M. Neubert, “Exclusive Radiative Higgs Decays as Probes of Light-Quark Yukawa Couplings,” *JHEP* **08** (2015) 012, [arXiv:1505.03870 \[hep-ph\]](#).
- [336] **ATLAS** Collaboration, M. Aaboud *et al.*, “Search for exclusive Higgs and  $Z$  boson decays to  $\phi\gamma$  and  $\rho\gamma$  with the ATLAS detector,” *JHEP* **07** (2018) 127, [arXiv:1712.02758 \[hep-ex\]](#).

- [337] **ATLAS** Collaboration, M. Aaboud *et al.*, “Searches for exclusive Higgs and  $Z$  boson decays into  $J/\psi\gamma$ ,  $\psi(2S)\gamma$ , and  $\Upsilon(nS)\gamma$  at  $\sqrt{s} = 13$  TeV with the ATLAS detector,” *Phys. Lett. B* **786** (2018) 134–155, [arXiv:1807.00802 \[hep-ex\]](https://arxiv.org/abs/1807.00802).
- [338] **CMS** Collaboration, A. M. Sirunyan *et al.*, “Search for rare decays of  $Z$  and Higgs bosons to  $J/\psi$  and a photon in proton-proton collisions at  $\sqrt{s} = 13$  TeV,” *Eur. Phys. J. C* **79** no. 2, (2019) 94, [arXiv:1810.10056 \[hep-ex\]](https://arxiv.org/abs/1810.10056).
- [339] **CMS** Collaboration, “Search for the standard model Higgs boson decaying to charm quarks,” Tech. Rep. CMS-PAS-HIG-18-031, CERN, Geneva, 2019.  
<http://cds.cern.ch/record/2682638>.
- [340] C. O. Dib, R. Rosenfeld, and A. Zerwekh, “Double Higgs production and quadratic divergence cancellation in little Higgs models with T parity,” *JHEP* **05** (2006) 074, [arXiv:hep-ph/0509179 \[hep-ph\]](https://arxiv.org/abs/hep-ph/0509179).
- [341] R. Gröber and M. Mühlleitner, “Composite Higgs Boson Pair Production at the LHC,” *JHEP* **06** (2011) 020, [arXiv:1012.1562 \[hep-ph\]](https://arxiv.org/abs/1012.1562).
- [342] R. Gröber, M. Mühlleitner, and M. Spira, “Signs of Composite Higgs Pair Production at Next-to-Leading Order,” *JHEP* **06** (2016) 080, [arXiv:1602.05851 \[hep-ph\]](https://arxiv.org/abs/1602.05851).
- [343] G. Blankenburg, J. Ellis, and G. Isidori, “Flavour-Changing Decays of a 125 GeV Higgs-like Particle,” *Phys. Lett. B* **712** (2012) 386–390, [arXiv:1202.5704 \[hep-ph\]](https://arxiv.org/abs/1202.5704).
- [344] G. D’Ambrosio, G. F. Giudice, G. Isidori, and A. Strumia, “Minimal flavor violation: An Effective field theory approach,” *Nucl. Phys. B* **645** (2002) 155–187, [arXiv:hep-ph/0207036 \[hep-ph\]](https://arxiv.org/abs/hep-ph/0207036).
- [345] **ATLAS** Collaboration, “Combined measurements of Higgs boson production and decay using up to  $80 \text{ fb}^{-1}$  of proton–proton collision data at  $\sqrt{s} = 13$  TeV collected with the ATLAS experiment,” Tech. Rep. ATLAS-CONF-2018-031, CERN, Geneva, Jul, 2018. <http://cds.cern.ch/record/2629412>.
- [346] **CMS** Collaboration, “Measurement of the top quark Yukawa coupling from  $t\bar{t}$  kinematic distributions in the lepton+jets final state in proton-proton collisions at  $\sqrt{s} = 13$  TeV,” Tech. Rep. CERN-EP-2019-119. CMS-TOP-17-004-003, CERN, Geneva, Jul, 2019. <https://cds.cern.ch/record/2681021>.
- [347] D. Egana-Ugrinovic, S. Homiller, and P. Meade, “Aligned and Spontaneous Flavor Violation,” *Phys. Rev. Lett.* **123** no. 3, (2019) 031802, [arXiv:1811.00017 \[hep-ph\]](https://arxiv.org/abs/1811.00017).
- [348] D. Egana-Ugrinovic, S. Homiller, and P. R. Meade, “Higgs bosons with large couplings to light quarks,” [arXiv:1908.11376 \[hep-ph\]](https://arxiv.org/abs/1908.11376).

- [349] S. R. Coleman, J. Wess, and B. Zumino, “Structure of phenomenological Lagrangians. 1.,” *Phys. Rev.* **177** (1969) 2239–2247.
- [350] C. G. Callan, Jr., S. R. Coleman, J. Wess, and B. Zumino, “Structure of phenomenological Lagrangians. 2.,” *Phys. Rev.* **177** (1969) 2247–2250.
- [351] R. Contino, C. Grojean, M. Moretti, F. Piccinini, and R. Rattazzi, “Strong Double Higgs Production at the LHC,” *JHEP* **05** (2010) 089, [arXiv:1002.1011 \[hep-ph\]](https://arxiv.org/abs/1002.1011).
- [352] R. Gröber, A. Maier, and T. Rauh, “Reconstruction of top-quark mass effects in Higgs pair production and other gluon-fusion processes,” *JHEP* **03** (2018) 020, [arXiv:1709.07799 \[hep-ph\]](https://arxiv.org/abs/1709.07799).
- [353] J. Davies, G. Mishima, M. Steinhauser, and D. Wellmann, “Double Higgs boson production at NLO in the high-energy limit: complete analytic results,” *JHEP* **01** (2019) 176, [arXiv:1811.05489 \[hep-ph\]](https://arxiv.org/abs/1811.05489).
- [354] J. Grigo, K. Melnikov, and M. Steinhauser, “Virtual corrections to Higgs boson pair production in the large top quark mass limit,” *Nucl. Phys.* **B888** (2014) 17–29, [arXiv:1408.2422 \[hep-ph\]](https://arxiv.org/abs/1408.2422).
- [355] D. de Florian and J. Mazzitelli, “Higgs Boson Pair Production at Next-to-Next-to-Leading Order in QCD,” *Phys. Rev. Lett.* **111** (2013) 201801, [arXiv:1309.6594 \[hep-ph\]](https://arxiv.org/abs/1309.6594).
- [356] J. Davies and M. Steinhauser, “Three-loop form factors for Higgs boson pair production in the large top mass limit,” [arXiv:1909.01361 \[hep-ph\]](https://arxiv.org/abs/1909.01361).
- [357] R. V. Harlander, M. Prausa, and J. Usovitsch, “The light-fermion contribution to the exact Higgs-gluon form factor in QCD,” [arXiv:1907.06957 \[hep-ph\]](https://arxiv.org/abs/1907.06957).
- [358] D. de Florian and J. Mazzitelli, “Higgs pair production at next-to-next-to-leading logarithmic accuracy at the LHC,” *JHEP* **09** (2015) 053, [arXiv:1505.07122 \[hep-ph\]](https://arxiv.org/abs/1505.07122).
- [359] D. Dicus, T. Stelzer, Z. Sullivan, and S. Willenbrock, “Higgs boson production in association with bottom quarks at next-to-leading order,” *Phys. Rev.* **D59** (1999) 094016, [arXiv:hep-ph/9811492 \[hep-ph\]](https://arxiv.org/abs/hep-ph/9811492).
- [360] C. Balazs, H.-J. He, and C. P. Yuan, “QCD corrections to scalar production via heavy quark fusion at hadron colliders,” *Phys. Rev.* **D60** (1999) 114001, [arXiv:hep-ph/9812263 \[hep-ph\]](https://arxiv.org/abs/hep-ph/9812263).
- [361] R. V. Harlander and W. B. Kilgore, “Higgs boson production in bottom quark fusion at next-to-next-to leading order,” *Phys. Rev.* **D68** (2003) 013001, [arXiv:hep-ph/0304035 \[hep-ph\]](https://arxiv.org/abs/hep-ph/0304035).

- [362] S. Dawson, C. Kao, Y. Wang, and P. Williams, “QCD Corrections to Higgs Pair Production in Bottom Quark Fusion,” *Phys. Rev.* **D75** (2007) 013007, [arXiv:hep-ph/0610284 \[hep-ph\]](https://arxiv.org/abs/hep-ph/0610284).
- [363] A. H. Ajjath, P. Banerjee, A. Chakraborty, P. K. Dhani, P. Mukherjee, N. Rana, and V. Ravindran, “Higgs pair production from bottom quark annihilation to NNLO in QCD,” *JHEP* **05** (2019) 030, [arXiv:1811.01853 \[hep-ph\]](https://arxiv.org/abs/1811.01853).
- [364] M. Spira, “Higgs Boson Production and Decay at Hadron Colliders,” *Prog. Part. Nucl. Phys.* **95** (2017) 98–159, [arXiv:1612.07651 \[hep-ph\]](https://arxiv.org/abs/1612.07651).
- [365] V. N. Gribov and L. N. Lipatov, “Deep inelastic e p scattering in perturbation theory,” *Sov. J. Nucl. Phys.* **15** (1972) 438–450. [Yad. Fiz.15,781(1972)].
- [366] G. Altarelli and G. Parisi, “Asymptotic Freedom in Parton Language,” *Nucl. Phys.* **B126** (1977) 298–318.
- [367] Y. L. Dokshitzer, “Calculation of the Structure Functions for Deep Inelastic Scattering and e+ e- Annihilation by Perturbation Theory in Quantum Chromodynamics.,” *Sov. Phys. JETP* **46** (1977) 641–653. [Zh. Eksp. Teor. Fiz.73,1216(1977)].
- [368] A. Djouadi, J. Kalinowski, and M. Spira, “HDECAY: A Program for Higgs boson decays in the standard model and its supersymmetric extension,” *Comput. Phys. Commun.* **108** (1998) 56–74, [arXiv:hep-ph/9704448 \[hep-ph\]](https://arxiv.org/abs/hep-ph/9704448).
- [369] A. Djouadi, J. Kalinowski, M. Muehlleitner, and M. Spira, “HDECAY: Twenty<sub>++</sub> years after,” *Comput. Phys. Commun.* **238** (2019) 214–231, [arXiv:1801.09506 \[hep-ph\]](https://arxiv.org/abs/1801.09506).
- [370] A. Azatov, R. Contino, G. Panico, and M. Son, “Effective field theory analysis of double Higgs boson production via gluon fusion,” *Phys. Rev.* **D92** no. 3, (2015) 035001, [arXiv:1502.00539 \[hep-ph\]](https://arxiv.org/abs/1502.00539).
- [371] U. Baur, T. Plehn, and D. L. Rainwater, “Probing the Higgs selfcoupling at hadron colliders using rare decays,” *Phys. Rev.* **D69** (2004) 053004, [arXiv:hep-ph/0310056 \[hep-ph\]](https://arxiv.org/abs/hep-ph/0310056).
- [372] F. Kling, T. Plehn, and P. Schichtel, “Maximizing the significance in Higgs boson pair analyses,” *Phys. Rev.* **D95** no. 3, (2017) 035026, [arXiv:1607.07441 \[hep-ph\]](https://arxiv.org/abs/1607.07441).
- [373] V. Barger, L. L. Everett, C. B. Jackson, and G. Shaughnessy, “Higgs-Pair Production and Measurement of the Triscalar Coupling at LHC(8,14),” *Phys. Lett.* **B728** (2014) 433–436, [arXiv:1311.2931 \[hep-ph\]](https://arxiv.org/abs/1311.2931).
- [374] A. Adhikary, S. Banerjee, R. K. Barman, B. Bhattacherjee, and S. Niyogi, “Revisiting the non-resonant Higgs pair production at the HL-LHC,” *JHEP* **07** (2018) 116, [arXiv:1712.05346 \[hep-ph\]](https://arxiv.org/abs/1712.05346).

- [375] T. Sjostrand, S. Mrenna, and P. Z. Skands, “PYTHIA 6.4 Physics and Manual,” *JHEP* **05** (2006) 026, [arXiv:hep-ph/0603175 \[hep-ph\]](https://arxiv.org/abs/hep-ph/0603175).
- [376] D. C. Hall, “RootTuple: A library enabling ROOT n-tuple output from FORTRAN HEP programs,” <http://roottuple.hepforge.org>.
- [377] M. Cacciari, G. P. Salam, and G. Soyez, “FastJet User Manual,” *Eur. Phys. J.* **C72** (2012) 1896, [arXiv:1111.6097 \[hep-ph\]](https://arxiv.org/abs/1111.6097).
- [378] J. M. Butterworth, A. R. Davison, M. Rubin, and G. P. Salam, “Jet substructure as a new Higgs search channel at the LHC,” *Phys. Rev. Lett.* **100** (2008) 242001, [arXiv:0802.2470 \[hep-ph\]](https://arxiv.org/abs/0802.2470).
- [379] CMS Collaboration, S. Chatrchyan *et al.*, “Inclusive  $b$ -jet production in  $pp$  collisions at  $\sqrt{s} = 7$  TeV,” *JHEP* **04** (2012) 084, [arXiv:1202.4617 \[hep-ex\]](https://arxiv.org/abs/1202.4617).
- [380] CMS Collaboration, “Performance of  $b$  tagging at  $\sqrt{s}=8$  TeV in multijet,  $t\bar{t}$ bar and boosted topology events,” Tech. Rep. CMS-PAS-BTV-13-001, CERN, Geneva, 2013. <https://cds.cern.ch/record/1581306>.
- [381] ATLAS Collaboration, “Performance assumptions based on full simulation for an upgraded ATLAS detector at a High-Luminosity LHC,” Tech. Rep. ATL-PHYS-PUB-2013-009, CERN, Geneva, 2013. [http://cds.cern.ch/record/1604420](https://cds.cern.ch/record/1604420).
- [382] CMS Collaboration, “Photon ID performance with  $19.6 \text{ fb}^{-1}$  of data collected at  $\sqrt{s} = 8$  TeV with the CMS detector,” Tech. Rep. CMS-DP-2013-010, CERN, Geneva, 2013. [http://cds.cern.ch/record/1542855](https://cds.cern.ch/record/1542855).
- [383] G. Cowan, K. Cranmer, E. Gross, and O. Vitells, “Asymptotic formulae for likelihood-based tests of new physics,” *Eur. Phys. J.* **C71** (2011) 1554, [arXiv:1007.1727 \[physics.data-an\]](https://arxiv.org/abs/1007.1727). [Erratum: Eur. Phys. J.C73,2501(2013)].
- [384] D. Kim and M. Park, “Enhancement of new physics signal sensitivity with mistagged charm quarks,” *Phys. Lett.* **B758** (2016) 190–194, [arXiv:1507.03990 \[hep-ph\]](https://arxiv.org/abs/1507.03990).
- [385] CMS Collaboration, S. Chatrchyan *et al.*, “Search for the standard model Higgs boson produced in association with a W or a Z boson and decaying to bottom quarks,” *Phys. Rev.* **D89** no. 1, (2014) 012003, [arXiv:1310.3687 \[hep-ex\]](https://arxiv.org/abs/1310.3687).
- [386] ATLAS Collaboration, G. Aad *et al.*, “Search for the  $b\bar{b}$  decay of the Standard Model Higgs boson in associated ( $W/Z$ ) $H$  production with the ATLAS detector,” *JHEP* **01** (2015) 069, [arXiv:1409.6212 \[hep-ex\]](https://arxiv.org/abs/1409.6212).
- [387] N. A. Heard and P. Rubin-Delanchy, “Choosing between methods of combining-values,” *Biometrika* **105** no. 1, (2018) .

- [388] **ATLAS** Collaboration, G. Aad *et al.*, “Search for Scalar Charm Quark Pair Production in  $pp$  Collisions at  $\sqrt{s} = 8$  TeV with the ATLAS Detector,” *Phys. Rev. Lett.* **114** no. 16, (2015) 161801, [arXiv:1501.01325 \[hep-ex\]](https://arxiv.org/abs/1501.01325).
- [389] **ATLAS** Collaboration, “Search for single top-quark production via FCNC in strong interaction in  $\sqrt{s} = 8$  TeV ATLAS data,” Tech. Rep. ATLAS-CONF-2013-063, CERN, Geneva, 2013.  
<http://cds.cern.ch/record/1562777>.
- [390] **ATLAS** Collaboration, M. Capeans, G. Darbo, K. Einsweiller, M. Elsing, T. Flick, M. Garcia-Sciveres, C. Gemme, H. Pernegger, O. Rohne, and R. Vuillermet, “ATLAS Insertable B-Layer Technical Design Report,” Tech. Rep. CERN-LHCC-2010-013. ATLAS-TDR-19, 2010.  
<https://cds.cern.ch/record/1291633>.
- [391] **ATLAS** Collaboration, “Track Reconstruction Performance of the ATLAS Inner Detector at  $\sqrt{s} = 13$  TeV,” Tech. Rep. ATL-PHYS-PUB-2015-018, CERN, Geneva, 2015. <http://cds.cern.ch/record/2037683>.
- [392] J. Alonso-Gonzalez, A. de Giorgi, L. Merlo, and S. Pokorski, “Searching for BSM Physics in Yukawa Couplings and Flavour Symmetries,” [arXiv:2109.07490 \[hep-ph\]](https://arxiv.org/abs/2109.07490).
- [393] C. Grojean, A. Paul, and Z. Qian, “Resurrecting  $b\bar{b}h$  with kinematic shapes,” *JHEP* **04** (2021) 139, [arXiv:2011.13945 \[hep-ph\]](https://arxiv.org/abs/2011.13945).
- [394] W. Beenakker, S. Dittmaier, M. Kramer, B. Plumper, M. Spira, and P. M. Zerwas, “Higgs radiation off top quarks at the Tevatron and the LHC,” *Phys. Rev. Lett.* **87** (2001) 201805, [arXiv:hep-ph/0107081](https://arxiv.org/abs/hep-ph/0107081).
- [395] D. Fäh and N. Greiner, “Diphoton production in association with two bottom jets,” *Eur. Phys. J. C* **77** no. 11, (2017) 750, [arXiv:1706.08309 \[hep-ph\]](https://arxiv.org/abs/1706.08309).
- [396] F. Campanario, R. Roth, and D. Zeppenfeld, “QCD radiation in  $WH$  and  $WZ$  production and anomalous coupling measurements,” *Phys. Rev. D* **91** (2015) 054039, [arXiv:1410.4840 \[hep-ph\]](https://arxiv.org/abs/1410.4840).
- [397] S. Dawson, C. Jackson, L. Reina, and D. Wackerlo, “Higgs production in association with bottom quarks at hadron colliders,” *Mod. Phys. Lett. A* **21** (2006) 89–110, [arXiv:hep-ph/0508293](https://arxiv.org/abs/hep-ph/0508293).
- [398] T. Sjöstrand, S. Ask, J. R. Christiansen, R. Corke, N. Desai, P. Ilten, S. Mrenna, S. Prestel, C. O. Rasmussen, and P. Z. Skands, “An introduction to PYTHIA 8.2,” *Comput. Phys. Commun.* **191** (2015) 159–177, [arXiv:1410.3012 \[hep-ph\]](https://arxiv.org/abs/1410.3012).

- [399] **DELPHES 3** Collaboration, J. de Favereau, C. Delaere, P. Demin, A. Giammanco, V. Lemaître, A. Mertens, and M. Selvaggi, “DELPHES 3, A modular framework for fast simulation of a generic collider experiment,” *JHEP* **02** (2014) 057, [arXiv:1307.6346 \[hep-ex\]](https://arxiv.org/abs/1307.6346).
- [400] G. Heinrich, S. P. Jones, M. Kerner, G. Luisoni, and E. Vryonidou, “NLO predictions for Higgs boson pair production with full top quark mass dependence matched to parton showers,” *JHEP* **08** (2017) 088, [arXiv:1703.09252 \[hep-ph\]](https://arxiv.org/abs/1703.09252).
- [401] M. Abadi *et al.*, “TensorFlow: Large-scale machine learning on heterogeneous systems,” 2015. <https://www.tensorflow.org/>. Software available from tensorflow.org.
- [402] T. Chen and C. Guestrin, “XGBoost: A Scalable Tree Boosting System,” in *Proceedings of the 22nd ACM SIGKDD International Conference on Knowledge Discovery and Data Mining*, KDD ’16, p. 785–794. Association for Computing Machinery, New York, NY, USA, 2016. <https://dl.acm.org/doi/10.1145/2939672.2939785>.
- [403] L. Breiman, “Random forests,” *Machine Learning* **45** no. 1, (Oct, 2001) 5–32. <https://doi.org/10.1023/A:1010933404324>.
- [404] A. Fisher, C. Rudin, and F. Dominici, “All models are wrong, but many are useful: Learning a variable’s importance by studying an entire class of prediction models simultaneously,” *Journal of Machine Learning Research* **20** no. 177, (2019) 1–81, [arXiv:1801.01489](https://arxiv.org/abs/1801.01489). <http://jmlr.org/papers/v20/18-760.html>.
- [405] M. T. Ribeiro, S. Singh, and C. Guestrin, “"why should i trust you?": Explaining the predictions of any classifier,” in *Proceedings of the 22nd ACM SIGKDD International Conference on Knowledge Discovery and Data Mining*, KDD ’16, p. 1135–1144. Association for Computing Machinery, New York, NY, USA, 2016. <https://doi.org/10.1145/2939672.2939778>.
- [406] S. M. Lundberg and S.-I. Lee, “A unified approach to interpreting model predictions,” in *Advances in Neural Information Processing Systems*, I. Guyon, U. V. Luxburg, S. Bengio, H. Wallach, R. Fergus, S. Vishwanathan, and R. Garnett, eds., vol. 30, pp. 4765–4774. Curran Associates, Inc., 2017. [1705.07874](https://proceedings.neurips.cc/paper/2017/file/8a20a8621978632d76c43dfd28b67767-Paper.pdf). <https://proceedings.neurips.cc/paper/2017/file/8a20a8621978632d76c43dfd28b67767-Paper.pdf>.
- [407] L. S. Shapley, “Notes on the n-Person Game-II: The Value of an n-Person Game,” *Rand Corporation* (1951) . [https://www.rand.org/pubs/research\\_memoranda/RM0670.html](https://www.rand.org/pubs/research_memoranda/RM0670.html).
- [408] C. Molnar, *Interpretable Machine Learning*. Lulu, 2020. <https://christophm.github.io/interpretable-ml-book/>.

## Bibliography

---

- [409] D. Alvestad, N. Fomin, J. Kersten, S. Maeland, and I. Strümke, “Beyond Cuts in Small Signal Scenarios - Enhanced Sneutrino Detectability Using Machine Learning,” [arXiv:2108.03125 \[hep-ph\]](https://arxiv.org/abs/2108.03125).
- [410] A. S. Cornell, W. Doorsamy, B. Fuks, G. Harmsen, and L. Mason, “Boosted decision trees in the era of new physics: a smuon analysis case study,” [arXiv:2109.11815 \[hep-ph\]](https://arxiv.org/abs/2109.11815).
- [411] S. M. Lundberg, G. G. Erion, and S.-I. Lee, “Consistent Individualized Feature Attribution for Tree Ensembles,” *arXiv e-prints* (Feb., 2018) , [arXiv:1802.03888 \[cs.LG\]](https://arxiv.org/abs/1802.03888).
- [412] S. M. Lundberg, G. Erion, H. Chen, A. DeGrave, J. M. Prutkin, B. Nair, R. Katz, J. Himmelfarb, N. Bansal, and S.-I. Lee, “From local explanations to global understanding with explainable AI for trees,” *Nature Machine Intelligence* **2** no. 1, (2020) 56–67. <https://www.nature.com/articles/s42256-019-0138-9>.
- [413] A. Alves, T. Ghosh, and K. Sinha, “Can We Discover Double Higgs Production at the LHC?,” *Phys. Rev. D* **96** no. 3, (2017) 035022, [arXiv:1704.07395 \[hep-ph\]](https://arxiv.org/abs/1704.07395).
- [414] **ATLAS Collaboration** Collaboration, “Search for Higgs boson pair production in the two bottom quarks plus two photons final state in  $pp$  collisions at  $\sqrt{s} = 13$  TeV with the ATLAS detector,”
- [415] **ATLAS Collaboration** Collaboration, “Measurement prospects of the pair production and self-coupling of the Higgs boson with the ATLAS experiment at the HL-LHC,.”
- [416] J. Baglio, F. Campanario, S. Glaus, M. Mühlleitner, J. Ronca, and M. Spira, “ $gg \rightarrow HH$  : Combined uncertainties,” *Phys. Rev. D* **103** no. 5, (2021) 056002, [arXiv:2008.11626 \[hep-ph\]](https://arxiv.org/abs/2008.11626).
- [417] **CLICdp, CLIC** Collaboration, T. K. Charles *et al.*, “The Compact Linear Collider (CLIC) - 2018 Summary Report,” [arXiv:1812.06018 \[physics.acc-ph\]](https://arxiv.org/abs/1812.06018).
- [418] J. Gao, “Probing light-quark Yukawa couplings via hadronic event shapes at lepton colliders,” *JHEP* **01** (2018) 038, [arXiv:1608.01746 \[hep-ph\]](https://arxiv.org/abs/1608.01746).
- [419] L. M. Carpenter, T. Han, K. Hendricks, Z. Qian, and N. Zhou, “Higgs Boson Decay to Light Jets at the LHC,” *Phys. Rev. D* **95** no. 5, (2017) 053003, [arXiv:1611.05463 \[hep-ph\]](https://arxiv.org/abs/1611.05463).
- [420] R. Harnik, J. Kopp, and J. Zupan, “Flavor Violating Higgs Decays,” *JHEP* **03** (2013) 026, [arXiv:1209.1397 \[hep-ph\]](https://arxiv.org/abs/1209.1397).
- [421] Y. Nir and N. Seiberg, “Should squarks be degenerate?,” *Phys. Lett. B* **309** (1993) 337–343, [arXiv:hep-ph/9304307](https://arxiv.org/abs/hep-ph/9304307).

- [422] M. Leurer, Y. Nir, and N. Seiberg, “Mass matrix models: The Sequel,” *Nucl. Phys. B* **420** (1994) 468–504, [arXiv:hep-ph/9310320](#).
- [423] G. C. Branco, W. Grimus, and L. Lavoura, “Relating the scalar flavor changing neutral couplings to the CKM matrix,” *Phys. Lett. B* **380** (1996) 119–126, [arXiv:hep-ph/9601383 \[hep-ph\]](#).
- [424] A. Peñuelas and A. Pich, “Flavour alignment in multi-Higgs-doublet models,” *JHEP* **12** (2017) 084, [arXiv:1710.02040 \[hep-ph\]](#).
- [425] A. Falkowski, F. Riva, and A. Urbano, “Higgs at last,” *JHEP* **11** (2013) 111, [arXiv:1303.1812 \[hep-ph\]](#).
- [426] M. Ciuchini, E. Franco, S. Mishima, and L. Silvestrini, “Electroweak Precision Observables, New Physics and the Nature of a 126 GeV Higgs Boson,” *JHEP* **08** (2013) 106, [arXiv:1306.4644 \[hep-ph\]](#).
- [427] A. Falkowski and F. Riva, “Model-independent precision constraints on dimension-6 operators,” *JHEP* **02** (2015) 039, [arXiv:1411.0669 \[hep-ph\]](#).
- [428] J. de Blas, M. Ciuchini, E. Franco, S. Mishima, M. Pierini, L. Reina, and L. Silvestrini, “Electroweak precision observables and Higgs-boson signal strengths in the Standard Model and beyond: present and future,” *JHEP* **12** (2016) 135, [arXiv:1608.01509 \[hep-ph\]](#).
- [429] J. de Blas, M. Ciuchini, E. Franco, S. Mishima, M. Pierini, L. Reina, and L. Silvestrini, “The Global Electroweak and Higgs Fits in the LHC era,” *PoS EPS-HEP2017* (2017) 467, [arXiv:1710.05402 \[hep-ph\]](#).
- [430] J. Haller, A. Hoecker, R. Kogler, K. Mönig, T. Peiffer, and J. Stelzer, “Update of the global electroweak fit and constraints on two-Higgs-doublet models,” *Eur. Phys. J. C* **78** no. 8, (2018) 675, [arXiv:1803.01853 \[hep-ph\]](#).
- [431] B. Bhattacharya, A. Datta, D. London, and S. Shivashankara, “Simultaneous Explanation of the  $R_K$  and  $R(D^{(*)})$  Puzzles,” *Phys. Lett. B* **742** (2015) 370–374, [arXiv:1412.7164 \[hep-ph\]](#).
- [432] F. Feruglio, P. Paradisi, and A. Pattori, “Revisiting Lepton Flavor Universality in B Decays,” *Phys. Rev. Lett.* **118** no. 1, (2017) 011801, [arXiv:1606.00524 \[hep-ph\]](#).
- [433] A. Celis, J. Fuentes-Martin, A. Vicente, and J. Virto, “Gauge-invariant implications of the LHCb measurements on lepton-flavor nonuniversality,” *Phys. Rev. D* **96** no. 3, (2017) 035026, [arXiv:1704.05672 \[hep-ph\]](#).
- [434] D. Buttazzo, A. Greljo, G. Isidori, and D. Marzocca, “B-physics anomalies: a guide to combined explanations,” *JHEP* **11** (2017) 044, [arXiv:1706.07808 \[hep-ph\]](#).

- [435] J. Kumar, D. London, and R. Watanabe, “Combined Explanations of the  $b \rightarrow s\mu^+\mu^-$  and  $b \rightarrow c\tau^-\bar{\nu}$  Anomalies: a General Model Analysis,” *Phys. Rev.* **D99** no. 1, (2019) 015007, [arXiv:1806.07403 \[hep-ph\]](https://arxiv.org/abs/1806.07403).
- [436] M. Ciuchini, A. M. Coutinho, M. Fedele, E. Franco, A. Paul, L. Silvestrini, and M. Valli, “New Physics in  $b \rightarrow s\ell^+\ell^-$  confronts new data on Lepton Universality,” *Eur. Phys. J.* **C79** no. 8, (2019) 719, [arXiv:1903.09632 \[hep-ph\]](https://arxiv.org/abs/1903.09632).
- [437] J. Aebischer, W. Altmannshofer, D. Guadagnoli, M. Reboud, P. Stangl, and D. M. Straub, “B-decay discrepancies after Moriond 2019,” *Eur. Phys. J.* **C80** no. 3, (2020) 252, [arXiv:1903.10434 \[hep-ph\]](https://arxiv.org/abs/1903.10434).
- [438] C. Cornella, J. Fuentes-Martin, and G. Isidori, “Revisiting the vector leptoquark explanation of the B-physics anomalies,” *JHEP* **07** (2019) 168, [arXiv:1903.11517 \[hep-ph\]](https://arxiv.org/abs/1903.11517).
- [439] **LHCb** Collaboration, R. Aaij *et al.*, “Test of lepton universality using  $B^+ \rightarrow K^+\ell^+\ell^-$  decays,” *Phys. Rev. Lett.* **113** (2014) 151601, [arXiv:1406.6482 \[hep-ex\]](https://arxiv.org/abs/1406.6482).
- [440] **LHCb** Collaboration, R. Aaij *et al.*, “Test of lepton universality with  $B^0 \rightarrow K^{*0}\ell^+\ell^-$  decays,” *JHEP* **08** (2017) 055, [arXiv:1705.05802 \[hep-ex\]](https://arxiv.org/abs/1705.05802).
- [441] **LHCb** Collaboration, R. Aaij *et al.*, “Search for lepton-universality violation in  $B^+ \rightarrow K^+\ell^+\ell^-$  decays,” *Phys. Rev. Lett.* **122** no. 19, (2019) 191801, [arXiv:1903.09252 \[hep-ex\]](https://arxiv.org/abs/1903.09252).
- [442] **Belle** Collaboration, A. Abdesselam *et al.*, “Test of lepton flavor universality in  $B \rightarrow K^*\ell^+\ell^-$  decays at Belle,” [arXiv:1904.02440 \[hep-ex\]](https://arxiv.org/abs/1904.02440).
- [443] G. Hiller and M. Schmaltz, “ $R_K$  and future  $b \rightarrow s\ell\ell$  physics beyond the standard model opportunities,” *Phys. Rev.* **D90** (2014) 054014, [arXiv:1408.1627 \[hep-ph\]](https://arxiv.org/abs/1408.1627).
- [444] G. Hiller and M. Schmaltz, “Diagnosing lepton-nonuniversality in  $b \rightarrow s\ell\ell$ ,” *JHEP* **02** (2015) 055, [arXiv:1411.4773 \[hep-ph\]](https://arxiv.org/abs/1411.4773).
- [445] M. Bordone, G. Isidori, and A. Pattori, “On the Standard Model predictions for  $R_K$  and  $R_{K^*}$ ,” *Eur. Phys. J. C* **76** no. 8, (2016) 440, [arXiv:1605.07633 \[hep-ph\]](https://arxiv.org/abs/1605.07633).
- [446] G. D’Amico, M. Nardecchia, P. Panci, F. Sannino, A. Strumia, R. Torre, and A. Urbano, “Flavour anomalies after the  $R_{K^*}$  measurement,” *JHEP* **09** (2017) 010, [arXiv:1704.05438 \[hep-ph\]](https://arxiv.org/abs/1704.05438).
- [447] L.-S. Geng, B. Grinstein, S. Jäger, J. Martin Camalich, X.-L. Ren, and R.-X. Shi, “Towards the discovery of new physics with lepton-universality ratios of  $b \rightarrow s\ell\ell$  decays,” *Phys. Rev. D* **96** no. 9, (2017) 093006, [arXiv:1704.05446 \[hep-ph\]](https://arxiv.org/abs/1704.05446).

- [448] B. Capdevila, A. Crivellin, S. Descotes-Genon, J. Matias, and J. Virto, “Patterns of New Physics in  $b \rightarrow s\ell^+\ell^-$  transitions in the light of recent data,” *JHEP* **01** (2018) 093, [arXiv:1704.05340 \[hep-ph\]](#).
- [449] M. Ciuchini, A. M. Coutinho, M. Fedele, E. Franco, A. Paul, L. Silvestrini, and M. Valli, “On Flavourful Easter eggs for New Physics hunger and Lepton Flavour Universality violation,” *Eur. Phys. J.* **C77** no. 10, (2017) 688, [arXiv:1704.05447 \[hep-ph\]](#).
- [450] G. Hiller and I. Nisandzic, “ $R_K$  and  $R_{K^*}$  beyond the standard model,” *Phys. Rev. D* **96** no. 3, (2017) 035003, [arXiv:1704.05444 \[hep-ph\]](#).
- [451] A. K. Alok, A. Dighe, S. Gangal, and D. Kumar, “Continuing search for new physics in  $b \rightarrow s\mu\mu$  decays: two operators at a time,” *JHEP* **06** (2019) 089, [arXiv:1903.09617 \[hep-ph\]](#).
- [452] M. Algueró, B. Capdevila, A. Crivellin, S. Descotes-Genon, P. Masjuan, J. Matias, M. Novoa, and J. Virto, “Emerging patterns of New Physics with and without Lepton Flavour Universal contributions,” *Eur. Phys. J. C* **79** no. 8, (2019) 714, [arXiv:1903.09578 \[hep-ph\]](#).
- [453] K. Kowalska, D. Kumar, and E. M. Sessolo, “Implications for new physics in  $b \rightarrow s\mu\mu$  transitions after recent measurements by Belle and LHCb,” *Eur. Phys. J. C* **79** no. 10, (2019) 840, [arXiv:1903.10932 \[hep-ph\]](#).
- [454] A. Arbey, T. Hurth, F. Mahmoudi, D. M. Santos, and S. Neshatpour, “Update on the  $b \rightarrow s$  anomalies,” *Phys. Rev. D* **100** no. 1, (2019) 015045, [arXiv:1904.08399 \[hep-ph\]](#).
- [455] A. Datta, J. Kumar, and D. London, “The  $B$  anomalies and new physics in  $b \rightarrow se^+e^-$ ,” *Phys. Lett. B* **797** (2019) 134858, [arXiv:1903.10086 \[hep-ph\]](#).
- [456] S. Descotes-Genon, J. Matias, and J. Virto, “Understanding the  $B \rightarrow K^*\mu^+\mu^-$  Anomaly,” *Phys. Rev. D* **88** (2013) 074002, [arXiv:1307.5683 \[hep-ph\]](#).
- [457] S. Descotes-Genon, L. Hofer, J. Matias, and J. Virto, “Global analysis of  $b \rightarrow s\ell\ell$  anomalies,” *JHEP* **06** (2016) 092, [arXiv:1510.04239 \[hep-ph\]](#).
- [458] **LHCb** Collaboration, R. Aaij *et al.*, “Measurement of  $CP$ -averaged observables in the  $B^0 \rightarrow K^{*0}\mu^+\mu^-$  decay,” [arXiv:2003.04831 \[hep-ex\]](#).
- [459] A. Khodjamirian, T. Mannel, A. A. Pivovarov, and Y. M. Wang, “Charm-loop effect in  $B \rightarrow K^{(*)}\ell^+\ell^-$  and  $B \rightarrow K^*\gamma$ ,” *JHEP* **09** (2010) 089, [arXiv:1006.4945 \[hep-ph\]](#).
- [460] J. Lyon and R. Zwicky, “Resonances gone topsy turvy - the charm of QCD or new physics in  $b \rightarrow s\ell^+\ell^-?$ ,” [arXiv:1406.0566 \[hep-ph\]](#).

- [461] V. Chobanova, T. Hurth, F. Mahmoudi, D. Martinez Santos, and S. Neshatpour, “Large hadronic power corrections or new physics in the rare decay  $B \rightarrow K^* \mu^+ \mu^-$ ,” *JHEP* **07** (2017) 025, [arXiv:1702.02234 \[hep-ph\]](#).
- [462] T. Blake, U. Egede, P. Owen, K. A. Petridis, and G. Pomery, “An empirical model to determine the hadronic resonance contributions to  $\bar{B}^0 \rightarrow \bar{K}^{*0} \mu^+ \mu^-$  transitions,” *Eur. Phys. J. C* **78** no. 6, (2018) 453, [arXiv:1709.03921 \[hep-ph\]](#).
- [463] C. Bobeth, M. Chrzaszcz, D. van Dyk, and J. Virto, “Long-distance effects in  $B \rightarrow K^* \ell \ell$  from analyticity,” *Eur. Phys. J. C* **78** no. 6, (2018) 451, [arXiv:1707.07305 \[hep-ph\]](#).
- [464] S. Jäger and J. Martin Camalich, “Reassessing the discovery potential of the  $B \rightarrow K^* \ell^+ \ell^-$  decays in the large-recoil region: SM challenges and BSM opportunities,” *Phys. Rev. D* **93** no. 1, (2016) 014028, [arXiv:1412.3183 \[hep-ph\]](#).
- [465] M. Ciuchini, M. Fedele, E. Franco, S. Mishima, A. Paul, L. Silvestrini, and M. Valli, “ $B \rightarrow K^* \ell^+ \ell^-$  decays at large recoil in the Standard Model: a theoretical reappraisal,” *JHEP* **06** (2016) 116, [arXiv:1512.07157 \[hep-ph\]](#).
- [466] A. Arbey, T. Hurth, F. Mahmoudi, and S. Neshatpour, “Hadronic and New Physics Contributions to  $b \rightarrow s$  Transitions,” *Phys. Rev. D* **98** no. 9, (2018) 095027, [arXiv:1806.02791 \[hep-ph\]](#).
- [467] M. Chrzaszcz, A. Mauri, N. Serra, R. Silva Coutinho, and D. van Dyk, “Prospects for disentangling long- and short-distance effects in the decays  $B \rightarrow K^* \mu^+ \mu^-$ ,” *JHEP* **10** (2019) 236, [arXiv:1805.06378 \[hep-ph\]](#).
- [468] M. Ciuchini, A. M. Coutinho, M. Fedele, E. Franco, A. Paul, L. Silvestrini, and M. Valli, “Hadronic uncertainties in semileptonic  $B \rightarrow K^* \mu^+ \mu^-$  decays,” *Pos BEAUTY2018* (2018) 044, [arXiv:1809.03789 \[hep-ph\]](#).
- [469] T. Hurth, F. Mahmoudi, and S. Neshatpour, “On the new LHCb angular analysis of  $B \rightarrow K^* \mu^+ \mu^-$ : Hadronic effects or New Physics?,” [arXiv:2006.04213 \[hep-ph\]](#).
- [470] B. Capdevila, S. Descotes-Genon, J. Matias, and J. Virto, “Assessing lepton-flavour non-universality from  $B \rightarrow K^* \ell \ell$  angular analyses,” *JHEP* **10** (2016) 075, [arXiv:1605.03156 \[hep-ph\]](#).
- [471] N. Serra, R. Silva Coutinho, and D. van Dyk, “Measuring the breaking of lepton flavor universality in  $B \rightarrow K^* \ell^+ \ell^-$ ,” *Phys. Rev. D* **95** no. 3, (2017) 035029, [arXiv:1610.08761 \[hep-ph\]](#).
- [472] **Belle** Collaboration, S. Wehle *et al.*, “Lepton-Flavor-Dependent Angular Analysis of  $B \rightarrow K^* \ell^+ \ell^-$ ,” *Phys. Rev. Lett.* **118** no. 11, (2017) 111801, [arXiv:1612.05014 \[hep-ex\]](#).

- [473] M. Algueró, B. Capdevila, S. Descotes-Genon, P. Masjuan, and J. Matias, “What  $R_K$  and  $Q_5$  can tell us about New Physics in  $b \rightarrow s\ell\ell$  transitions?,” *JHEP* **07** (2019) 096, [arXiv:1902.04900 \[hep-ph\]](#).
- [474] **Belle-II** Collaboration, W. Altmannshofer *et al.*, “The Belle II Physics Book,” *PTEP* **2019** no. 12, (2019) 123C01, [arXiv:1808.10567 \[hep-ex\]](#). [Erratum: PTEP 2020, 029201 (2020)].
- [475] **LHCb** Collaboration, R. Aaij *et al.*, “Search for the rare decays  $B_s^0 \rightarrow e^+e^-$  and  $B^0 \rightarrow e^+e^-$ ,” *Phys. Rev. Lett.* **124** no. 21, (2020) 211802, [arXiv:2003.03999 \[hep-ex\]](#).
- [476] **CMS** Collaboration, S. Chatrchyan *et al.*, “Measurement of the  $B_s^0 \rightarrow \mu^+\mu^-$  Branching Fraction and Search for  $B^0 \rightarrow \mu^+\mu^-$  with the CMS Experiment,” *Phys. Rev. Lett.* **111** (2013) 101804, [arXiv:1307.5025 \[hep-ex\]](#).
- [477] **LHCb** Collaboration, R. Aaij *et al.*, “Measurement of the  $B_s^0 \rightarrow \mu^+\mu^-$  branching fraction and effective lifetime and search for  $B^0 \rightarrow \mu^+\mu^-$  decays,” *Phys. Rev. Lett.* **118** no. 19, (2017) 191801, [arXiv:1703.05747 \[hep-ex\]](#).
- [478] **ATLAS** Collaboration, M. Aaboud *et al.*, “Study of the rare decays of  $B_s^0$  and  $B^0$  mesons into muon pairs using data collected during 2015 and 2016 with the ATLAS detector,” *JHEP* **04** (2019) 098, [arXiv:1812.03017 \[hep-ex\]](#).
- [479] C. Bobeth, M. Gorbahn, T. Hermann, M. Misiak, E. Stamou, and M. Steinhauser, “ $B_{s,d} \rightarrow l^+l^-$  in the Standard Model with Reduced Theoretical Uncertainty,” *Phys. Rev. Lett.* **112** (2014) 101801, [arXiv:1311.0903 \[hep-ph\]](#).
- [480] A. Azatov, D. Bardhan, D. Ghosh, F. Sgarlata, and E. Venturini, “Anatomy of  $b \rightarrow c\tau\nu$  anomalies,” *JHEP* **11** (2018) 187, [arXiv:1805.03209 \[hep-ph\]](#).
- [481] A. K. Alok, D. Kumar, S. Kumbhakar, and S. Uma Sankar, “Solutions to  $R_D$ - $R_{D^*}$  in light of Belle 2019 data,” *Nucl. Phys. B* **953** (2020) 114957, [arXiv:1903.10486 \[hep-ph\]](#).
- [482] C. Murgui, A. Peñuelas, M. Jung, and A. Pich, “Global fit to  $b \rightarrow c\tau\nu$  transitions,” *JHEP* **09** (2019) 103, [arXiv:1904.09311 \[hep-ph\]](#).
- [483] R.-X. Shi, L.-S. Geng, B. Grinstein, S. Jäger, and J. Martin Camalich, “Revisiting the new-physics interpretation of the  $b \rightarrow c\tau\nu$  data,” *JHEP* **12** (2019) 065, [arXiv:1905.08498 \[hep-ph\]](#).
- [484] **BaBar** Collaboration, J. Lees *et al.*, “Measurement of an Excess of  $\overline{B} \rightarrow D^{(*)}\tau^-\bar{\nu}_\tau$  Decays and Implications for Charged Higgs Bosons,” *Phys. Rev. D* **88** no. 7, (2013) 072012, [arXiv:1303.0571 \[hep-ex\]](#).
- [485] **Belle** Collaboration, M. Huschle *et al.*, “Measurement of the branching ratio of  $\overline{B} \rightarrow D^{(*)}\tau^-\bar{\nu}_\tau$  relative to  $\overline{B} \rightarrow D^{(*)}\ell^-\bar{\nu}_\ell$  decays with hadronic tagging at Belle,” *Phys. Rev. D* **92** no. 7, (2015) 072014, [arXiv:1507.03233 \[hep-ex\]](#).

- [486] **LHCb** Collaboration, R. Aaij *et al.*, “Measurement of the ratio of the  $B^0 \rightarrow D^{*-} \tau^+ \nu_\tau$  and  $B^0 \rightarrow D^{*-} \mu^+ \nu_\mu$  branching fractions using three-prong  $\tau$ -lepton decays,” *Phys. Rev. Lett.* **120** no. 17, (2018) 171802, [arXiv:1708.08856 \[hep-ex\]](https://arxiv.org/abs/1708.08856).
- [487] L. Di Luzio, A. Greljo, and M. Nardecchia, “Gauge leptoquark as the origin of B-physics anomalies,” *Phys. Rev. D* **96** no. 11, (2017) 115011, [arXiv:1708.08450 \[hep-ph\]](https://arxiv.org/abs/1708.08450).
- [488] L. Calibbi, A. Crivellin, and T. Li, “Model of vector leptoquarks in view of the B-physics anomalies,” *Phys. Rev. D* **98** no. 11, (2018) 115002, [arXiv:1709.00692 \[hep-ph\]](https://arxiv.org/abs/1709.00692).
- [489] M. Bordone, C. Cornella, J. Fuentes-Martin, and G. Isidori, “A three-site gauge model for flavor hierarchies and flavor anomalies,” *Phys. Lett. B* **779** (2018) 317–323, [arXiv:1712.01368 \[hep-ph\]](https://arxiv.org/abs/1712.01368).
- [490] R. Barbieri and A. Tesi, “ $B$ -decay anomalies in Pati-Salam SU(4),” *Eur. Phys. J. C* **78** no. 3, (2018) 193, [arXiv:1712.06844 \[hep-ph\]](https://arxiv.org/abs/1712.06844).
- [491] N. Assad, B. Fornal, and B. Grinstein, “Baryon Number and Lepton Universality Violation in Leptoquark and Diquark Models,” *Phys. Lett. B* **777** (2018) 324–331, [arXiv:1708.06350 \[hep-ph\]](https://arxiv.org/abs/1708.06350).
- [492] J. Heeck and D. Teresi, “Pati-Salam explanations of the B-meson anomalies,” *JHEP* **12** (2018) 103, [arXiv:1808.07492 \[hep-ph\]](https://arxiv.org/abs/1808.07492).
- [493] B. Fornal, S. A. Gadom, and B. Grinstein, “Left-Right SU(4) Vector Leptoquark Model for Flavor Anomalies,” *Phys. Rev. D* **99** no. 5, (2019) 055025, [arXiv:1812.01603 \[hep-ph\]](https://arxiv.org/abs/1812.01603).
- [494] A. Crivellin, C. Greub, D. Müller, and F. Saturnino, “Importance of Loop Effects in Explaining the Accumulated Evidence for New Physics in B Decays with a Vector Leptoquark,” *Phys. Rev. Lett.* **122** no. 1, (2019) 011805, [arXiv:1807.02068 \[hep-ph\]](https://arxiv.org/abs/1807.02068).
- [495] A. Crivellin, D. Müller, and F. Saturnino, “Flavor Phenomenology of the Leptoquark Singlet-Triplet Model,” *JHEP* **06** (2020) 020, [arXiv:1912.04224 \[hep-ph\]](https://arxiv.org/abs/1912.04224).
- [496] M. Bordone, O. Catà, and T. Feldmann, “Effective Theory Approach to New Physics with Flavour: General Framework and a Leptoquark Example,” *JHEP* **01** (2020) 067, [arXiv:1910.02641 \[hep-ph\]](https://arxiv.org/abs/1910.02641).
- [497] **UTfit** Collaboration, M. Bona *et al.*, “Model-independent constraints on  $\Delta F = 2$  operators and the scale of new physics,” *JHEP* **03** (2008) 049, [arXiv:0707.0636 \[hep-ph\]](https://arxiv.org/abs/0707.0636).

- [498] L. Silvestrini and M. Valli, “Model-independent Bounds on the Standard Model Effective Theory from Flavour Physics,” *Phys. Lett. B* **799** (2019) 135062, [arXiv:1812.10913 \[hep-ph\]](https://arxiv.org/abs/1812.10913).
- [499] A. Greljo and D. Marzocca, “High- $p_T$  dilepton tails and flavor physics,” *Eur. Phys. J.* **C77** no. 8, (2017) 548, [arXiv:1704.09015 \[hep-ph\]](https://arxiv.org/abs/1704.09015).
- [500] M. J. Baker, J. Fuentes-Martín, G. Isidori, and M. König, “High-  $p_T$  signatures in vector-leptoquark models,” *Eur. Phys. J.* **C79** no. 4, (2019) 334, [arXiv:1901.10480 \[hep-ph\]](https://arxiv.org/abs/1901.10480).
- [501] L. Calibbi, A. Crivellin, and T. Ota, “Effective Field Theory Approach to  $b \rightarrow s\ell\ell^{(*)}$ ,  $B \rightarrow K^{(*)}\nu\bar{\nu}$  and  $B \rightarrow D^{(*)}\tau\nu$  with Third Generation Couplings,” *Phys. Rev. Lett.* **115** (2015) 181801, [arXiv:1506.02661 \[hep-ph\]](https://arxiv.org/abs/1506.02661).
- [502] I. Doršner, S. Fajfer, A. Greljo, J. Kamenik, and N. Košnik, “Physics of leptoquarks in precision experiments and at particle colliders,” *Phys. Rept.* **641** (2016) 1–68, [arXiv:1603.04993 \[hep-ph\]](https://arxiv.org/abs/1603.04993).
- [503] **Belle** Collaboration, S. Hirose *et al.*, “Measurement of the  $\tau$  lepton polarization and  $R(D^*)$  in the decay  $\bar{B} \rightarrow D^*\tau^-\bar{\nu}_\tau$ ,” *Phys. Rev. Lett.* **118** no. 21, (2017) 211801, [arXiv:1612.00529 \[hep-ex\]](https://arxiv.org/abs/1612.00529).
- [504] **Belle** Collaboration, A. Abdesselam *et al.*, “Measurement of  $\mathcal{R}(D)$  and  $\mathcal{R}(D^*)$  with a semileptonic tagging method,” [arXiv:1904.08794 \[hep-ex\]](https://arxiv.org/abs/1904.08794).
- [505] D. Bigi and P. Gambino, “Revisiting  $B \rightarrow D\ell\nu$ ,” *Phys. Rev. D* **94** no. 9, (2016) 094008, [arXiv:1606.08030 \[hep-ph\]](https://arxiv.org/abs/1606.08030).
- [506] F. U. Bernlochner, Z. Ligeti, M. Papucci, and D. J. Robinson, “Combined analysis of semileptonic  $B$  decays to  $D$  and  $D^*$ :  $R(D^{(*)})$ ,  $|V_{cb}|$ , and new physics,” *Phys. Rev. D* **95** no. 11, (2017) 115008, [arXiv:1703.05330 \[hep-ph\]](https://arxiv.org/abs/1703.05330). [Erratum: *Phys. Rev. D* 97, 059902 (2018)].
- [507] D. Bigi, P. Gambino, and S. Schacht, “ $R(D^*)$ ,  $|V_{cb}|$ , and the Heavy Quark Symmetry relations between form factors,” *JHEP* **11** (2017) 061, [arXiv:1707.09509 \[hep-ph\]](https://arxiv.org/abs/1707.09509).
- [508] S. Jaiswal, S. Nandi, and S. K. Patra, “Extraction of  $|V_{cb}|$  from  $B \rightarrow D^{(*)}\ell\nu_\ell$  and the Standard Model predictions of  $R(D^{(*)})$ ,” *JHEP* **12** (2017) 060, [arXiv:1707.09977 \[hep-ph\]](https://arxiv.org/abs/1707.09977).
- [509] J. F. Kamenik, Y. Soreq, and J. Zupan, “Lepton flavor universality violation without new sources of quark flavor violation,” *Phys. Rev. D* **97** no. 3, (2018) 035002, [arXiv:1704.06005 \[hep-ph\]](https://arxiv.org/abs/1704.06005).
- [510] P. J. Fox, I. Low, and Y. Zhang, “Top-philic  $Z'$  forces at the LHC,” *JHEP* **03** (2018) 074, [arXiv:1801.03505 \[hep-ph\]](https://arxiv.org/abs/1801.03505).

- [511] J. E. Camargo-Molina, A. Celis, and D. A. Faroughy, “Anomalies in Bottom from new physics in Top,” *Phys. Lett. B* **784** (2018) 284–293, [arXiv:1805.04917 \[hep-ph\]](#).
- [512] L. Di Luzio and M. Nardecchia, “What is the scale of new physics behind the  $B$ -flavour anomalies?,” *Eur. Phys. J. C* **77** no. 8, (2017) 536, [arXiv:1706.01868 \[hep-ph\]](#).
- [513] A. Buras, P. Gambino, M. Gorbahn, S. Jager, and L. Silvestrini, “Universal unitarity triangle and physics beyond the standard model,” *Phys. Lett. B* **500** (2001) 161–167, [arXiv:hep-ph/0007085](#).
- [514] A. L. Kagan, G. Perez, T. Volansky, and J. Zupan, “General Minimal Flavor Violation,” *Phys. Rev. D* **80** (2009) 076002, [arXiv:0903.1794 \[hep-ph\]](#).
- [515] A. Efrati, A. Falkowski, and Y. Soreq, “Electroweak constraints on flavorful effective theories,” *JHEP* **07** (2015) 018, [arXiv:1503.07872 \[hep-ph\]](#).
- [516] R. Coy, M. Frigerio, F. Mescia, and O. Sumensari, “New physics in  $b \rightarrow s\ell\ell$  transitions at one loop,” *Eur. Phys. J. C* **80** no. 1, (2020) 52, [arXiv:1909.08567 \[hep-ph\]](#).
- [517] M. Ciuchini, M. Fedele, E. Franco, S. Mishima, A. Paul, L. Silvestrini, and M. Valli, “ $B \rightarrow K^*\ell^+\ell^-$  in the Standard Model: Elaborations and Interpretations,” *PoS ICHEP2016* (2016) 584, [arXiv:1611.04338 \[hep-ph\]](#).
- [518] M. Ciuchini, M. Fedele, E. Franco, S. Mishima, A. Paul, L. Silvestrini, and M. Valli, “Knowns and Unknowns in the Predictions for  $B \rightarrow K^*\mu^+\mu^-$ ,” *Nucl. Part. Phys. Proc.* **285-286** (2017) 45–49.
- [519] M. Ciuchini, A. M. Coutinho, M. Fedele, E. Franco, A. Paul, L. Silvestrini, and M. Valli, “On hadronic uncertainties polluting the New Physics hunt in  $b \rightarrow s$  transitions,” *Nucl. Part. Phys. Proc.* **303-305** (2018) 8–13.
- [520] W. Buchmuller and D. Wyler, “Effective Lagrangian Analysis of New Interactions and Flavor Conservation,” *Nucl. Phys. B* **268** (1986) 621–653.
- [521] W. Altmannshofer, A. J. Buras, D. M. Straub, and M. Wick, “New strategies for New Physics search in  $B \rightarrow K^*\nu\bar{\nu}$ ,  $B \rightarrow K\nu\bar{\nu}$  and  $B \rightarrow X_s\nu\bar{\nu}$  decays,” *JHEP* **04** (2009) 022, [arXiv:0902.0160 \[hep-ph\]](#).
- [522] A. J. Buras, J. Girrbach-Noe, C. Niehoff, and D. M. Straub, “ $B \rightarrow K^{(*)}\nu\bar{\nu}$  decays in the Standard Model and beyond,” *JHEP* **02** (2015) 184, [arXiv:1409.4557 \[hep-ph\]](#).
- [523] S. Descotes-Genon, S. Fajfer, J. F. Kamenik, and M. Novoa-Brunet, “Implications of  $b \rightarrow s\mu\mu$  Anomalies for Future Measurements of  $B \rightarrow K^{(*)}\nu\bar{\nu}$  and  $K \rightarrow \pi\nu\bar{\nu}$ ,” [arXiv:2005.03734 \[hep-ph\]](#).

- [524] J. Aebischer, A. Crivellin, M. Fael, and C. Greub, “Matching of gauge invariant dimension-six operators for  $b \rightarrow s$  and  $b \rightarrow c$  transitions,” *JHEP* **05** (2016) 037, [arXiv:1512.02830 \[hep-ph\]](#).
- [525] C. Bobeth, A. J. Buras, A. Celis, and M. Jung, “Yukawa enhancement of  $Z$ -mediated new physics in  $\Delta S = 2$  and  $\Delta B = 2$  processes,” *JHEP* **07** (2017) 124, [arXiv:1703.04753 \[hep-ph\]](#).
- [526] G. Buchalla, A. J. Buras, and M. E. Lautenbacher, “Weak decays beyond leading logarithms,” *Rev. Mod. Phys.* **68** (1996) 1125–1144, [arXiv:hep-ph/9512380](#).
- [527] A. J. Buras, “Weak Hamiltonian, CP violation and rare decays,” in *Les Houches Summer School in Theoretical Physics, Session 68: Probing the Standard Model of Particle Interactions*, pp. 281–539. 6, 1998. [arXiv:hep-ph/9806471](#).
- [528] L. Silvestrini, “Effective Theories for Quark Flavour Physics,” in *Les Houches summer school: EFT in Particle Physics and Cosmology*. 5, 2019. [arXiv:1905.00798 \[hep-ph\]](#).
- [529] J. de Blas, G. Durieux, C. Grojean, J. Gu, and A. Paul, “On the future of Higgs, electroweak and diboson measurements at lepton colliders,” *JHEP* **12** (2019) 117, [arXiv:1907.04311 \[hep-ph\]](#).
- [530] B. Capdevila, A. Crivellin, C. A. Manzari, and M. Montull, “Explaining  $b \rightarrow sl^+l^-$  and the Cabibbo Angle Anomaly with a Vector Triplet,” [arXiv:2005.13542 \[hep-ph\]](#).
- [531] B. Belfatto, R. Beradze, and Z. Berezhiani, “The CKM unitarity problem: A trace of new physics at the TeV scale?,” *Eur. Phys. J. C* **80** no. 2, (2020) 149, [arXiv:1906.02714 \[hep-ph\]](#).
- [532] Y. Grossman, E. Passemar, and S. Schacht, “On the Statistical Treatment of the Cabibbo Angle Anomaly,” [arXiv:1911.07821 \[hep-ph\]](#).
- [533] A. Caldwell, D. Kollár, and K. Kröninger, “BAT - The Bayesian analysis toolkit,” *Computer Physics Communications* **180** no. 11, (Nov., 2009) 2197–2209, [arXiv:0808.2552 \[physics.data-an\]](#).
- [534] **SLD** Collaboration, K. Abe *et al.*, “First direct measurement of the parity violating coupling of the  $Z_0$  to the  $s$  quark,” *Phys. Rev. Lett.* **85** (2000) 5059–5063, [arXiv:hep-ex/0006019 \[hep-ex\]](#).
- [535] **ALEPH, DELPHI, L3, OPAL, LEP Electroweak** Collaboration, S. Schael *et al.*, “Electroweak Measurements in Electron-Positron Collisions at W-Boson-Pair Energies at LEP,” *Phys. Rept.* **532** (2013) 119–244, [arXiv:1302.3415 \[hep-ex\]](#).

- [536] **ATLAS** Collaboration, M. Aaboud *et al.*, “Measurement of the  $W$ -boson mass in  $pp$  collisions at  $\sqrt{s} = 7$  TeV with the ATLAS detector,” *Eur. Phys. J. C* **78** no. 2, (2018) 110, [arXiv:1701.07240 \[hep-ex\]](#). [Erratum: Eur.Phys.J.C 78, 898 (2018)].
- [537] **CMS** Collaboration, V. Khachatryan *et al.*, “Measurement of the t-channel single-top-quark production cross section and of the  $|V_{tb}|$  CKM matrix element in  $pp$  collisions at  $\sqrt{s}= 8$  TeV,” *JHEP* **06** (2014) 090, [arXiv:1403.7366 \[hep-ex\]](#).
- [538] **D0** Collaboration, V. Abazov *et al.*, “Measurement of  $\sin^2 \theta_{\text{eff}}^\ell$  and  $Z$ -light quark couplings using the forward-backward charge asymmetry in  $p\bar{p} \rightarrow Z/\gamma^* \rightarrow e^+e^-$  events with  $\mathcal{L} = 5.0 \text{ fb}^{-1}$  at  $\sqrt{s} = 1.96$  TeV,” *Phys. Rev. D* **84** (2011) 012007, [arXiv:1104.4590 \[hep-ex\]](#).
- [539] **ATLAS** Collaboration, M. Aaboud *et al.*, “Angular analysis of  $B_d^0 \rightarrow K^*\mu^+\mu^-$  decays in  $pp$  collisions at  $\sqrt{s} = 8$  TeV with the ATLAS detector,” *JHEP* **10** (2018) 047, [arXiv:1805.04000 \[hep-ex\]](#).
- [540] **CMS** Collaboration, V. Khachatryan *et al.*, “Angular analysis of the decay  $B^0 \rightarrow K^{*0}\mu^+\mu^-$  from  $pp$  collisions at  $\sqrt{s} = 8$  TeV,” *Phys. Lett. B* **753** (2016) 424–448, [arXiv:1507.08126 \[hep-ex\]](#).
- [541] **CMS** Collaboration, A. M. Sirunyan *et al.*, “Measurement of angular parameters from the decay  $B^0 \rightarrow K^{*0}\mu^+\mu^-$  in proton-proton collisions at  $\sqrt{s} = 8$  TeV,” *Phys. Lett. B* **781** (2018) 517–541, [arXiv:1710.02846 \[hep-ex\]](#).
- [542] **LHCb** Collaboration, R. Aaij *et al.*, “Angular analysis of the  $B^0 \rightarrow K^{*0}e^+e^-$  decay in the low- $q^2$  region,” *JHEP* **04** (2015) 064, [arXiv:1501.03038 \[hep-ex\]](#).
- [543] **LHCb** Collaboration, R. Aaij *et al.*, “Measurements of the S-wave fraction in  $B^0 \rightarrow K^+\pi^-\mu^+\mu^-$  decays and the  $B^0 \rightarrow K^*(892)^0\mu^+\mu^-$  differential branching fraction,” *JHEP* **11** (2016) 047, [arXiv:1606.04731 \[hep-ex\]](#). [Erratum: JHEP04,142(2017)].
- [544] A. Paul and D. M. Straub, “Constraints on new physics from radiative  $B$  decays,” *JHEP* **04** (2017) 027, [arXiv:1608.02556 \[hep-ph\]](#).
- [545] **HFLAV** Collaboration, Y. S. Amhis *et al.*, “Averages of  $b$ -hadron,  $c$ -hadron, and  $\tau$ -lepton properties as of 2018,” [arXiv:1909.12524 \[hep-ex\]](#).
- [546] **LHCb** Collaboration, R. Aaij *et al.*, “Differential branching fractions and isospin asymmetries of  $B \rightarrow K^{(*)}\mu^+\mu^-$  decays,” *JHEP* **06** (2014) 133, [arXiv:1403.8044 \[hep-ex\]](#).
- [547] **LHCb** Collaboration, R. Aaij *et al.*, “Angular analysis and differential branching fraction of the decay  $B_s^0 \rightarrow \phi\mu^+\mu^-$ ,” *JHEP* **09** (2015) 179, [arXiv:1506.08777 \[hep-ex\]](#).

- [548] **LHCb** Collaboration, R. Aaij *et al.*, “Measurement of the ratio of branching fractions  $BR(B_0 \rightarrow K^{*0}\gamma)/BR(B_{s0} \rightarrow \phi\gamma)$  and the direct CP asymmetry in  $B_0 \rightarrow K^{*0}\gamma$ ,” *Nucl. Phys.* **B867** (2013) 1–18, [arXiv:1209.0313 \[hep-ex\]](#).
- [549] T. Hurth, F. Mahmoudi, and S. Neshatpour, “Global fits to  $b \rightarrow s\ell\ell$  data and signs for lepton non-universality,” *JHEP* **12** (2014) 053, [arXiv:1410.4545 \[hep-ph\]](#).
- [550] **CCFR** Collaboration, S. Mishra *et al.*, “Neutrino tridents and W Z interference,” *Phys. Rev. Lett.* **66** (1991) 3117–3120.
- [551] **ATLAS** Collaboration, M. Aaboud *et al.*, “Search for new high-mass phenomena in the dilepton final state using  $36 \text{ fb}^{-1}$  of proton-proton collision data at  $\sqrt{s} = 13 \text{ TeV}$  with the ATLAS detector,” *JHEP* **10** (2017) 182, [arXiv:1707.02424 \[hep-ex\]](#).
- [552] **CMS** Collaboration, A. M. Sirunyan *et al.*, “Search for standard model production of four top quarks with same-sign and multilepton final states in proton–proton collisions at  $\sqrt{s} = 13 \text{ TeV}$ ,” *Eur. Phys. J. C* **78** no. 2, (2018) 140, [arXiv:1710.10614 \[hep-ex\]](#).
- [553] **ATLAS** Collaboration, M. Aaboud *et al.*, “Search for pair production of heavy vector-like quarks decaying into high- $p_T gy$  bosons and top quarks in the lepton-plus-jets final state in  $pp$  collisions at  $\sqrt{s} = 13 \text{ TeV}$  with the ATLAS detector,” *JHEP* **08** (2018) 048, [arXiv:1806.01762 \[hep-ex\]](#).
- [554] **CMS** Collaboration, A. M. Sirunyan *et al.*, “Search for vector-like leptons in multilepton final states in proton-proton collisions at  $\sqrt{s} = 13 \text{ TeV}$ ,” *Phys. Rev. D* **100** no. 5, (2019) 052003, [arXiv:1905.10853 \[hep-ex\]](#).
- [555] S. D. Thomas and J. D. Wells, “Phenomenology of Massive Vectorlike Doublet Leptons,” *Phys. Rev. Lett.* **81** (1998) 34–37, [arXiv:hep-ph/9804359](#).
- [556] F. del Aguila, J. de Blas, and M. Perez-Victoria, “Effects of new leptons in Electroweak Precision Data,” *Phys. Rev. D* **78** (2008) 013010, [arXiv:0803.4008 \[hep-ph\]](#).
- [557] K. Kannike, M. Raidal, D. M. Straub, and A. Strumia, “Anthropic solution to the magnetic muon anomaly: the charged see-saw,” *JHEP* **02** (2012) 106, [arXiv:1111.2551 \[hep-ph\]](#). [Erratum: JHEP10,136(2012)].
- [558] N. Kumar and S. P. Martin, “Vectorlike Leptons at the Large Hadron Collider,” *Phys. Rev. D* **92** no. 11, (2015) 115018, [arXiv:1510.03456 \[hep-ph\]](#).
- [559] P. N. Bhattacharya and S. P. Martin, “Prospects for vectorlike leptons at future proton-proton colliders,” *Phys. Rev. D* **100** no. 1, (2019) 015033, [arXiv:1905.00498 \[hep-ph\]](#).

- [560] J. C. Pati and A. Salam, “Lepton Number as the Fourth Color,” *Phys. Rev. D* **10** (1974) 275–289. [Erratum: Phys.Rev.D 11, 703–703 (1975)].
- [561] H. Georgi and S. L. Glashow, “Unity of all elementary-particle forces,” *Phys. Rev. Lett.* **32** (Feb, 1974) 438–441.  
<https://link.aps.org/doi/10.1103/PhysRevLett.32.438>.
- [562] D. Bećirević and O. Sumensari, “A leptoquark model to accommodate  $R_K^{\text{exp}} < R_K^{\text{SM}}$  and  $R_{K^*}^{\text{exp}} < R_{K^*}^{\text{SM}}$ ,” *JHEP* **08** (2017) 104, [arXiv:1704.05835](https://arxiv.org/abs/1704.05835) [hep-ph].
- [563] W. Buchmuller, R. Ruckl, and D. Wyler, “Leptoquarks in Lepton - Quark Collisions,” *Phys. Lett. B* **191** (1987) 442–448. [Erratum: Phys.Lett.B 448, 320–320 (1999)].
- [564] F. del Aguila, J. de Blas, and M. Perez-Victoria, “Electroweak Limits on General New Vector Bosons,” *JHEP* **09** (2010) 033, [arXiv:1005.3998](https://arxiv.org/abs/1005.3998) [hep-ph].
- [565] R. Alonso, B. Grinstein, and J. Martin Camalich, “Lepton universality violation and lepton flavor conservation in  $B$ -meson decays,” *JHEP* **10** (2015) 184, [arXiv:1505.05164](https://arxiv.org/abs/1505.05164) [hep-ph].
- [566] A. Angelescu, D. Bećirević, D. Faroughy, and O. Sumensari, “Closing the window on single leptoquark solutions to the  $B$ -physics anomalies,” *JHEP* **10** (2018) 183, [arXiv:1808.08179](https://arxiv.org/abs/1808.08179) [hep-ph].
- [567] **LHCb** Collaboration, R. Aaij *et al.*, “Physics case for an LHCb Upgrade II - Opportunities in flavour physics, and beyond, in the HL-LHC era,” [arXiv:1808.08865](https://arxiv.org/abs/1808.08865) [hep-ex].
- [568] **FCC** Collaboration, A. Abada *et al.*, “FCC Physics Opportunities: Future Circular Collider Conceptual Design Report Volume 1,” *Eur. Phys. J. C* **79** no. 6, (2019) 474.
- [569] **FCC** Collaboration, A. Abada *et al.*, “FCC-ee: The Lepton Collider: Future Circular Collider Conceptual Design Report Volume 2,” *Eur. Phys. J. ST* **228** no. 2, (2019) 261–623.
- [570] **LCC Physics Working Group** Collaboration, K. Fujii *et al.*, “Tests of the Standard Model at the International Linear Collider,” [arXiv:1908.11299](https://arxiv.org/abs/1908.11299) [hep-ex].
- [571] Z. Han and W. Skiba, “Effective theory analysis of precision electroweak data,” *Phys. Rev. D* **71** (2005) 075009, [arXiv:hep-ph/0412166](https://arxiv.org/abs/hep-ph/0412166).
- [572] F. del Aguila and J. de Blas, “Electroweak constraints on new physics,” *Fortsch. Phys.* **59** (2011) 1036–1040, [arXiv:1105.6103](https://arxiv.org/abs/1105.6103) [hep-ph].

- [573] J. de Blas, “Electroweak limits on physics beyond the Standard Model,” *EPJ Web Conf.* **60** (2013) 19008, [arXiv:1307.6173 \[hep-ph\]](https://arxiv.org/abs/1307.6173).
- [574] L. Berthier and M. Trott, “Towards consistent Electroweak Precision Data constraints in the SMEFT,” *JHEP* **05** (2015) 024, [arXiv:1502.02570 \[hep-ph\]](https://arxiv.org/abs/1502.02570).
- [575] J. de Blas, M. Ciuchini, E. Franco, S. Mishima, M. Pierini, L. Reina, and L. Silvestrini, “Electroweak precision constraints at present and future colliders,” *PoS ICHEP2016* (2017) 690, [arXiv:1611.05354 \[hep-ph\]](https://arxiv.org/abs/1611.05354).
- [576] S. Dawson and P. P. Giardino, “Electroweak and QCD corrections to  $Z$  and  $W$  pole observables in the standard model EFT,” *Phys. Rev. D* **101** no. 1, (2020) 013001, [arXiv:1909.02000 \[hep-ph\]](https://arxiv.org/abs/1909.02000).